UTS UNIVERSITY OF TECHNOLOGY SYDNEY

Feasibility and Energy Output of Wind Turbines in New South Wales

by Nour Khlaifat

Thesis submitted in fulfilment of the requirements for the degree of

Doctor of Philosophy

under the supervision of Dr. Ali Altaee
Co-Supervisor: Prof. John Zhou

University of Technology Sydney
Faculty of Engineering and Information Technology

June 2021

Certificate of Original Authorship

I, *NOUR KHLAIFAT* declare that this thesis is submitted in fulfilment of the requirements for the award of *Doctor of Philosophy*, in the *School of Civil and Environmental Engineering/Faculty of Engineering and Information Technology* at the University of Technology Sydney.

This thesis is wholly my own work unless otherwise referenced or acknowledged. In addition, I certify that all information sources and literature used are indicated in the thesis.

This document has not been submitted for qualifications at any other academic institution.

This research is supported by the Australian Government Research Training Program.

Signature of Student: Production Note:
Signature removed prior to publication.

Date: 23/05/2021

Acknowledgements

Pursuing a doctoral degree can be a long and challenging journey. Fortunately, I received a lot of help and support through this journey from the following wonderful people who made doing this thesis enjoyable and fruitful.

Primarily, I would thank God for being able to complete this project with success. I would like to say a special thank you to my supervisor, Dr Ali Altaee; His support, guidance, and overall insights in this field have made this an inspiring experience for me. The door to, Dr Ali Altaee office was always open whenever I ran into a trouble spot or had a question about my research or writing. He steered me in the right direction whenever he thought I needed it. Also, I would like to thank my supervisory committee, Prof. John Zhou, for his enthusiasm for the project, support, guidance, and patience; the thoughtful comments and recommendations on this dissertation. Without the supervisory panel's assistance and dedicated involvement in every step throughout the process, this research would have never been accomplished.

I would like to sincerely thank Isra University, Jordan, for its doctoral scholarship. I gratefully acknowledge the University of Technology Sydney (UTS) for awarding me the "FEIT Women in Engineering Top-up Scholarship." I am also thankful to the Faculty of Engineering and its staff for all the considerate guidance. I would like to acknowledge the Australian Government Bureau of Meteorology for supplying wind data.

I would like to thank my parents, family, daughter, and son, who have been very supportive and helpful in various stages of my Ph.D. research study.

Finally, To my soulmate husband – it would be an understatement to say that, as a family, we have experienced some ups and downs in the past four years. You did not let me every time I was ready to quit, and I am forever grateful. This dissertation stands as a testament to your unconditional love and encouragement.

List of Publications

Journal articles

[1] **N. Khlaifat**, A. Altaee, J. Zhou. Assessment of wind energy potential at Yanco, New South Wales, Australia. International Journal of Industrial Electronics and Electrical Engineering. 8 (2020) 26-30.

[2] **N. Khlaifat**, A. Altaee, J. Zhou, Y. Huang, A. Braytee. Optimization of a Small Wind Turbine for a Rural Area: A Case Study of Deniliquin, New South Wales, Australia. Energies. 13 (2020) 2292.

[3] **N. Khlaifat**, A. Altaee, J. Zhou, Y. Huang. A review of the key sensitive parameters on the aerodynamic performance of a horizontal wind turbine using Computational Fluid Dynamics modelling. AIMS Energy. 8 (2020) 493-524.

[4] **N. Khlaifat**, A. Altaee, J. Zhou, Y. Huang. Evaluation of wind resource potential using statistical analysis of probability density functions in New South Wales, Australia. Energy Sources, Part A: Recovery, Utilization, and Environmental Effects. (2020) 1-18.

[5] **N. Khlaifat**, A. Altaee, J. Zhou, Y. Huang. Statistical analysis of wind characteristic in Yanco agricultural institute, Australia. International Journal of Smart Grid and Clean Energy. 10 (2021) 1-7.

Abstract

The horizontal axis wind turbine (HAWT) is considered as the forefront of modern technology due to its reliability and cost-effectiveness. However, the efficiency of wind turbines is sometimes not at the desired level due to inefficient extraction of power from the wind by the turbine blades. Small wind turbines have emerged as a popular renewable energy source for remote sites and rural areas. Critical parameters influence the aerodynamics performance of small-sized HAWT, such as atmospheric conditions and the wind blade's geometry. The location also wields a significant effect on the annual energy production of wind turbines. When designing the HAWT for a specific area or region, accounting for environmental conditions could improve the power produced.

This study aims to optimize the performance of a small HAWT with 20 kW capacity under local wind conditions in rural New South Wales (NSW). Five rural locations in NSW have been selected for this study according to wind data availability. This study addresses the gap in our knowledge of combining wind turbine shape design and the available wind resources in Australia using updated and refined methodologies to maximize the annual energy production (AEP). One of the key objectives of this study is to understand the aerodynamics performance of small-scale HAWT under different conditions. The topic was investigated using computational fluid dynamics (CFD) modelling to understand the main aerodynamics characteristics of each section along the blade. Ansys Fluent (version 18.2, Canonsburg, PA, USA) was used to examine the aerodynamics performance of the HAWT. Four Reynolds Averaged Navier-Stokes (RANS) turbulence models, namely the Realizable k-ε, k-ω SST, Spalart-Allmaras and Transition SST models, are specifically researched. This is done to assess the ability to predict the flow over the wind turbine under different wind velocities where the flow varies from the attached to separated flow conditions. The CFD model was validated using the NREL CER measurement data. The results demonstrate that all RANS models expect Realizable k-ε can well predict the pressure coefficient in the area where the flow is still attached. The differences between turbulence models become significant as wind speed increases. The Transition SST model does agree with the experimental data on the prediction of pressure coefficient airfoil. The best performing CFD model will examine the mechanical output with different rotational speeds and variable pitch angles for the baseline wind turbine based on this numerical validation.

This study also highlights the feasibility of wind potential at five rural sites in NSW,

specifically Ballina, Merriwa, Deniliquin, Yanco, and Bega areas. The local wind conditions can fluctuate daily in many rural environments, and seasonal variations are significant. Therefore, accurate wind data models are necessary to find the best possible location for a wind turbine in an urban environment. The types of wind speed distribution function dramatically affect the output of the available wind energy and wind turbine performance at a particular site. Consequently, the accuracy of applying the four probability density functions was evaluated, namely Rayleigh, Weibull, gamma, and lognormal distributions. The outcomes showed Weibull provided the most accurate distribution.

Several numerical methods are applied to estimate the Weibull parameters depending on wind data measurement at the five sites. The accuracy and performance of numerical models have been evaluated using statistical indicators. The results showed that Deniliquin employed the maximum scale and shape parameters, while the minimum scale and shape parameters were utilized at the Bega area. Assessment of power density indicated that Deniliquin had a marginal wind speed resource, while Ballina, Bega, and Merriwa had poor wind resources. The wind data model of shape and scale parameters of 2.096 and 5.042 m/s, respectively, were used to improve the overall optimization process. The aerodynamics shape of the rotor was optimized to maximize the AEP in the Deniliquin region. The HARP_Opt (National Renewable Energy Laboratory, Golden, CO, USA) specifically enhanced the design variables concerning the shape of the blade, rated rotational speed, and pitch angle. The pitch angle remained at 0◦ while the rising wind speed improved rotor speed to 148.4482 rpm at rated speed. This optimization improved the AEP rate by 9.068% when compared to the original NREL design.

Contents

List of Tables

List of Figures

Definitions and Abbreviations

Acronyms

AEP	Annual energy production
AIC	Akaike information criterion
BEM	Blade element momentum
BIC	Bayesian information criterion
CER	Combined experiment rotor
CFD	Computational fluid dynamics
DES	Detached-eddy simulation
DNS	Direct numerical simulation
HARP_Opt	Horizontal axis rotor performance optimization
HAWT	Horizontal axis wind turbine
GA	Genetic algorithm
LES	Large eddy simulation
LIDAR	Light detection and ranging
MPPT	Maximum power point tracking
MRF	Moving reference frame
NACA	National Advisory Committee for Aeronautics
NREL	National Renewable Energy Laboratory
NSW	New South Wales
PMSG	Permanent magnet synchronous generator
RANS	Reynolds Averaged Navier-Stokes
RMSE	Root mean square error
SEDA	Sustainable Energy Development Authority
SMI	Sliding mesh interface

SST	Shear stress transport
VAWT	Vertical axis wind turbine
URANS	Unsteady Reynolds Averaged Navier-Stokes
WRSG	Wound rotor synchronous generator

Symbols

Re_{Θ}	Reynolds number
y^+	Dimensionless wall distance
y	First layer thickness
u_t	Friction velocity
$\overrightarrow{v_r}$	Velocity seen from the moving frame
$\overrightarrow{V_{sta}}$	Velocity seen from the stationary frame
$\bar{\bar{\tau}}_r$	Viscous stress
$\acute{u}_i$	Fluctuating velocity
$\bar{u}_i$	Mean velocity
ρ	Air density
$\cap$	Magnitude of the vorticity
ε	Turbulent dissipation rate
k	Turbulent kinetic energy
v_t	Turbulence eddy viscosity
ω	Turbulent dissipation rate
μ_t	Turbulence eddy viscosity
$Re_{\theta t}$	Transition momentum thickness Reynolds number
γ	Intermittency
V_{inelt}	Inlet velocity
A_{inelt}	Inlet area
V_{outlet}	Outlet velocity
A_{outlet}	Outlet area

Cp	Pressure coefficient
P_{static}	Local static pressure
P_{rel}	Free stream pressure
Ω	Rotational wind speed
V_{rel}	Relative wind speed
$\overline{U}$	Mean wind speed
U_i	Wind speed at i number of observations
N	Number of observations
σ_U	Standard deviation
s	Skewness
$f(U)$	Probability density function
$F(U)$	Cumulative distribution function
c	Scale parameter for Weibull distribution
K	Shape parameter for Weibull distribution
σ_c	Scale parameter for Rayleigh distribution
α_{Sh}	Shape parameter for lognormal distribution
β_c	Scale parameter for lognormal distribution
ξ	Shape parameter for gamma function
β_G	Scale parameter for gamma function
ψ	Digamma function
Γ	Gamma function
Q	Number of parameters in the model (dimension θ)
$\hat{\theta}$	Maximum likelihood estimate
$erf(U)$	Error function
R^2	Coefficient of determination
X^2	Chi-square
KS	Kolmogorov–Smirnov
$X_{observed}$	Frequency of observations

$X_{predicted}$	Frequency of predicted value from probability density function
E_{pf}	Energy pattern factor
$\overline{U^3}$	Mean of wind speed cubes
A	Area of actuator disc
P	Output power
V_O	Free wind speed
a	Axial induction factor
$Cpower$	Power coefficient
$c(r)$	Chord length
$\beta(r)$	Twist angle
φ	Flow angle
a'	Tangential induction factor
α	Angle of attack
θ_p	Pitch angle
F_n	Projected normal aerodynamics force on the rotor blade
F_t	Projected tangential aerodynamics force on the rotor blade
l	Lift force
d	Drag force
C_t	Tangential force coefficient
dT	Thrust force
C_T	Thrust coefficient
B	Number of blades
$\sigma(r)$	Local solidity
$U_{cut,in}$	Cut-in wind speed
$U_{cut,out}$	Cut-out wind speed
$X_{i\,min}$	Lower limit for the chord length and the twist angle
$X_{i\,max}$	Upper limit for the chord length and the twist angle
PD	Wind power density

h_0	Reference height
α_{power}	Power exponent
h_y	Desired height

Chapter One

1 Introduction

1.1 Research background and motivation

Energy demands are increasing as the world's population and industrial growth continue to expand [1]. The world's consumption of energy is predicted to increase by 56%, from 553 quadrillion kJ in 2010 to 865 quadrillion kJ in 2040 [2]. The most popular sources of energy consumption are fossil fuels, which release carbon dioxide and other harmful gases into the atmosphere and subsequently adding to the global warming crisis. The extensive consumption of fossil fuels is the primary source of carbon dioxide emissions in the atmosphere [3]. The CO_2 released from the burning of fossil fuels is estimated to rise from 1,000 million metric tons in 2010 to 36 billion metric tons in 2020 and may reach 45 billion metric tons by the end of 2040 [4]. The demands for clean energy sources have risen dramatically and rapidly due to people's greater environmental awareness, declining reliance on traditional fuel sources (especially fossil fuels), and strict government policies about environmental matters [5]. Of all the renewable energy sources, wind energy is one of the most popular emerging technologies due to its low cost and speedy global development [6].

The world's total installed power from wind energy increased from 318,914 MW at the end of 2013 to 597,000 MW by the end of 2018, and it is predicted to reach 840,000 MW by 2022 [4, 7, 8]. The World Wind Energy Association updated its statistics regarding added wind capacity during 2018 to around 50.1 GW, which is slightly less than the installed wind energy capacity in 2017, as shown in **Figure 1.1** (a) [4]. The installed wind capacity in 2017 achieved the fourth-largest installation level during the following record numbers between 2014 and 2019. Conversely, 2018 demonstrated the lowest market growth rate, about 9.1% from 2014, as shown in **Figure 1.1** (b). Again in 2018, the countries contributing the most to wind turbine energy were China

(34.81%), the USA (16.48%), and Germany (10.41%), as shown in **Figure 1.2** [9].

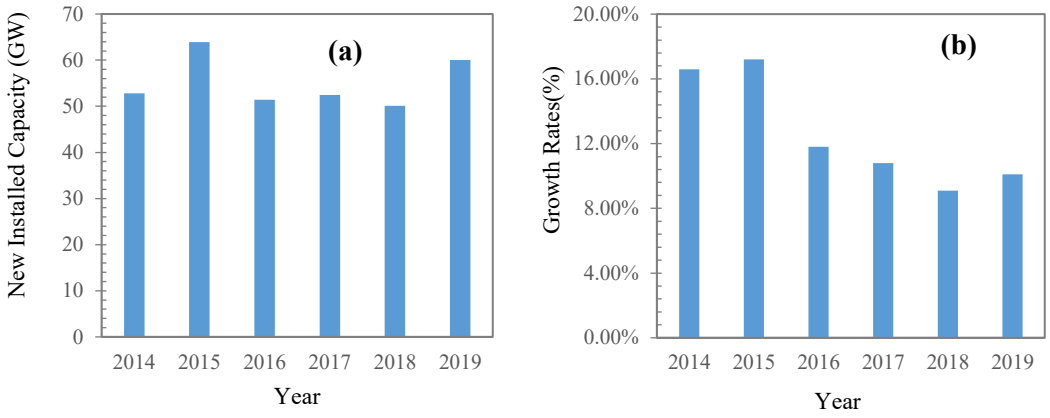

Figure 1.1. (a) New installed capacity of wind energy and **(b)** Growth rates of wind energy [4].

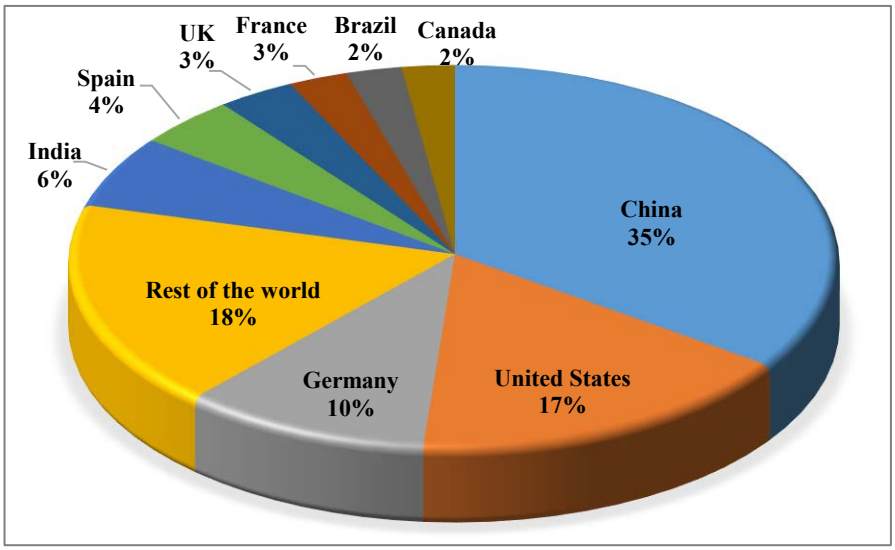

Figure 1.2. Countries' percentage of the world's wind energy market at the end of 2018.

The Australian population by 2016-2017 reached 24.6 million, and this represented an annual increase of 1.7%. This increase was reflected in the rising demand for total energy consumption, which grew in 2016-2017 by 1.1% to 6,146 petajoules. The energy growth was 65 petajoules which is equal to the amount of energy required to fill a petrol tank with a 55-litre capacity, 34 million times. In 2016-2017, the largest share (38%) of Australia's primary energy was oil, including liquefied petroleum gas, crude oil, and refined products. Coal is the second-largest energy source (32%), followed by natural gas (25%), while the remaining 6% of energy consumption

originates from renewable energy sources [10]. Therefore, incorporating renewable energy into the national grid is a timely concern for satisfying the rapidly growing energy demand and improving sustainability. The acceptability of renewable energy will continue to rise, reflecting government policy of renewable energy targets. The government initiative has encouraged several new projects for generating energy from renewable resources. Thus, from 2016 to 2017, renewable energy shared 16% of Australia's electricity generation. In 2017, renewable energy resources shared around 39 terawatt-hours (TWh) according to total electricity generation. Hydro is the largest source of renewable energy used for electricity generation, followed by wind energy [10].

Australia has a range of wind resources, and some locations are considered the best in the world. Wind energy is considered one of the cleanest renewable energy resources for electricity generation and has attracted much attention in Australia. Power from wind energy has grown greatly in the past decade, and on average, wind power generation rose by 17% per year during 2007-2017 [10]. Since different wind sites generally have different wind characteristics like mean wind speed, frequency, and direction, the energy output of a wind turbine changes accordingly. This study introduces an optimized design to obtain a three-HAWT suitable for environmental conditions at studied sites in NSW.

At the beginning of this research, an important step is to have a baseline of a small wind turbine model validated against experimental data. Currently, computational fluid dynamics (CFD) modelling has proved to be a useful tool to investigate the aerodynamics characteristics of the wind turbine. This research aims to predict the aerodynamics characteristics of the twisted/tapered horizontal wind turbine under different wind velocities where the flow varies from the attached state to a separated flow state. Investigated here are the following: effect of four Reynolds Averaged Navier-Stokes (RANS) turbulence models on predicting the aerodynamics characteristics of 20 kW wind turbine, and mechanical torque and blade pressure distribution for model validation with a comparison made to the National Renewable Energy Laboratory (NREL) test results.

Critical parameters influence the aerodynamics performance of a horizontal axis wind turbine (HAWT), such as atmospheric conditions and the wind blade's shape. The location has a significant effect on the power output of wind turbines. When designing the HAWT for a specific area or region, accounting for environmental conditions could improve the power output. The first step in wind resources utilization is identifying candidate sites for assessment, which includes surveying a large area of land or a selected region for a particular wind turbine location.

Thus, wind resource assessment is an essential step for predicting the AEP to determine the feasibility and profitability of a given wind power output at a particular site. The statistical analysis method for wind data serves to determine mean wind speed, probability density function, and annual energy production of wind turbines. In the last decade, some investigators studied the wind power potential of some sites and their wind characteristics in different locations around the world. Therefore, the wind speed distribution function dramatically influences the outcome of the available wind energy and wind turbine performance at a particular site. This research focuses on estimating the potential wind evaluation using different probability distribution functions in Australia, specifically in five rural areas in NSW. A technical assessment based on the wind data recorded at five meteorological stations, namely Deniliquin, Ballina, Bega, Merriwa and Yanco.

Another objective of this study, besides assessing wind resources in the five rural locations, is to define the modified shape of wind turbines that increases the AEP. Research has focused on aerodynamics optimization of the blade shape of the wind turbine; this is critical in the manufacturing and design of the wind turbine. This study aimed to optimize the performance of a 20 kW HAWT under local wind conditions in New South Wales (NSW), Australia. A genetic algorithm is used to optimize the wind turbine's shape and improve the annual energy production (AEP) depending on the wind data reported in Australia.

1.2 Research methodology

Various attempts have been carried out to investigate the aerodynamics performance

of the wind turbine using CFD. There are many turbulence models employed for discretizing the flow fields around the wind turbine. To date, there is no unique model that predicts all physical characteristics of turbulent flow. In the present research work, the wind turbine model is simulated by CFD using Ansys Fluent solver. Four different RANS turbulence models were studied to investigate their sensitivity in predicting the wind turbine's performance. The comparison between models investigates the effect of four RANS turbulence models on predicting the aerodynamics characteristics of the twisted wind turbine. Depending on the numerical validation, the best performing CFD model will examine the mechanical output with different rotational speeds and variable pitch angles to compared the optimized blade designs.

Defining a suitable environmental locale has a significant effect on the wind turbines' power output. The geometry of the blade of small wind turbines exerts a high impact on the performance of the wind turbine. This study aims to optimize a 20 kW wind turbine suitable for the natural environment in NSW, using the horizontal axis rotor performance optimization (HARP_Opt) code to maximize AEP, depending on the probability density function.

1.3 Research Objectives

Wind as a resource varies from one place to another and has seasonal and daily variations for even the same location. This explains the need to analyse the feasibility and potential of wind energy at a specific site. As discussed before, some statistical analyses of wind data resources will be investigated in different parts of NSW. The main objective of this study is to evaluate the feasibility of wind potential at five sites in that state. This research comprehensively investigates wind power density and the fitness of different probability density functions. Wind direction and frequency are assessed for selected sites using wind rose plots. Wind energy potential is evaluated to define the feasibility of wind resources in rural and remote areas. This study addresses the gap in our knowledge of combining wind turbine design and the available wind resources in Australia using updated and refined methodologies to maximize wind turbines' annual energy production.

The NREL CER (combined experiment rotor) wind turbine will use the original blade geometry design. The numerical modelling of wind turbines will investigate the mechanical output at different rotational speeds and variable pitch angles. The most accurate RANS model was selected for use when the output power of the original blade geometry was compared with the optimized blade design. The detailed objectives of this project are as follows:

- Develop a CFD model for the flow around wind turbine using Ansys Fluent (version18.2, Canonsburg, PA, USA). The blade geometry will be created using SolidWorks.
- Model validation against the NREL CER experiment and evaluate the sensitivity and reliability of different RANS turbulence models' accuracy in numerical modelling.
- Define the wind data model and do a statistical analysis of wind data at five sites in NSW, Australia.
- Assess the accuracy of four different probability density functions: Rayleigh, Weibull, gamma, and lognormal, using different statistical parameters so the goodness-of-fit to define suitable probability distribution functions can be evaluated. Furthermore, wind direction and frequency are assessed for selected sites using wind rose plots.
- After defining the most accurate probability density functions according to the statistical analysis of wind speed data, another investigation using seven numerical methods presents their performance for modelling the wind speed.
- The validated wind turbine model of 20 kW, which has been previously modeled in Ansys Fluent, is used as a baseline for the optimization process. This process's objective is to maximize the AEP of the 20 kW wind turbine depending on wind speed data. The new modified shape of the blade design has been defined using chord and twist distribution along the blade.

1.4 Thesis outline

The thesis comprises the following chapters, which are summarized here.

Chapter Two reviews the background information on wind energy potentials, CFD techniques, wind probability distribution models, and wind turbine optimization by addressing our knowledge gaps on this topic.

Chapter Three introduces the methodology of CFD modelling using selected turbulence models, statistical analysis of wind data using probability density functions, and optimization processes.

Chapter Four presents and discusses the numerical modelling of the horizontal wind turbine under different conditions.

Chapter Five assesses the wind speed profile using four probability distribution functions to evaluate the most suitable function, based on a statistical analysis of wind data recorded from meteorological stations in Ballina, Merriwa, Deniliquin, Yanco and Bega areas.

Chapter Six presents and discusses an in-depth statistical evaluation of wind characteristics and energy potential using seven numerical methods for adjusting the Weibull distribution of wind speeds at five sites in NSW, Australia.

Chapter Seven discusses the optimization results of the modified blade shape design using chord and twist distribution along the blade

Chapter Eight concludes this thesis by summarizing the outcomes of each chapter and making recommendations on future work in this field.

Chapter Two

2 Literature Review

2.1 Statistics of wind power

Renewable energy is now a key ‘buzz term’ that refers to alternatives to fossil fuels and coal, but it still not growing as fast as it should. Climate change is a real environmental threat caused by the increased emissions of greenhouse gases from burning fossil fuels, making renewable energies such as wind, solar power, water, or bio-oils much more viable, sustainable and urgently required. Climate change is gradually altering the dynamics of the Earth, not helped by the threat of air pollution that is generating higher than normal temperatures that also threaten the ozone layer. The increase in greenhouse gases means that the natural greenhouse effect that keeps the earth warm enough for life to exist is seriously compromised. The burning of fossil fuels such as oil, coal, and natural gas adds extra CO_2 to the Earth’s atmosphere, triggering human-made climate change, making the planet hotter each day. Adding more CO_2 to the planet’s atmosphere is akin to putting on a jumper over the Earth and making it hotter. The effects of global warming caused the polar ice caps to melt and harm the climate and all living creatures.

For the past 3000 years, people have used windmills to pump water or grind grains. However, it was only in the late nineteenth century that Charles Brush in the USA, with the help of Poul la Cour's research from Denmark, managed to construct the first of what is known today as wind turbines able to generate 12 kW of electricity. The use of wind energy to produce electricity was not widespread during the 20th century, except for the development of one 1250 kW wind turbine by Smith-Putnam in the USA [11]. From an economic perspective, what drives the growth of wind capacity generators is the cost of other sources compared to wind. As discussed in the introduction, wind power is a precise power-generating technology and helps to mitigate air pollution caused by other unclean resources. Clean energy was one of the

significant motives for China to investigate developing wind stations, given that the country must overcome extremely high levels of pollution caused by coal combustion [11].

The wind industry's growth rate is limited to how many wind turbines can be manufactured each year. Technical improvements indicate that wind turbines are now much larger, more productive, and use intelligent technology. Rotor diameters and hub heights have increased, which makes it possible to generate more energy per turbine. Advances in technology suggest that fewer turbines are required to generate the same energy, and wind farms frequently have advanced adaptive capability [12]. Also, increasing investment in wind energy projects will lead to a broad and interconnected base of international projects that will benefit millions of people worldwide.

In the world's most developed parts today, renewables are now low-cost sources of power generation. As costs proceed to drop for solar and wind technologies, this will help many developing countries. According to the International Renewable Energy Agency (IRENA) cost database, since 2010, the weighted average levelized cost of electricity (LCOE) from bioenergy, geothermal, hydropower, onshore and offshore wind projects has dropped rapidly. It is predicted that the LCOE for a renewable energy source for electricity generation will be less than fossil fuel-fired electricity generation costs within just a few years. The global weighted-average expense of power from all commercially accessible renewable energy production technologies encountered fell in 2018, with concentrating solar power (CSP), bioenergy, solar Photovoltaics (PV) and onshore wind experiencing the most significant declines. In 2018, with new wind power projects capability in China, South Africa, and Morocco, the global weighted mean LCOE for onshore wind projects dropped by 22% from 2010 to 2017. The global weighted mean LCOE for offshore wind costs declined by 13% [13].

According to the IRENA report, by 2025, the LCOE of CSP will reduce by at least 43%, while onshore wind and offshore wind will decrease by at least 26% and 35%, respectively [14]. The global weighted average LCOE of onshore wind plants commissioned in 2017 was US$ 0.06/ kW-hr, while it was US$ 0.05 kW-hr for

hydropower plants. At the end of 2017, offshore wind projects were commissioned, and the global weighted average LCOE was US$ 0.14/ kW-hr, while for CSP, it was US$ 0.22 / kW-hr [13]. Current sales data suggest that by the end of 2020, CSP and offshore wind will supply electricity costs between the ranges of US$ 0.06 to US$ 0.10/ kW-hr [13].

Table 2.1. Global weighted average solar and wind power investment costs, capacity factors and LCOEs, 2015 and 2025 [14].

	Global weighted average data								
	Investment costs (2015 US$ /kW)		Percentage change	Capacity factor		Percentage change[2]	LCOE (2015 US$ / kW-hr)		Percentage change
	2015	2025		2015	2025		2015	2025	
Solar PV	1810	790	-57%	18%	19%	8%	0.13	0.06	-59%
CSP (PTC: parabolic trough collector)	5550	3700	-33%	41%	45%	8.4%	0.15	0.09	-37%
CSP: (ST:Solar tower)	5700	3600	-37%	46%	49%	7.6%	0.15	0.08	-43%
Onshore wind	1560	1370	-12%	27%	30%	11%	0.07	0.05	-26%
Offshore wind	4650	3950	-15%	43%	45%	4%	0.18	0.12	-35%

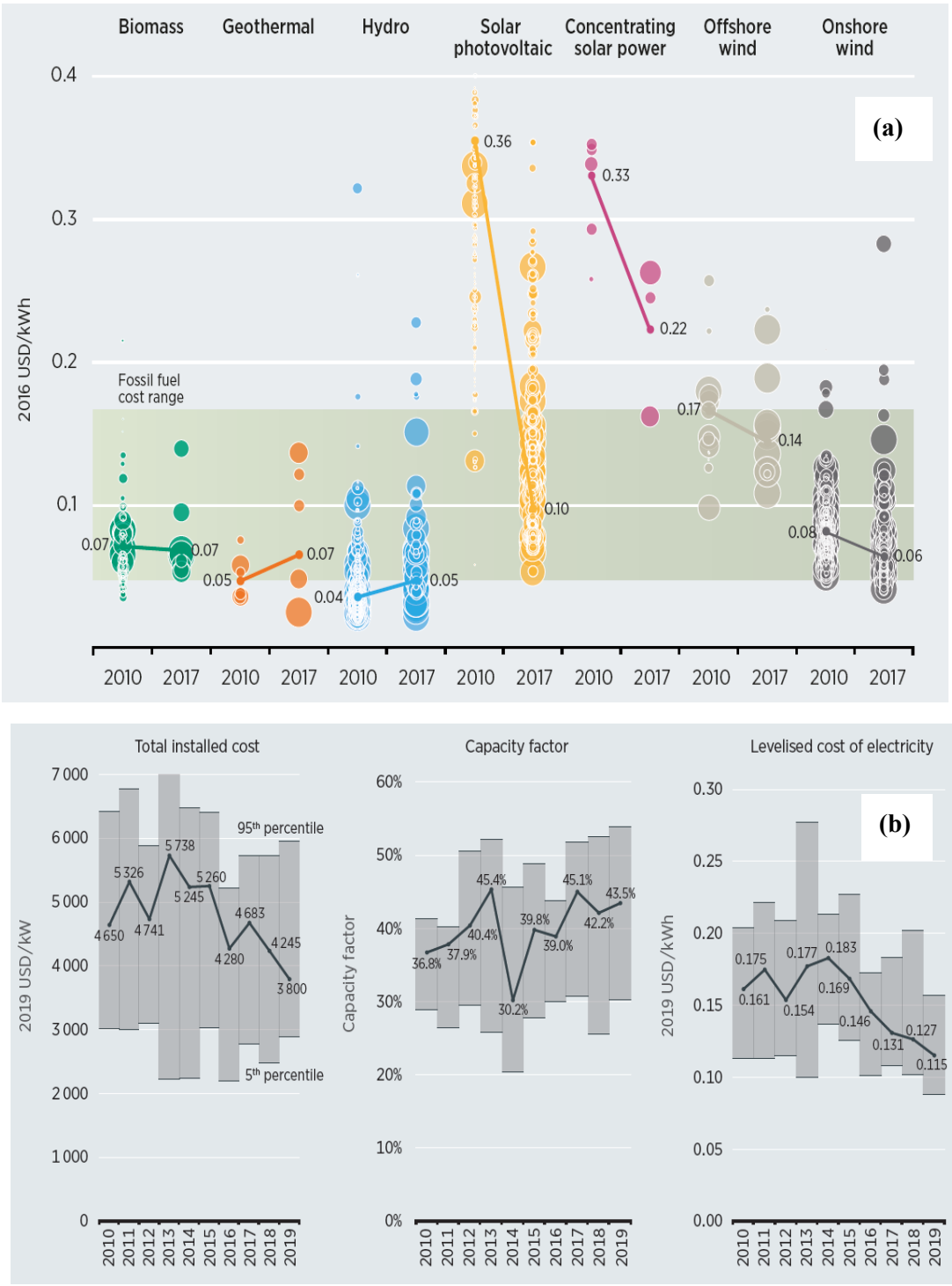

Figure 2.1. (a) Global levelized cost of electricity from utility-scale renewable power generation technologies, 2010-2017 and **(b)** Global weighted average total installed costs, capacity factors and LCOE for offshore wind power, 2010-2019 [13].

While turbine power has been operating in Australia for years, wind power generation on a utility scale did not make its mark until the 1980s. In the following decade, wind farm development gradually increased. By the start of the 2000s, there were

significantly much more plans with much larger production quantities envisaged. According to the Australian Renewable Energy Agency (ARENA), at the end of 2018, 94 wind farms were operating in Australia, producing 5,679MW in cumulative energy capacity. With an additional 20 projects scheduled to be constructed in 2019, this number will increase considerably soon [15]. In **Table 2.2**, the top largest wind farms currently operating in Australia are listed.

Table 2.2. Top largest wind farms in NSW, Victoria, Queensland, South Australia, Western Australia, and Tasmania.

Project	Ownership	Capacity
NSW		
Rye Park Wind Farm	Tilt Renewables	327 MW
Yass Valley Wind Farm	Epuron	284 MW
Sapphire Wind Farm	CWP Renewables	270 MW
Silverton Wind Farm	PARF	200 MW
White Rock Wind Farm	Goldwind-CECEP	175 MW
Gullen Range Wind Farm	Goldwind-JNEC	165 MW
Capital Wind Farm	Infigen Energy	141 MW
Crudine Ridge	Wind Prospect CWP	135 MW
Boco Rock Wind Farm	Wind Prospect CWP	113 MW
Bodangora Wind Farm	Infigen Energy	113 MW
Victoria		
Macarthur Wind Farm	AGL Energy-Meridian Energy	420 MW
Murra Warra Wind Farm	RES Australia	350 MW
Moorabool Wind Project	WestWind Energy	321 MW
Ararat Wind Farm	RES Australia	240 MW
Berrybank	Union Fenosa Wind Australia	237 MW
Waubra Wind Farm	Acciona Energy-ANZ Infra	192 MW
Lal Lal Wind Farm	WestWind Energy	150 MW

Crowlands/Glenlofty	Pacific Hydro	140 MW
Ryan's Corner	Union Fenosa Wind Australia	134 MW
Mt Gellibrand Wind Farm	Acciona Energy	132 MW
Queensland		
Coopers Gap	AGL Energy	460 MW
Crows Nest Wind Farm	Energreen	200 MW
Mt Emerald Wind Farm	RATCH-Australia	180 MW
Forsayth Wind Farm	Infigen Energy	75 MW
High Road Wind Farm	Transfield Services	50 MW
Kennedy Energy Park	Windlab	41 MW
Windy Hill Wind Farm	RATCH-Australia	12 MW
South Australia		
Snowtown Wind Farm	Trust Power	368 MW
Hornsdale Wind Farm	Neoen	213 MW
Lake Bonney 2	Infigen Energy	159 MW
Hallett 4 Wind Farm	AGL Energy	132 MW
Lincoln Gap	Wing Energy Solutions	124 MW
Waterloo Wind Farm	Energy Australia	111 MW
Woakwine	Beacon Energy	100 MW
Hallet 1 Wind Farm	AGL Energy	94 MW
Wattle Point Wind Farm	Infrastructure Capital Group	91 MW
Lake Bonney 1	Infigen Energy	80 MW
Western Australia		
Collgar Wind Farm	UBS-Rest Super	206 MW
Walkaway Wind Farm	Infigen Energy	89 MW
Emu Downs Wind Farm	APA Group	80 MW
Mumbida Wind Farm	Energy Infrastructure Trust	55 MW
Albany Wind Farm	Verve Energy	35 MW
Nine Mile Wind Farm	Synergy	3.6 MW

Mt Barker Community Wind Farm	Mt Barker Power	2.4 MW
Ten Mile Lagoon Wind Farm	Synergy	2 MW
Kalbarri Wind Project	Synergy	1.6MW
Denmark Community Wind Farm	Denmark Community Wind Farm	1.6 MW
Tasmania		
Musselroe Wind Farm	Hydro Tasmania	168 MW
Studland Bay Wind Farm	Woolnorth Wind Farm Holdings	75 MW
Bluff Point Wind Farm	Woolnorth Wind Farm Holdings	65 MW
King Island Wind Farm	Hydro Tasmania	2.5 MW

The state of NSW, Australia, uses different technologies to generate energy with various technical, operating, and economic characteristics. Traditionally, coal has been used as the main source of power used to generate, for example, electricity. Coal is still the primary fuel source for electricity as it covers 80% of the state's electricity supply. **Figure 2.2** illustrates the source of NSW's power generation for 2018-2019 as follows [16].

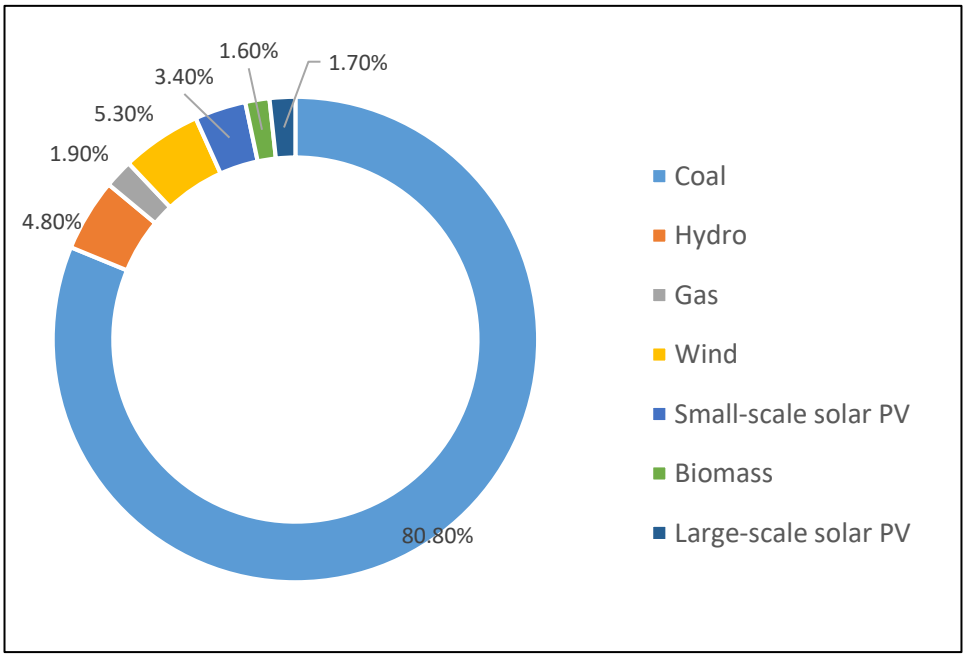

Figure 2.2. NSW's electricity was generated in 2018-2019 [16].

One-quarter of Australia's total energy consumption occurs in NSW, using natural gas, coal, and renewable resources. Two indicators that will reveal the energy consumption in NSW are the final energy consumption indicator and the energy used by fuel type and sector indicator. The energy supplied to the end-user is called the final energy. Final energy consumption includes secondary energy, for example, electricity, and therefore excludes using gas and coal to generate electricity. Figure 2.3 (a) presents the sectoral trends in the final energy consumed for the ACT and NSW economies. Meanwhile, Figure 2.3 (b) presents the final energy consumption by sector and fuel type (petroleum, electricity, gas, coal, and renewable fuels) in NSW and the ACT in 2015–2016 [17].

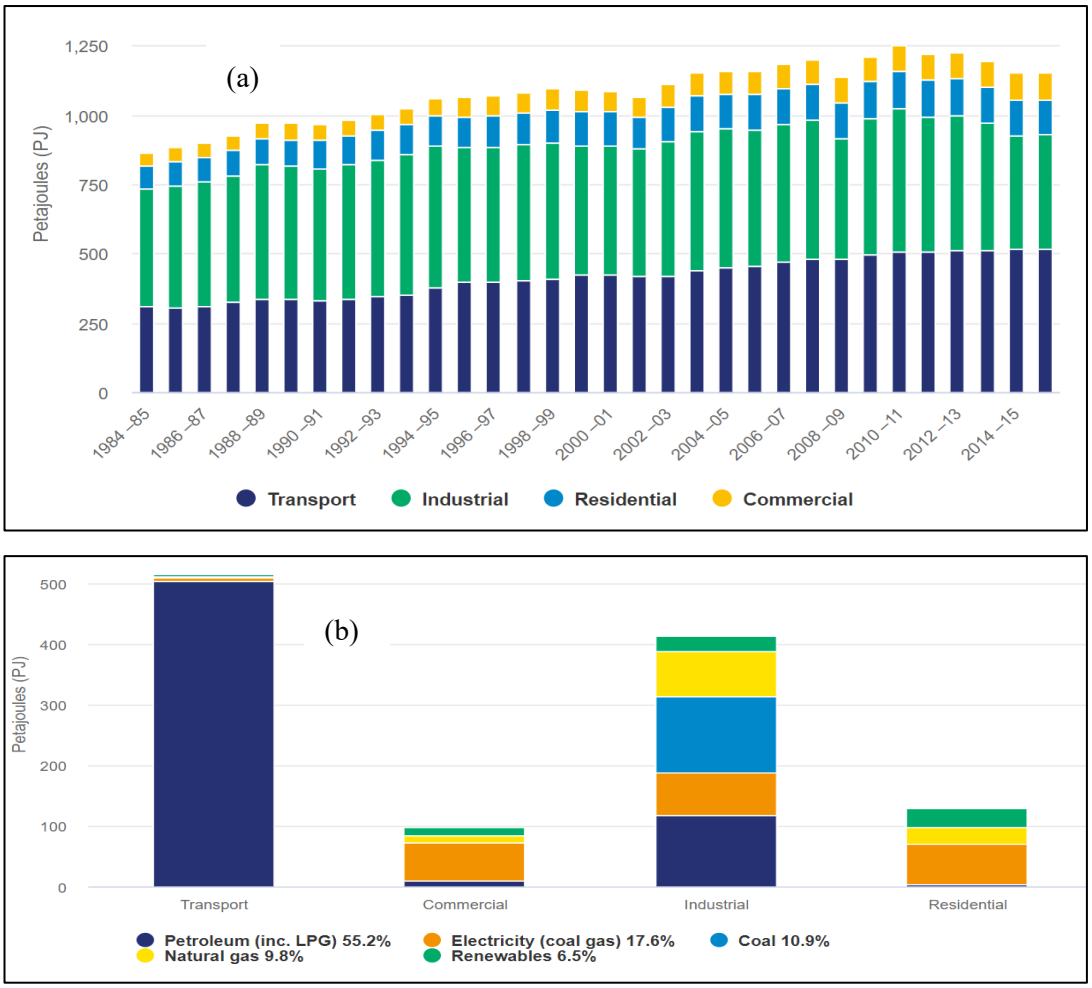

Figure 2.3 (a) Final energy consumption by sector in NSW and the ACT 1984–1985 to 2015– 2016 and **(b)** Final energy consumption for each sector by fuel type, NSW and the ACT, 2015–2016 [17].

2.2 Wind turbine technology

Conventional wind turbines are classified in different ways based on various criteria. According to the rotation axis as noted in [18], the first classification is the HAWT in which the rotating axis of the blade is parallel to the wind stream [19]. In contrast, for the vertical axis wind turbine (VAWT), the rotating axis of the blade is vertical to the wind stream. HAWT dominates the wind industry due to its greater efficiency and energy output when compared to the VAWT [20]. The second classification is based on the magnitude of a wind speed or the Reynolds number (Re_Θ) at which they operate, where is classified as a Low-speed wind turbine ($Re_\Theta < 10^3$), Medium-speed wind turbine ($10^3 < Re_\Theta < 10^5$), and High-speed wind turbine ($Re_\Theta > 10^5$) [21]. The third classification is based on the diameter of the blade [22] into: micro-scale wind turbine (μSWT) (diameter < 0.1 m); small-scale (μSWT< diameter <1 m); mid-scale (1 m < diameter <5 m); and large-scale diameter >5 m. The fourth classification is based on the positioning of the turbine to the flow direction [23]: upwind positioned wind turbine and downwind-positioned wind turbines. The fifth classification is based on the type of aerodynamics forces [20]: drag-type wind turbine and lift-type wind turbine. The sixth classification is based on the number of blades on the rotor, i.e. single-bladed wind turbine or multi-bladed wind turbine. The seventh classification is based on the wind turbine's location [24], either offshore or onshore. The eighth classification is predicated on the wind turbine's connection to the grid [25], as either an on-grid or off-grid technology.

Wind turbine designs depend on aerodynamic conditions and the number of blades in the wind turbine. However, the 3-bladed upwind horizontal wind turbine is the most popular design [26]. As shown in **Figure 2.4**, the foundation component is the tower, and this tower holds the nacelle, which contains the transmission system, generator, and control systems. The transmission system transmits the mechanical torque from the rotor to the generator, including the gearbox and mechanical brake system [27]. This mechanical power is converted into electrical energy using an electromagnetic component called a generator [28]. Two types of generators are used throughout the

industry sector: i) wound rotor synchronous generator (WRSG), and ii) permanent magnet synchronous generator (PMSG). More details about these can be found elsewhere [29, 30]. The rotor captures the wind power by converting it to mechanical torque. The rotor contains the blade component that was attached to the nacelle by the hub [31].

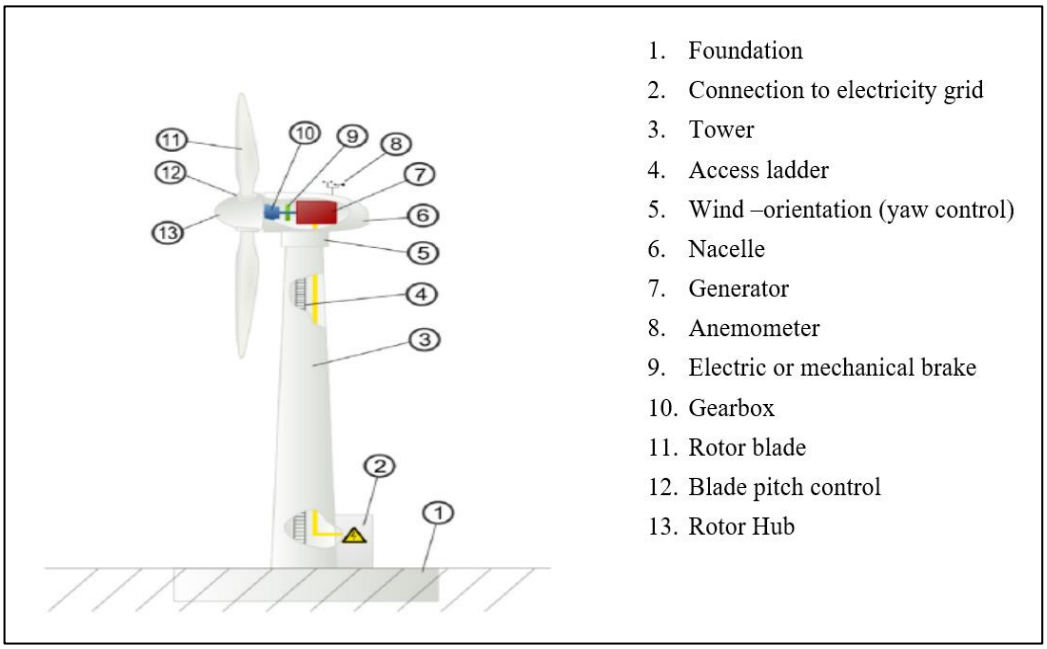

Figure 2.4: Components of upwind three-bladed HAWT [27].

2.3 CFD techniques

In the early 1990s, CFD techniques were used to solve flow problems around wind turbines utilizing available commercial software, for example, EllipSys3D and Fluent [32-35]. The environmental conditions, for example, wind speed and direction, exert a real influence on the lifetime of the wind turbine. Understanding the turbulence model, which simulates the aerodynamics of wind flow around a wind turbine, is essential for obtaining reliable findings. In this section, different turbulence models for flow Navier-Stokes equations will be discussed. Regarding CFD techniques, the finite volume method is used for solving the momentum and mass equations.

2.3.1 Turbulence modelling

Until now, no one model can predict all physical characteristics of turbulent flow. Various models are employed in the turbulent flow of wind turbines, such as Direct

numerical simulation (DNS) [36], Reynolds Averaged Navier-Stokes (RANS), and Large eddy simulation (LES) [37]. DNS has great accuracy in the turbulence model solution, yet the required computational time and cost are relatively high [38, 39]. The most common model used for solving Navier-Stokes equations is RANS [40]. The mathematical principle is based on the calculation method of the Navier-Stokes equation, which divides the flow into a fluctuating part and average part where the average equation is called the Reynolds decomposition. Various turbulence models are used to solve the RANS equation [41].

Firstly, the *k-ε* turbulence model series calculates the eddy viscosity by solving two parameters: the turbulent dissipation rate (ε) parameter; and a turbulent kinetic energy (*k*) parameter. Standard *k-ε* was specified by Launder and Sharma [42], which is very popular and widely used. However, it sometimes gives poor results for flow simulation where there is a separate phenomenon comprising separation at flow around the wind turbine when high wind speeds are evident [43].

Further improvement and modification on standard *k-ε* has led to the *RNG k-ε* and Realizable *k-ε* turbulence models [44, 45]. The renormalization group theory was used as a statistical method for solving the *RNG k –ε* turbulence model. The *RNG k-ε* turbulence model has different modifications from standard *k-ε*; for example, it takes the impact of rotation in eddy viscosity into account. The *RNG k–ε* is more accurate and better able to predict separation flows than standard *k-ε* [46]. The Realizable *k-ε* model is recommended for rotating bodies because the results can be improved compared with standard *k-ε* for swirling flow problems under specific Reynolds numbers [47].

The *k-ω* turbulence model is another RANS that is widely used for simulation flow around the wind turbine. Kolmogorov proposed the first form of the *k-ω* model [48]. The Imperial College group has completed a new improvement on this model, but the most distinguished development was undertaken by Wilcox [49]. In some applications, the *k-ω* model is superior to the standard *k-ε* model for several reasons. For example, it achieves higher accuracy for boundary layers with adverse pressure gradient and can easily be integrated into the viscous sub-layer without additional damping functions.

However, k-ω is still sensitive to some flow with free stream boundaries that restrict its implementation.

k-ω Shear stress transport (SST) turbulence model is an advanced turbulence model devised by Menter [50], and it combines the advantages of the k-ω and k-ε turbulence models. The inner part of the boundary layer is used in the k-ω model and then converted gradually to k-ε in the free shear layer and the wake region's outer layers. The translation between the two models is related to blending functions. The other advantage of this model is the modification of eddy viscosity, which considers the effect of turbulent shear stress transportation. Different modifications of k-ω SST had been done to enhance rotation and streamline curvature [51].

Another RANS model is the Transition SST (γ-$Re_{\theta t}$) model, which was extended based on the k-ω SST [52]. The Transition SST model is more precise than classical turbulence models because it can deal with the laminar-turbulent transition flow model where the separation of flow and stall phenomena occur [53]. The Spalart-Allmaras (SA) is the simplest RANS turbulence model, and it uses one transport equation [54]. Here the computation of turbulence quantity is formulated by one transport equation, in which the eddy turbulent viscosity is the equation's variable [55]. This model was designed and optimized for aerospace and industrial applications, for example, a compressible flow over airfoils and wings. It may be used with a different type of grid for practical situations. Here, adverse pressure gradients are included to become easily stable and converge with the solution [56]. In the meantime, the model could enable significant diffusion, especially in regions of 3D vortices flow [53]. Research to improve the model has been done by Spalart and Shur [57], and Rahman et al. [58], who considered the effects of rotation near the wall and reduction of the diffusion effect. The advantage of this model's fast convergence is the minimal computation time required compared to other turbulence models [56].

Large eddy simulation (LES) is another model developed with less computational demand than the Direct Navier-Stokes model. The first trial of LES in engineering was done by Deardorff [59]. Unlike the RANS model, the LES turbulence model has wider applicability and more accurate results. Another advantage is decreasing the length of

scales in the LES approaches in which turbulence is divided into two parts in the computational domain. The first part concerns the important large-scales part that was fully resolved, while the second concerns the modelled small sub-grid scales [60]. The superiority of LES models is evident in high Reynolds number turbulence models investigations, and they provide an adequate prediction of complex flow compared to other turbulence models [61]. Unfortunately, the required computational time for the LES model is higher than the RANS model [62].

The Detached-eddy simulation (DES) was developed in 1997 and applied for high Reynolds number with a massively separated flow [63]. The latter method is a model that blends the LES and RANS approaches [64]. Hence, LES is applied with external flow regions with massive separations, whereas the attached boundary layer is solved by RANS [65]. Travin et al. [66] described the DES as a single turbulence model that uses unsteady three-dimensional numerical methods.

2.3.2 Application of turbulence models used for aerodynamics simulation of the wind turbine

The numerical simulation of flow around the wind turbine is sensitive to the numerical models used for wind turbine design under operating conditions. The literature is abundant with various turbulence models that validated different numerical methods against experimental analyses. For example, Li et al. [67] used CFDShip-Iowa code with dynamic overset grid strategy for simulating the flow NREL Phase VI wind turbine to examine the Unsteady Reynolds Averaged Navier-Stokes (URANS) and DES models. The study found that the results of thrust forces and moments differed from the experimental work for URANS and DES. However, using DES did considerably improve the results of unsteady flow around the wind turbine.

k-*ε* turbulence models are used to analyse the flow around the wind turbine and dynamic wake behavior. El Kasmi and Masson [68] and Abdelsalam et al. [69] performed a full-scale study of three wind turbines based on different *k*-*ε* turbulence models and compared results. These showed that the modified *k*-*ε* agrees better with previous experimental measurements than standard *k*-*ε*.

Several studies evaluated the reliability of predicting wind turbine performance using

various turbulence models. Abdulqadir et al. [70] investigated the reliability of RANS and 12 turbulence models for predicting the NREL Phase VI wind turbine. All RANS numerical key performance coefficients at low tip speed ratios revealed a good value when validated against experimental results. However, during high tip speed ratios, the poorest simulation results were achieved by k-ω SST, whereas Realizable k-ε highlighted relatively good results. Abdelsalam et al. [71] simulated the upstream and downstream velocities for a 2 MW horizontal wind turbine on an Indian wind farm using a modified k-ε turbulence model. There was a good agreement between measured data in the wind farm and estimated data from the CFD using modified k-ε turbulence models.

Lanzafame et al. [72], and Rajvanshi et al. [73] studied the numerical simulation of NREL Phase VI using k-ω SST and Transition SST. Their results demonstrated the better capabilities of Transition SST compared to k-ω SST according to the experimental work. Elsewhere, Moshfeghi et al. [74] looked at the effects of near-wall grid treatment on the aerodynamics performance of the wind turbine. NREL Phase VI model with nine cases was examined for a near-wall grid that used k-ω SST and gamma–Theta transitional turbulence models. Different wind speeds are used for predicting thrust forces and pressure coefficients. The thrust force results of k-ω SST did not agree well with the thrust values in test results. In general, the k-ω SST model over-predicts the performance of the wind turbine. However, gamma–Theta transitional behavior is different from the k-ω SST model, particularly in the inboard regions, but the outcomes are close to the experimental work.

Siddiqui et al. [75] studied the dynamic wake behavior of NREL 5MW wind turbine with two different approaches, these being moving reference frame (MRF) modelling and sliding mesh interface (SMI). They discovered that the SMI method had a better prediction ability near the hub when compared to the MRF method. However, the SMI method demanded a huge amount of computational resources to give fully converged results that were free from the effect of initialization.

You et al. [76] investigated the effect of different RANS turbulence models (Spalart-Allmaras, k-ω SST, and Transition SST) on estimating the aerodynamics

characteristics around the NREL Phase VI blade rotor. Their results demonstrated the ability of the Transition SST model to capture the laminar separation bubbles around the airfoil surface and rotor blade. Subsequently, the results derived from the Transition SST model agrees well with experimental data due to a good prediction of the boundary layer's transition area. Another investigation into predicting the numerical performance of a New Mexico wind turbine looked at the effect of RANS turbulence models using two different near-wall methods of high and low Reynolds models [53]. The RANS models used in the high Reynolds model were the Spalart-Allmaras and *RNG k-ε*. In contrast, the models employed for low Reynolds number were *k-ω* SST and Transition SST. All four models, under low wind speed ranges, predict well the wind turbine's aerodynamics performance. When the wind speeds increased, more differences between the models appeared, and the high Reynolds model had better results compared with the low Reynolds model. A swirl effect was considered with wall function corrections, where the *RNG k-ε* turbulence model is recommended at high wind speed [53].

The blade element momentum (BEM) theory and CFD are the most popular methods for estimating wind turbines' performance and aerodynamics characteristics. Plaza et al. [77] analysed the aerodynamics performance of a New Mexico wind turbine rotor using the *k-ω* SST model and compared the results with that of the BEM method. At low wind speeds, the BEM model achieved better results than the *k-ω* SST CFD model. However, at high wind speeds the BEM method failed in separating the flow conditions when a detachment occurred in the blade. This evident inaccuracy was due to the three-dimensional (3D) effects and blade tip losses. Conversely, CFD agreed well with the experimental data over a wide range of wind speeds. The following table summarizes the previous studies on the CFD summary for HAWT.

Table 2.3. Studies done on the CFD summary for HAWT.

Authors	Year	Turbine Type	Method/Tool	Transient /steady	Reynolds number	Numerical Turbulence model	Mesh (full or periodic)	Key investigated parameters	Comments
Sørensen et al. [78]	2002	NREL Phase VI 2-bladed turbine	EllipSys3D CFD code	Transient	The Reynolds number varies between $(0.7\text{-}1.4)10^6$ at the root and for the tip $(1.0\text{-}1.1)10^6$	k-ω SST	Using 90° section with the periodic plane. 3.1, 4.2 million cells for free and tunnel configuration ,respectively.	Validate computed value of flap and edge moments, aerodynamics coefficient, and pressure distribution during wind speed variation against the experimental results.	Airfoil type is S809. Diameter 10.058 m The influence of tower and nacelle will be ignored in this study. 0° yaw angle and 3° tip pitch angle.
Johansen et al. [79]	2002	NREL Phase VI, 2-bladed turbine	EllipSys3D CFD code	Transient	Free Flow velocity V=20 m/s	DES, k-ω SST	Using section of half spherical domain with the periodic plane. 8.9 million cells.	Validate predicting values of the normal and tangential force coefficient at different radial distributions; focus is on on static and dynamic stall regions with experimental NREL data.	Airfoil type is S809. Diameter 10.058 m In the study of aerodynamics, the influence of tower and nacelle will be ignored.
Duque et al. [80]	2003	NREL Phase VI, 2-bladed turbine	OVERFLOW-D2 code and CAMRAD II code	Transient	Velocity 7, 10, 13, 15, 20, 25 m/s			OVERFLOW-D2 predicted good results against experimental work in stall conditions.	Yaw angle at 10°, 30°, 60°

Continued on next page

Johansen and Sørensen [81]	2004	NREL Phase VI (2-bladed), Danish 95 kW Tellus and Danish 500 kW	BEM& EllipSys3D CFD code	Transient	Re=1*10^6	DES, *k-ω* SST		Computed mechanical power using CFD has a proper alignment with BEM method.	Stall-regulated wind turbine 0° yaw angle. New correction models could be derived by extracted airfoil characteristics Danish 95 kW Tellus and Danish 500 kW (3-bladed) wind turbine.
Mandas et al. [82]	2006	Nordtank 41/500 turbine, 500 kW 3-bladed turbine	Fluent	Steady	Free Flow velocity range 6.8-12 m/s	Spalart-Allmaras, *k-ω* SST	1.5 million cells. 120° periodicity used for the rotor	Study mechanical power as a function of the wind velocity, and the corresponding power coefficient as a function of tip speed ratio.	Fixed pitch, stall-regulated. NACA 63-4xx. Tower and nacelle will be ignored. The rotor diameter is 41 m. Good agreement of aerodynamics performance from CFD when compared with BEM method.
Sezer-Uzol and Long [83]	2006	NREL Phase VI, 2-bladed turbine	PUMA2 solver	Transient	Velocity at 7, 15 m/s	LES	3.6 million rotating tetrahedral cells	The flow attached at cases 1 and 2 but in case 3 there is a massive separation with the entire blade	Different yaw cases: 1) 7m/s yaw angle 0° 2) 7m/s yaw angle 30° 3) 15 m/s yaw angle 0°

Continued on next page

Hu et al. [84]	2006	The combined experimental rotor (NREL) 3-bladed downwind rotor	Fluent	Steady	Mean velocity varies from 0-15 m/s	*RNG k-ε*	3,52,080 cells. 120° periodicity used for the rotor	Using the boundary layer analysis method to develop a detailed understanding of the essential physics of stall delay phenomena.	NREL S809 airfoil. Diameter of 1m Coriolis and centrifugal forces play important roles in 3D stall delay Validated against Simms et al. [85].
Wußow et al. [86]	2007	3-bladed HAWT Type ENERCON E66	Fluent	Transient	Velocity range 4-14 m/s	LES	4.05 million cells Full blade simulated	Compared the local values of velocity magnitude and turbulence intensity inside the wake with field measurement.	Validated against data which was collected during field project of "Deutsche Institut für Bautechnik". Tower included during simulation analysis.
Thumthae and Chitsomboon [87]	2009	NREL Phase II 3-bladed wind turbine	Fluent	Steady	Velocity at 7.2, 8.0, 9.0, 10.6 m/s	*Standard k-ε*	120° periodicity used for the rotor	Find the best angle of attack which achieves the greatest power output for each wind speed cases.	NREL S809 airfoil. The rotor diameter of 10.1 m. Rotational speed at 72 rpm. Pitch angles are 1°, 3°, 5°, 7° and 12°. Validated against NREL Phase II [88].

Continued on next page

Fletcher et al. [89]	2009	NREL Phase VI, 2-bladed turbine		Steady	Wind speeds at 7, 10, 25 m/s	RANS equations. Vorticity Transport Model.		Study normal, tangential force and power coefficient.	Good ability of the Vorticity Transport Model for wake structure. Validated against NREL Phase VI.
Sørensen [90]	2009	NREL Phase VI, 2-bladed turbine	EllipSys3D	Transient	Reynolds number of $7.2 * 10^6$	*k-ω* SST, Transition SST	512 × 128 cells in chordwise and normal direction	Used the *Transition* SST for predicting lift and drag of two turbines.	S809, NACA63-415 Variable turbulence intensity will vary from 1.20% to 0.38%. 0° yaw angle. Validated against NREL Phase VI.
Gómez-Iradi et al [91]	2009	NREL Phase VI 2-bladed turbine		Transient	Wind speeds at 7, 10, 20 m/s	URANS	Different mesh distribution used for each case	Investigated the effect of the wind tunnel wall on the blade aerodynamics and blade/tower interaction on aerodynamics of wind turbine.	Validated against NREL Phase VI. Compressible flow. Tower and nacelle included in the study.
Tachos et al. [92]	2010	NREL Phase VI 3-bladed turbine	Fluent	Steady	Velocity at 7.2 m/s	Spalart-Allmaras , *RNG k-ε*, *standard k-ε*, *k-ω* SST	4.2 million cells, 120° periodicity used for the rotor	Comparison for pressure distribution between different turbulence models against experiment work.	Airfoil type is S809. Diameter 10.068 (m) Incompressible Tower and nacelle will be ignored.

Continued on next page

Fu and Farzaneh [93]	2010	NREL Phase VI 3-bladed turbine	Fluent	Steady	Velocity at 7, 10, 13 m/s	*k-ε*	1.7 million cells, 120° periodicity used for the rotor	Model HAWT under the process of icing conditions.	Airfoil type is S809. The rotor diameter 10.068 m Different rotation speeds 5, 7.5 and 10 rad/s.
Bechmann et al. [94]	2011	MEXICO 3-bladed turbine	EllipSys3D	Steady	Velocity at (10, 15, 24) m/s	*k-ω* SST	120° periodicity used for the rotor	Validating aerodynamics forces against experiment.	4.5 m diameter DU91-W2-250, RISØ -A21, NACA 64418
Elfarra et al. [95]	2014	NREL Phase VI 2-bladed turbine	Fine/Turbo of NUMECA	Transient	12 different wind speeds between 5 and 25 m/s	RANS *k-ε Launder–Sharma*	350,000 cells, using 90° section with periodic plane	Comparison between optimized blade (with winglet) and the original blade (without winglet).	The optimized blade (with winglet) increased the power production by 9% compared to the original blade at 7m/s wind speed. Validated against NREL Phase VI.
Abdelsalam et al. [71]	2014	2 MW wind turbine	Fluent	Steady	Velocity at 8, 10, 12, 14 m/s	*Standard k-ε*	Unstructured mesh ANSYS ICEM	Validated against El Kamsi and Masson [68].	The results showed that *k-ε* could generate a good outcome if the blade was modelled accurately.
Song and Perot [96]	2015	NREL Phase VI 2-bladed turbine	OpenFOAM	Transient	wind speeds =5, 10, 21 m/s	RANS Spalart-Allmaras	10 million cells	Studied the 3D flow under separation conditions.	0° yaw angle 3° tip pitch angle The rotation speed of 72 rpm.

Continued on next page

Derakhshan and Tavaziani [97]	2015	NREL Phase VI	Fluent	Steady	Low wind speed (5-20) m/s	Spalart-Allmaras *k-ω* SST k-ε	2,697,136 mesh	Validated against NREL Phase VI.	*k-ω* SST showed better results when compared to experimental values.
Sørensen et al. [98]	2016	MEXICO 3-bladed turbine	EllipSys3D	Steady	Velocity at 10, 15, 24 m/	*k-ω* SST	Span-wise direction (129 cells) chord-wise direction (256 cells) normal direction (128 cells)	The results showed good agreement with experimental values.	The numerical results investigated the pressure distributions and wake characteristics.
Wang et al [99]	2016	WindPACT 1.5 MW	Fluent	Steady	Velocity at (8, 12, 16, 20, 24) m/s	*k-ω* SST	5,460,679 cells	The model is validated against literature data test.	
Menegozzo et al. [100]	2018	NREL Phase VI 2-bladed wind turbine	Fluent	Transient	Different wind velocity range	*k-ω* SST	8.5 million cells unstructured moving mesh strategy.	Validated against NREL Phase VI.	A numerical study of the extreme load has been investigated.

The main objective of Chapter Four is to analyse the flow field around the horizontal axis wind turbine by numerically solving the governing equations using a finite-volume method and RANS approach. Until now, a unique model has not been devised for predicting all physical characteristics of turbulent flow. Several RANS models are used to calculate the characteristics of turbulent flow of wind turbines such as Realizable k-ε, k-ω SST, Spalart-Allmaras, and Transition SST. Chapter Four aims to investigate the effect of four turbulence models on predicting the aerodynamics characteristics of the twisted wind turbine, where the mechanical torque and blade pressure distribution are used for model validation compared with NREL test results. Secondly, the differences between turbulence models under different wind speeds that included stall conditions are captured through simulation of the wind turbine. Thirdly, the main aerodynamics parameters such as lift coefficient have been extracted at different span-wise along the blade. Fourthly and finally, the aerodynamics flow of S809 airfoil is visualized under different attack angles, highlighting the flow variation from the attached condition to the separated flow condition. Depending on this numerical validation, the best performing CFD model will examine the mechanical output with different rotational speeds and variable pitch angles to compare the optimized blade design.

2.4 Models of wind speed probability distribution

Wind speed plays a vital role in the performance of the wind turbine since it is the primary source of energy. The wind speeds at a specific site vary according to annual, seasonal, and daily changes. It is, therefore, important to describe these variations by different mathematical distribution models [101]. A highly accurate analysis of wind data is essential to encourage stakeholders to increase or at least consider their investment in wind energy technology. Assessing the potential of wind energy resources in a specific region is an important step in developing an efficient and effective wind turbine design. Studying the statistical characteristics of wind speeds is essential to determine the analytical method for assessing the potential of wind energy in a specific site [102]. There is a requirement to develop an efficient method to present

the distribution of wind speeds. A probability distribution function was proposed for studying the potential of wind resources in a specific location. The probability density function describes the occurrence frequency of wind speed using common functions. Thus the type of wind speed distribution function greatly influences the outcome of the available wind energy and wind turbine performance at a particular site.

The most popular models are Rayleigh and Weibull distribution models [103-106]. Shu et al. [107] performed a statistical analysis of the wind characteristics using the Weibull distribution model at typical sites in Hong Kong. The results showed that the scale parameter changed from 2.85 m/s to 10.19 m/s, where the annual shape parameter varied between 1.65–1.99. The highest scale parameter was found at a hilltop, while the lowest value was observed at an urban locale. Irwanto et al. [108] examined the wind resources at Kangar and Chuping in Malaysia using recorded daily, monthly, and yearly mean wind speed. At Chuping, based on Weibull distribution, the result showed the wind speed and probability density are 0.97 m/s and 73%, respectively. In comparison, the wind speed and probability density at Kangar was 2.5 m/s and 45%, respectively. These results confirmed that the wind power density at 50 m height above the ground was 19.69 W/m^2 and 2.13 W/m^2 at Kangar and Chuping, respectively, and subsequently categorized as poor wind regions.

Hernandez-Escobedo et al. [109] assessed the potential of wind as a resource in northern Mexico. Their results showed the high wind potentials during the year occur in September and October with a value of 1000 W/m^2 of wind power density at Tamaulipas. Ahmed [110] investigated the wind potential for the meteorological station in the city of Shark El-Ouinat, Egypt using Weibull distribution, where the shape and scale parameters are 2.1 and 7.4 m/s, respectively. Janajreh et al. [111] assessed wind potential using the Weibull function in Masdar City, UAE, finding the scale and shape parameters at 10 m height are 3.36 m/s and 1.56, respectively. Keyhani et al. [112] studied the potential of wind energy in Tehran, Iran. They found that the Weibull distribution fitted well with the experimental data over a suitable range of wind speeds. According to the monthly wind speed values, the shape values range between 1.72 and 2.68 according to where the scale parameters range between 4.09

and 5.67 m/s. Islam et al. [113] assessed wind energy potential at Kudat and Labuan, Malaysia using Weibull distribution. Their results confirmed the unsuitability of these sites for large-scale commercial wind energy generation. Elsewhere, Celik [114] evaluated the potential of wind energy on Turkey's Mediterranean coast based on Rayleigh and Weibull models. The results showed that the Weibull model gives better power density distribution accuracy than the Rayleigh model. Thus, the Weibull model gives an annual average error when calculating power density around 4.9% compared with 36.5% for the Rayleigh model. Mentis et al. [115] used the daily wind speed at different sites in Africa for one year utilizing the Weibull and Rayleigh distributions. Results showed 5% energy yield differences with the findings between Rayleigh and Weibull distribution, but the variation exceeded 100% at specific locations. As such, the Rayleigh model was not valid at those sites, especially at the country level. It can only be used for estimating wind power potential on a continental level.

Ozay and Celiktas [116] highlighted the great potential of wind energy in the Alaçatı region, Izmir, Turkey. The measured wind data from 2008 to 2014 were studied using Weibull and Rayleigh distributions. Findings showed that the Weibull distribution showed the best fit of wind characteristics (a correlation coefficient of 0.989). The shape and scale parameters were found to be 2.05 and 9.16 m/s, respectively. Also, in Turkey, Oner [117] used Weibull and Rayleigh probability distribution functions to describe the wind speed frequency at Çanakkale, which is in the Intepe region. The results showed the Weibull function is better than Rayleigh when compared with actual data. According to the recorded probability density functions studies, the Weibull distribution offers a better fit than the Rayleigh distribution. Different numerical methods are used to calculate the Weibull distribution function; for example, Rocha et al. [118] assessed seven methods to get the most effective method for determining parameters of the Weibull distribution method. The wind data was measured in the northeast area of Brazil. The results showed the most efficient method for determining the Weibull parameter for data recorded in the cities of Camocim and Paracuru was the equivalent energy method. Solyali et al. [119] studied wind power potential in northern Cyprus using three numerical models for fitting the Weibull distribution

function; graphical, maximum likelihood, and equivalent energy methods. These have helped to calculate shape and scale parameters. Results found that the highest match of curve fitting of the recorded wind data has been done via the equivalent energy method.

As shown above, most assessments of wind power studies employed the Weibull distribution. Various analyses focused on investigating the suitability of other probability density functions such as lognormal [120-122], Burr distribution, and gamma functions for fitting measured wind data [123-127]. Brano et al. [128] examined different probability density functions for four weather stations in Palermo, Italy. The statistical indicators are used to rank the different probability density functions to define the better fitting with the wind speed data. Tar [129] investigated different statistical characteristics for various probability distribution functions such as lognormal, gamma, and Weibull for seven Hungarian meteorological stations. Good accuracy of Weibull distribution resulted, and it was used to define the shape and scale parameters of monthly average speeds at different altitudes of 20, 40, 60, 80, and 100 m.

In effect, wind speed varies from one place to another and at the same location, there is a seasonal and daily variation. This variation explains the need for feasibility studies on the performance of wind energy to predict the potential of wind in a specific site. Morgan [130] investigated the wind characteristics at Lindfield, Sydney, where Weibull distribution recorded wind data for 32 months. Katsigiannis and Stavrakakis [131] examined the large-scale wind turbine for electricity generation application in the listed regions in Australia: Gingin, Armidale, and Gold Coast Seaway. Maunsell et al. [132] investigated wind resources at a location on the north-western coast of Western Australia employing the Wind Atlas methodology. Prasad et al. [133] studied the complementarity characteristics of wind and solar resources throughout Australia. As discussed above, most research on a statistical analysis of wind data resources has been undertaken worldwide. The study aims to identify an optimal location for a wind turbine in the five rural sites in NSW. An optimal location is a place of the frequently high wind speed where the operative blades of the wind turbine are placed in an area

of little or no turbulence, maximizing the power production. Five potential regions for installing a wind turbine have already been identified. To identify feasible areas, techniques depending on the analysis of probability distribution functions, especially in NSW, Australia, have been done. Chapter Five of this study highlighted the feasibility of wind potential at five locations in that state: Ballina, Merriwa, Deniliquin, Yanco, and the Bega Region. The recorded hourly wind speed data from wind stations from August 2018 until July 2019 have been statistically analysed using the four different probability distribution functions in Chapter Five. The chapter investigated in-depth several key points which should be investigated regarding the statistical analysis of wind speed. Firstly, four different probability density functions - Rayleigh, Weibull, gamma, and lognormal - are used for evaluating the wind potential at these five sites. Secondly, descriptive statistical characteristics of wind speed that recorded from meteorological stations in Ballina, Merriwa, Deniliquin, Yanco, and the Bega areas are analysed. Thirdly, different statistical parameters evaluate the goodness of fit to define suitable probability distribution functions.

For a given data set, several numerical methods can be applied to estimate the Weibull parameters depending on wind data measurement on the site. Different researchers have proposed several numerical methods to estimate the Weibull parameters to minimize uncertainties in wind speed modeling. Researchers have attempted to compare the different numerical methods in different studies to select the best for specific sites and climatology conditions. The comprehensive results of using the seven methods for Weibull distribution are presented in Chapter Six. This chapter presents and investigates an in-depth statistical evaluation of wind characteristics and energy potential using seven numerical methods for adjusting the Weibull distribution of wind speeds at the five sites in NSW depending on wind data measurement. The objective is to obtain the most accurate values of shape and scale parameters. Also, wind direction and frequency are assessed for selected sites using wind rose plots. Finally, the variation of wind speeds according to changes in height level is considered. Thus, Chapters Five and Six document valid insights into wind potential and feasibility in NSW, Australia.

2.5 Optimization of wind turbine

2.5.1 Sensitive parameters of design and performance of the horizontal wind turbine

Several parameters influence the aerodynamics characteristics of HAWT, such as atmospheric conditions and the shape of the wind blade. The objective of optimization of the wind turbine is to maximize the energy output, which requires understanding the critical operating parameters on the performance of the design of the wind turbine. The following section discusses the essential designs and operating parameters of the wind turbine.

2.5.1.1 The shape of the wind turbine blade

The number of blades in wind turbines varies depending on the design [12]. Currently, the 3-bladed upwind horizontal wind turbine is the most popular modern wind turbine design due to its system efficiency, stability, and economic feasibility. Different materials are used to manufacture wind turbine blades, such as carbon fibers and S-glass [134-138]. Various studies demonstrated that decreasing the rotor and nacelle weight will reduce manufacturing costs. It should be noted that this reduction has a dynamic aero-structural limitation, and balancing issues need to be considered in the design [139, 140]. One of the key design parameters of the wind turbine's shape is determining the airfoil chord length and twist angle distribution along the blade [141]. There are different methods for determining the chord length, where the Betz distribution method is deemed the most straightforward theory and offers reasonable approximation values of the airfoil section's chord length [142, 143]. This method approximates a good optimum value of blade chord length, with a 6–8 tip speed ratio when neglecting losses from the tip and drag. Consequently, this method is inaccurate, with low tip speeds, blade sections near the hub, and high drag airfoil sections being reported [144, 145]. The wind turbine blade is divided into three essential parts, i.e. root, mid-span, and tip, based on the structural and aerodynamics roles [146]. Due to structural loads, the larger chord length should be in the root area, while the slender airfoil sections will be in the tip region area [147]. Consequently, the area near the hub

is responsible for the required starting torque, while most of the production torque is initiated from the tip region [148]. Research has focused on aerodynamics optimization of the shape of the wind turbine design [149-153] as discussed later in the following section.

2.5.1.2 Wind power curve and tip speed ratio

The power curve gives the power output of the wind turbine at each wind speed. This curve is essential for forecasting wind speed performance, which improves grid planning and connecting wind energy to the power systems. The least wind speed required to deliver a useful power is called the cut-in speed, while the turbine is shut down at the cut-out wind speed for engineering safety reasons to prevent damage caused by massive wind loads [154]. Some methods used to enhance the aerodynamics performance of the HAWT over different wind speeds include decreasing the cut-in wind speed [155]. For example, Singh et al. [156] designed a wind turbine with a better start-up performance at low wind speed using a numerical method to reduce the cut-in wind speed and achieve a better combination of lift to drag ratios.

The tip speed ratio (λ) is a key design factor, which affects the calculation of different design parameters of the optimum rotor geometry dimensions [157]. The definition of the tip speed ratio is the ratio between the speed of the rotor blade and free stream wind speed [158]. The aerodynamics design of the wind turbine is sensitive to any changes in the tip speed ratio. Thus, a rotor blade that had been designed for operation at a relatively high wind speed will generate a lower torque at minimum wind speed. This outcome increases the value of the cut-in speed and self-starting difficulties [148].

As shown in **Table 2.4**, selecting an appropriate tip speed ratio should take into account the design of different parameters such as output torque, mechanical stress and efficiency, aerodynamics characteristics, and noise [159]. Practically, raising the tip speed ratio will increase the noise pollution to the sixth power [160]. The tip speed ratio should be six to nine for a modern three-blade wind turbine and nine to ten for a two-blade wind turbine, an efficient mechanical to electrical conversion is to be produced [161].

Table 2.4. Design consideration of tip speed ratio [159].

Tip speed Ratio	**Low (λ about 1, 2)**	**High (λ >10)**
Application	Traditional windmills	Single or two-bladed prototypes
Torque	Increases	Decreases
Aerodynamics stress	Decreases	Increases proportionally with a rotational velocity
Efficiency	Decreases significantly below five due to rotational wake created by high torque	Insignificant increases after eight
Aerodynamics	Simple	Critical
Blade profile	Large	Significantly narrow
Noise	Increases to the sixth power approximately	

2.5.1.3 Airfoil Configuration

The efficient blade design is formed from different airfoil profiles, blending at an angle of twist for each airfoil terminating at a circular blade root. Different simplifications facilitate industrial production and curtail manufacturing costs, such as minimizing the number of varying airfoil profiles, linearization of chord width, and decreasing the twist angle [162]. The decision to select airfoils plays a critical role in the output torque from a wind turbine. The direct impact of airfoil design defines the aerodynamics performance of wind turbines. The lift to drag ratio is an essential aspect of the aerodynamics characteristics of the airfoil. Over the past decade, several experimental studies tested the lift and the drag coefficients of airfoils with different Reynolds number and angles of attack [163, 164]. The angle of attack is a very sensitive aerodynamics parameter for calculating the drag and lift coefficients of the airfoil. This angle is evaluated as the difference between the flow angle and the rotor plane angle [165]. Consequently, the most critical factor in designing the wind turbine is to get the optimum value of the lift to drag ratio at a specific angle of attack [166].

The power output in a horizontal wind turbine is affected mainly by the lift to drag ratio of the airfoil, which is usually designed to operate at a low angle of attack where the lift coefficient is often much higher than the drag coefficient [164]. Different airfoil families have been used to design modern wind turbines such as NACA sub-families four and five-digit, for example, NACA 65-415, NACA 63-215 [167, 168]. NACA was developed by the National Advisory Committee for Aeronautics [169]. NACA 63 series are known for their characteristics of stall delay and less sensitivity to roughness in leading-edge than other families [170]. Yılmaz et al. [171] investigated the lift and drag coefficients of NACA 4412 and NACA 0012 using numerical simulation. The optimal lift to drag coefficient value is related to the angle of attack 6°, 7° for NACA 4412 and NACA 0012, respectively.

RISØ-A-XX is another family used in the wind turbine blade design and has been developed and optimized by RISØ National Laboratory in Denmark [172, 173]. The family contained seven airfoils that varied relative thickness to chord from 12% to -30% [172]. The DU series airfoil family is another airfoil family developed by the Delft University of Technology, Netherlands [174]. The relative thickness to the chord of DU series airfoil varies from 15% to 40%, for example, DU 91-W2-250 and DU 93-W-210, which has an airfoil thickness of 25% and 21%, respectively [174, 175].

Many airfoils are devised for wind turbine design; for example, the Aeronautical Research Institute of Sweden has developed the FFA airfoil family [168]. Elsewhere, the NREL developed the S airfoil family in the USA [176-178]. Some issues should be taken into account when determining the type of airfoil used in wind turbines such as achieving a maximum lift to drag ratio, dynamic and structural requirements, and the sensitivity of airfoil to environmental conditions. Typically, using a single airfoil profile along the whole wind turbine blade results in compromising the efficiency of the blade design. In some applications, different airfoil shapes can be used to design a wind blade, but using different airfoils along the blade in the design process would increase efficiency [179].

The sections of an airfoil with a high thickness to chord length ratio are usually used in the root region according to structural load requirements, as seen in **Table 2.5** [173].

However, airfoils of high thickness have a lower value of lift to drag ratio. Therefore, significant research has been conducted to increase the lift coefficient of the thick airfoil used in wind turbine design. The aerodynamics characteristics is critical to maximizing the lift to drag ratio in the tip regions, which explains using a thin airfoil.

Table 2.5. The airfoil requirements for blade regions [173]

	Root	Mid-Span	Tip
Thickness to chord length (%)	>27	27-21	21-15
Geometrical compatibility	Med	Med	Med
Structural load-bearing requirement	High	Med	Low
Maximum lift insensitive to leading-edge roughness.			High
Maximum lift coefficient and post-stall behavior		Low	High

In large modern wind turbine blades, the inboard and mid-span regions utilize airfoils that have a relative thickness of 25% or above [180]. For example, FFA- W3-241 and FFA-W3-301 airfoils are used for inboard and mid-span regions due to their relatively high thickness [181]. Different studies investigate different airfoils in wind turbine design; for example, Van Rooij et al. [180] used RISØ, DU, NACA, FFA, and S8xx airfoil families to assess the performance of those airfoils in meeting the aerodynamics and structural requirements. For airfoils of relative thickness to chord ranging between 25% and 30%, the best performing airfoils are S814 (24%), DU 91-W2-250 (25%), and RISØ -A1-24 (24%), where the performance differences between those airfoils are relatively small. Meanwhile, for airfoil thickness of 30%, the DU 97-W-300 has the best performance according to restricted requirements.

Recently, a lot of work concentrated on designing blades for wind turbine rotors depending on the investigation of aerodynamics performance [182-184]. The generated power of a wind turbine varies with the speed and turbulence of the wind. Many countries have low wind speed in some locations. There is a lot of research in

developing small wind turbines to meet the energy needs of such countries. Ahmed et al. [185] studied lift, drag coefficient, and flow behavior of SG6043 at low Reynolds number to assess the airfoil aerodynamics characteristics used in wind turbines for regions having wind speeds of 4–6 m/s, which is usually the case in the Pacific Ocean island nations. The results showed that increasing the freestream turbulence level from 1% up to 10% will not significantly change the slope of the lift curve. However, with an increasing angle of attack, the separation was delayed from the upper surface, reflecting on increasing the lift coefficient and reducing the drag coefficient. When the turbulence level rises, the lift to drag ratio also increases from 8% to 15% in the range of angle of attack.

Sayed et al. [186] simulated the aerodynamics performance of different S-series in low wind velocities. The study found that S825, S826, S830, and S831 airfoils are the most efficient in S-series for low and high wind velocities because they give a maximum lift to drag ratio, which achieves maximum power. Airfoil characteristics such as flow separation vary with the level of wind turbulence [187-189]. Thus, Larsen et al. investigated the lift coefficient of the airfoil with delayed flow separation under dynamic stall conditions [190]. Hoffmann [191] looked at the impact of changing the wind freestream turbulence of NACA 0015 airfoil from 0.25% to 9% at Re = 250,000. The analysis found that the impact on delayed flow separation related to increasing the peak lift coefficient due to changing turbulent intensity. Kamada et al. [192] discussed the dynamic and static characteristics at Re = 3.5 $*10^5$ for DU93-W-210 at two different turbulent intensity levels. This airfoil had 21% relative thickness, which was tested in a wind tunnel with a turbulence grid that helped to obtain a high turbulent flow. They observed a delay in flow separation when increasing the level of freestream intensity, which reflected an increase in the stall angle.

2.5.1.4 Control system of wind turbine

Wind energy is an uncontrollable source since wind flows randomly. Wind flows' unsteadiness explained the need for a control system that captured wind power with an efficient energy conversion system [193]. The main goals of using a control system

in HAWT are increasing power production and decreasing static and dynamic structural loads, which can be done by regulating the desired value's operating parameters. The dynamic stall phenomenon results from unsteady variations in the operating conditions, such as changing the angle of attack through the blade [194]. Two different types of control systems regulate the power to avoid stall conditions, these being stall-regulated and pitch-regulated [195]. According to the wind turbine generator, HAWT is classified into fixed speed operation or variable speed operation, as seen in **Figure 2.5**.

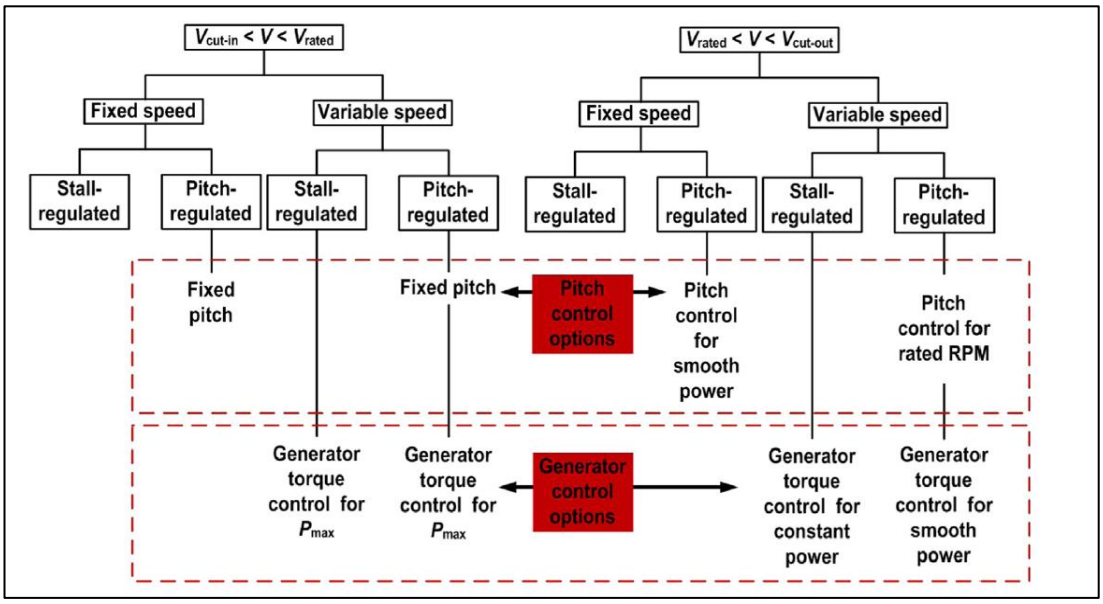

Figure 2.5. Classification of control systems of HAWT [196].

The wind turbine works at a constant speed for the fixed speed generator after reaching the rated wind speed. With increasing wind speed, the stall happens in a stall-regulated system with many stall problems related to high speed. The pitch-regulated system functions to improve the performance of the wind turbine. A pitch-regulated control system's essential role is to regulate power in the operating zone when the wind speed is higher than the rated wind. This regulation reduces the severe load on structural HAWT [197]. Recently HAWT has been used as an active pitch control system with hydraulic and electrical actuators to overcome power fluctuating drawbacks [198].

In the variable speed generator, the wind turbine rotational speed varies according to the wind speed. Different control methods undergo the concept of the stall-regulated system. For example, the rotor speed will vary accordingly to the Maximum power

point tracking (MPPT) in the generator's torque control system. Similarly, the smooth output power controls the wind input torque in the pitch-regulated system [199]. Regarding control methods, the MPPT method is easily implemented; however, it results in significant fluctuations in the load that are reflected in reducing the wind turbine components' life [200]. Another technology is used for the control system of rotor speed, known as Light Detection and Ranging (LIDAR) [201] and it measures the wind speed ahead of the rotor blade and then controls the wind speed when a gradual change in wind speed occurs. However, this method is not accurate in turbulent wind weather conditions. Improving control system efficiency has been investigated [202, 203]. Research has been done to develop the best possible control strategy to increase power production efficiency [204].

2.5.2 Optimization of the rotor shape of the wind turbine

Many researchers have optimized the rotor shape of wind turbines to maximize the annual energy output. Optimizing the shape of the wind turbine blade was undertaken at Gökçeada [205] in Turkey using different blade design parameters, i.e. twist angle and chord length. Results showed that the highest AEP of 92,972 kW-hr was comparable to the combined experiment rotor (CER) test. Darwish et al. [206] improved the AEP for low wind speed regions by selecting, laying out, and matching the most suitable wind turbine system for a case study conducted in Iraq. Liu et al. [207] demonstrated a novel optimal blade design method for the twist angle and chord length radial profiles of a fixed-pitch fixed-speed wind turbine which performed excellently with less expensive manufacturing costs. They concluded there is a good increment in annual energy production when designing an optimal blade using novel linearization for wind speed ranging from 4-7 m/s. Optimization of design results according to the annual mean wind speed of 5 m/s improved 3.33% of AEP with the preliminary design.

BEM theory helped design the rotor for a 300 kW HAWT based on wind speed data in Semnan, Iran [164]. The results defined the optimal shape of the wind turbine, which related to the input design parameters such as power coefficient by taking into

consideration easy manufacturing. Al-Abadi et al. [208] investigated the optimization of the wind turbine shape using the BEM method with a gradient-based optimization algorithm. Derakhshan et al. [209] tested the effectiveness of shape optimization in their numerical study of a wind turbine. Their study noted that the optimization of chord distribution would increase by 3.7% the power of wind turbines at rated speed (10 m/s). While at the same rated wind speed, the optimization of twist distribution will reflect the wind turbine's power by an 8.3% increase. The global optimization increased the output power rated by 8.58%.

Currently, research is lacking on the design of wind turbines, especially considering the prevailing environmental conditions in Australia. Chapter Seven addresses the gap in our knowledge of combining wind turbine shape design and the available wind resources in Australia using updated and refined methodologies. The wind turbine's blade shape is defined by the airfoil, chord length, and twist angle of each section along the blade. The wind turbine model of 20 kW, which will be simulated and validated in Chapter Four, is used as a baseline for the optimization process. This process aims to maximize the AEP of the 20 kW wind turbine depending on wind speed data at the site, which has the highest wind speed potential. The Bezier curves are used to define the chord length and twist angle distributions to smooth the span-wise distribution along the blade to achieve optimal chord length and twist distributions along the wind turbine blade.

Chapter Three

3 Methodology

This thesis focuses on optimizing the wind turbine design where the objective function is to maximize the AEP depending on wind data measurement in selected sites in NSW. The methodology of the four-stage work is discussed in this chapter. The first section explains the CFD modelling of the wind turbine section in all stages to visualize the aerodynamics flow around the base wind turbine design. Determining a precise wind data model is very important in this study as it will be used as input for the optimization process. Furthermore this process will include defining an accurate wind data model, which is very important.

Section 3.2 discusses the method used to evaluate wind resource potential using statistical analysis of probability density functions in selected sites in NSW, Australia. The detailed study of evaluating wind energy potential at different sites in Chapter Five's results revealed that the Weibull distribution is the most accurate model. Several numerical methods to estimate the scale and shape parameters of the Weibull distribution function have been used. Section 3.3 discusses the statistical analysis method for defining the shape and scale parameters, which will be used in optimization. Finally, section 3.4 describes the optimization methodology.

3.1 CFD Modelling of the wind turbine

This section discusses the CFD modelling of the small wind turbine using the following steps, as shown in **Figure 3.1**. The CFD modelling starts with a pre-processor, which includes creating the wind turbine blade geometry and computational domain. Furthermore, the Meshing generation is considered to be the second step in pre-processor work. The pre-processor usually consumes more work and time, which are necessary to get accurate output results. The second stage is the solver box, which defines all details concerning the set-up for the turbulence models, boundary

conditions, and numerical solution algorithm. Finally, the post-processor stage highlights results and visualizes the aerodynamics flow around the wind turbine.

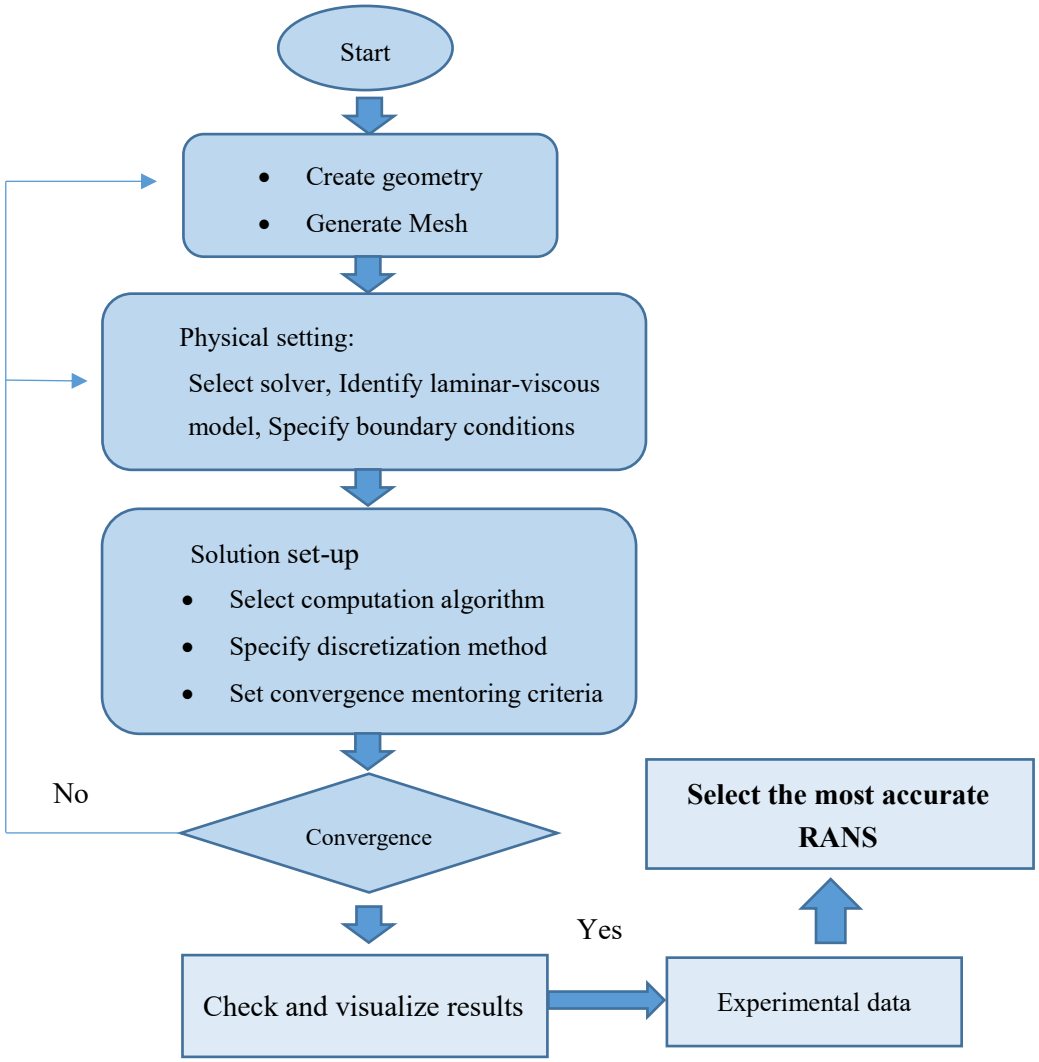

Figure 3.1. Numerical modelling of HAWT.

3.1.1 Computational domain

The NREL CER extends the NREL VI experiment rotor [210], the subject of work conducted in the National Renewable Energy Laboratory. The geometry of the 20 kW wind turbine blade was optimized to maximize the annual energy [211]. Results explained the prediction complexity of the aerodynamics performance of the tapered-twisted HAWT turbine when compared with an untwisted blade. As such, the NREL CER performs excellently compared to commercial blades. The NREL CER was used as a reference for validating the aerodynamics performance of a three-blade wind

turbine with variable speed operations. **Table 3.1** summarizes the main characteristics of the wind turbine blade with S809 airfoil applied from a 25% span at the root to the tip.

Table 3.1. Specification and operating parameters of the NREL CER.

Parameters	Value
Rated power	20 kW
Blade diameter	10.58 m
Number of blades	3 blades
Hub height	12.192 m
Pitch angle	5°
Rotational direction	Counterclockwise
Rotational speed	72 rpm
Power regulation	Stall regulation

The blade geometry was created using SolidWorks [212] and disregarded the effect of the tower and nacelle to reduce computational time and enhance numerical stability [170]. The wind blade consisted of 18 sections, as shown in **Figure 3.2(a)**. These sections had different twist angles and chord lengths along the blade illustrated in **Figure 3.2(b)**. The geometry of the cylindrical part ended at 0.66 m from the axis of rotation and then started to change until the transition area ended at 1.25 m. From **Figure 3.2(b)**, the maximum twist angle reached 20.040° at 0.25 span and later became zero at a 0.75 span and a negative value at a 1.00 span.

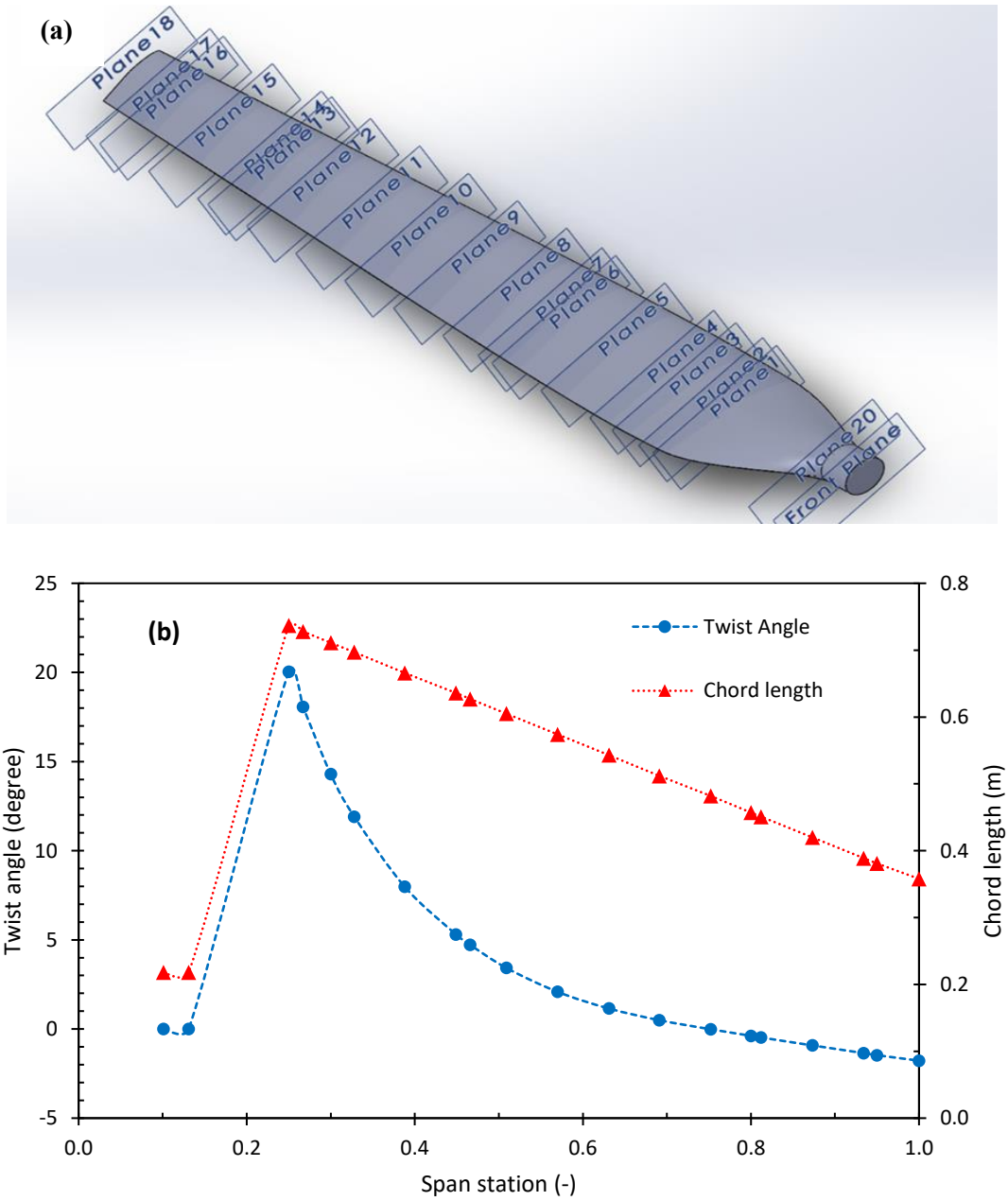

Figure 3.2 (**a**) A 3D geometry model of a 20 kW wind turbine blade and **(b)** The chord and twist distribution along the span of the blade.

The fluid domain was divided into two zones, as shown in **Figure 3.3**. The first zone with a 120° radial stream tube was generated with periodic faces to reduce computational time due to the symmetrical flow around the wind turbine model. The upstream velocity was specified with an 18 m radius, offset 12 m in front of the blade. Meanwhile, the downstream outlet was defined with a 36 m radius, offset 24 m behind the blade, and specified as an atmospheric pressure outlet. The second zone was near the blade with a 10 m radius and 5 m from the centre of the

root. This zone was created to separate the rotating and stationary zones; and, secondly, increase the number of mesh cells near the blade. The upstream velocity and upper surface of the domain were specified as free stream wind speed. This conical shape of the domain served to make the wake conical expansion on the back of the blade possible. An important step is choosing the most suitable computational domain. First of all, a proper computational domain that permits rotation of the wind turbine blade with a no-slip wall effect is essential when considering the optimization of mesh quality. Consequently, a small computational domain will not permit enough grid generation around the wind turbine. On the other hand, a vast domain would increase the computational time corresponding with an increase in the calculated number of cells.

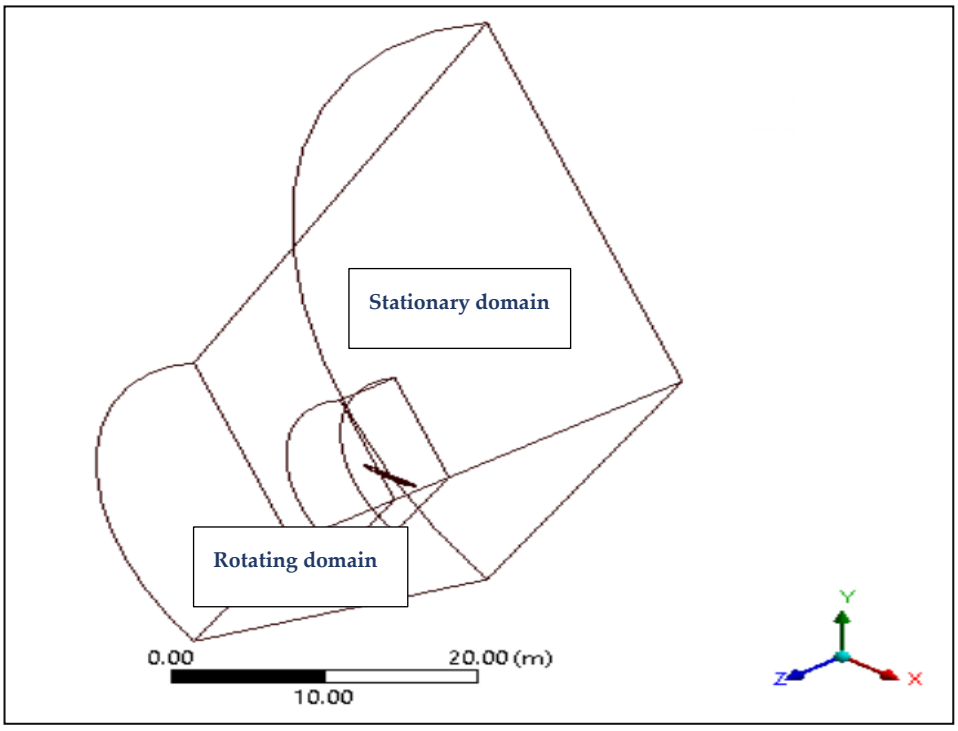

Figure 3.3. Computational domain.

3.1.2 Computational mesh generation

The S809 airfoil has a sharp trailing edge along the blade, producing non-orthogonal face cells [213]. These cells lead to low-quality mesh and inaccurate or unstable CFD solutions. Generating a sharp trailing edge is not possible in the experimental work, so rounding this sharp edge through a radius of 1 mm will

improve the quality of the mesh with an insignificant effect on the CFD results. The present study used different turbulence models to predict the output power and pressure distribution under various wind speed conditions, which was crucial to refining the mesh around the blade rotor. **Figure 3.4 (a)** shows that the cells were refined gradually away from the blade to reduce the computational time. The ANSYS meshing was used to generate unstructured mesh, and local and global sizing was used to produce a high-quality grid [214]. The minimum mesh size was 0.008 m^3 around the blade. After that, inflation was used to refine the prismatic cells at the blade surface, and it generated fifteen prismatic layers with a growth rate of 1.2, as shown in **Figure 3.4 (b)**. The first layer thickness (y), the nearest distance between the first grid point to the blade, was changed with air velocity and calculated from Equation 3.1. In this study, the restriction has been imposed for the dimensionless wall distance of $y^+ < 1$ [72]:

$$y^+ = \frac{u_t\, y}{v} \qquad \text{Equation 3.1}$$

where u_t is the friction velocity, and v is the kinematic viscosity of the air.

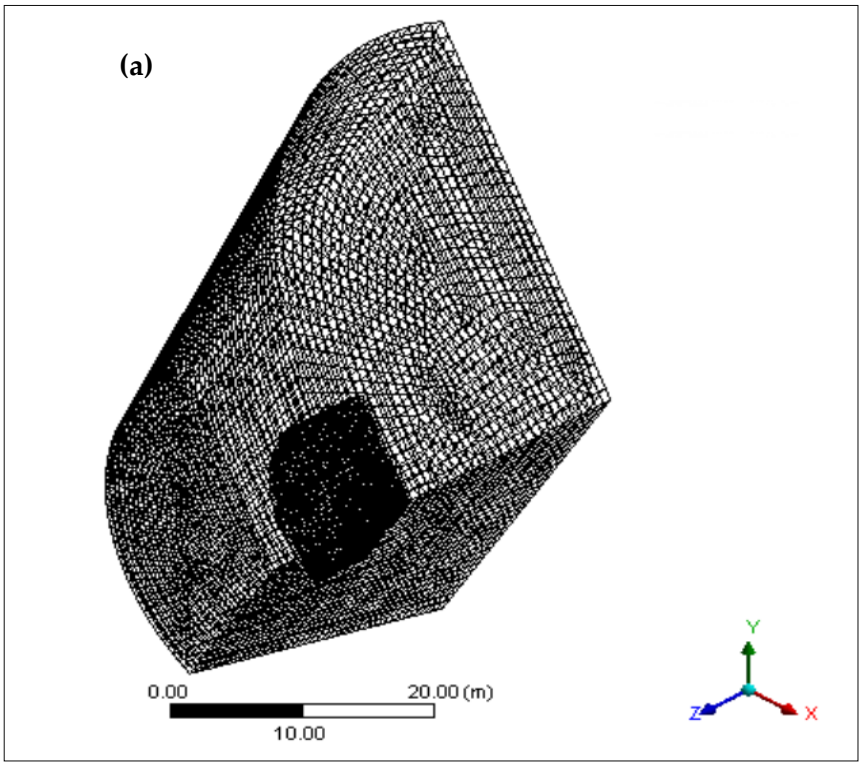

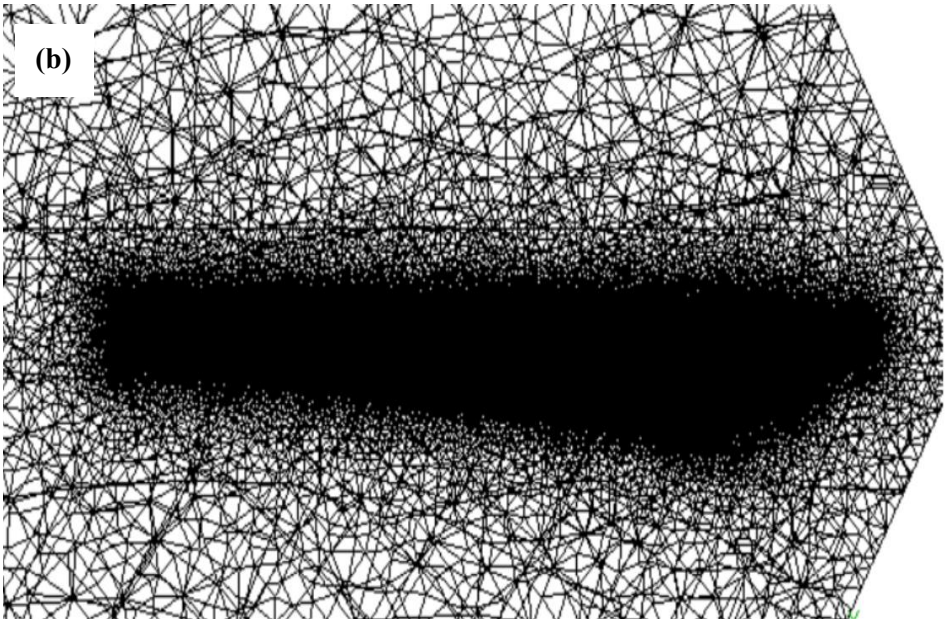

Figure 3.4 (**a**) computational mesh generation and (**b**) cell meshing around the rotor.

Also, the proximity and curvature with the fine relevance center were defined as the local mesh size function specification, which helped refine the mesh grid. Mesh quality plays a crucial role in the accuracy of CFD results. However, a smaller mesh size requires a longer computation time and more computer memory. For this reason, it is essential to compromise between accuracy and computational time. On the other hand, it is crucial to achieving mesh independence. Nine meshes were tested at a 7.2 m/s wind speed to achieve grid independence by monitoring the mechanical torque. As shown in **Figure 3.5**, the CFD results converged when the number of mesh cells was 3,559,082, which had an error rate of 3.82% compared with the measurement value. Any further increase in the number of mesh cells will significantly raise the computational time but will lead to no improvement in the accuracy. For this reason, 3,559,082 mesh cells are deemed to constitute the most suitable mesh configuration in terms of computational time and efficiency.

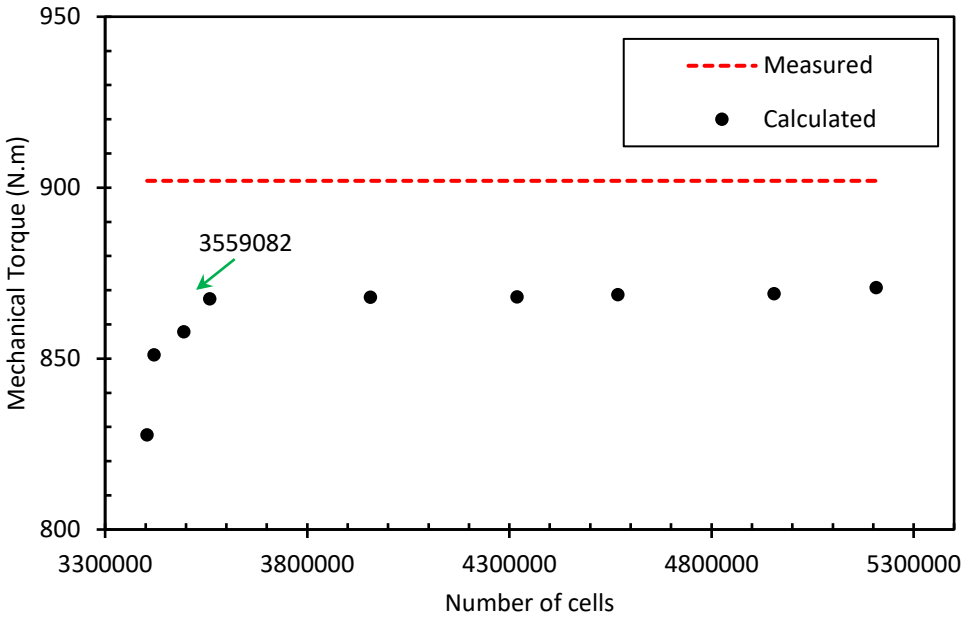

Figure 3.5. Grid sensitivity.

Three models are used in ANSYS Fluent to handle the rotational effect: dynamic mesh, SMI, and MRF models. The SMI model is appropriate for the transient flow problem but requires a full-scale model. Both dynamic mesh and SMI models require high computational resources. The MRF model is the simplest way of modelling the flow of steady-state rotating objects without using rotating mesh to reduce the computational time [53], as seen in **Figure 3.6**. Thus, MRF is applied in the small zone near the blade so that the rotational speed of the wind turbine with periodic boundary conditions can be applied.

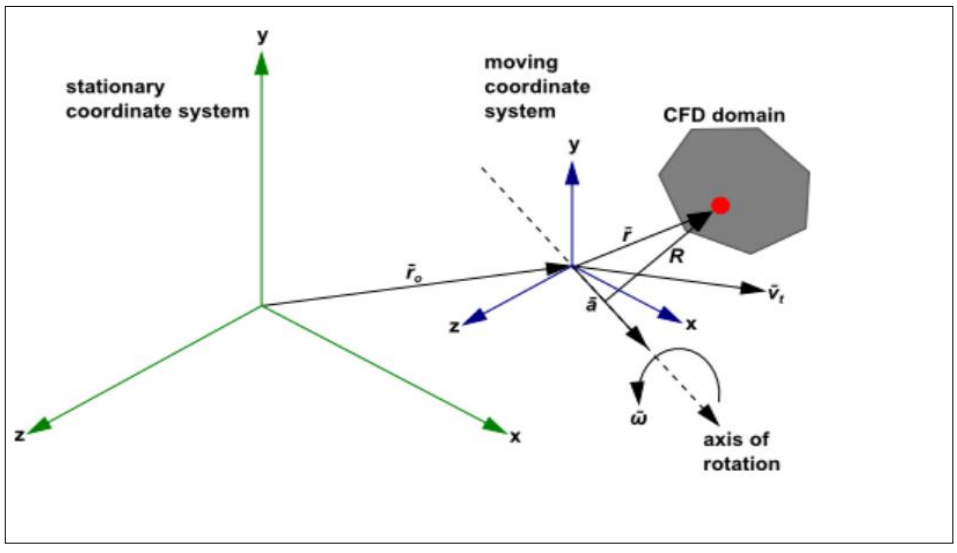

Figure 3.6. Stationary and Moving Reference Frames.

The transformation from a stationary to a moving frame in terms of relative fluid particle velocities, Coriolis, and centripetal accelerations have been used to calculate the MRF model, as following equations [53]:

$$\overrightarrow{v_r} = \overrightarrow{V_{sta}} - \vec{\Omega} \times \vec{r} \quad \text{Equation 3.2}$$

where $\overrightarrow{v_r}$ is the velocity seen from the moving frame (the relative velocity), $\overrightarrow{V_{sta}}$ is velocity seen from the stationary frame (the absolute velocity), and $\vec{\Omega}$ is the angular velocity.

The mass and momentum conservation equations using MRF are shown as follows:

$$\frac{d\rho}{dt} + \nabla \cdot \rho\overrightarrow{v_r} = 0 \quad \text{Equation 3.3}$$

$$\frac{d}{dt}(\rho\overrightarrow{v_r}) + \nabla \cdot (\rho\overrightarrow{v_r}\,\overrightarrow{v_r}) + \rho\,(2\,\vec{\Omega} \times \overrightarrow{v_r} + \vec{\Omega} \times \vec{\Omega} \times \vec{r}) = -\nabla p + \nabla \cdot \overline{\overline{\tau_r}} + \vec{F} \quad \text{Equation 3.4}$$

where $(2\vec{\Omega} \times \vec{v}_r)$ is the Coriolis acceleration, $(\vec{\Omega} \times \vec{\Omega} \times \vec{r})$ is the centripetal acceleration, and $\overline{\overline{\tau_r}}$ is the viscous stress [215].

The MRF was set up for the computation domain by applying a rotational speed of 72 rpm with the absolute reference frame. The blade was assumed to be a non-slip stationary wall that had a zero-relative velocity with other adjacent cells.

3.1.3 Mathematical and governing equations of the selected turbulence models

Understanding the turbulence model, which simulates the aerodynamics of wind flow around a wind turbine, is essential for obtaining reliable results. Ansys Fluent (version 18.2, Canonsburg, PA, USA) was used to investigate the aerodynamics performance of the HAWT [216]. The principle of the mathematical concept of the RANS equations is based on the calculation method of the Navier-Stokes equation, which is divided into the instantaneous fluctuating part and the average flow part. The flow around a wind turbine blade is considered to be incompressible and is modelled utilizing the RANS method. The software uses the finite volume method for solving the mass and momentum equations in addition to equations of turbulence for each control volume cell. The mass and momentum conservation equations are:

$$\frac{d\bar{u}_i}{dx} = 0 \quad \text{Equation 3.5}$$

$$\frac{\partial \bar{u}_i}{\partial t} + \frac{\partial}{\partial x_j}\left(\bar{u}_i\,\bar{u}_j\right) = -\frac{1}{\rho}\frac{\partial \bar{p}}{\partial x_i} + v\,\frac{\partial^2 \bar{u}_i}{\partial x_j \partial x_j} - \frac{\partial}{\partial x_j}\left(\overline{\acute{u}_i\,\acute{u}_j}\right) \quad \text{Equation 3.6}$$

where $\acute{u}_i$ is the fluctuating velocity, $\bar{u}_i$ the mean velocity, and ρ is the air density (kg/m^3) [217].

The flow around the wind turbine is predicted to be turbulent due to the high Reynolds number [218]. The Realizable *k-ε* [217], *k-ω* SST [219], Spalart–Allmaras [55], and Transition SST models are the four RANS models which were investigated. The governing equations of the four RANS models are described in the following sections in more detail.

3.1.3.1 Realizable *k-ε*

RNG k-ε and Realizable *k-ε* use the same transport equation as standard *k-ε* for dissipation rate (ε) and turbulent kinetic energy (k). Still, the turbulent viscosity generation and calculation methods are different in these models. The governing equations of the Realizable k-ε model are written immediately below:

$$v_t = C_\mu\,\frac{k^2}{\varepsilon} \quad \text{Equation 3.7}$$

$$\frac{\partial k}{\partial t} + \bar{u}_j\frac{\partial\, k}{\partial x_j} = \frac{\partial}{\partial x_j}\left[\left(\frac{v+V_t}{\sigma_k}\right)\frac{\partial k}{\partial x_j}\right] - \varepsilon + \tau_{ij}\frac{\partial \bar{u}_i}{\partial x_j} \quad \text{Equation 3.8}$$

$$\frac{\partial \varepsilon}{\partial t} + \bar{u}_j\frac{\partial \varepsilon}{\partial x_j} = \frac{\partial}{\partial x_j}\left[\left(\frac{v+V_t}{\sigma_\varepsilon}\right)\frac{\partial \varepsilon}{\partial x_j}\right] + C_{\varepsilon 1}\frac{\varepsilon}{k}\tau_{ij}\frac{\partial \bar{u}_i}{\partial x_j} - C_{\varepsilon 2}\frac{\varepsilon^2}{k} \quad \text{Equation 3.9}$$

where v_t is the turbulence eddy viscosity, σ_ε = 1.2 and σ_k =1.0 are the Prandtl numbers for ε and k, respectively. The residual model constants are: $C_{\varepsilon 1}$=1.44 and $C_{\varepsilon 2}$=1.9 [217].

3.1.3.2 *k-ω* SST

The advantages of this model are related to the modification of eddy viscosity, which considers the effect of turbulent shear stress transportation of k and ω [220]. The following equations are discussed with reference to the transport equations for the eddy viscosity [221]:

$$\rho\frac{\partial k}{\partial t} + \rho\bar{u}_j\frac{\partial k}{\partial x_j} = \tilde{P}_k - \beta^*\rho k\omega + \frac{\partial}{\partial x_j}\left[\left[\mu + \sigma_k\mu_t\right]\frac{\partial k}{\partial x_j}\right] \quad \text{Equation 3.10}$$

$$\rho\frac{\partial \omega}{\partial t} + \rho\bar{u}_j\frac{\partial \omega}{\partial x_j} = \alpha_{\dot{w}}\rho S^2 - \beta\rho\omega^2 + \frac{\partial}{\partial x_j}\left[(\mu + \sigma_\omega\mu_t)\frac{\partial \omega}{\partial x_j}\right] + 2(1-F_1)\rho\sigma_{\omega 2}\,\frac{1}{\omega}\frac{\partial k}{\partial x_j}\frac{\partial \omega}{\partial x_j} \quad \text{Equation 3.11}$$

$$\mu_t = \frac{\rho a_1 k}{\max(a_1\omega, SF_2)} \quad \text{Equation 3.12}$$

where ω is the turbulent dissipation rate, and μ_t is the turbulence eddy viscosity. $\tilde{P}_k$ represents a production limiter used in the model to prevent the build-up of turbulence in stagnation regions, β^*, β are computed through auxiliary functions as presented in Wilcox [222] and the following coefficients: $\alpha_{\dot{w}}$= 0.52; σ_k= 0.5; σ_ω= 0.5; a_1=0.31. S is defined as the second invariant of the deviatoric stress tensor, and F_1, & F_2 are the first and second blending function, respectively [221] as the following equations:

$$F_1 = \tanh\left[\left(min\left(\max\left(\frac{\sqrt{k}}{\beta^*\omega y}, \frac{500v}{y^2\omega}\right), \frac{4\rho\sigma_{\omega 2}k}{CD_{k\omega}y^2}\right)\right)^4\right] \quad \text{Equation 3.13}$$

$$CD_{k\omega} = \max\left(2\rho\sigma_{\omega 2}\frac{1}{\omega}\frac{\partial k}{\partial x_j}\frac{\partial \omega}{\partial x_j}, 10^{-10}\right) \quad \text{Equation 3.14}$$

$$F_2 = \tanh\left[\left[max\left(\frac{2\sqrt{k}}{\beta^*\omega y}, \frac{500v}{y^2\omega}\right)\right]^2\right] \quad \text{Equation 3.15}$$

3.1.3.3 Spalart-Allmaras

The Spalart-Allmaras is the simplest RANS turbulence model, which uses one transport equation and has the advantage of requiring minimal computational time [223]. The computation of turbulence quantity is formulated by one transport equation, in which the eddy turbulent viscosity is the equation variable [55]. The turbulence eddy viscosity (v_t) is calculated as written in the following equation [224]:

$$v_t = \tilde{v} f_{v1}, f_{v1} = \frac{X^3}{{C_{v1}}^3 + X^3}, X \equiv \tilde{v}/v \quad \text{Equation 3.16}$$

where f_{v1} is a damping function ranges from zero value at the wall to 1 at far away from the boundary, and $\tilde{v}$ denotes a new operating parameter calculated by the following equation [224, 225]:

$$\frac{\partial \tilde{v}}{\partial t} = c_{b1}\tilde{S}\,\tilde{v} + \frac{1}{c_\sigma}\left[\nabla\cdot((v+\tilde{v})\nabla\tilde{v} + c_{b2}(\nabla\tilde{v})^2\right] - c_{w1}f_w\left(\frac{\tilde{v}}{d}\right)^2 \quad \text{Equation 3.17}$$

where the equation parameters of $\widetilde{S}$, f_w, f_{v2} and c_{w1} are found in

$$\tilde{S} \equiv \cap + \frac{\tilde{v}}{z^2d^2}\,f_{v2}, f_{v2} = 1 - \frac{X}{1+Xf_{v1}} \quad \text{Equation 3.18}$$

$$f_w = g\left(\frac{1+{c^6}_{w3}}{g^6+{c^6}_{w3}}\right)^{1/6} \quad \text{Equation 3.19}$$

$$c_{w1} = \frac{c_{b1}}{z^2} + \frac{1+c_{b2}}{c_\sigma} \quad \text{Equation 3.20}$$

where d is the distance to the nearest wall, the von Karman constant (z), depending on

the magnitude of the vorticity (∩), and the other parameters are summarized in the following equations:

$$\cap = \sqrt{2W_{ij}\,W_{ij}} \qquad \text{Equation 3.21}$$

$$W_{ij} = \frac{1}{2}\left(\frac{\partial u_i}{\partial x_j} - \frac{\partial u_j}{\partial x_i}\right) \qquad \text{Equation 3.22}$$

$$g = r + c_{w2}(r^6 - r) \qquad \text{Equation 3.23}$$

$$r \equiv \frac{\tilde{v}}{\tilde{S}z^2\,d^2} \qquad \text{Equation 3.24}$$

Other constants are found from experimental work and they are as follows: $c_\sigma = 2/3$, $c_{v1} = 7.1$, $c_{b1} = 0.1355$, $c_{b2} = 0.622$, $c_{w2} = 0.3$, $z = 0.418$, $C_{w3} = 2.0$ [226].

3.1.3.4 Transition SST (γ-$Re_{\theta t}$)

Another RANS model is the Transition SST (γ-$Re_{\theta t}$) model, which was extended based on the *k*-*ω* SST [72]. This model has four transport equations that combine *k*-*ω* SST equations with the transition momentum thickness Reynolds number ($Re_{\theta t}$) and the intermittency (γ) transport equations [90]. The Transition SST model is more precise than classical fully turbulent models due to its ability to deal with the laminar-turbulent transition flow model where the separation of flow and stall phenomena occurred. The eddy viscosity transport equations for the intermittency equation and transition momentum thickness Reynolds number is calculated as follows [227]:

$$\frac{\partial(\rho\gamma)}{\partial t} + \frac{\partial(\rho U_j\,\gamma)}{\partial x_j} = P_\gamma - E_\gamma + \frac{\partial}{\partial x_j}\left[\left(\mu + \frac{\mu_t}{\sigma_f}\right)\frac{\partial\gamma}{\partial x_j}\right] \qquad \text{Equation 3.25}$$

$$\frac{\partial(\rho\,\overline{Re_{\theta t}})}{\partial t} + \frac{\partial(\rho U_j\,\overline{Re_{\theta t}})}{\partial x_j} = P_{\theta t} + \frac{\partial}{\partial x_j}\left[\,\sigma_{\theta t}\,(\mu + \mu_t)\frac{\partial\overline{Re_{\theta t}}}{\partial x_j}\right] \qquad \text{Equation 3.26}$$

where σ_f= 1, $\sigma_{\theta t}$ =2 and other parameters of the equation P_γ, E_γ and $P_{\theta t}$ are found in the following equations:

The transition source term is calculated as:

$$P_{\gamma 1} = F_{length}\,c_{a1}\,\rho S[\gamma\,F_{onset}]^{0.5}(\,1-\gamma) \qquad \text{Equation 3.27}$$

where F_{length} is transition length function, S is the strain rate magnitude, $c_{a1}$is a constant which equals to 2, and $F_{onset}$is the function used to triggering the intermittency production.

The destruction source is calculated as follows:

$$E_\gamma = c_{a2}\,\rho \cap \gamma\, F_{turb}\,(c_{e2}\gamma - 1) \qquad \text{Equation 3.28}$$

where $c_{a2} = 0.06, c_{e2} = 50, F_{turb}$ is used to disable the destruction source in the fully turbulent regime.

The source term is calculated as:

$$P_{\theta t} = c_{\theta t}\,\frac{\rho}{t}\,(Re_{\theta t} - \overline{Re_{\theta t}})(1.0 - F_{\theta t}) \qquad \text{Equation 3.29}$$

where $F_{\theta t}$ is a blending function, $c_{\theta t} = 0.03$ and t is the time scale.

3.1.4 Numerical method and boundary conditions

Four turbulence models were used to predict wind turbine aerodynamics. All regions in the domain were applied to the boundary conditions. Domain outlet was applied to the pressure boundary conditions of zero gauges pressure with 101,325 Pa of atmospheric conditions. The current investigation focused on 15 inlet velocities ranging from 4.9 m/s to 15.2 m/s, which was enough to investigate the prediction of different turbulence models for stall delay phenomena. The air density was approximately constant due to the assumption of incompressible fluid [67]. In this study, the standard air properties were used, where air density and dynamic viscosity were 1.225 kg/m^3 and 1.7894 $\times$ 10^{-5} kg/ms^{-1}, respectively [99]. The steady-state, pressure-based method was employed to solve the incompressible RANS models. A coupled algorithm was selected as a Pressure-Velocity Coupling Scheme that solved pressure-based continuity equations together. The Coupled Scheme is robust and recommended in many simulation cases due to the convergence rate having improved when using a coupled algorithm rather than a simple algorithm. The solution methods were used for the problem simulation, as seen in **Figure 3.7**. The First Order Upwind was utilized to solve turbulent kinetic energy and the turbulent dissipation rate, while a Second Oorder Upwind scheme helped solve the momentum equations. The Least Squares Cell-Based method was used in a gradient spatial discretization scheme. A standard discretization scheme was used in the pressure values interpolation.

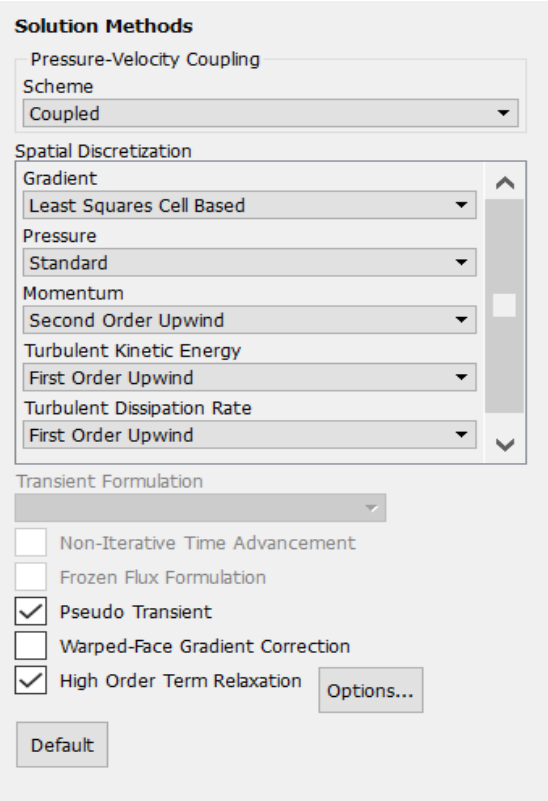

Figure 3.7. Solution method.

In the simulation process (**Figure 3.8**), it is essential to monitor the convergence of the simulation analysis. In this study, two methods were used to assess the convergence of the fluent analysis. Firstly, the residual values method is a popular method for evaluating the convergence of the CFD solution. During the calculation process, different variables of the residual values were monitored in this study, such as continuity, x-velocity, y-velocity, z-velocity, specific dissipation rate, and turbulence kinetic energy. The solution was considered to be converged when these residual values were below 10^{-6}. Secondly, a net mass imbalance was used to check the convergence of the solution. This method is the difference between the inlet and outlet mass flows. It was considered converged when the net mass imbalance was less than 0.001 kg/s [228].

Due to the non-linear nature of the fluid flow, the solution should be calculated iteratively. In this study, the solution was achieved after 1500 iterations. Also, the study used the standard initialization method, where the inlet boundary layer was used for calculating the initial values. Once the solution was converged, the

aerodynamics power output results were validated against experimental data which will be discussed in Chapter Four.

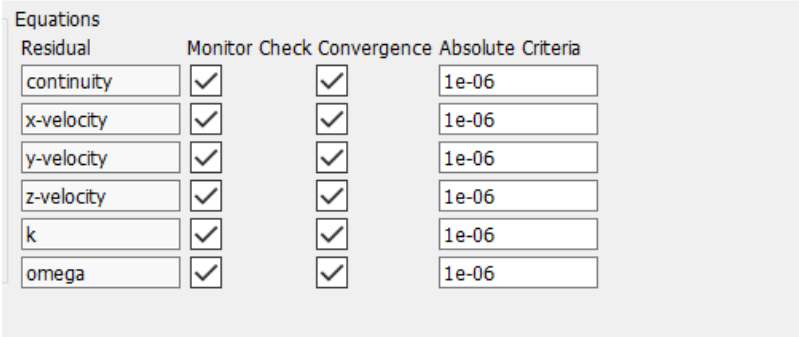

Figure 3.8. Convergence of equation residuals.

3.1.5 Numerical validation

3.1.5.1 Verification of mass flow rate

Verification of the continuity law states that the entering mass flow rate is equal to the outing mass flow rate, so this is a significant indication about the correct solution for all simulation models. Thus for incompressible flow, the net mass flow rate should obey the mass continuity law which can be simplified to a volume continuity law, since the airflow density is assumed to be constant as shown in the following equation:

$$V_{inlet}\, A_{inlet} = V_{outlet} A_{outlet} \qquad \text{Equation 3.30}$$

where V_{inelt}, A_{inelt} are the inlet velocity and inlet area, respectively, and V_{outlet} and A_{outlet} represent the outlet velocity and outlet area, respectively. Thus, all simulation models verified as the net mass flow rate achieved a value under 0.001kg/s.

3.1.5.2 Verification of the convergence integral static pressure on the blade surface

The most important key parameter when evaluating the numerical results for conducting the simulation is to check the convergence behavior of integral static pressure on the blade surface [229]. This means the solution is converged after enough number iterative solution processes have been completed, as shown in **Figure 3.9** below.

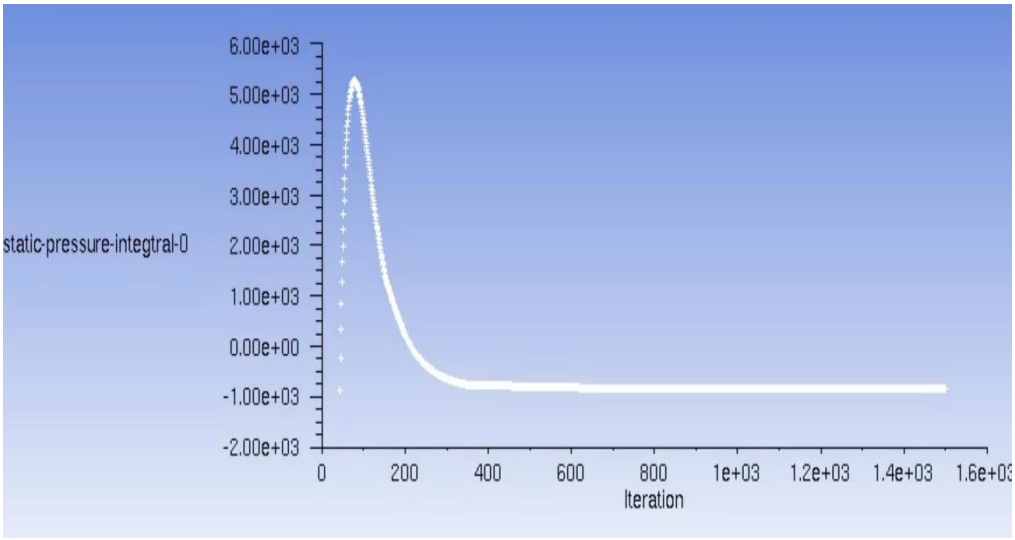

Figure 3.9. Convergence of the integral static pressure on the blade surface.

3.1.6 CFD Main Output

The pressure coefficient is calculated utilizing the equation below [230]:

$$Cp = \frac{P_{static} - P_{rel}}{0.5\rho\,(V_{rel}{}^2 + (r\Omega)^2)} \qquad \text{Equation 3.31}$$

where P_{static} is the local static pressure, P_{rel} is the free stream pressure, V_{rel} is relative wind speed, Ω is the rotational wind speed (rad/s), and *r* is the radius of the section (m) [97].

3.2 Evaluation of wind resource potential using statistical analysis of probability density functions in NSW, Australia

3.2.1 Description of the case study locations and the data used

Research has indicated that Australia has wind resources that are in places comparable to high wind resources in northern Europe [231], as shown in the distribution of average wind speed in Australia in **Figure 3.10**. Wind energy is a vital part of the NSW energy mix, which has world-class wind resources. Different governments' Sustainable Energy Development legislation served to optimize the usage of renewable energy in NSW. The Sustainable Energy Development Authority (SEDA) aimed to increase

investment in the wind energy sector [232]. Most wind energy developments in NSW will be in the state's rural and regional areas. Wind energy is especially attractive to those communities because of the potential for employment, developing industry, and generating income for landholders.

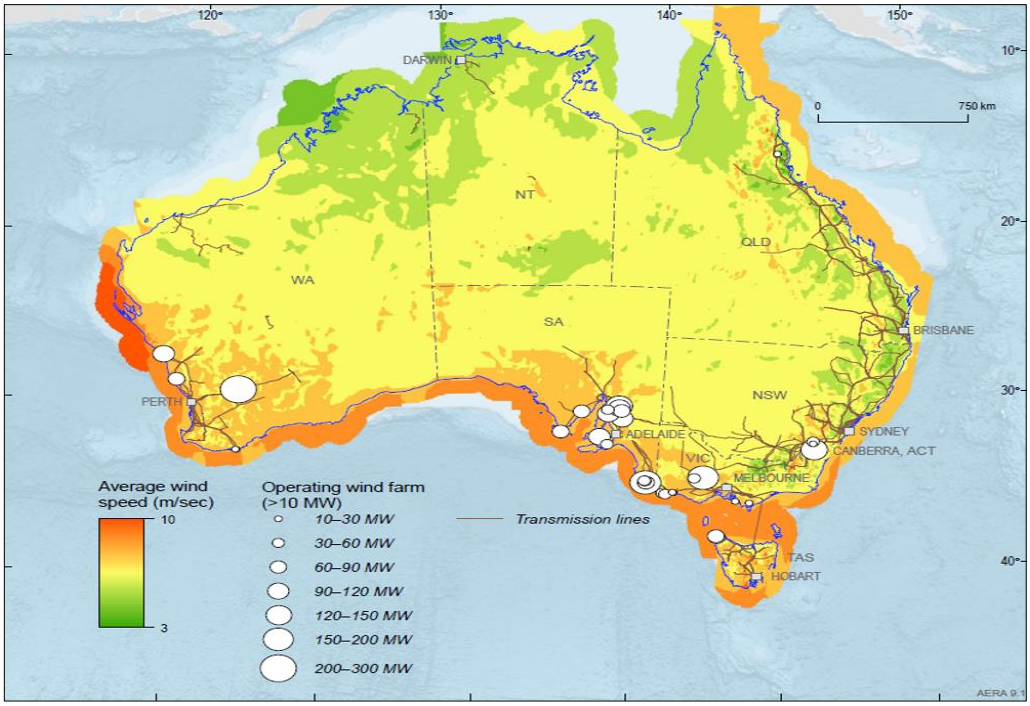

Figure 3.10. Australia's wind resources [233].

In this study, five sites have been selected to create useful insights into the wind potential in NSW. Specifically, Ballina, Bega, Deniliquin, Merriwa and Yanco are the five locations investigated here. As seen in **Figure 3.11**, the five locations are very far from each other in NSW, giving an overall insight into the wind resource potential for that state. The geographical coordinates of the five meteorological stations are illustrated in **Table 3.2**.

Table 3.2. Geographical coordinates of selected sites.

Station		Geographical coordinates		
Name	ID	Latitude	Longitude	Height
Ballina airport AWS	058198	-28.8353	153.5585	1.3 m
Bega AWS	069139	-36.6722	149.8191	41.0 m

Deniliquin airport AWS	074258	-35.5575	144.9458	94.0 m
Merriwa (Roscommon)	061287	-32.1852	150.1737	375.0 m
Yanco Agricultural Institute	074037	-34.6222	146.4326	164.0 m

Figure 3.11. Geographical map of NSW with all 5 sites shown.

3.2.2 Governing equation of descriptive statistical values of wind speed

In this study, the hourly wind speed data for five sites in NSW from August 2018 to July 2019 were analysed. The uncertainties of wind speed measurements are ±10% for wind speeds greater than 10 m/s and ±1 m/s for wind speeds at or below 10 m/s. Based on that measurement, the hourly wind speed data varies with day and from one site to another. This section discusses some descriptive statistical values of wind speed, including standard deviation, mean, kurtosis, and skewness. Mean wind speed is the uncomplicated statistical tool and most popular method to roughly estimate a specific location's annual energy production, which determines the central tendency of a given time series data. The mean value can be calculated by dividing the sum of the time series of wind data to the number of observations:

$$\overline{U} = \frac{1}{N}\sum_{i=1}^{N} U_i \qquad \text{Equation 3.32}$$

where U_i is the wind speed at i number of observation, $\overline{U}$ is the mean wind speed and N is the number of observations [104].

The standard deviation offers a clear insight into the wind data dispersion and is critically significant in wind resource assessment [234]. It gives a clear representation of how the wind speeds are distributed throughout the period, and secondly, how far the individual wind speeds are from average wind speed. Also, defining the standard deviation for the same mean wind speed, wind turbines can obtain different power outputs depending on wind speed distribution. The standard deviation (σ_U) is obtained from the following equation [104]:

$$\sigma_U = \sqrt{\frac{1}{N-1}\sum_{i=1}^{N}(U_i - \overline{U})^2} \qquad \text{Equation 3.33}$$

Skewness and kurtosis are two common statistical parameters that give insights into the distribution shape [235-239]. Skewness is a measure of the symmetry for a dataset distribution around the sample mean [240]. The skewness (s) is expressed as the following equation [241]:

$$s = \frac{1}{N-1}\sum_{i=1}^{N}\frac{(U_i-\overline{U})^3}{{\sigma_U}^3} \qquad \text{Equation 3.34}$$

Kurtosis is a measure of the "peakedness" of the probability distribution of a real-valued random variable that measures the tail heaviness of distribution when compared to that of normal distribution [242, 243]. The kurtosis of distribution is calculated as [244]:

$$\text{kurtosis} = \frac{1}{N-1}\sum_{i=1}^{N}\frac{(U_i-\overline{U})^4}{{\sigma_U}^4} - 3 \qquad \text{Equation 3.35}$$

3.2.3 Mathematical models of probability density functions

This section offers a brief overview of the methodology used for Chapter Five, which focuses on a statistical analysis of wind speed variation using four probability density functions.

The probability density function $f(U)$ can be used to determine the number of occurrences of specific wind speeds at a particular site. The probability of wind speed between $u(a)$ and $u(b)$ as explained above is computed as:

$$f(U) = f(U_a \leq U \leq U_b) = \int_{U_a}^{U_b} f(U)dU \quad \text{Equation 3.36}$$

For this reason, it is essential to assess the probability density functions being used to describing wind speed frequency distributions in a different location. The selected stations had various wind speed frequency histograms, permitting flexibility in the analysis of the four probability density functions when describing different wind speed regimes.

The cumulative distribution function $F(U)$ highlights the probability that wind speed is less than or equal to given wind speed. The following equation expresses the cumulative distribution function $F(U)$ [245]:

$$F(U) = \sum_{i=1}^{j} F(U_i) \quad \text{Equation 3.37}$$

where $\leq i$, and $i = 1,2,3, \ldots . N$, then the cumulative distribution function is calculated as follows:

$$F(U) = \sum_{i=1}^{N} F(U_i) = 1 \quad \text{Equation 3.38}$$

The different four probability density functions are: Weibull distribution [246, 247], Rayleigh distribution [248], gamma distribution [249, 250] and lognormal distribution. The probability density function $f(U)$ and cumulative distribution function $F(U)$ of four distribution models are expressed using the equations documented in the following sections. Different numerical methods have been used over the last few years for calculating scale and shape parameters [251]. The iterative way is used in the maximum likelihood algorithm to calculate shape and scale parameters for four listed distribution models [252]

3.2.3.1 Weibull distribution

The Weibull distribution is the popular probability density function used to analyse the wind speed characteristics of many researchers [107, 114]. The probability density function for Weibull distribution is expressed as [253, 254]:

$$f(U) = \frac{\mathrm{K}}{c}\left(\frac{U}{c}\right)^{\mathrm{K}-1} . \exp\left[-\left(\frac{U}{c}\right)^{\mathrm{K}}\right] \quad \text{Equation 3.39}$$

where c is the scale parameter (m/s), and K is the shape parameter (dimensionless) [255]. The cumulative distribution function of Weibull distribution $F(U)$ is calculated

as:

$$F(U) = 1 - \exp\left[-\left(\frac{U}{c}\right)^{\mathrm{K}}\right] \quad \text{Equation 3.40}$$

The following equation is expressed as the maximum likelihood algorithm to calculate the shape and scale parameters [256]:

$$\mathrm{K} = \left(\frac{\sum_{i=1}^{N} {U_i}^{\mathrm{K}} \ln(U_i)}{\sum_{i=1}^{N} {U_i}^{\mathrm{K}}} - \frac{\sum_{i=1}^{N} \ln(U_i)}{N}\right)^{-1} \quad \text{Equation 3.41}$$

After finding the shape parameter, the scale parameter could be found as the following equation [256]:

$$c = \left(\frac{\sum_{i=1}^{N} {U_i}^{\mathrm{K}}}{N}\right)^{\frac{1}{\mathrm{K}}} \quad \text{Equation 3.42}$$

After finding the two parameters of the Weibull distribution, the probability density function and cumulative distribution function could be calculated.

3.2.3.2 Rayleigh distribution

This function is a special case of Weibull distribution with shape parameter equal to 2 [257]. The Rayleigh distribution is the simplest function which used the average wind speed for calculating the probability density function and cumulative distribution function, as shown in the equations written below [123]:

$$f(U) = \frac{U}{{\sigma_c}^2} \exp\left(-\frac{U^2}{2\,{\sigma_c}^2}\right) \quad \text{Equation 3.43}$$

$$F(U) = 1 - \exp\left[-\frac{1}{2}\left(\frac{U}{\sigma_c}\right)^2\right] \quad \text{Equation 3.44}$$

where σ_c is a scale parameter which is solved by the maximum likelihood method as demonstrated by the following equation:

$$\sigma_c = \sqrt{\frac{\sum_{i=1}^{N} {U_i}^2}{2N}} \quad \text{Equation 3.45}$$

3.2.3.3 Lognormal distribution

A lognormal distribution is a continuous probability density function of a random variable whose logarithm is normally distributed [128]. The probability density function $f(U)$ and cumulative distribution function $F(U)$ for lognormal distribution is calculated using the following equation, respectively [258]:

$$f(U) = \frac{1}{U\,\alpha_{Sh}\sqrt{2\pi}} \exp\left[\frac{-1}{2}\left(\frac{\ln(U)-\beta_c}{\alpha_{Sh}}\right)^2\right] \quad \text{Equation 3.46}$$

$$F(U) = \frac{1}{2} + \frac{1}{2}\, erf\left(\frac{\ln(U)-\beta_c}{\alpha_{Sh}\sqrt{2}}\right) \quad \text{Equation 3.47}$$

where α_{Sh}, β_c are the shape and scale parameters, respectively, and $erf(U)$ is the error function, which defined in the following equation [123]:

$$erf(U) = \frac{2}{\sqrt{\pi}} \int_0^U exp(-t^2)\, dt \quad \text{Equation 3.48}$$

The maximum likelihood function is used to estimate the shape and scale parameters, as shown in the following equation [258]:

$$\alpha_{Sh} = \sqrt{\frac{1}{N}\sum_{i=1}^{N}[\ln(U_i) - \beta_c]^2} \quad \text{Equation 3.49}$$

$$\beta_c = \frac{\sum_{i=1}^{N} \ln U_i}{N} \quad \text{Equation 3.50}$$

3.2.3.4 Gamma distribution

The probability density function $f(U)$ and cumulative distribution function $F(U)$ of the gamma distribution is expressed using the following equation [259, 260]:

$$f(U) = \frac{U^{\xi-1}}{\beta_G{}^{\xi}\Gamma(\xi)} exp(-\frac{U}{\beta_G}) \quad \text{Equation 3.51}$$

$$F(U) = \int \frac{U^{\xi-1}}{\beta_G{}^{\xi}\Gamma(\xi)} exp\left[\frac{-U}{\beta_G}\right]\, dU \quad \text{Equation 3.52}$$

where Γ is the gamma function, ξ and β_G are shape and scale parameters, respectively, which can be solved utilizing the following equations [123, 261]:

$$\beta_G = \frac{1}{N\xi} \sum_{i=1}^{N}(U_i) \quad \text{Equation 3.53}$$

$$\text{N}\ln(\beta_G) - N\psi(\xi) = \sum_{i=1}^{N}\ln(U_i) \quad \text{Equation 3.54}$$

where ψ is the digamma function, which is calculated using the following equation:

$$\psi(\xi) = \frac{d}{d\xi}\ln(\Gamma(\xi)) \quad \text{Equation 3.55}$$

3.2.4 Evaluation criteria of wind probability density functions

Four statistical indicators are deemed to reflect the superiority of those distribution models which can evaluate the accuracy and performance of four distribution models: root mean square error (RMSE), coefficient of determination (R^2), Schwarz's Bayesian information criterion and Akaike information criterion. The coefficient of

determination (R^2) cannot display the precision of distributions alone; thus, various indicators were used to assess the accuracy. The RMSE calculates the difference between calculated values from the probability density function and actual measurement, which is close to zero as much as possible. This indicator is defined as [262]:

$$\mathrm{RMSE} = \sqrt{\frac{1}{N}\sum_{i=1}^{N}(X_{observed} - X_{predicted})^2} \quad \text{Equation 3.56}$$

where $X_{observed}$ is the frequency of observations, and $X_{predicted}$ is the frequency of predicted value from probability density function.

The coefficient of determination (R^2) shows the goodness-of-fit of different probability density functions. This is done by evaluating the square of the empirical correlation between predicted wind speed and observations values [263]. This parameter can be calculated as [118, 248, 249]:

$$R^2 = \frac{\sum_{i=1}^{N}(X_{observed} - Z_i)^2 - \sum_{i=1}^{N}(X_{observed} - X_{predicted})^2}{\sum_{i=1}^{N}(X_{observed} - Z_i)^2} \quad \text{Equation 3.57}$$

Akaike information criterion (AIC) is the selection criterion employed to compare models that used a maximum likelihood method for estimating the parameters of the probability density functions. AIC is calculated as [264]:

$$\mathrm{AIC} = -2\log\{\, p(E|\hat{\theta})\,\} + 2Q \quad \text{Equation 3.58}$$

where $p(E|\hat{\theta})$ is the density of E observed data, Q is the number of parameters in the model (dimension θ), and $\hat{\theta}$ is the maximum likelihood estimate.

Schwarz's Bayesian information criterion (BIC) is another criterion that serves to compare model selections [265]. It is more complicated than AIC selection since BIC is essentially an attempt to distinguish the true model. This BIC is asymptotically consistent with choosing the model in contrast to the AIC criterion, which is not asymptotically consistent [264]. BIC is expressed as [264]:

$$\mathrm{BIC} = -2\log\{\, p(E|\hat{\theta})\,\} + Q\log(n) \quad \text{Equation 3.59}$$

When performing the probability density function selection, the method with the lowest AIC or BIC is preferred [266].

3.3 Comparison of seven numerical methods for determining Weibull parameters for wind energy generation in NSW, Australia

The previous section described the use of four probability density functions: Weibull distribution, Rayleigh distribution, gamma distribution, and lognormal distribution. The evaluation of wind energy potential at different sites revealed that the Weibull distribution is the most accurate model. Several numerical methods to estimate the scale and shape parameters of the Weibull distribution function have been documented in the literature. At the beginning of this study, the comprehensive mathematical distributions used to fit wind data and procedures helped define the Weibull distribution's shape and scale parameters. The examination of different numerical models or fitting the Weibull distribution using evaluation parameters will be discussed. The second part investigates the wind direction of wind data for all sites. Finally, the power-law, which is the variation of wind speed with heights and wind power density, will be demonstrated.

3.3.1 Numerical methods for evaluating Weibull parameters

The numerical methods investigated in Chapter Six are the graphical method, maximum likelihood method, energy pattern factor method, modified maximum likelihood method, equivalent energy method, moment method, and empirical method. The governing equations of shape and scale parameters for each numerical method are listed in **Table 3.3** [267].

Table 3.3. The governing equations of shape and scale parameters for the seven numerical methods.

Numerical method	Governing Equations	
Graphical method	$\ln\{-\ln[1-F(U)]\} = \mathrm{K}\ln(U) - \mathrm{K}\ln(c)$	Equation 3.60
Maximum likelihood method	The shape and scale parameters calculated from Equation 3-41 and Equation 3-42, respectively.	
Moment method	The shape and scale parameters are calculated depending on the numerical iteration of the following equations:	
	$\bar{U} = c\Gamma(1+\frac{1}{\mathrm{K}})$	Equation 3.61
	$\sigma_U = c[\Gamma\left(1+\frac{2}{\mathrm{K}}\right) - \Gamma^2\left(1+\frac{1}{\mathrm{K}}\right)]^{1/2}$	Equation 3.62
	where Γ is the gamma function calculated as the following equation:	
	$\Gamma(x) = \int_0^\infty t^{x-1}\exp(-t)\,dt$	Equation 3.63
Empirical method	The shape and scale parameters are calculated by:	
	$\mathrm{K} = (\frac{\sigma_U}{\bar{U}})^{-1.086}$	Equation 3.64
	$c = \frac{\bar{U}}{\Gamma\left(1+\frac{1}{\mathrm{K}}\right)}$	Equation 3.65
Energy pattern factor method	$E_{pf} = \frac{\overline{(U^3)}}{\bar{U}^3}$	Equation 3.66
	$\mathrm{K} = 1 + \frac{3.69}{(E_{pf})^2}$	Equation 3.67
	where E_{pf} is the energy pattern factor, and $\overline{U^3}$ is the mean of wind speed cubes. The scale parameter calculated from Equation 3.65	
Modified maximum likelihood method	The shape and scale parameters are expressed as:	
	$\mathrm{K} = \left[\frac{\sum_{i=1}^N U_i{}^{\mathrm{K}}\ln(U_i)f(U_i)}{\sum_{i=1}^N U_i{}^{\mathrm{K}}f(U_i)} - \frac{\sum_{i=1}^N \ln(U_i)f(U_i)}{f(U\geq 0)}\right]^{-1}$	Equation 3.68
	$c = \left(\frac{1}{f(U\geq 0)}\sum_{i=1}^N U_i{}^{\mathrm{K}}\,f(U_i)\right)^{\frac{1}{\mathrm{K}}}$	Equation 3.69

	where $f(U \geq 0)$ is the probability for wind speed equal to or exceeding zero.
Equivalent energy method	$\sum_{i=1}^{N}\left[W_{Ui} - e^{-\left\{\frac{(U_i-1)\left[\Gamma\left(1+\frac{3}{K}\right)\right]^{\frac{1}{3}}}{\left(\overline{U^3}\right)^{\frac{1}{3}}}\right\}^{K}} + e^{-\left\{\frac{(U_i)\left[\Gamma\left(1+\frac{3}{K}\right)\right]^{\frac{1}{3}}}{\left(\overline{U^3}\right)^{\frac{1}{3}}}\right\}^{K}}\right]^2 =$ $\sum_{i=1}^{N} {\varepsilon_{U_i}}^2$ Equation 3.70 $c = \left[\frac{\overline{U^3}}{\Gamma\left(1+\frac{3}{K}\right)}\right]^{\frac{1}{3}}$ Equation 3.71 where W_{Ui} is the observed frequency of the wind speed, and ε_{U_i} is the error of the approximation.

In this study, the wind speed data will be presented using different numerical methods for Weibull distribution. The performance of the probability density function of seven models will be compared with measured data to evaluate the most suitable numerical model depending on statistical indicators. The following flow chart describes the methodology used, and the results will be illustrated in Chapter Six.

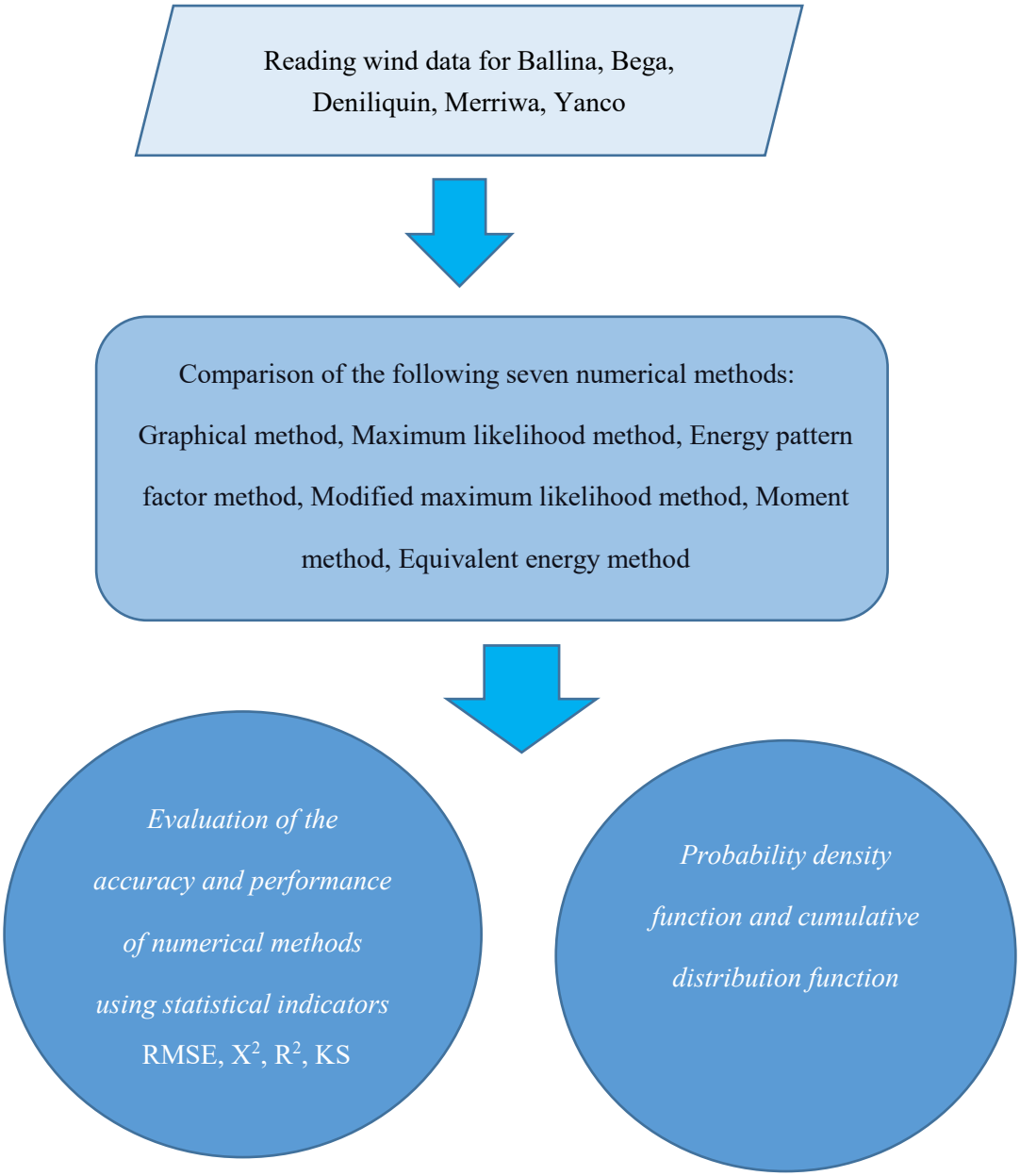

Figure 3.12. Flow chart of the comparative study of numerical methods for determining Weibull parameters at the selected sites.

3.3.2 Wind direction

For developing a successful wind farm, a state-of-the-art wind speed and direction measuring system is necessary to identify the suitable candidate site. To measure mean wind speed, wind direction estimation is critically important for both wind assessment and the control system of the wind turbine [268]. The frequency distribution of wind direction can be displayed in a polar form known as a wind rose. The wind rose plots divide each segment of the polar plot in colours to display the amount of time at which the wind is blowing in a certain speed range [113, 269]. The wind can be plotted by

dividing wind sample data into several divisions, such as 12 or 16 and calculating the statistical share of each sector. Finding the overall wind direction and frequency by applying the wind rose diagram is important for specifying the position of wind farm constructions [246].

3.3.3 Power-law and surface roughness and wind power density

Most of the wind measuring devices are installed at an elevation of 10 m, and any rise in elevation influences a wind speed to a specific height level. Topographical features such as hills and mountain tops also greatly affect wind speed. The wind speed reduces remarkably on the lee side while it increases on the top or luff side of a mountain perpendicular to the wind flow. Thus, wind speed increases with elevation as the speed is decreased by the roughness of the terrain [270]. The most common expression is used to calculate wind speeds with varying elevations, and this is known as the power-law [271, 272]. The power-law adjusts the observed wind speed according to different heights using the following equation [273]:

$$\frac{U_y}{U_0} = \left(\frac{h_y}{h_0}\right)^{\alpha_{power}} \quad \text{Equation 3.72}$$

where h_0 is the reference height, h_y is the desired height, U_y and U_0 are wind speeds at h_y and h_0, respectively, and α_{power} is the power exponent relying on different factors. These include such things as atmospheric stability, surface roughness and the nature of the terrain. Numerically, the power exponent has different values, with the most frequently used value being 1/7 because it is suitable for sites having neutral stability [253, 274]. The monthly mean wind speed profile at different elevations at the selected five sites will be calculated according to Equation 3.72.

One of the most important indicators used to classify a capacity of wind resources in a specific location is wind power density. It is expressed in the following equation [275]:

$$PD = \int_0^\infty \frac{1}{2}\,\rho U^3 f(U)\,dU \quad \text{Equation 3.73}$$

where PD is the wind power density (W/m^2). After calculating the wind power density at five selected sites, the wind resource is categorized according to the classification

in reference [108]. Chapters Five and Six revealed that Deniliquin has the highest wind potential, depending on an in-depth evaluation of wind resources at the five sites. Deniliquin area will be used to optimize the wind turbine due to its highest wind potential, as discussed in the following section.

3.4 Optimization of the wind turbine

The statistical analysis results showed the highest wind potential was at Deniliquin. Assessment of the available resource at Deniliquin was defined by the shape and scale parameters of the Weibull function. The shape and scale parameters are used as inputs for the optimization process, of which the objective is to maximize the AEP of a 20 kW wind turbine depending on the wind speed data in Deniliquin. The following section describes the optimization methodology.

3.4.1 Blade element momentum theory

The actuator disc concept has introduced the methodology for an ideal rotor devised by Rankine, which assumed a permeable disc has a uniform load distribution over the rotor area with no fractional drag force and wake rotating. However, the physical explanation has been explained by Froude [276]. The concept of 1D momentum theory used a linear conservation momentum equation; there is a force enclosing the control volume system called thrust force, which is equal to the difference in pressure across the wind disc multiplied by the area of the rotor. The output power (P) calculated by multiplying the thrust force by the rotor area is shown in the following equation [165]:

$$P = 2\rho a(1-a)^2 {V_o}^3 A \qquad \text{Equation 3.74}$$

where A is the area of actuator disc, V_O is the free wind speed, and a is the axial induction factor. Betz [277] defined the maximum value of the power coefficient ($Cpower$) using the axial induction factor as the following equation:

$$Cpower = 4a(1-a)^2 \qquad \text{Equation 3.75}$$

The maximum theoretical power coefficient is achieved at around 60% at a = 1/3 value, which is called the Betz limit for the ideal actuator disc.

The BEM theory is a mathematical model used as a fast method to study the aero-

elastic and aerodynamics performance of the wind turbine rotor blade. It is used to determine the optimal rotor geometry to achieve the maximum power design. The two essential concepts of BEM are blade element theory and momentum theory [165]. Drzewiecki [278] proposed the concept of blade element theory which divides disconnected airfoils along the rotor blade, where the flow past a given section is considered 2D. The effective inflow velocity can be constructed as the vector sum of the incoming velocity and the rotational speed [279].

As seen below in **Figure 3.13(a),** the discrete radial stations along the blade have been used to describe the shape of the blade, as shown in **Figure 3.13(b)**. The chord length, *c(r)*, and twist angle *β(r)*, which is the angle between the local airfoil along the blade and the tip airfoil, have been used to define the shape of the blade [165].

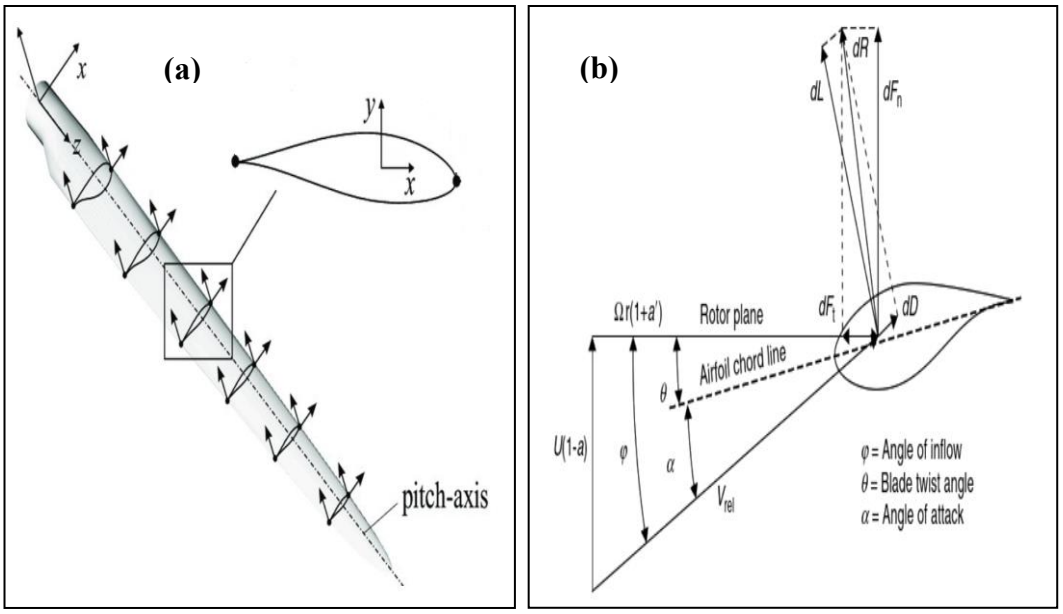

Figure 3.13 (a) Schematic of wind blade and **(b)** Sketch showing twist angle, chord length and pitch angle on a blade.

Figure 3.13(b) depicts the velocity triangle. It has been drawn according to the forces considered in 2D airfoil, which are composed as the vector sum of the rotational speed of the rotor and relative wind speed. This is apart from the induced velocities that are the reaction on the incoming flow from the aerodynamics blade loads. Thus, the angle between relative wind speed with rotor plane is called the flow angle (φ), which is calculated using axial (a) and tangential (a') induction factors and stated in the following equation:

$$\tan \varphi = \frac{(1-a)V_O}{(1+a')\Omega r} \quad \text{Equation 3.76}$$

The magnitude of relative wind speed on the airfoil section is calculated using the following equation:

$$V_{rel}{}^2 = (1 - \mathrm{a})^2 V_O{}^2 + (1 + a')^2 (\Omega r)^2 \quad \text{Equation 3.77}$$

The angle of attack (α) is a very important parameter for calculating the lift and drag coefficient of the airfoil. This angle is calculated from the difference between the flow angle (φ) and the angle between the rotor plane and airfoil chord (θ) as in the following equation:

$$\alpha = \varphi - \theta \quad \text{Equation 3.78}$$

The pitch angle (θ_p) is the angle between the tip airfoil and the rotor plane the plane angle, where Θ(r) is the angle between one section on the blade, and the rotor plane is calculated as the following equation:

$$\Theta(\mathrm{r}) = \theta_p + \beta(r) \quad \text{Equation 3.79}$$

After knowing all angles, lift and drag forces for each section, the projected normal F_n and tangential F_t aerodynamics forces, which projected on the rotor blade could be calculated as:

$$F_n = l \cos \varphi + d \sin \varphi \quad \text{Equation 3.80}$$

$$F_t = l \sin \varphi - d \cos \varphi \quad \text{Equation 3.81}$$

where l and d is the lift and drag forces.

Torque on each airfoil section along the blade can be expressed as:

$$dM = 0.5 \rho B \frac{V_O(1-a)\Omega r(1+a')}{\cos \varphi \ \sin \varphi} r c(r) \, C_t dr \quad \text{Equation 3.82}$$

where, B is the number of blades, C_t is the tangential force coefficient that can be calculated as:

$$C_t = C_l \sin \varphi - C_d \cos \varphi \quad \text{Equation 3.83}$$

while the normal force coefficient C_n is expressed as:

$$C_n = C_l \cos \varphi + C_d \sin \varphi \quad \text{Equation 3.84}$$

Finally, as seen in **Figure 3.14**, the thrust force (dT) and thrust coefficient C_T at the

stream tube can be calculated utilizing:

$$dT = B\mathrm{F_n}\, dr \qquad \text{Equation 3.85}$$

$$\mathrm{C}_T = \frac{\sigma(r)(1-a)^2(C_\mathrm{l}\cos\varphi + C_\mathrm{d}\sin\varphi)}{\sin^2\varphi} \qquad \text{Equation 3.86}$$

where the local solidity $\sigma(r)$ is calculated as:

$$\sigma(r) = \frac{c(r)B}{2\pi r} \qquad \text{Equation 3.87}$$

The axial and tangential induction factor, which significantly affect the value of the forces on the airfoil section can be expressed as:

$$a = \frac{1}{\frac{4\sin^2\varphi}{\sigma \mathrm{C_n}} + 1} \qquad \text{Equation 3.88}$$

$$\mathrm{a}' = \frac{1}{\frac{4\sin\varphi\cos\varphi}{\sigma \mathrm{C_t}} - 1} \qquad \text{Equation 3.89}$$

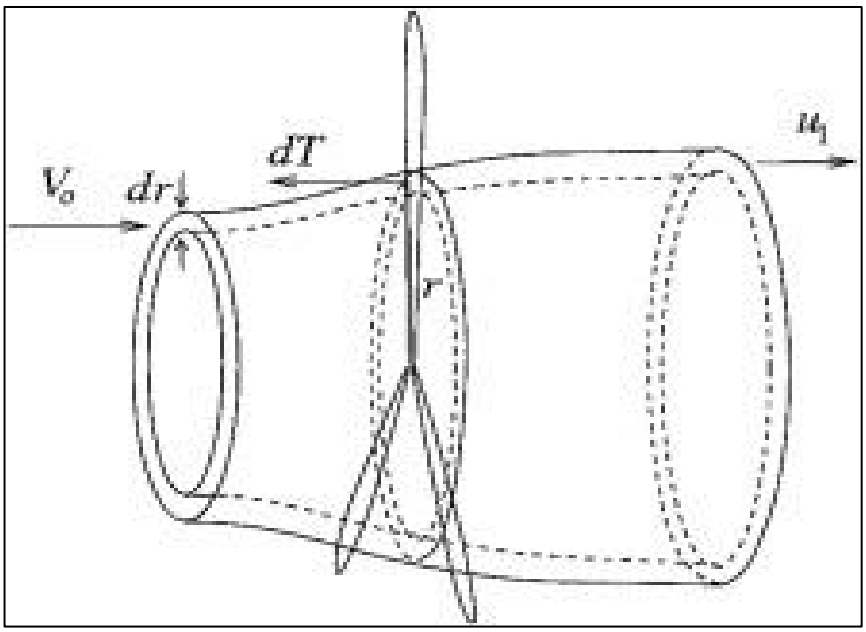

Figure 3.14. A stream tube of thickness,dr, intersecting the radial position, r, on the rotor plane [165].

The assumptions in the BEM method are an infinite number of blades, non-rotating wake, incompressible steady-state flow, no aerodynamics and structural interaction among sections, and absence of drag fractions [196]. Moreover, different modification and correction factors such as Prandtl's tip speed factors are developed to improve BEM theory [279, 280].

3.4.2 Optimization Blade Shape Methodology

NREL developed HARP_Opt in the USA [281]. The HARP_Opt open-source code is used to conduct the horizontal axis rotor performance optimization process. The HARP_Opt gathers a BEM theory code with a genetic algorithm (GA) code to optimize and design the wind turbine's rotor shape. Genetic algorithms [282] are evolutionary algorithms, and they are robust and reliable search techniques depending on the mechanism of natural selection [283]. The optimization process of the GA is done by iterating a set of individual solutions, where a set of solutions is called a population. An iteration is carried out from one population to the next to obtain subsequent populations of superior individuals. The WT_Perf software (NREL, Golden, CO, USA) [284] is used as the essential BEM code in HARP_Opt. The WT_Perf is developed to analyse the aerodynamics performance of the wind turbine using the BEM code. The HARP_Opt uses the WT_Perf code to predict the performance of the rotor wind turbine and the MATLAB GA code to carry out the optimization. The HARP_Opt could be employed for a single or multiple objective optimization code for the objective function in the HARP_Opt software, either maximization of the AEP of the wind turbine or wind turbine efficiency.

3.4.2.1 Design Variables and Objective Function

The blade shape of the wind turbine is defined by the airfoil, chord length, and twist angle of each section along the blade. The validated wind turbine model of 20 kW, which has been discussed previously, is used as a baseline for the optimization process and the same family of S809 airfoil was used.

The airfoil lift and drag polar was done using the spreadsheet AirfoilPrep v2.02 (v2.02.03, Windward Engineering, LLC, USA). This type of Excel formatting enabled the airfoil data to be imported into WT_Perf. After preparing the airfoil data file, the file was imported into HARP_Opt. The objective of the optimization process was to maximize the AEP of 20 kW wind turbine depending on the wind speed data in Deniliquin using the output of optimal chord length and twist distributions along the wind turbine blade. In this study, a single objective method was considered where the optimization was focused on the aerodynamics shape without including structural

optimization studies [285-289]. To define the AEP of the wind turbine, the probability distribution $f(U)$ is combined with the power curve of the wind turbine $P(U)$ as shown in the following equation:

$$\text{AEP} = \int_{U_{cut,in}}^{U_{cut,out}} P(U)\, f(U) dU \qquad \text{Equation 3.90}$$

where $U_{cut,in}$ is the cut-in wind speed (m/s), and $U_{cut,out}$ is the cut-out wind speed (m/s).

The Bezier curves defines the chord length and twist angle distributions to smooth the span-wise distribution along the blade. There were five control points for each chord length and twist angle parameters; thus, the total overall decision variables amounted to 25 control points. The same rated power, the rotor diameter, and the hub height were used as input in HARP_Opt, with the baseline validated wind turbine model as shown in **Figure 3.15**.

In this study, the variable rotor speed and variable pitch control were used for the control system to produce more energy output [32]. The allowable rotor speeds range from 25 rpm to 150 rpm. **Table 3.4** below summarizes different parameters of turbine configurations.

Table 3.4. Turbine configurations.

Wind Turbine Parameters	Value
Rotor diameter	11 m
Rated power capacity	20 kW
Number of the blade segments	30
Number of blades	3
Hub diameter	0.6
Hub distance from the bottom surface	13 m
Air density	1.225 kg/m^3

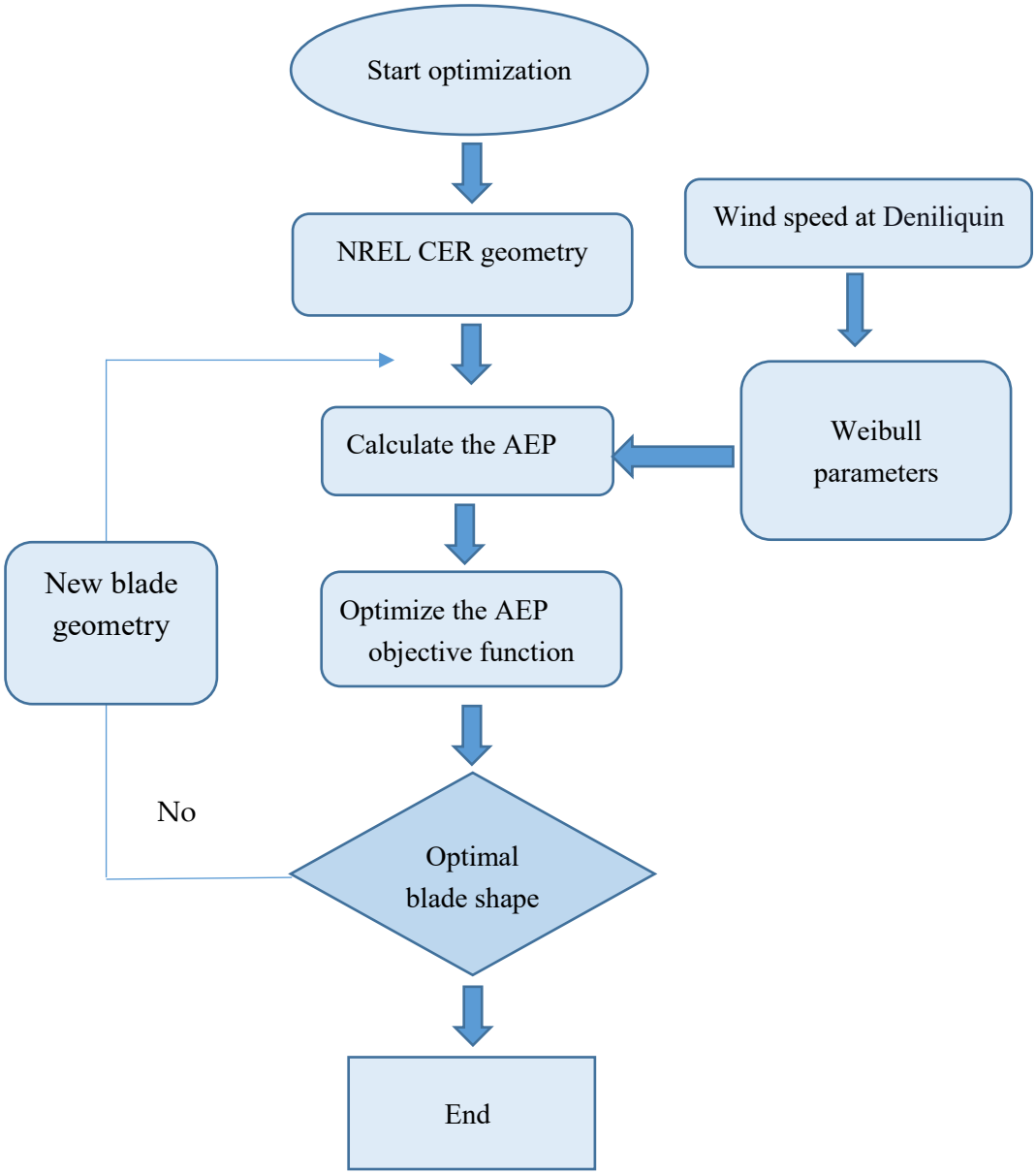

Figure 3.15. Optimization flowchart.

3.4.2.2 Constraints

Specific design parameters should be in place to generate acceptable blade geometry [170, 290, 291]. In Reference [290], the maximum and minimum values for twist angle and chord length at the control points were decreased along the radial direction as indicated in the following equation:

$$X_{i\,min} \leq X_i \leq X_{i\,max} \qquad i = 1, 2, 3, 4, 5 \qquad \text{Equation 3.91}$$

where $X_{i\,min}$ is the lower limit and $X_{i\,max}$ is the upper limit for the chord length and the twist angle [292].

This limitation was applied in the current study. The twist angle was given a lower

bound of −10 degree, which was used in two studies [291, 293]. The upper limit was calculated to the original twist angle, adding 0.3 increments to the twist angle. In two studies, the lower bound of the chord length was 0.05 m, except for the first section, which should be the maximum chord length, then declined with the chord length. In this study, the chord length was given a lower bound of 0.1 m, except for the 25% radial station of the blade, where the maximum chord value should be higher than 0.5 m. The chord value decreased after this section. The maximum bond was calculated to the original chord, adding 4% increments according to the chord length. As shown in **Table 3.5**, the lower and upper bounds represent the five control sections' control twist and chord values, respectively.

Table 3.5. Genetic algorithm (GA) configuration.

Radial Position	1.25	1.535	2.345	3.565	5.5
Twist angle (degree)					
Minimum	−10	−10	−10	−10	−10
Maximum	25	17	5	3	−1
Chord length (m)					
Minimum	0.5	0.1	0.1	0.1	0.1
Maximum	0.8	0.72	0.65	0.55	0.37

Trial and error were used to tune the GA's parameters. The values entered into this optimization run were the final ones after using trial and error. **Table 3.6** summarizes the GA configuration employed.

Table 3.6. Genetic algorithm configuration.

Optimization Parameters	**Value**
Population size	200
Generation	150
The cross-over fraction	0.25
Error tolerance for the GA fitness values	1×10^{-6}

This study applied CFD modelling for the NREL CER wind turbine. It investigated the aerodynamics characteristics of a 20 kW wind turbine at three-bladed twisted angles and tapered blades. The grid independence was achieved in terms of mechanical torque. The study also investigated the effect of four turbulence models in predicting the mechanical torque and pressure distributions. Simulated wind conditions varied from attached to separated flow conditions. Finally, a HARP_Opt code was used to optimize the wind turbine design using a genetic algorithm to maximize the AEP at the Deniliquin site.

Chapter Four

4 Numerical modelling of the horizontal wind turbine under separation conditions

This chapter presents and discusses the numerical modelling of the horizontal wind turbine under separation conditions. The NREL CER experiment was used as a reference for validating the aerodynamics performance of a three-blade wind turbine which has been investigated in CFD modelling using Ansys Fluent in this thesis. It is organized into four sections. Section 4.1 investigates the effect of four RANS turbulence models on predicting the aerodynamics characteristics of the twisted wind turbine, where the mechanical torque is used for model validation compared with NREL test results. Section 4.2 discusses the differences between turbulence models under different wind speeds that included stall conditions using blade pressure distribution along the blade. Section 4.3 investigates the main aerodynamics parameters such as lift coefficient, which have been extracted at a different span-wise section along the blade. Also, the aerodynamics flow of S809 airfoil is visualized under different angles of attack, and they reveal the flow variation from attached separated flow conditions. In section 4.4, characteristics of the blade have been investigated using pressure contour and axial velocity presentation. The main results are summarized in the final part of this chapter, section 4.5.

4.1 Mechanical torque

Figure 4.1 compares the modelled shaft torque values using different RANS models and the measured results for the NREL rotor, which operated at a fixed speed of 72 rpm and a pitch angle of 5°. The CFD results agreed well with the measurements at low and medium wind speeds between 4.9 and 9.0 m/s. Transition plays an insignificant role in the prediction of the flow behavior of the wind turbine during this

speed range. All RANS models excellently predict the flow around the wind turbine at the area where the flow is still attached.

It is important to note here that at a flow velocity between 9.0 and 10.5 m/s, the boundary layer was driven from the laminar to the turbulent transition area where the onset of a stall occurs. The Transition SST model made the best prediction for that region because it can resolve the laminar transition where the turbulent boundary layer, which starts at the stall phenomenon, is considered. After 10 m/s, the results showed a marked difference for mechanical torque between the measured and RANS models. The significant separation of the flow and stall phenomena played a role in the difficulty of mechanical torque prediction using RANS models.

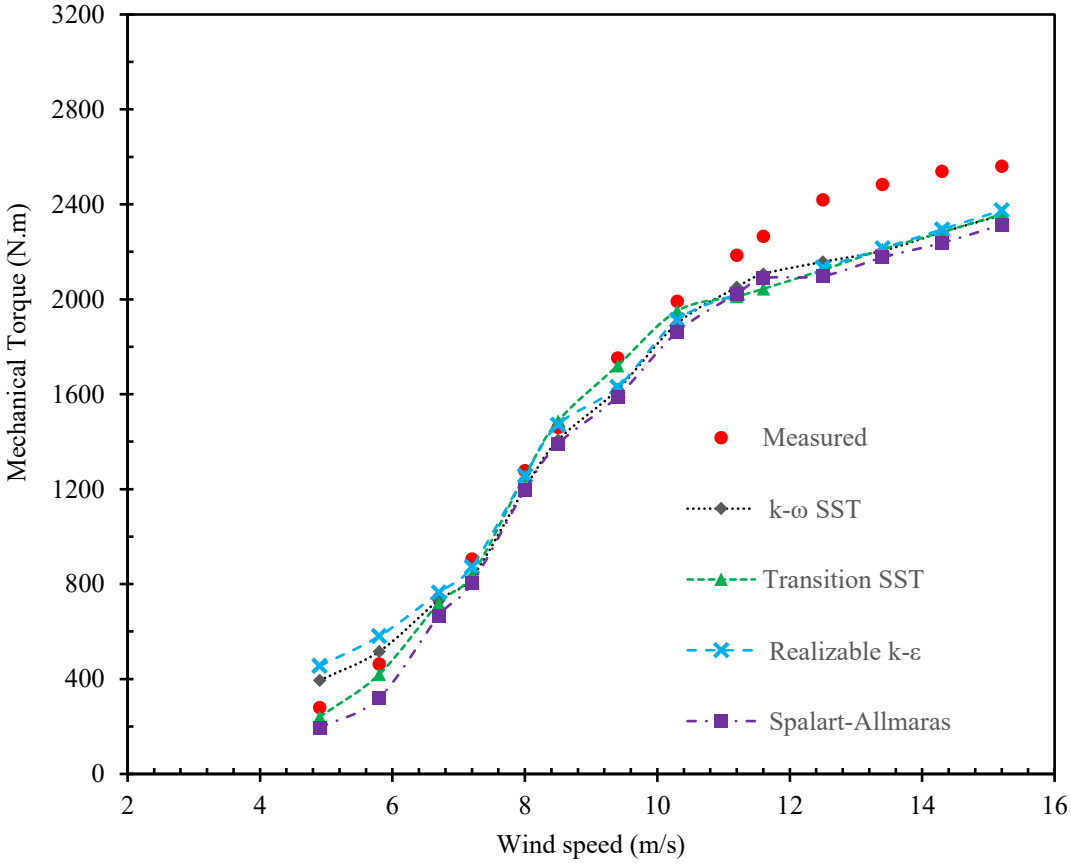

Figure 4.1. Mechanical torque.

The computing system details are discussed in **Table 4.1(a)**. The corresponding computation time is illustrated in **Table 4.1(b)**. As can be seen in the table, the computation times for the four models exhibit no noticeable differences. Consequently, the selected model will depend on the accuracy rather than

computational time.

Table 4.1. (**a**) Computing system. (**b**) Model-related computation time.

(a)	
CPU	2.9 GHz Intel Xeon E5-2690 (8 cores) 20 megabytes L3 QuickPath Interconnect (QPI) (max turbo frequency 3.8 GHz, min 3.3 GHz)
Random access memory (RAM)	32 gigabytes 1600 MHz ECC DDR3-RAM (quad channel)
Memory	2 × 1 terabyte 7200 rpm sata III hard drives (raid)
(b)	
Realizable k-ε	4.15 h
Transition SST	5.46 h
k-ω SST	4.66 h
Spalart–Allmaras	3.74 h

4.2 Pressure distribution

Figure 4.2 and **Figure 4.3** illustrate comparisons of the measured and computed pressure coefficients at the four most important radial span sections (0.47R, 0.63R, 0.8R and 0.95R) for two different wind speeds of 7.2 and 10.2 m/s. Referring to the 7.2 m/s inlet wind speed, as shown in **Figure 4.2**, the modelled pressure distributions match well with the experimental values where the flow is almost attached to this wind speed with no stall boundary layer separation having yet started. Thus, all RANS models agree well with the experimental data except Realizable k-ε. In effect, this model has some limitations when the domain includes two fluid zones, i.e., stationary and rotating zones [294]. In this case, non-physical turbulent viscosities are produced, affecting the value of the turbulent viscosity. Since the present simulation consists of

two domains, the Realizable *k-ε* is not appropriate for predicting the current wind turbine simulation.

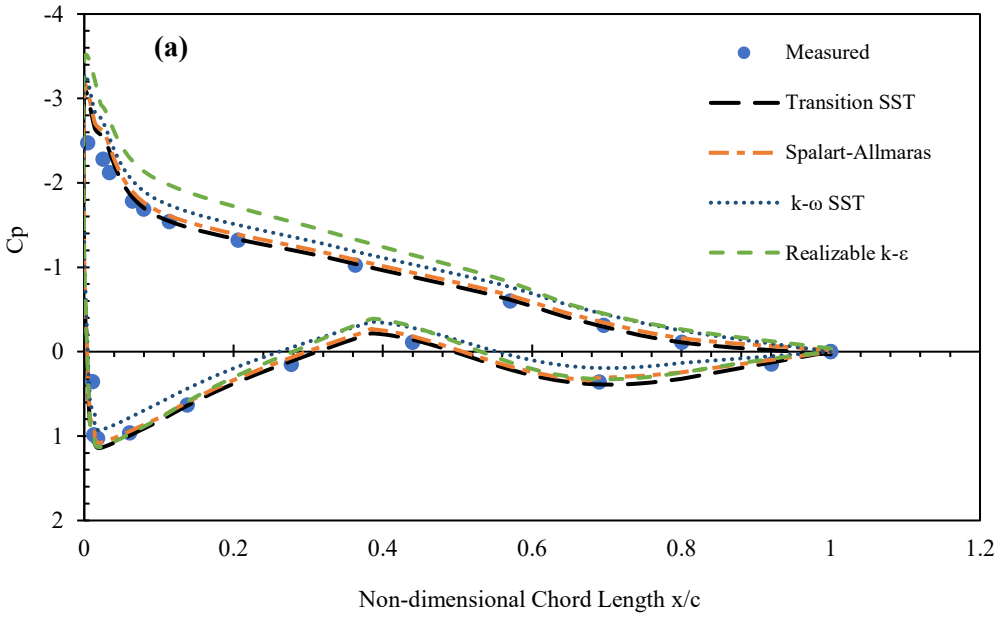

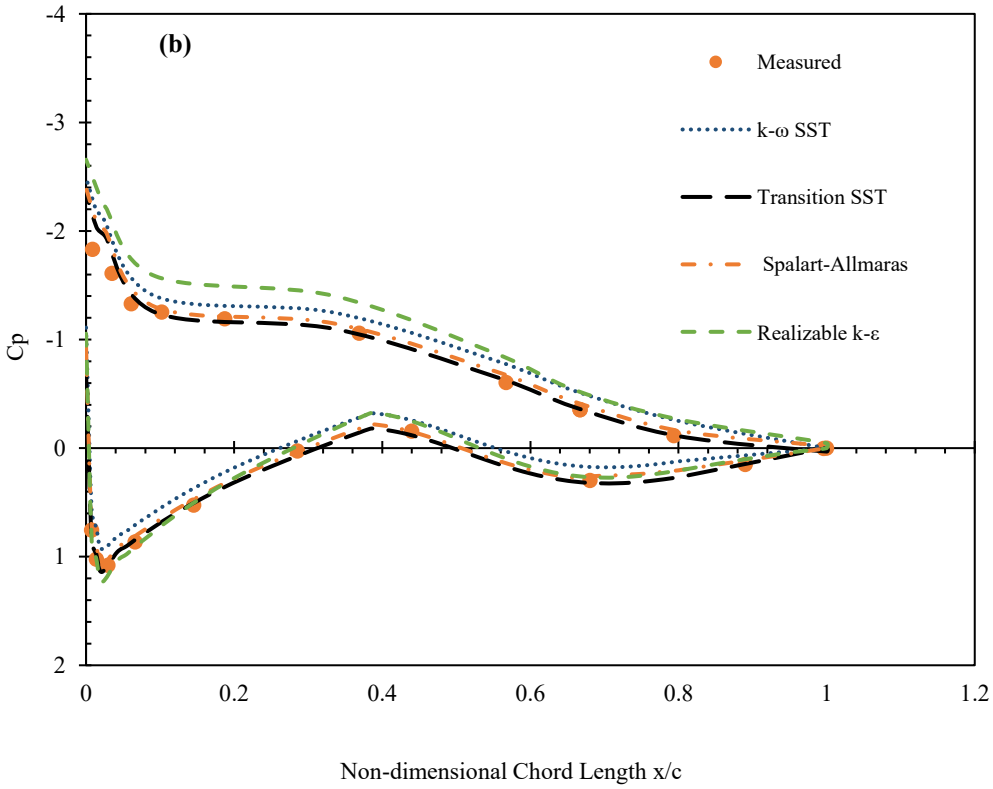

Continued on next page

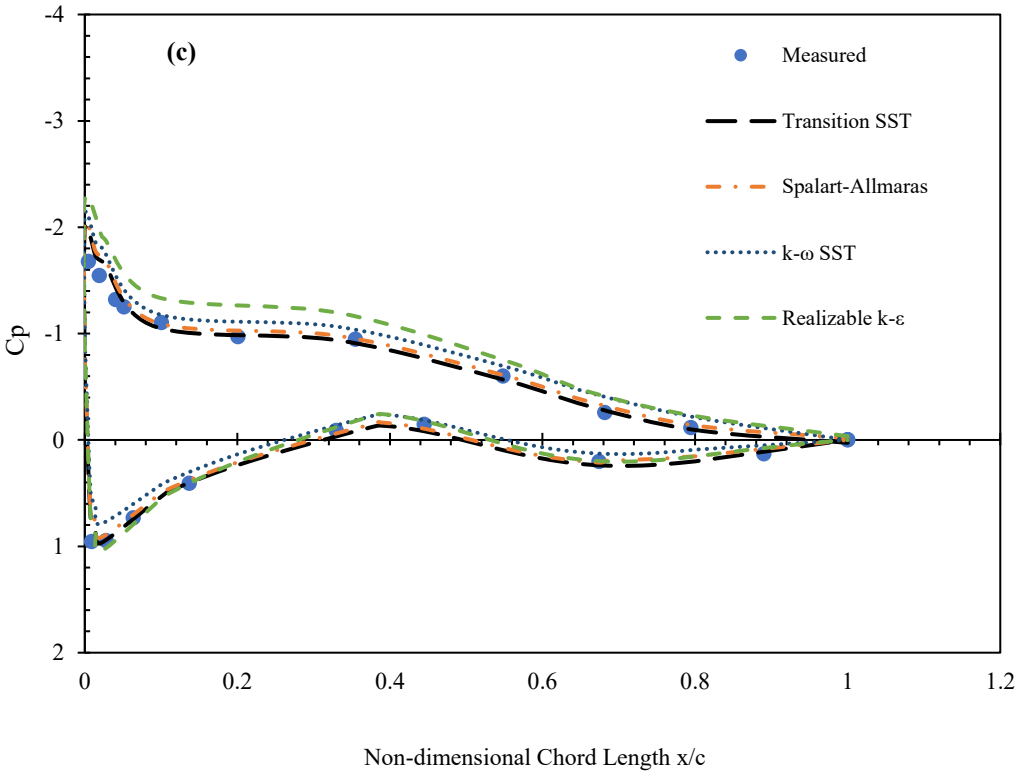

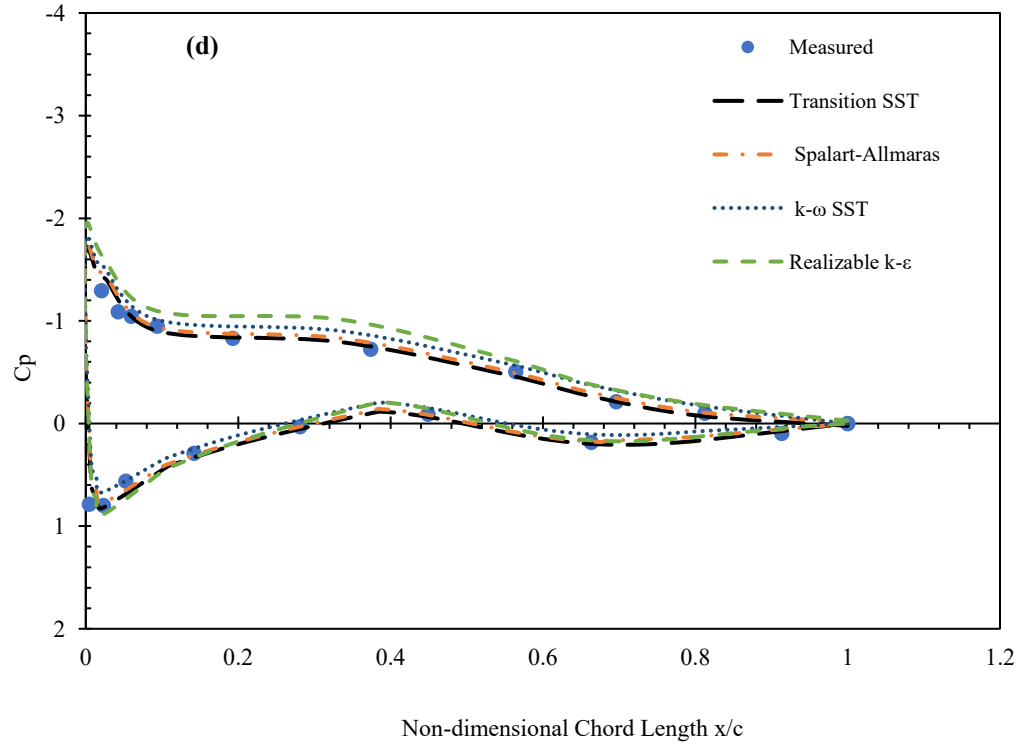

Figure 4.2. Comparison of span-wise pressure distribution between different turbulence models and NREL measurements at 7.2 m/s at: (a) 47% section, (b) 63% section, (c) 80% section, and (d) 95% section.

For inlet wind speed of 10.2 m/s, which was classified as the onset of the stall as shown

in **Figure 4.3**, the best way to predict the airfoil's pressure coefficient was to use the Transition SST model. Any changes in the adverse pressure gradients would be reflected directly on the laminar boundary layer. Hence, the early separation for the laminar boundary layer will happen compared to the turbulent boundary layer. The Transition SST model could predict the boundary layer for the flow region that changed from the laminar flow region to the turbulent transition region. Changing between boundary layers enabled the Transition SST model to better predict the aerodynamics flow of the wind turbine for a stall wind condition compared with other RANS models, as shown in **Figure 4.3(a)**. The stall phenomena began at the 47% span location, and the separation was evident among the RANS models for predicting the wind turbine's aerodynamics.

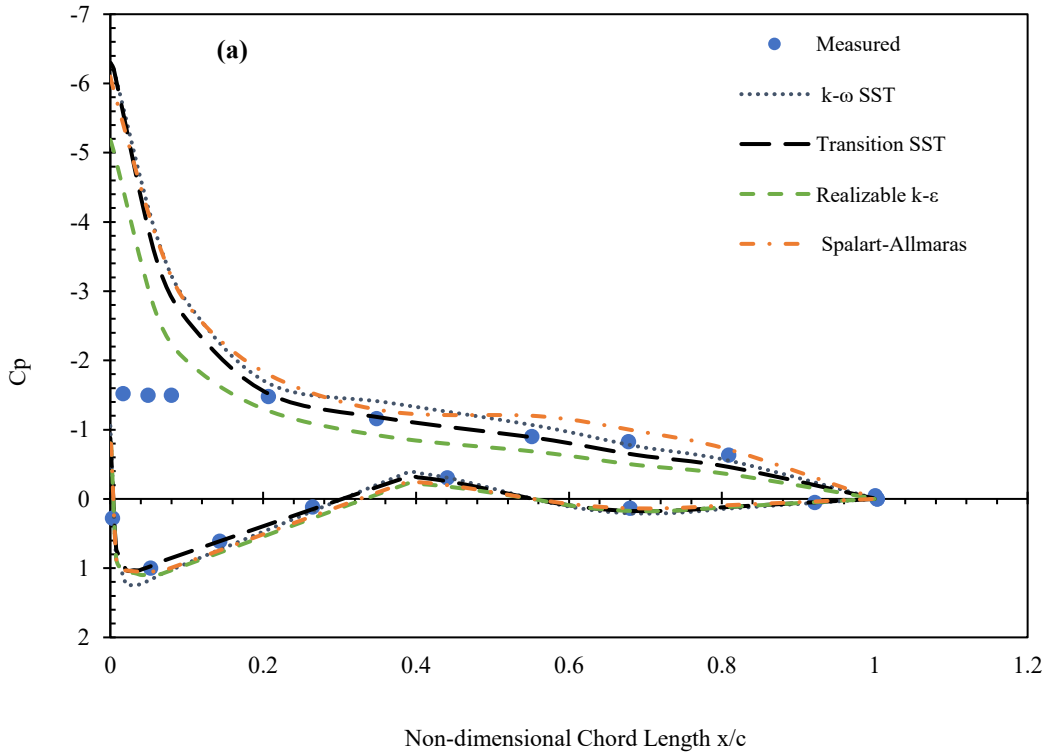

Continued on next page

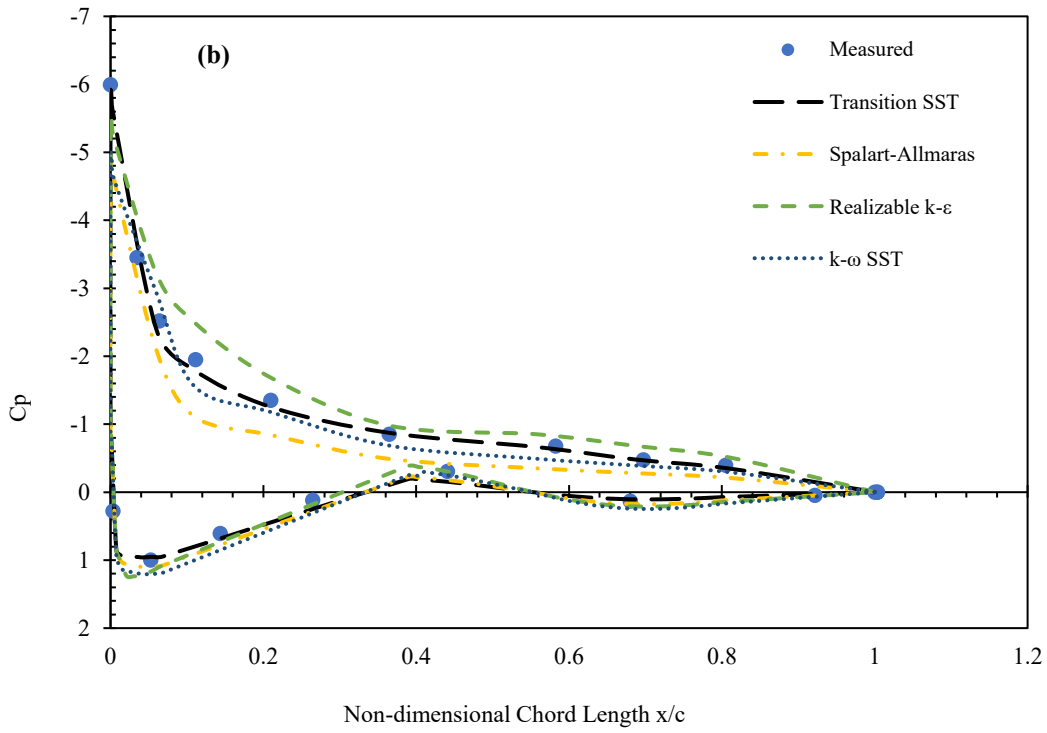

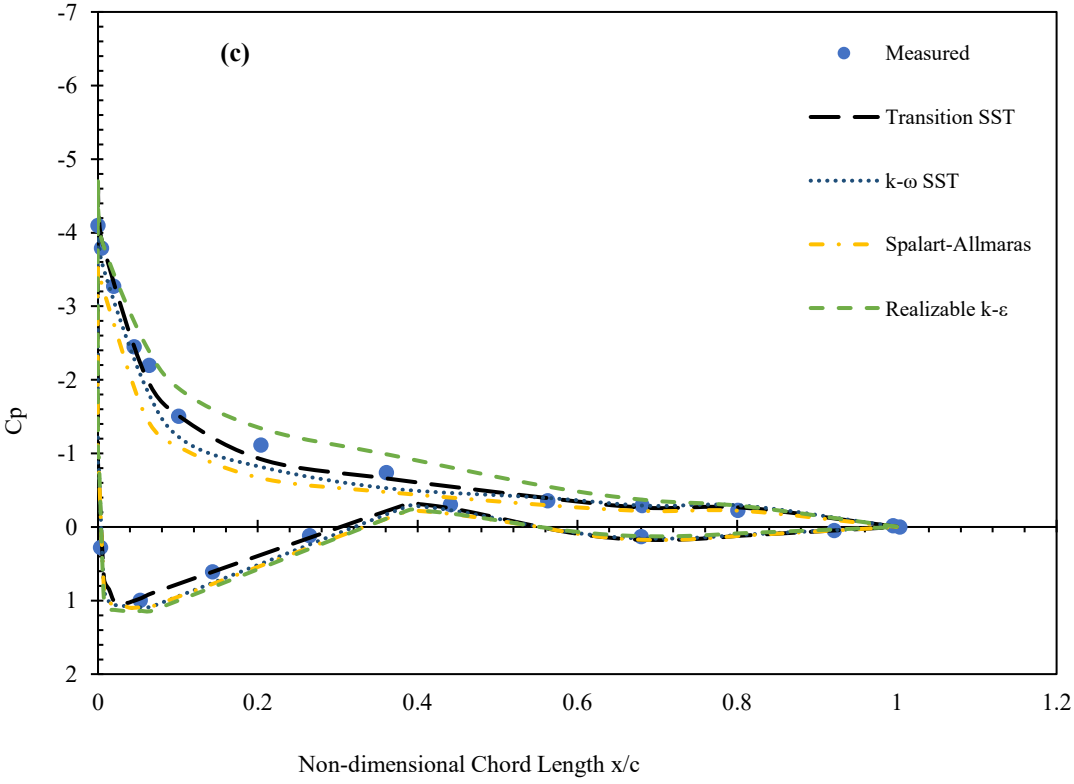

Continued on next page

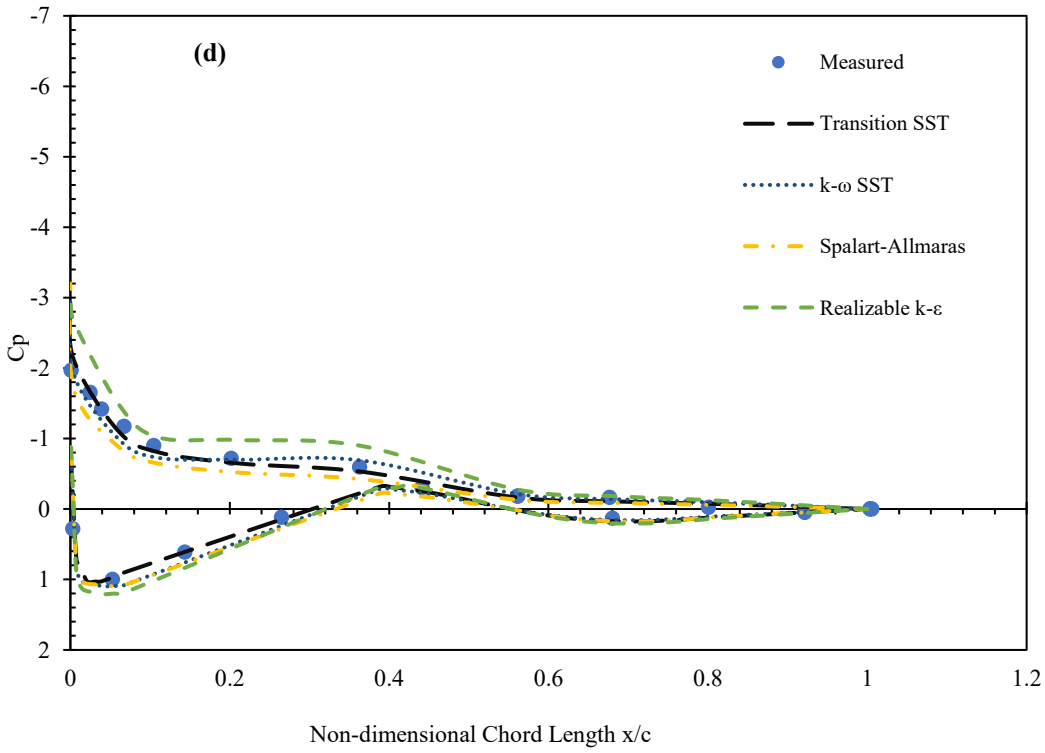

Figure 4.3. Comparison of span-wise pressure distribution between different turbulence models and NREL measurements at 10.2 m/s at: (a) 47% section, (b) 63% section, (c) 80% section, and (d) 95% section.

4.3 Investigation of the airfoil characteristics

It is essential to improve our understanding of the main aerodynamics characteristics of each section along the blade. Determination of the lift and drag coefficient of each airfoil section along the blade is a critical parameter for calculating the angle of attack. The Reynolds number increases at high wind speed, which affects the angle of attack and the corresponding lift coefficient [295]. Results of the lift coefficient were obtained from a simulation over NREL at a pitch angle equal to 5° and wind speeds varied from 4.9 to 15.2 m/s at a fixed angular speed, i.e., 72 rpm. As shown in **Figure 4.4**, the lift coefficient varied with both radial sections and velocities.

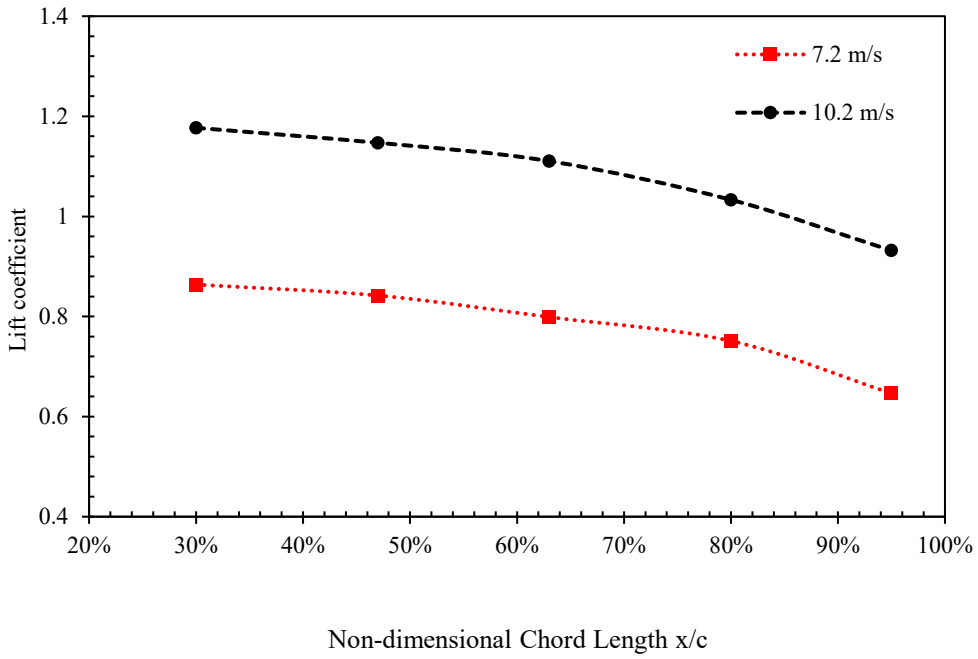

Figure 4.4. Variation of lift coefficient with different Non-dimensional chord length sections along the blade.

As shown in **Figure 4.5**, the calculated angle of attack had a high twist angle of 12.13° at 7.2 m/s wind speed on a plane through the blade at a distance of 1.51 m. At the same length, the angle of attack at 10.2 m/s was 22.04°. Thus, the angle of attack increased with increasing wind speed and decreased with the radial position [210]. At 7.2 m/s near the hub region, minor transition and separation may occur due to the slightly high angle of attack, but the flow was still below the stall region and almost always attached. When increasing the wind velocity, the angle of attack increased at 10.2 m/s to the onset of the stall. The full separation occurred between the hub and 80% of the tip sections at this wind speed. Thus, the separation on the flow from the leading edge to the trailing edge occurred at 47% of the blade and remained until 80% of the blade.

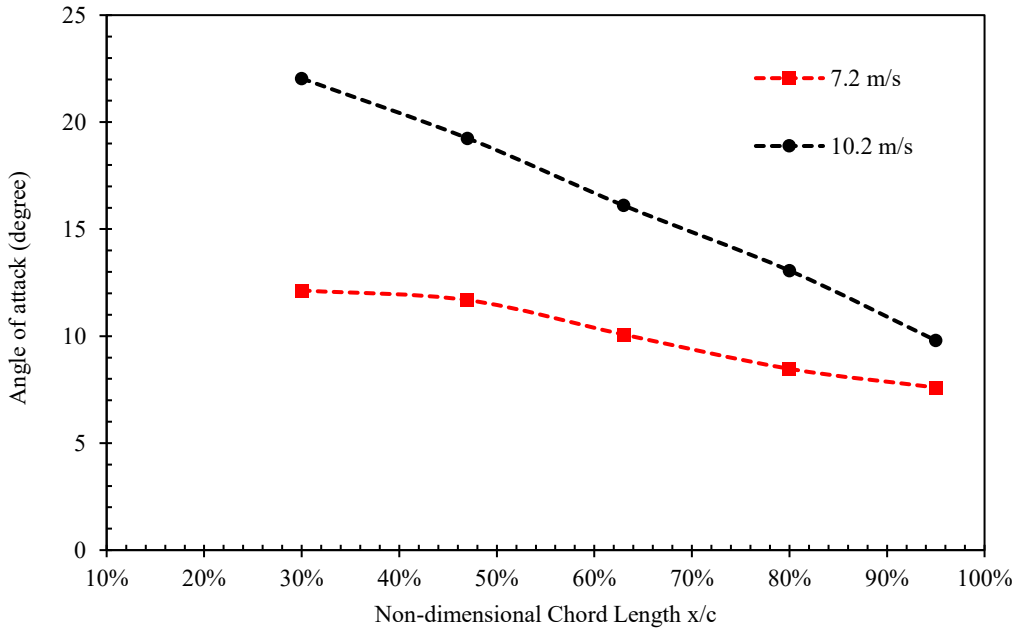

Figure 4.5. Variation of the angle of attack with different Non-dimensional chord length sections along the blade.

The flow behavior at different airfoil sections along the blade was visualized around the airfoil with velocity and pressure contours. Transition SST indicated good results amongst the four turbulence models with the measurements shown above. As such, the velocity vectors and pressure contours results were predicted by the Transition SST model. The blade cross-section at a 1.51 m radius investigated the flow on the inner region of the blade. In contrast, the blade cross-section at 4.78 m radius studied the flow on the outer area of the blade. The flow characteristics around the airfoil at the condition when the flow is almost attached at 7.2 m/s of different span stations are depicted in **Figure 4.6**. This figure shows that the pressure fell to a small value as the flow over the airfoil accelerated. As the results in **Figure 4.6** (a,c,e,g, and i) indicate, the pressure coefficient dropped quickly to zero and reached a negative value. As the flow slowed down, the pressure increased, and the magnitude of the pressure coefficient decreased.

Consequently, the pressure of the lower surface became larger than the pressure of the upper surface, causing the blade to rotate. These results confirmed that the values of the pressure coefficient were negative at higher velocities. To understand the flow at

boundary layer separation [296], the pressure and velocity vector distributions at the velocity of 10.2 m/s are shown in **Figure 4.7**. The separation will start when the flow on the upper surface at the airfoil's trailing edge decelerates and mixes with the airflow from the lower surface. The point of flow separation happens earlier at larger angles of attack, and as the intensity of the adverse pressure rises, the separation point shifts forward on the airfoil.

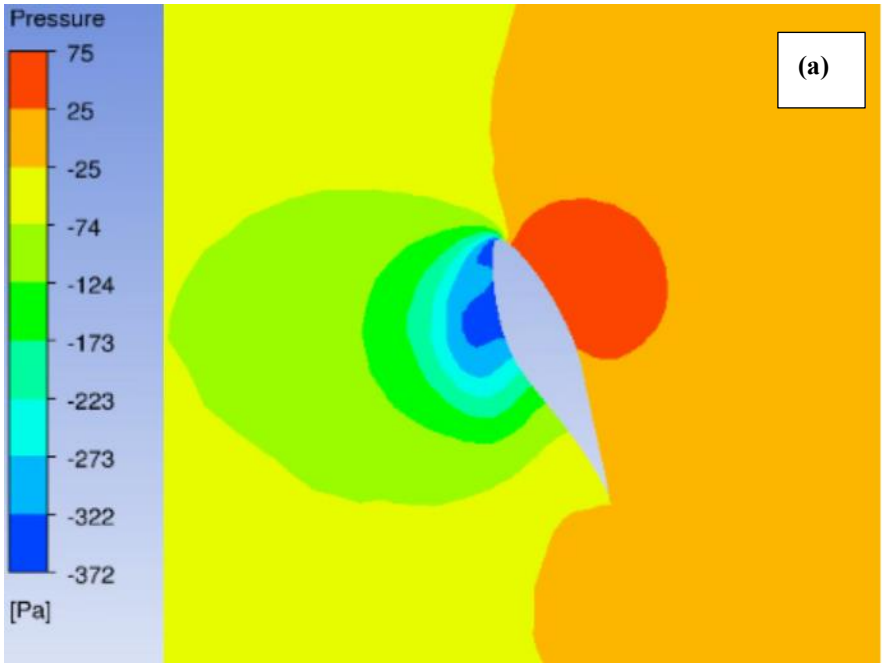

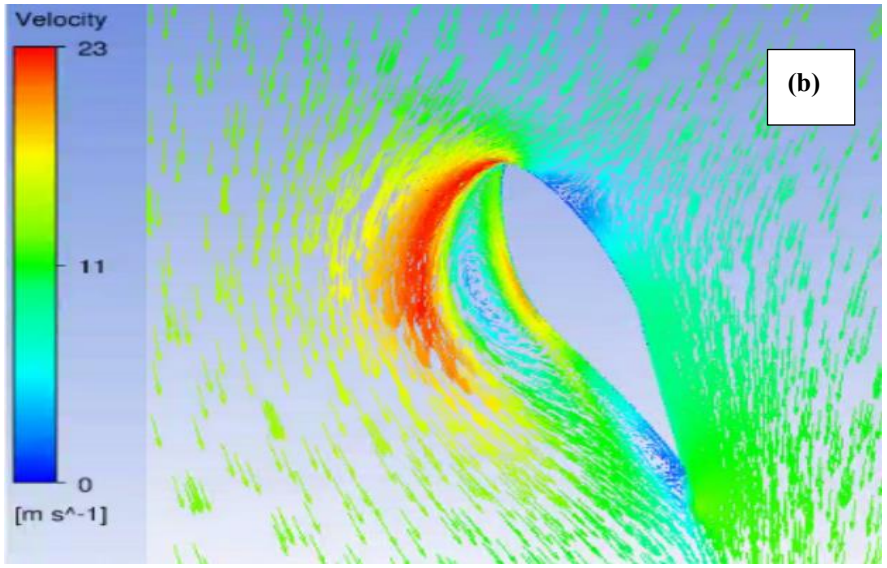

Continued on next page

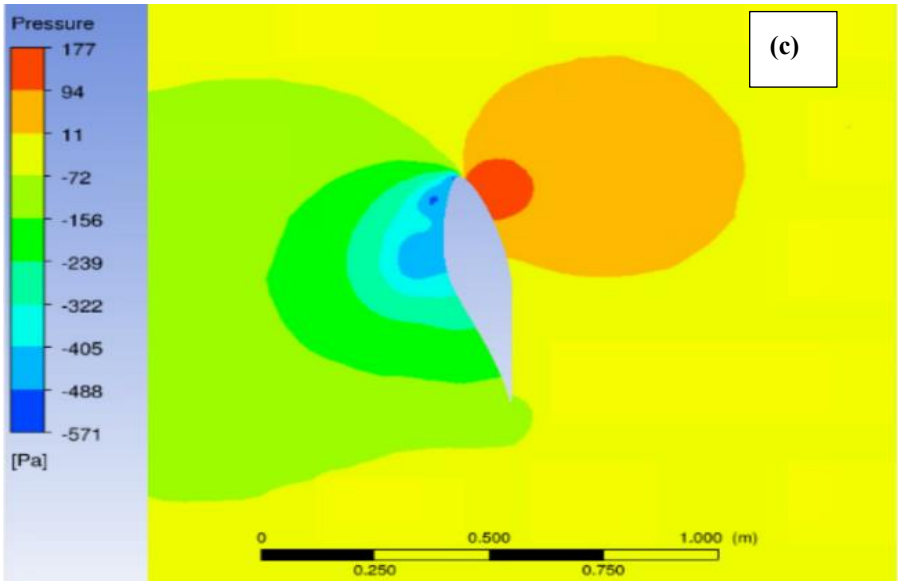

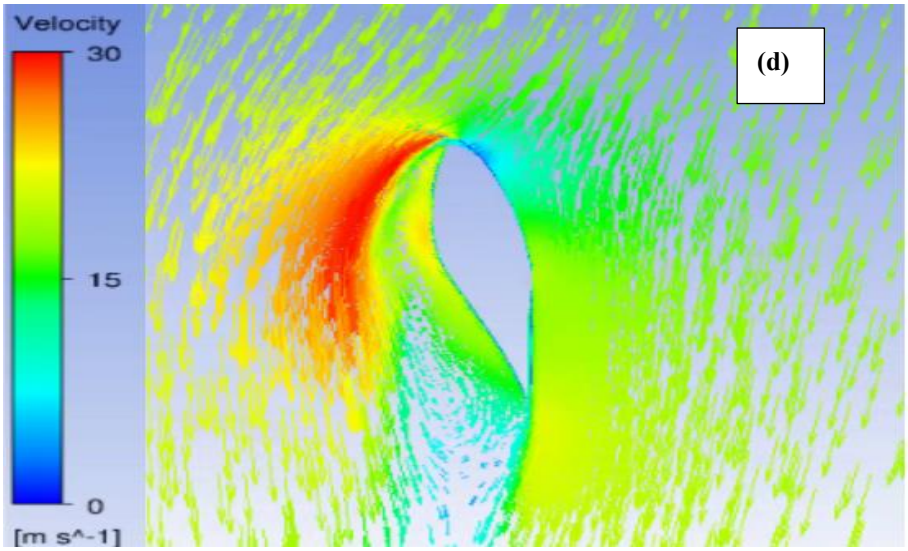

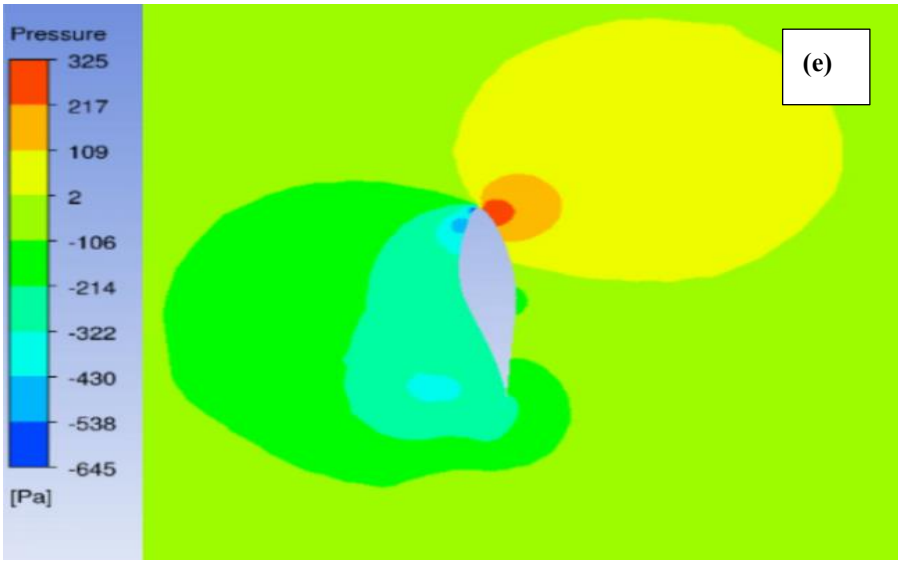

Continued on next page

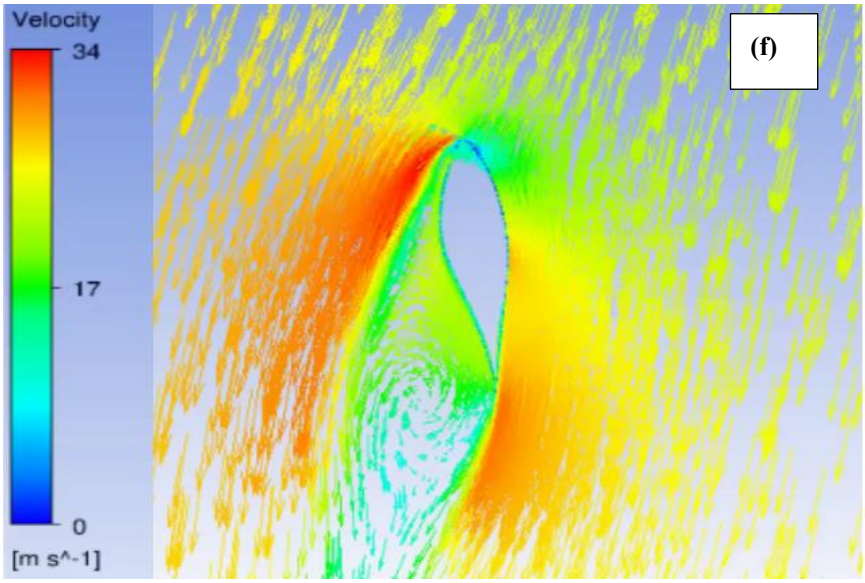

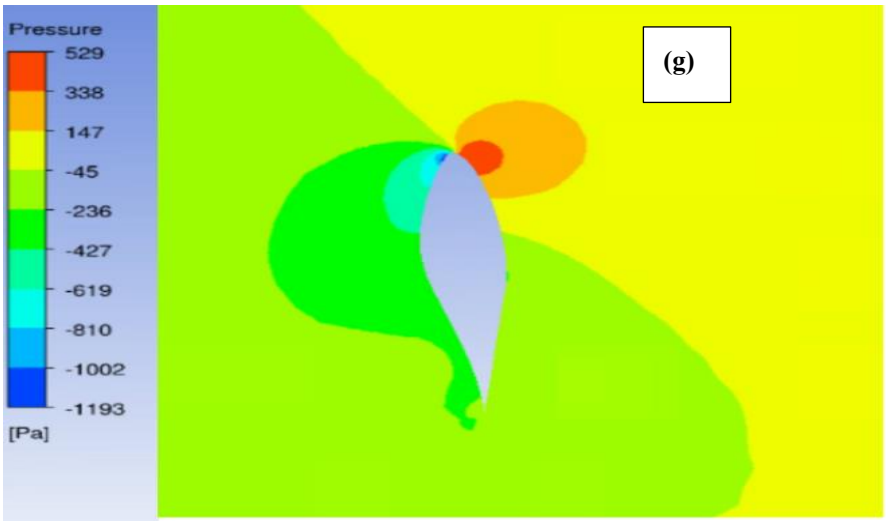

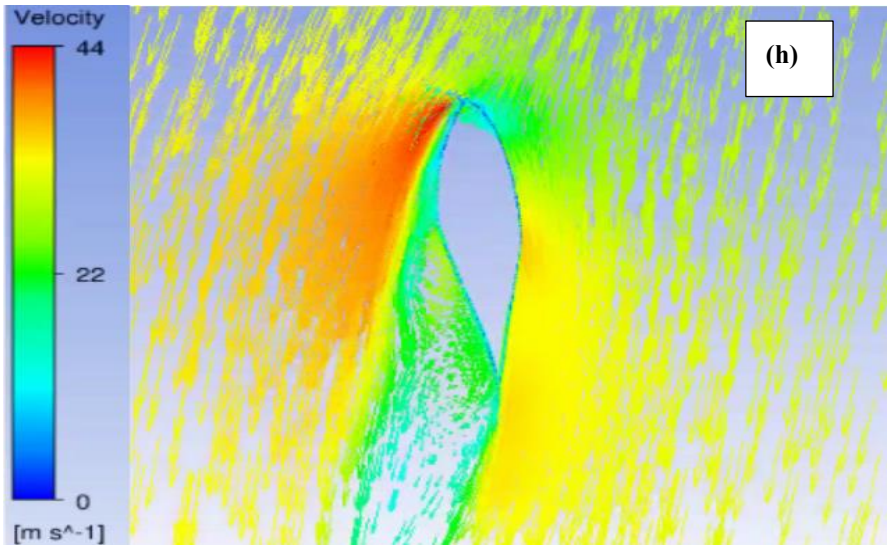

Continued on next page

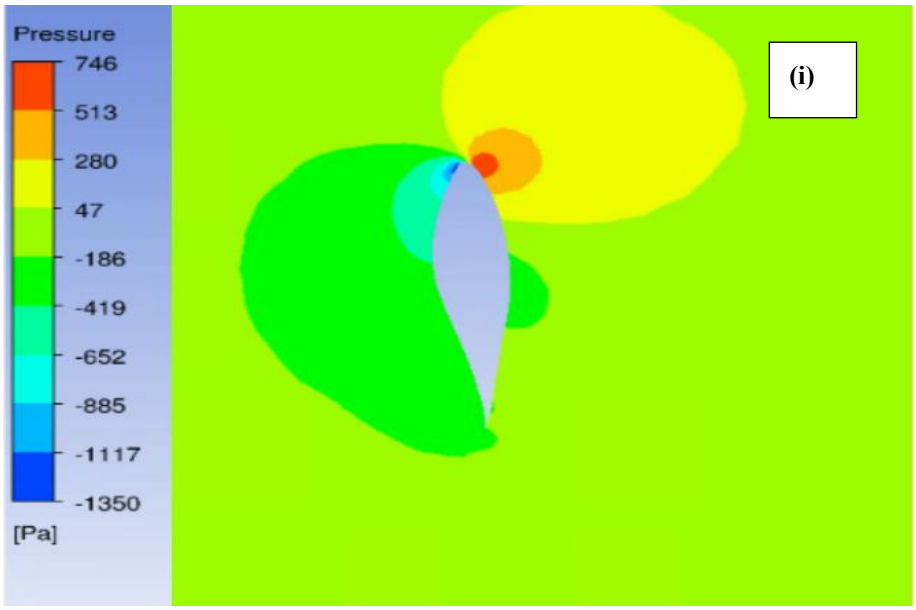

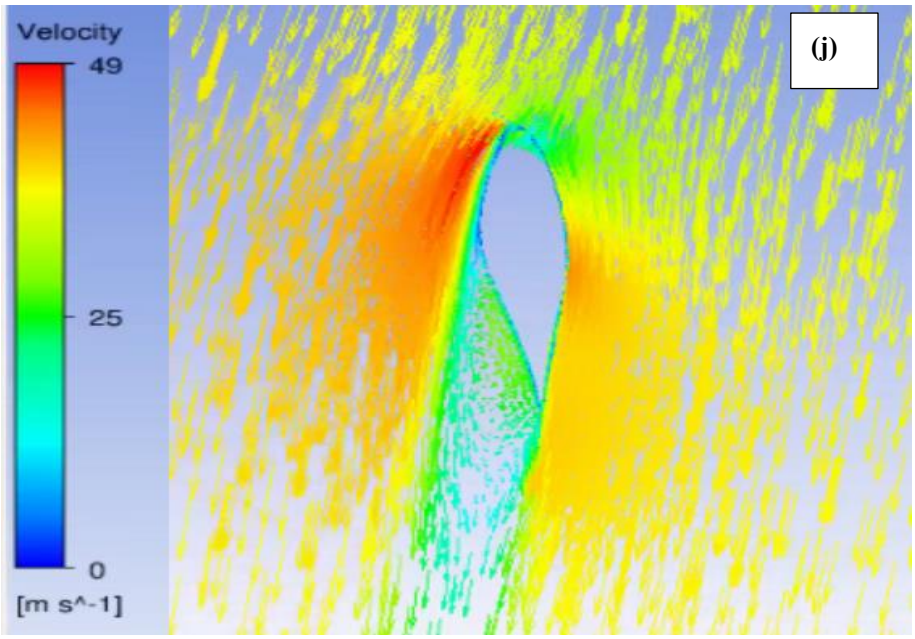

Figure 4.6. Pressure and velocity vector distributions at 7.2 m/s of different span stations: (a) pressure; (b) velocity vector of 30% span; (c) pressure; (d) velocity vector of 47% span; (e) pressure; (f) velocity vector of 63% span; (g) pressure; (h) velocity vector of 80% span; (i) pressure; and (j) velocity vector of 95% span.

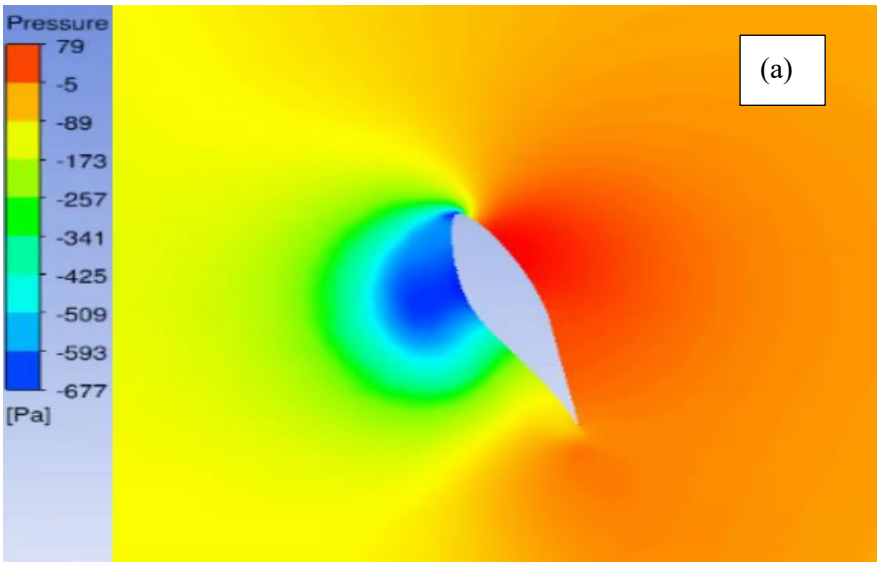

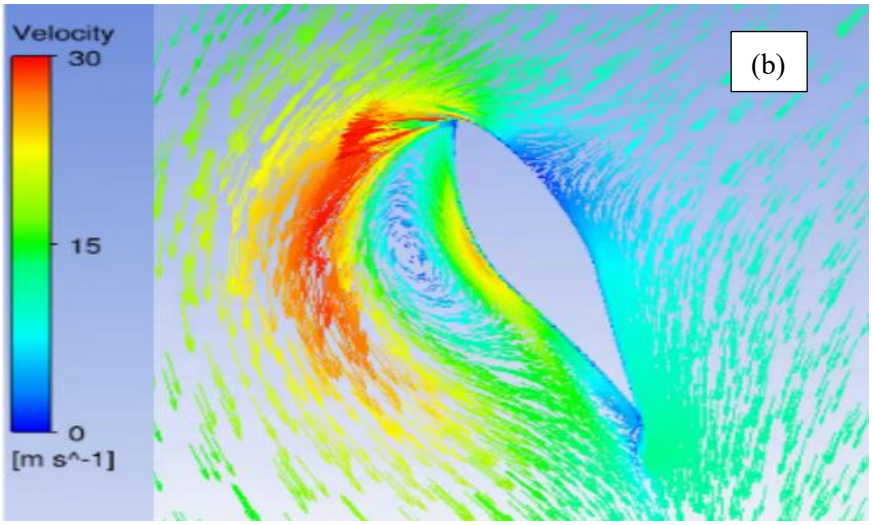

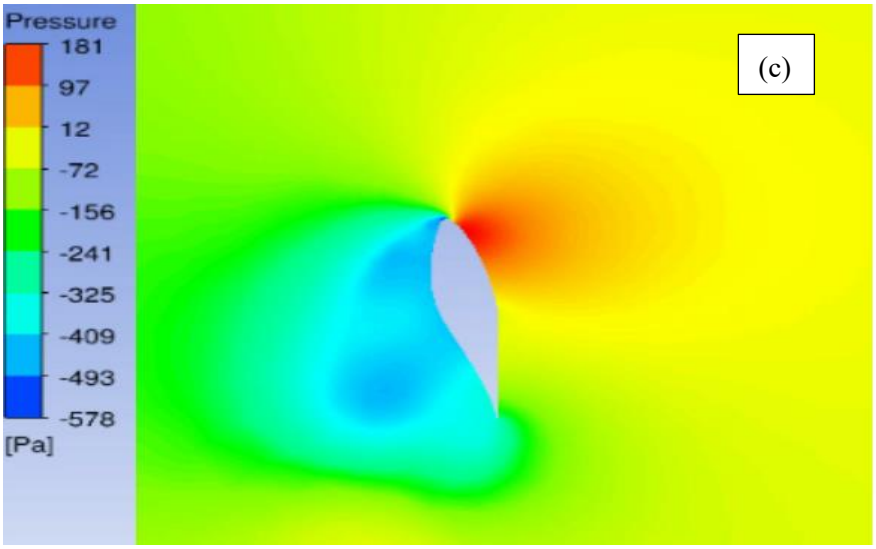

Continued on next page

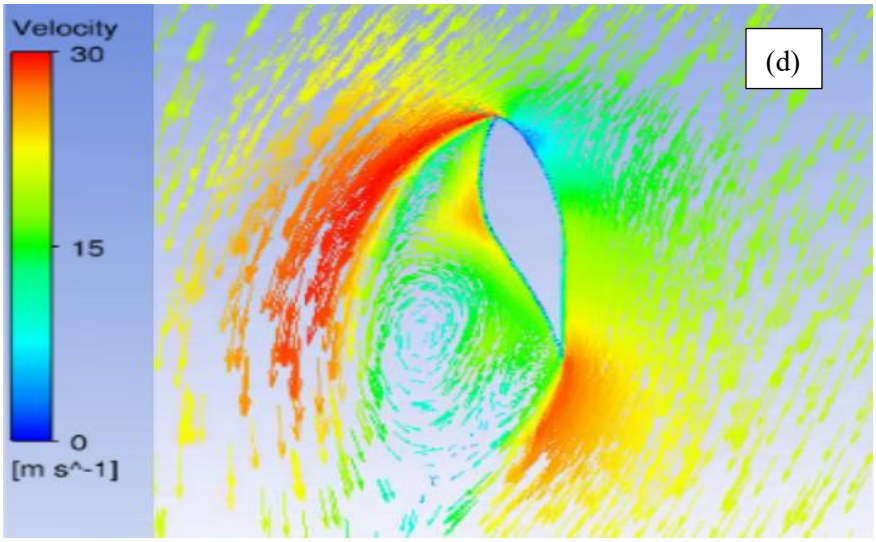

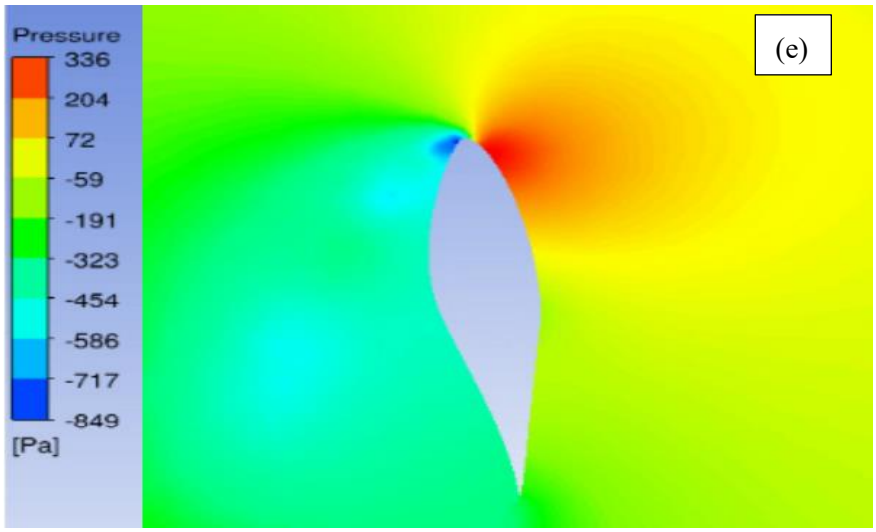

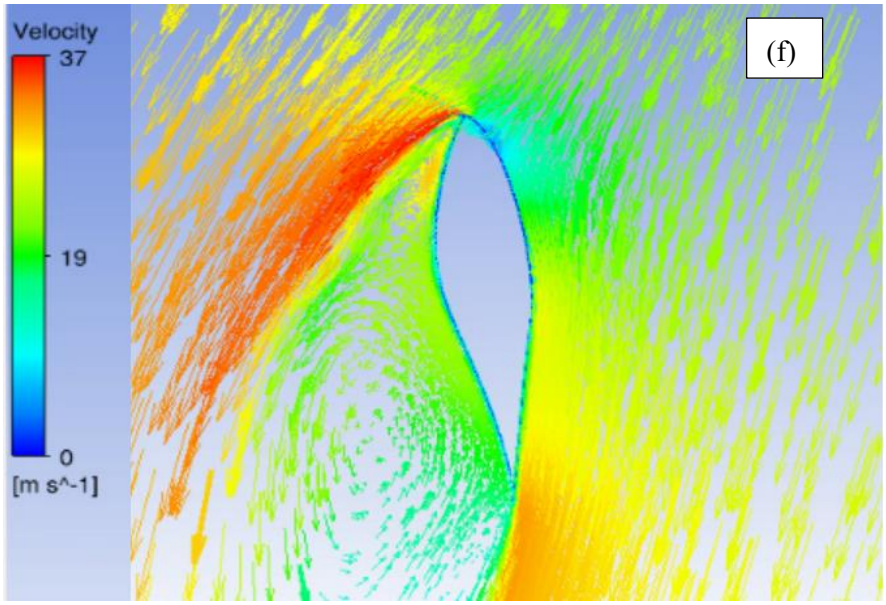

Continued on next page

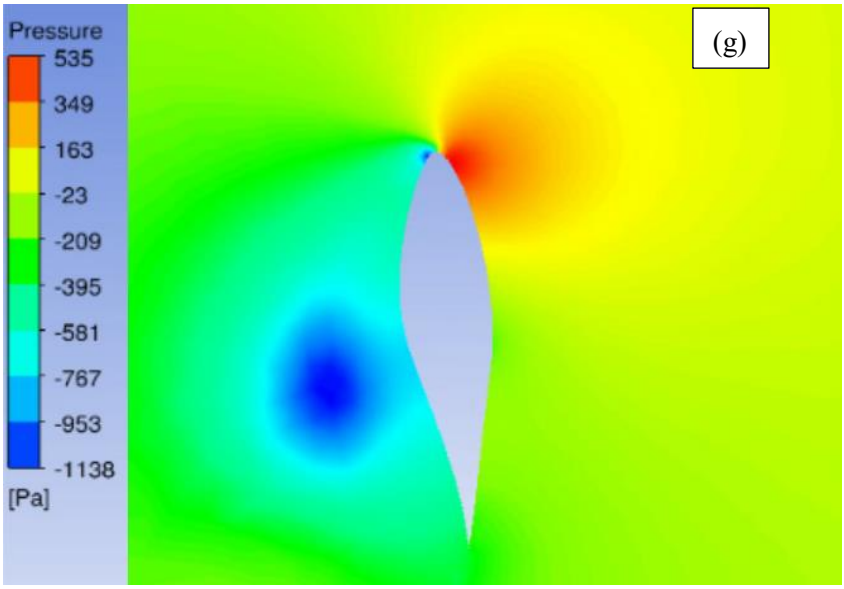

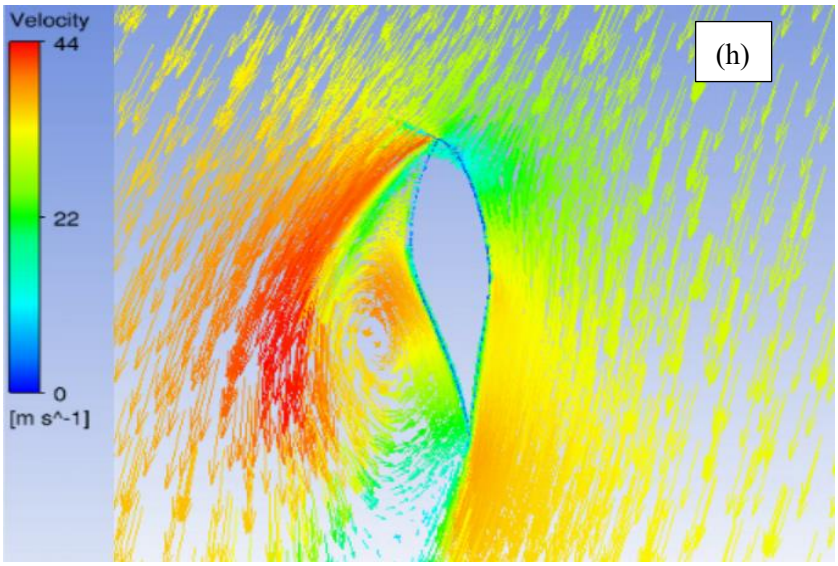

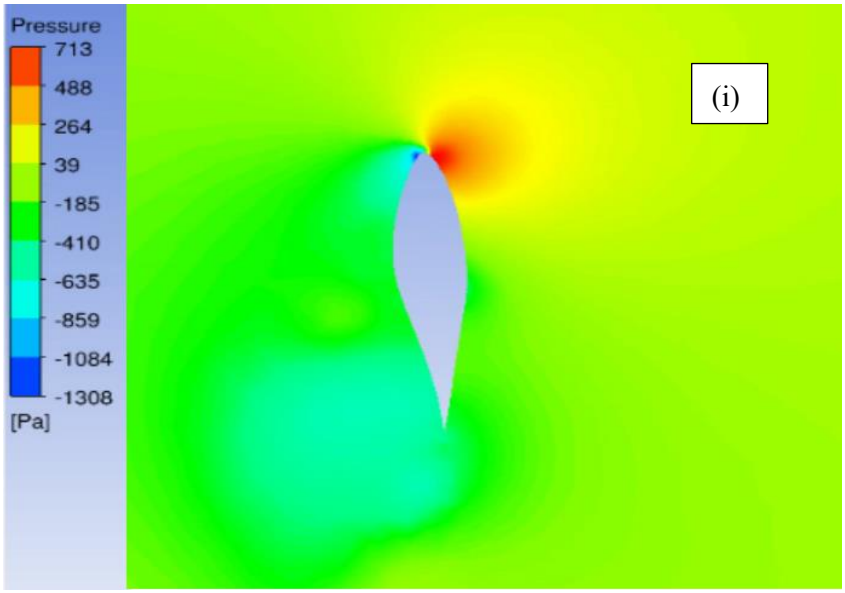

Continued on next page

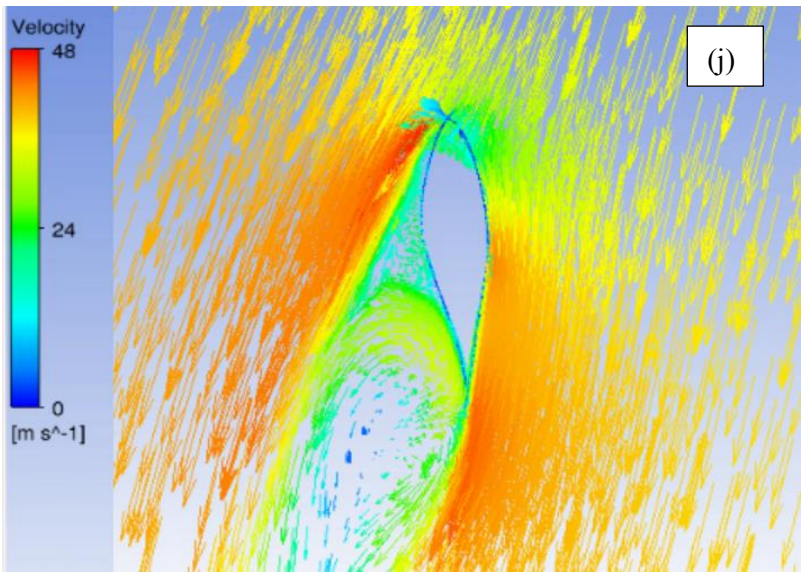

Figure 4.7. Pressure and velocity vector distributions at 10.2 m/s of different span stations: (a) pressure; (b) velocity vector of 30% span; (c) pressure; (d) velocity vector of 47% span; (e) pressure; (f) velocity vector of 63% span; (g) pressure; (h) velocity vector of 80% span; (i) pressure; and (j) velocity vector of 95% span.

4.4 Characteristics of the wind turbine blade

As shown in **Figure 4.8**, the pressure distribution on two sides of the wind turbine obeyed the main principle of aerodynamics, which states a pressure difference between the front and back of the wind turbine. The detailed investigation demonstrates the pressure difference is lower at the inner portion compared to the blade's outer part, where the centrifugal and Coriolis forces play a role in this matter. The centrifugal force transports the flow from the inner area at the root towards the mid-region of the blade, which influenced the fall in pressure on the suction side of the blade [297]. Thus, the 3-D rotation effect is responsible for the low-pressure portion at the leading tip edge of the wind turbine blade.

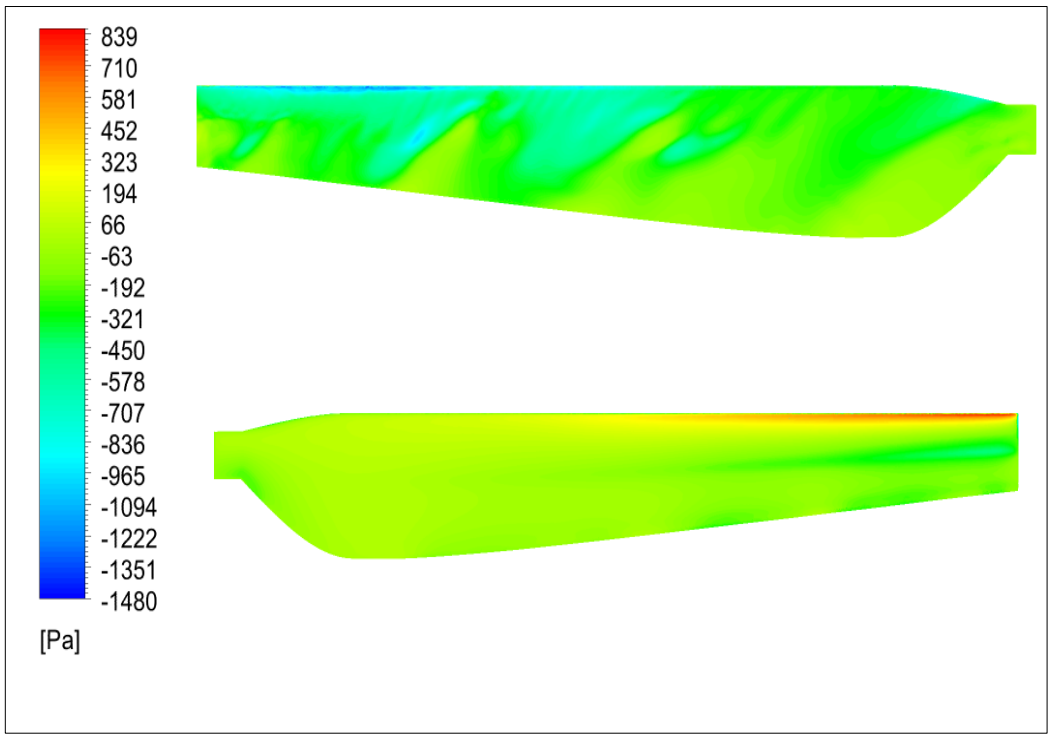

Figure 4.8. Pressure distribution of two sides of the blade at 7.2 m/s.

As seen in **Figure 4.9**, the axial velocity varied along the blade and it rose from the root to the tip. The highest velocity is achieved by the tip section, where the axial velocity increases at a uniform pattern along the blade. The axial velocity increased at a uniform pattern along the blade, which explains why the centrifugal force affected the wind turbine blade.

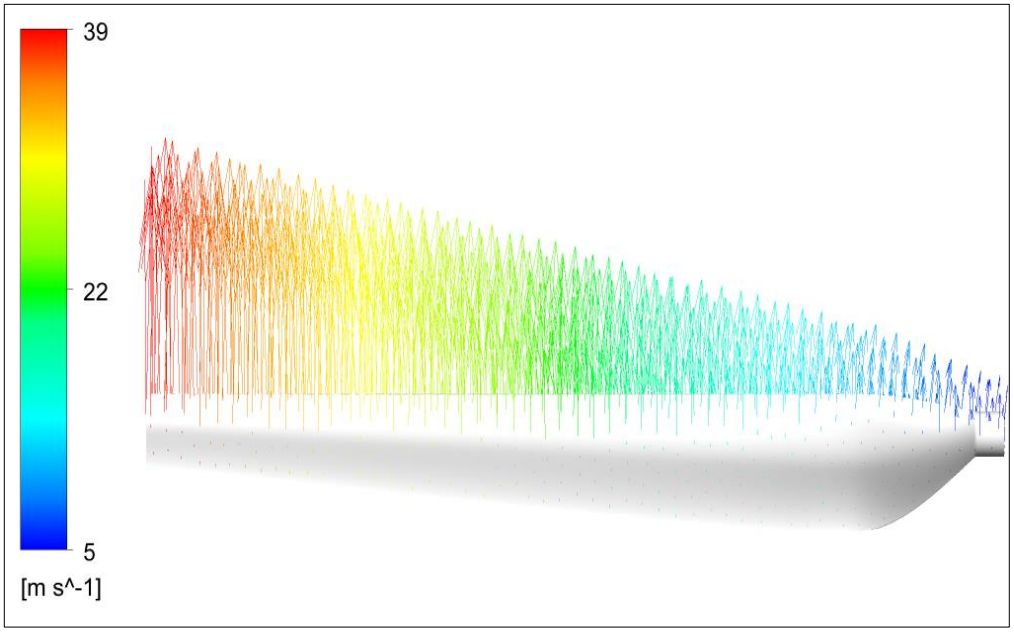

Figure 4.9. Axial velocity along the blade at 7.2 m/s.

The NREL CER wind turbine will use the original blade geometry design. The numerical modelling of this wind turbine will serve to investigate the mechanical output at different rotational speeds and variable pitch angles. Transition SST is the RANS model chosen for use when the output power of the original blade geometry was compared with the optimized blade design. Transition SST can predict well the mechanical torque and the pressure distribution of different sections along the blade.

4.5 Summary

CFD modelling was used to investigate the aerodynamics characteristics of a three-twisted and tapered blade wind turbine that had a 20 kW rating capacity. Grid independence was achieved in terms of mechanical torque. The effect of four turbulence models in predicting the mechanical torque and pressure distribution of different sections along the blade was examined. The simulated wind conditions varied from attached to separated flow conditions, and the major results of this chapter can be concluded as follows. Firstly, all four RANS models agreed well with experimental data at low wind speed ranges. Differences appeared among the four turbulence models as the wind speed increased. Secondly, at the onset of a stall condition of 10.2 m/s, the Transition SST reported the best accuracy for predicting the pressure coefficient of the airfoil. The angle of attack rose with increasing wind speed and declined with the radial position. Full separation occurred between the hub and 80% of the tip sections.

Chapter Five

5 Estimation of wind speed probability distribution and wind energy assessment

Wind resources vary from one place to another, according to seasonal and daily variations even for the same location, which explains the need to conduct a case analysis on the feasibility and potential of wind energy at a specific site. As stated above, some statistical analyses of wind data resources have been undertaken in different parts of the world. This chapter presents an in-depth statistical analysis of wind energy potential as a power source in NSW. A technical assessment based on the wind data recorded at five meteorological stations has been undertaken. The first section demonstrates the descriptive statistical characteristics of wind speed that were recorded at meteorological stations in Ballina, Merriwa, Deniliquin, Bega and Yanco. In the second section, the four different probability density functions, Rayleigh, Weibull, gamma, and lognormal, are used to evaluate the wind potential at five sites located in NSW, Australia. The type of wind speed distribution function dramatically affects the output of the available wind energy and wind turbine performance at a particular site. Thus, four probability density functions have been evaluated in detail using statistical parameters to assess their fitness. The comparison reveals the most accurate probability distribution function, which presents the frequency of wind speed. Finally, conclusions are drawn in section 5.4.

5.1 Analysis of the statistical characteristics of wind data

In this section, some descriptive statistical values of wind speed, including standard deviation, mean, kurtosis and skewness are discussed in more detail.

5.1.1 Maximum and mean wind speed

In this study, the hourly wind speed data for five sites in NSW from August 2018 till July 2019 was analysed. Based on that measurement, the hourly wind speed varies with day and from one site to another. The maximum and mean wind speed is an important indicator used for installing the wind turbine in a specific site. It is easier to study the monthly wind speed for the selected sites and its mean and maximum, as shown in **Figure 5.1 (a-e)**. For Ballina, the maximum wind speed was recorded in February 2019, with a value of 12.8 m/s. In the same month, the highest mean wind speed value was recorded in the Ballina area, with a value of 5.0 m/s. For the Bega area, the highest value of the maximum wind speed was achieved in November 2018, with a value of 13.3 m/s. Again in November 2018, the mean wind speed had the highest value of 3.5 m/s, while other mean wind speed values were around the value of 2 m/s. For Deniliquin, the greater value of 15.3 m/s for the maximum wind speed was recorded in January 2019, while the mean wind speed had a mean value ranges between 3 m/s to 5m/s. The highest value (5.3 m/s) of mean wind speed was recorded in November 2018. For Merriwa, in December 2018, the highest value of maximum wind speed was measured. In February 2019, the greatest value of mean wind speed attained a value of 4.9 m/s. For Yanco, the mean wind speed varied between a maximum of 3.9 m/s in February 2019, while the minimum mean wind speed was 2.2 m/s in December 2018. The largest value of the maximum wind speed of 12.3 m/s was measured in February 2019.

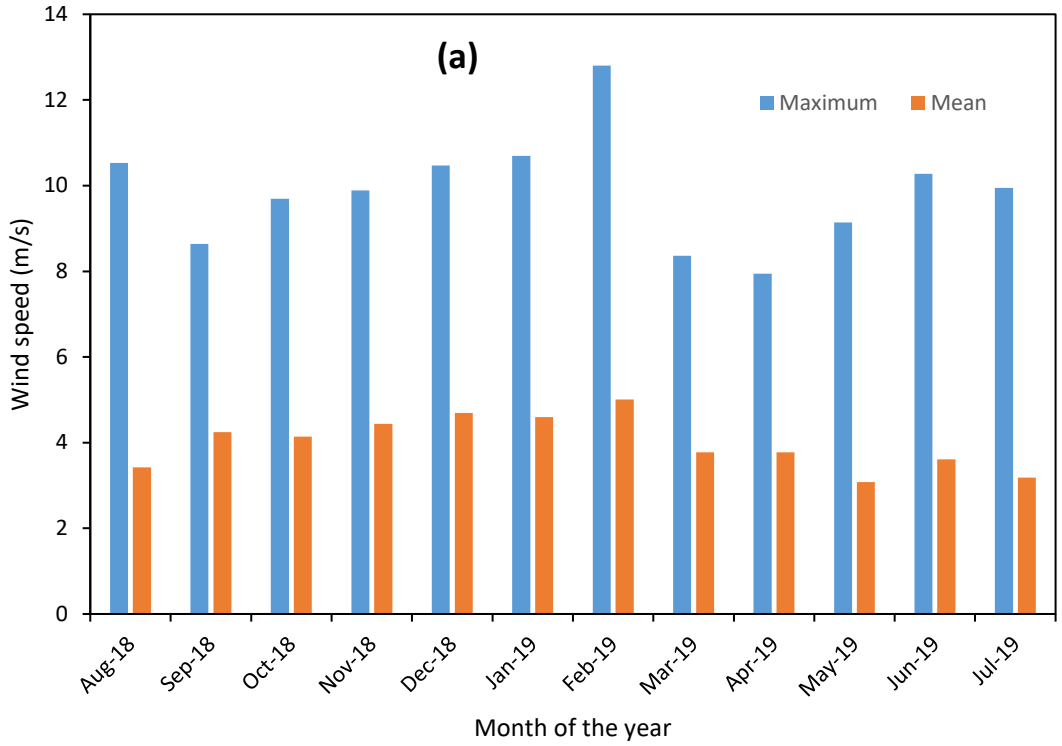

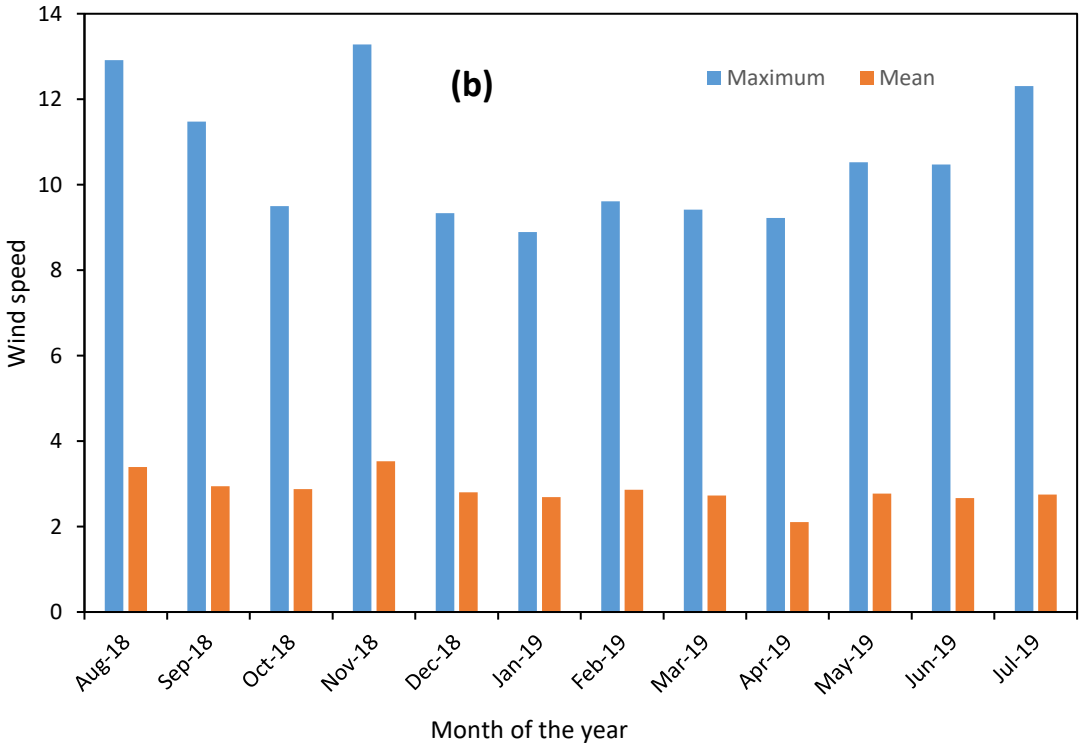

Continued on next page

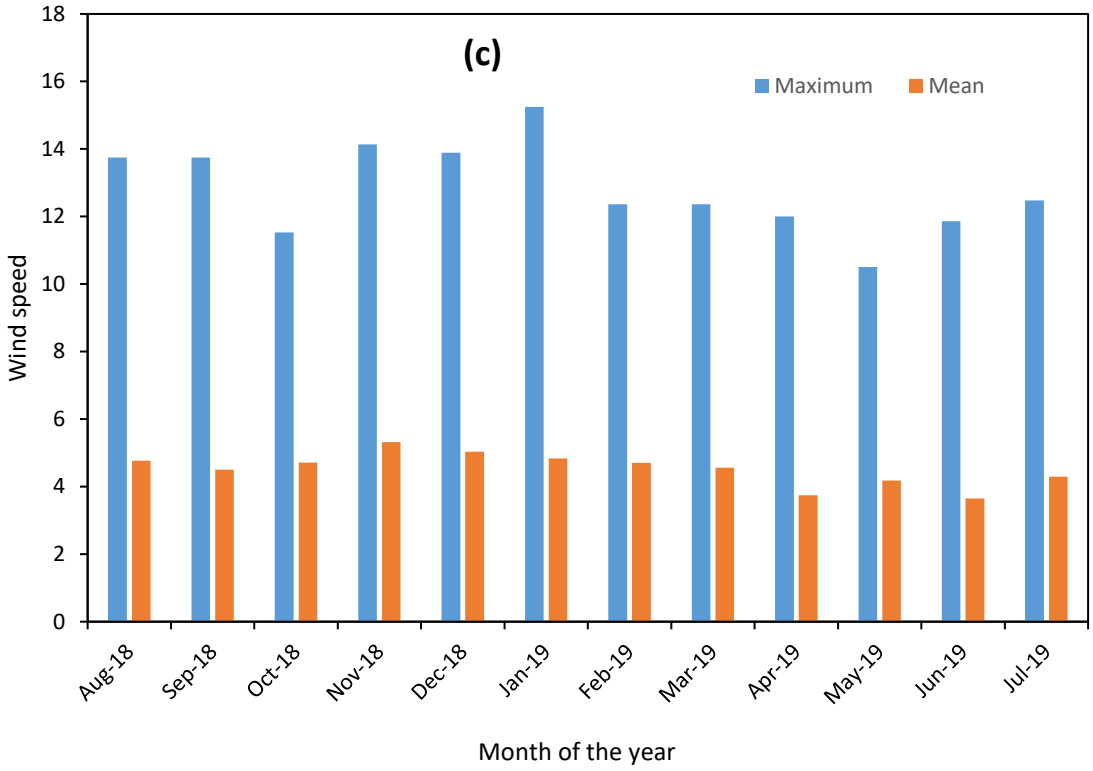

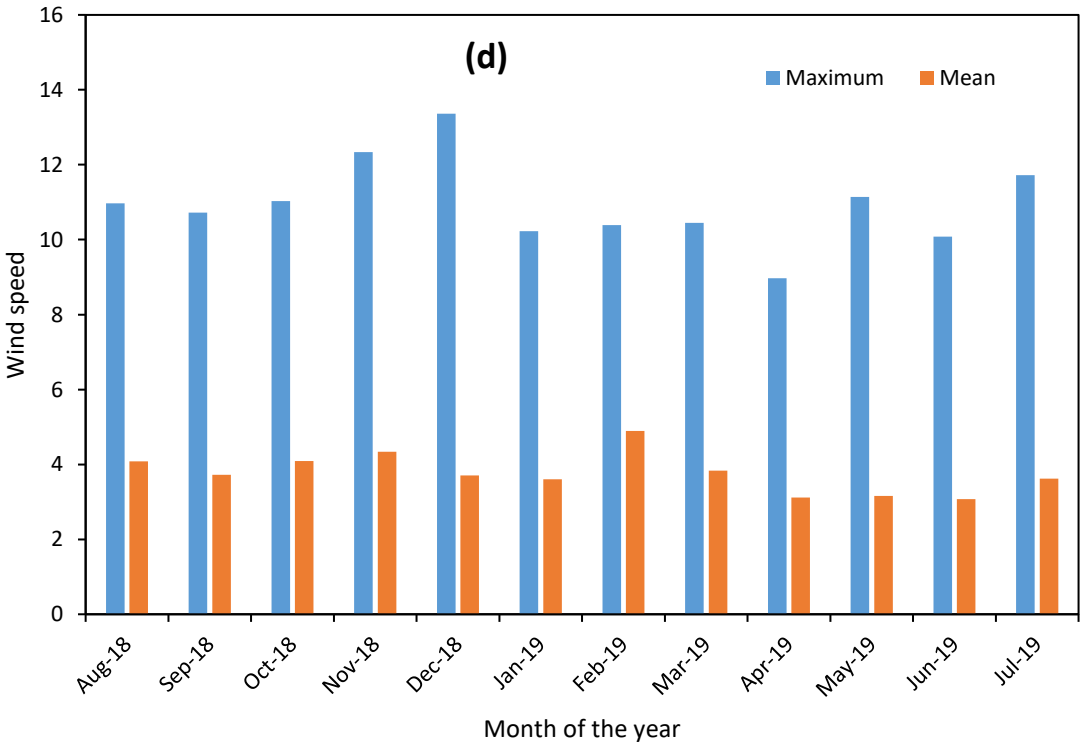

Continued on next page

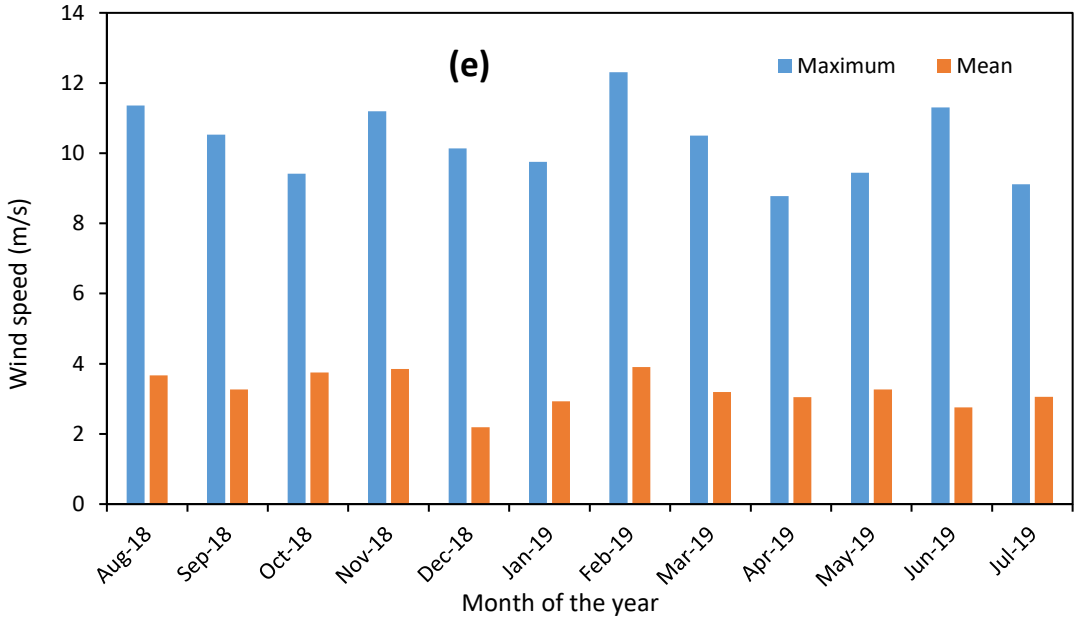

Figure 5.1. Monthly maximum and mean wind speed at the following locations: **(a)** Ballina, (**b)** Bega, **(c)** Deniliquin, **(d)** Merriwa, and **(e)** Yanco.

5.1.2 Median and standard deviation

The standard deviation offers good insights into the wind data dispersion and emerges as being critically significant for wind resource assessment. It gives a clear representation of: firstly, how the wind speeds are distributed throughout the period; and secondly, how far the individual wind speeds diverge from average wind speed. Also, defining the standard deviation for the same mean wind speed, wind turbines can obtain different power outputs depending on the distribution of wind speed. The monthly standard deviation and median are presented in **Figure 5.2 (a-e)** for the selected sites.

Ballina exhibits the highest median and standard deviation values in April 2019, which are 5.08 m/s, 2.65 m/s, respectively. Bega and Deniliquin areas revealed the highest median values in November 2018. For Merriwa and Yanco, the highest median value was recorded in February 2019, and these are 4.7 m/s, and 3.6 m/s. For all selected sites, the variation of standard deviations during these months is less than the median variation.

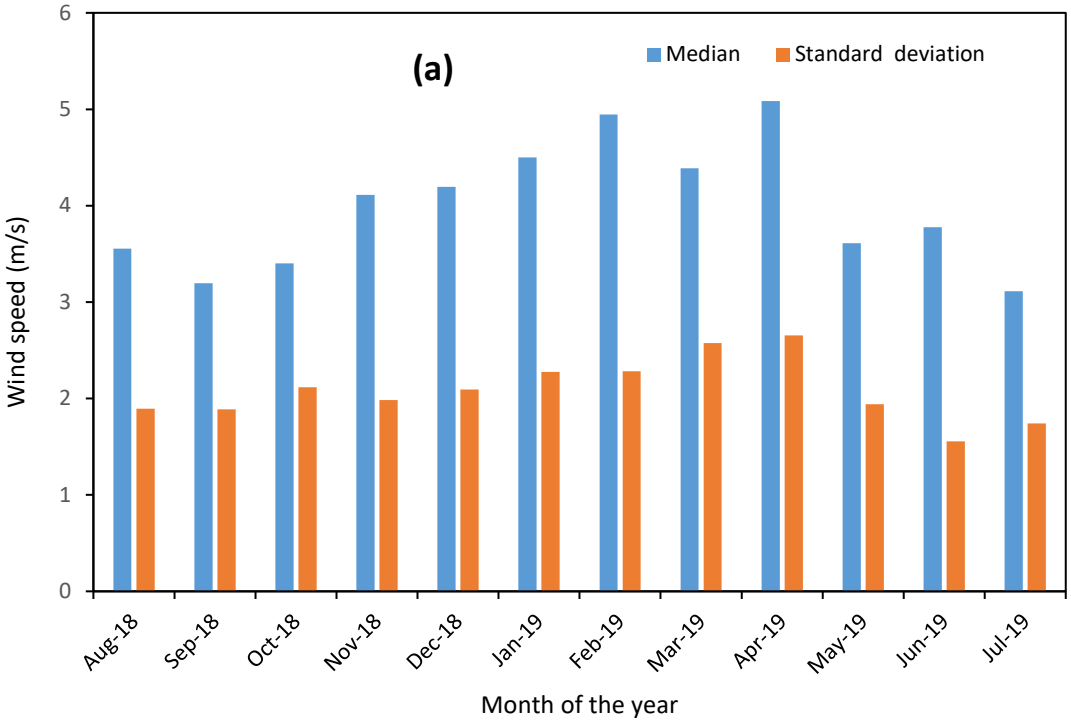

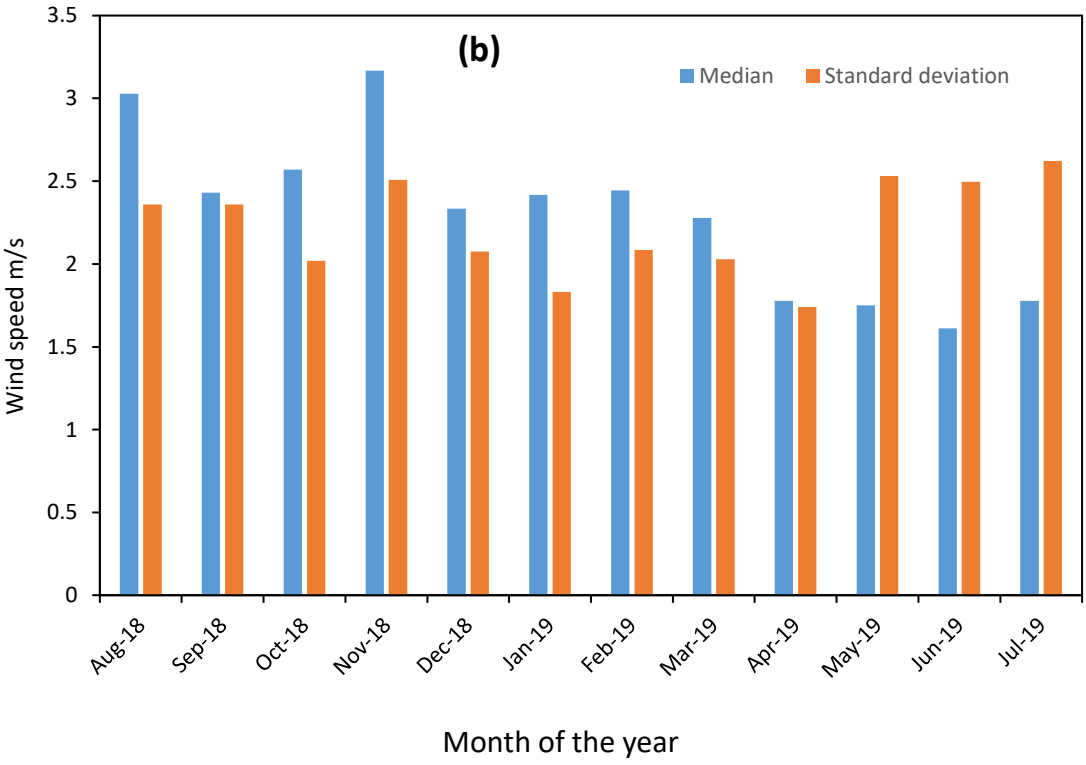

Continued on next page

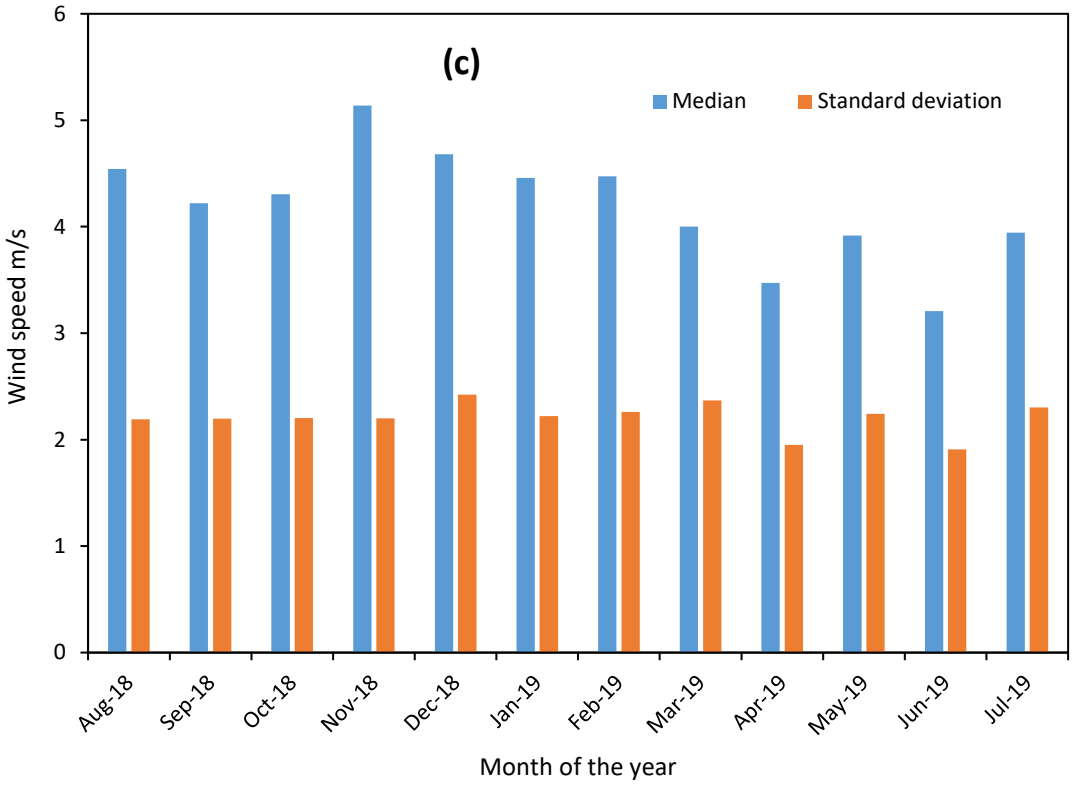

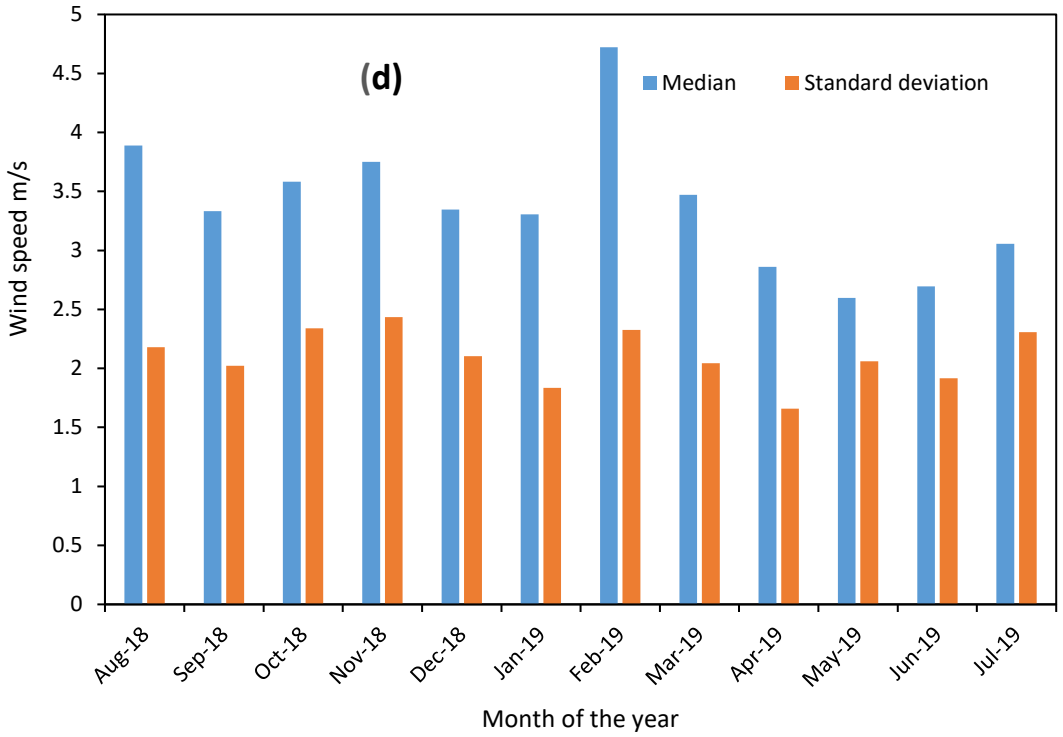

Continued on next page

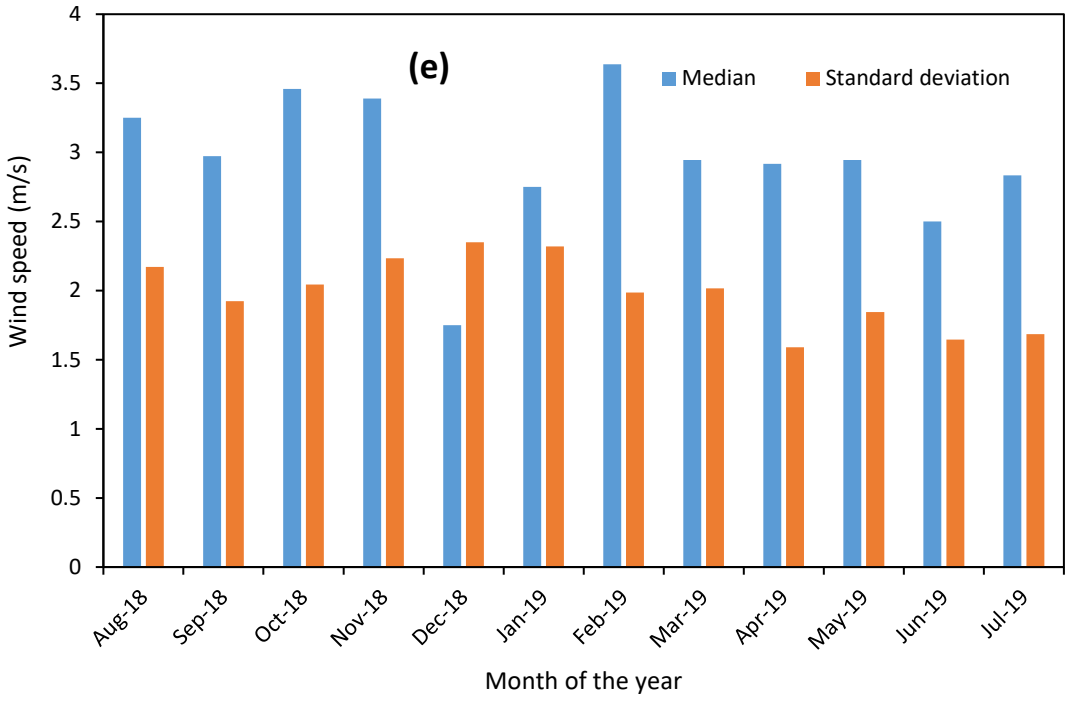

Figure 5.2. Monthly Median and standard deviation of wind speed at the following locations: **(a)** Ballina, **(b)** Bega, **(c)** Deniliquin, **(d)** Merriwa, and **(e)** Yanco.

5.1.3 Skewness and kurtosis

Some significant descriptive statistics for skewness and kurtosis are investigated in this study. As can be observed from **Figure 5.3 (a, b)** for the selected sites, skewness and kurtosis are two common statistical parameters that describe the distributional pattern of wind data. The symmetric distribution will have skewness equal to zero due to the normal distribution [298]. A positive value of skewness indicates the data spread out to the right, while the skewness has a negative value when the data are more spread out to the left-hand side of the mean rather than to the right [299]. Kurtosis describes the steep degree of the data [300], where the value is often compared to the kurtosis of the normal distribution, which is equal to 0. If the kurtosis is higher than 0, then subsequently, the dataset is steeper than a normal distribution. If the kurtosis is less than 0, the dataset is less steep than the normal distribution

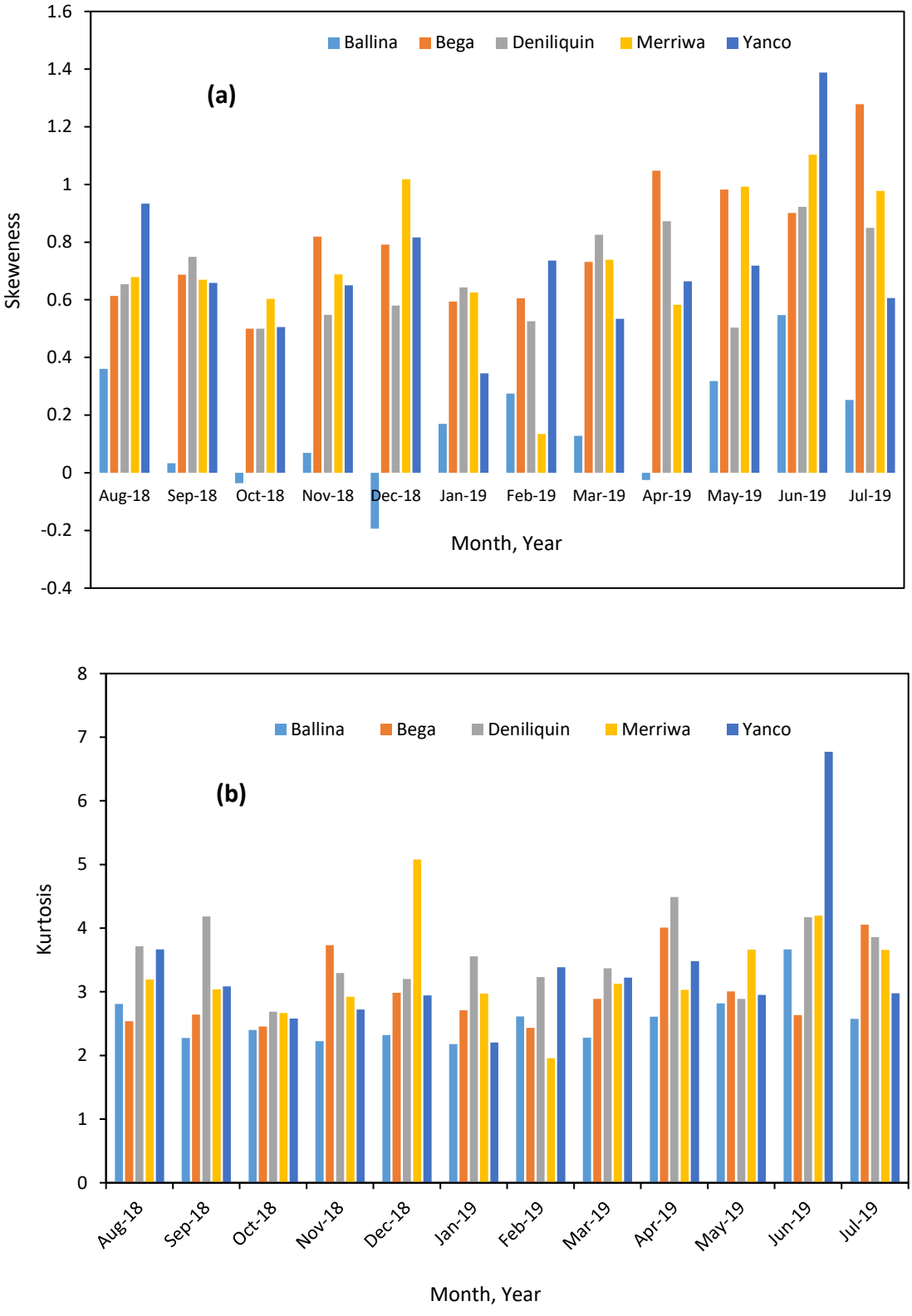

Figure 5.3. (a) Skewness, **(b)** Kurtosis of the measured wind speed data at the selected sites.

Some significant statistics values, including yearly maximum, mean, median, standard deviation, skewness, and kurtosis, are presented in **Table 5.1**. For the five sites, the mean wind speed values vary from 2.81 to 4.53 m/s. The standard deviation has a value

between 1.990 and 2.288. Skewness has a value between 0.282 and 0.914, while kurtosis is between 2.759 and 3.523. The descriptive statistical parameters of the measured wind speed data at five stations in the east and southeast of Iran were evaluated by Alavi et al. [266]. In their study, the skewness values varied between 0.24 and 1.22, and kurtosis values varied between 2.16 and 3.59.

Table 5.1. Annual descriptive statistical parameters of the measured wind speed data for selected stations.

	Maximum (m/s)	Mean (m/s)	Median (m/s)	Standard Deviation (m/s)	Skewness	Kurtosis
Ballina	12.806	3.945	3.833	2.134	0.282	2.759
Bega	13.278	2.810	2.222	2.288	0.914	3.348
Deniliquin	15.250	4.530	4.111	2.211	0.688	3.523
Merriwa	13.361	3.745	3.306	2.157	0.748	3.200
Yanco	12.3056	3.242	2.972	1.990	0.698	3.375

5.2 Analysis of probability density functions

The wind speed values vary continuously over time. The measured wind speed data for a specific period can be studied using statistical analysis to obtain the required information about the frequency of wind distribution. Various probability distribution functions can show the wind speed frequency curve. The Rayleigh, Weibull, gamma and lognormal are the most popular probability distribution functions used in this chapter for wind speed analysis. Graphical representations of the listed four probability distribution functions at the five sites in NSW are presented in **Figure 5.4(a-d)**. This figure compares the observed data and fitting functions using Rayleigh, Weibull, gamma, and lognormal distribution to understand which probability functions give the best fitting wind speed data. Also, **Figure 5.5(a-d)** presents the fitted cumulative distribution function plots with a measured wind speed curve for all stations. The cumulative distribution function shows the probability that wind speed is less than or equal to given wind speed.

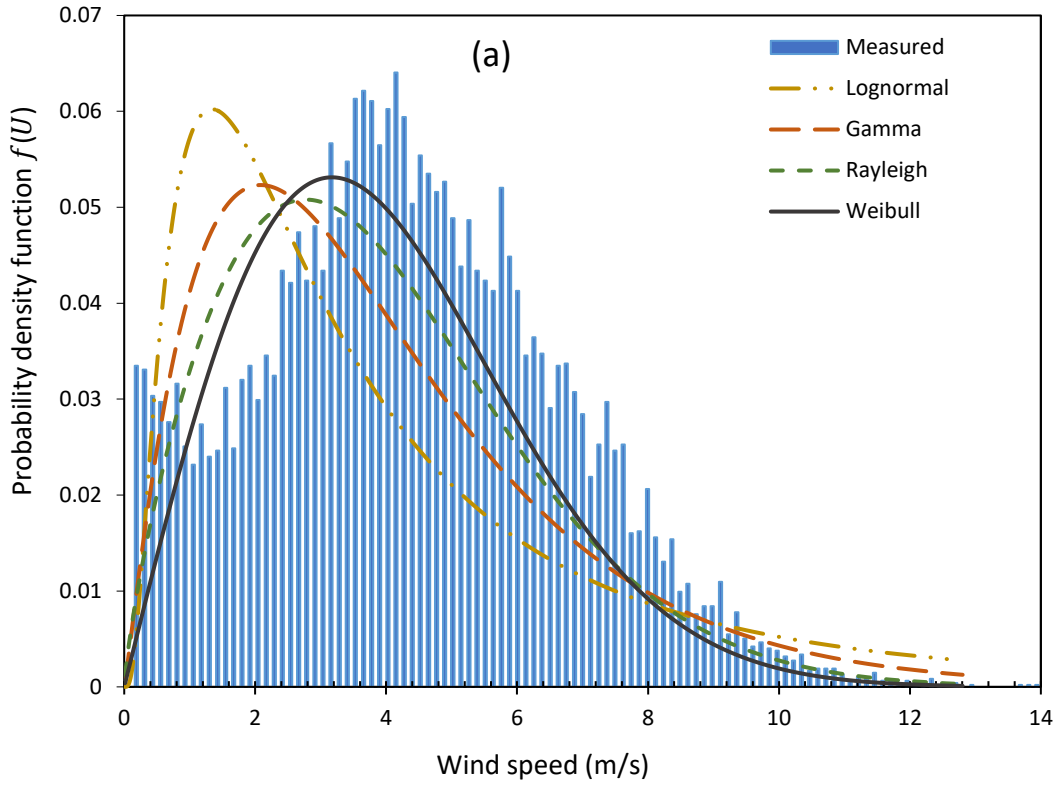

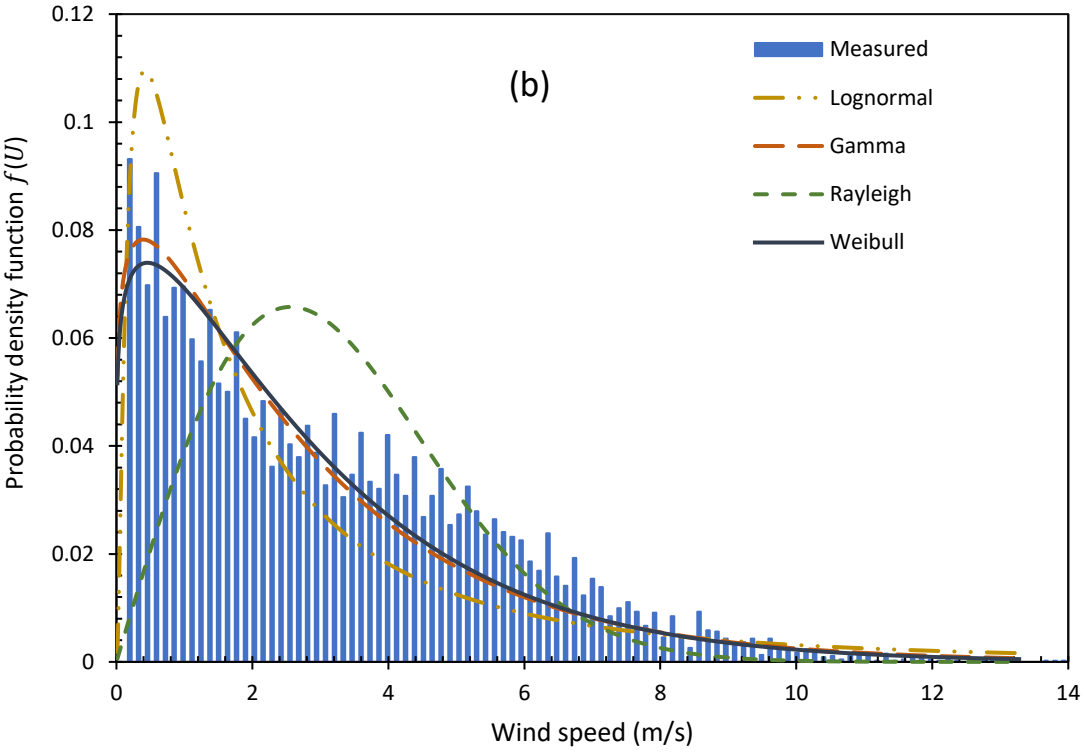

Continued on next page

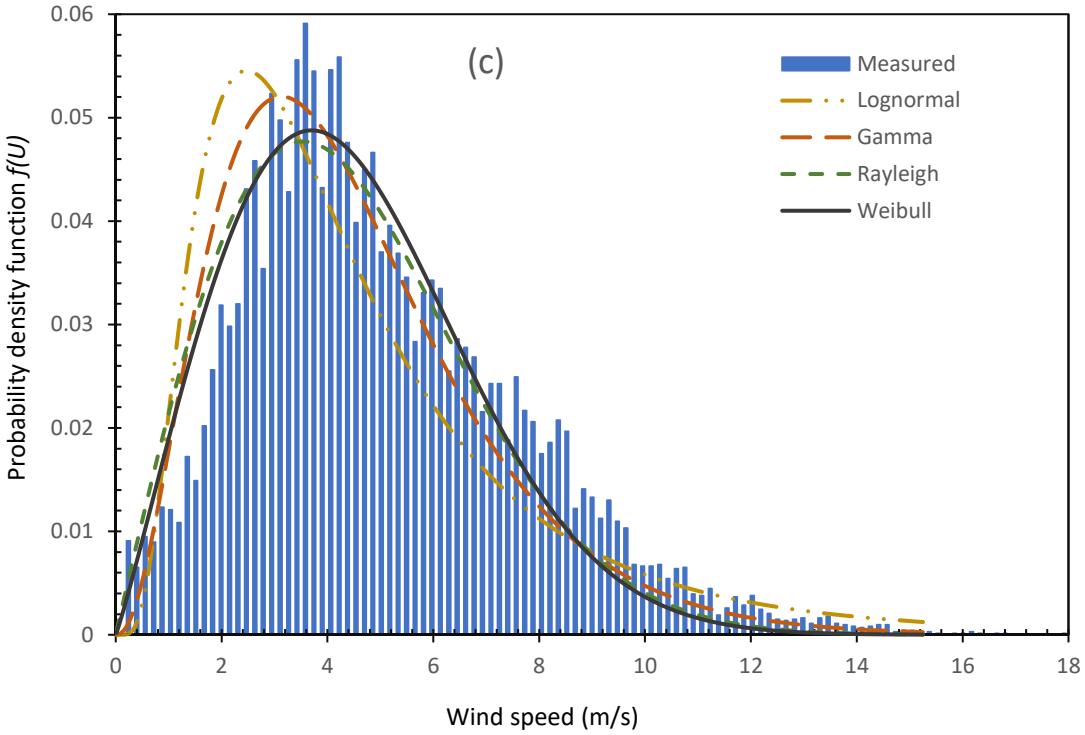

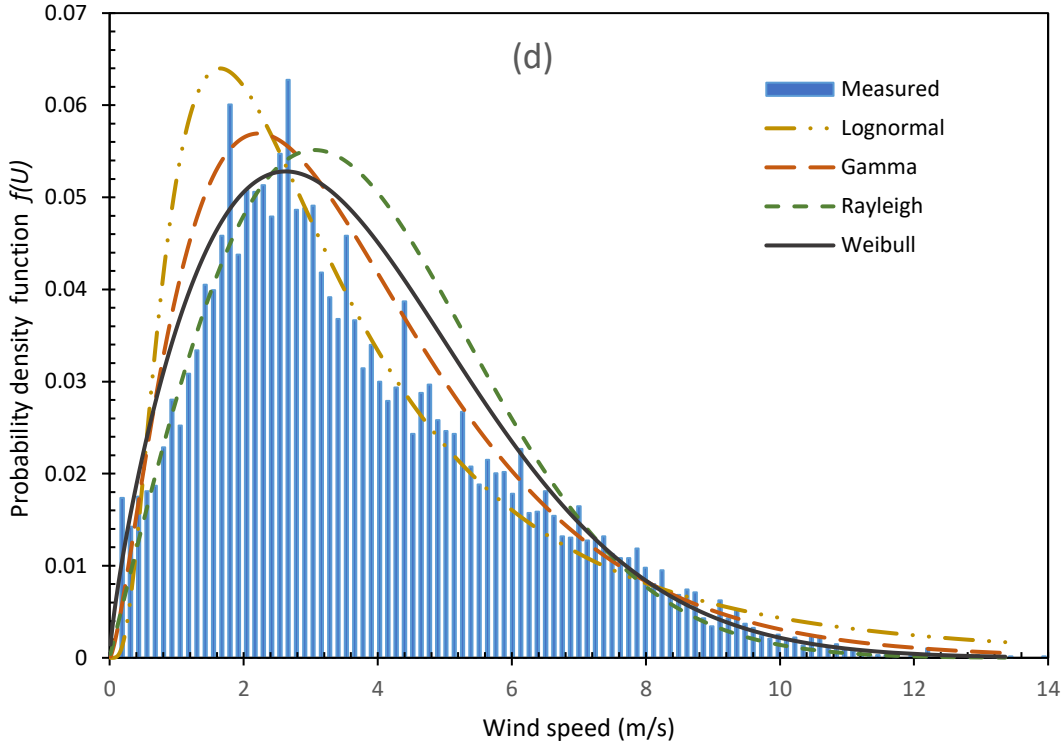

Continued on next page

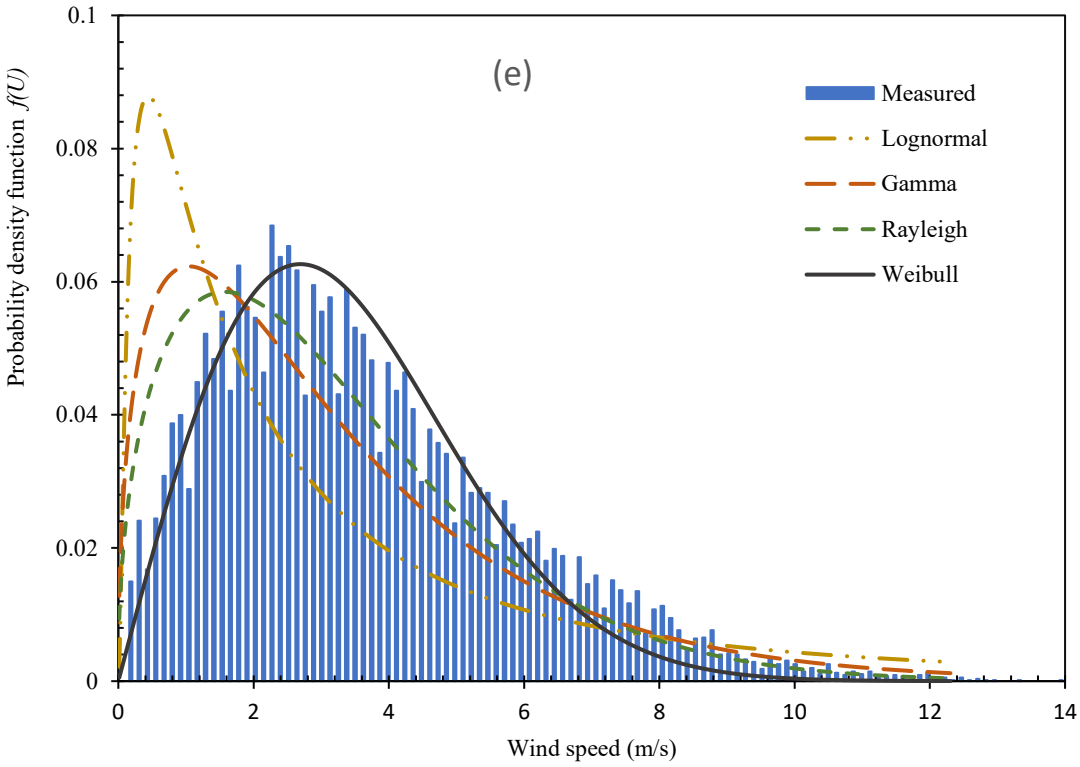

Figure 5.4. Probability density function at the following locations: **(a)** Ballina, **(b)** Bega, **(c)** Deniliquin, **(d)** Merriwa, and **(e)** Yanco.

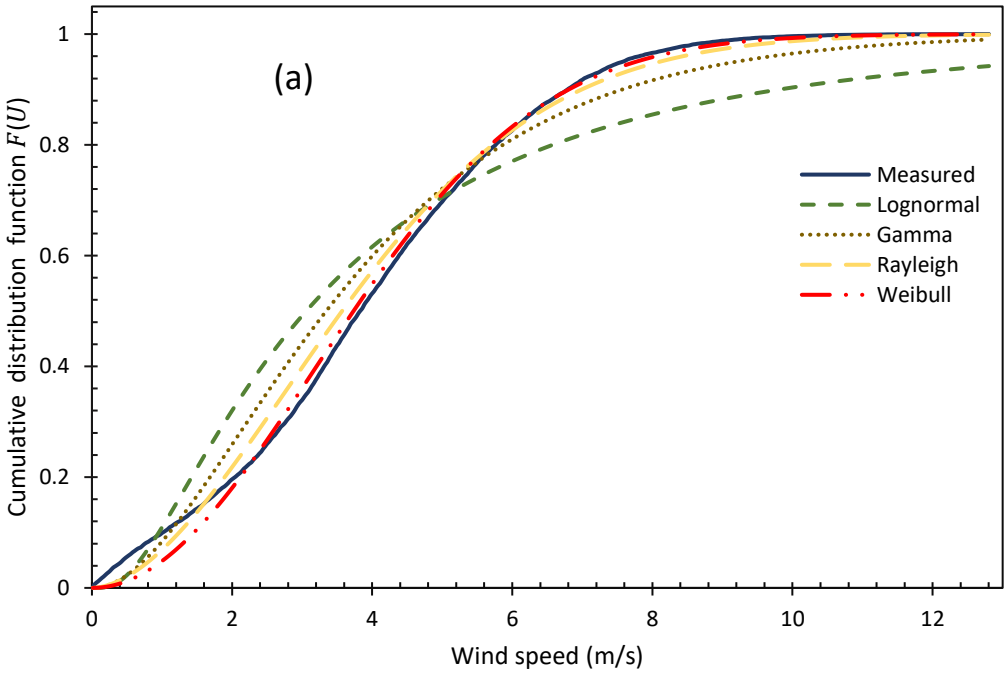

Continued on next page

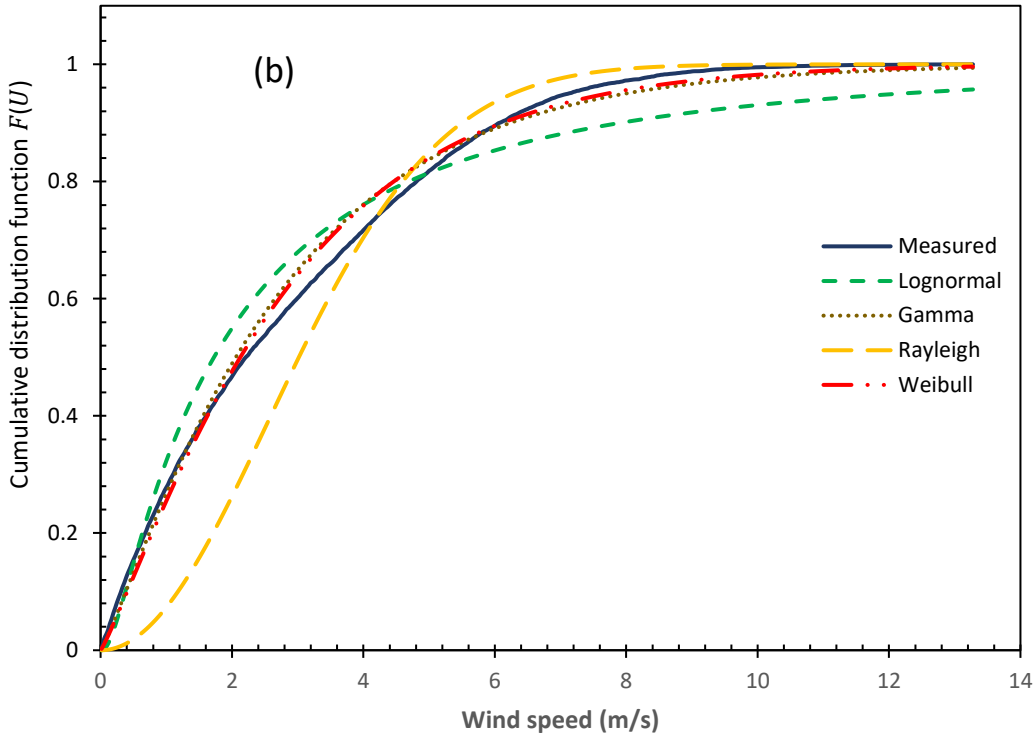

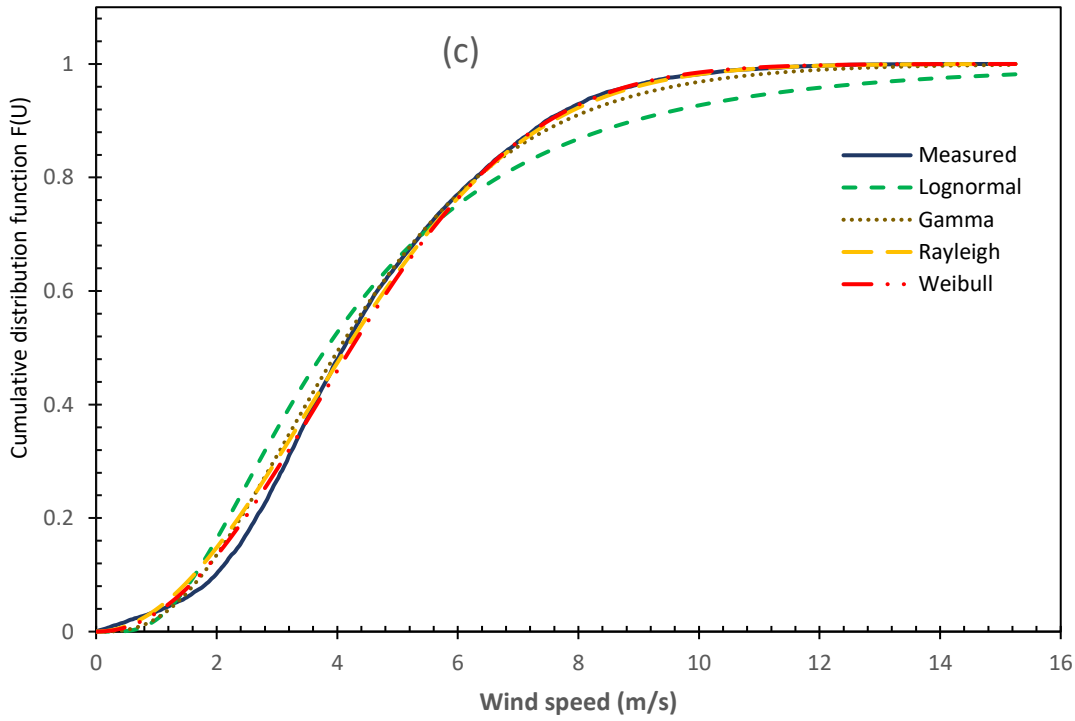

Continued on next page

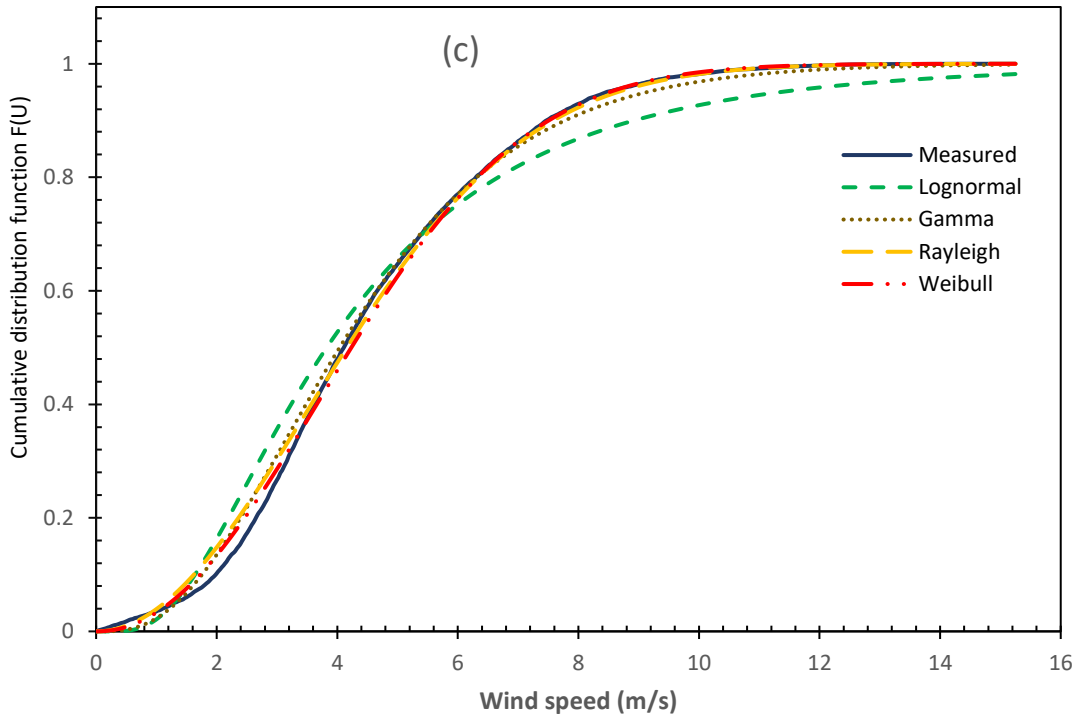

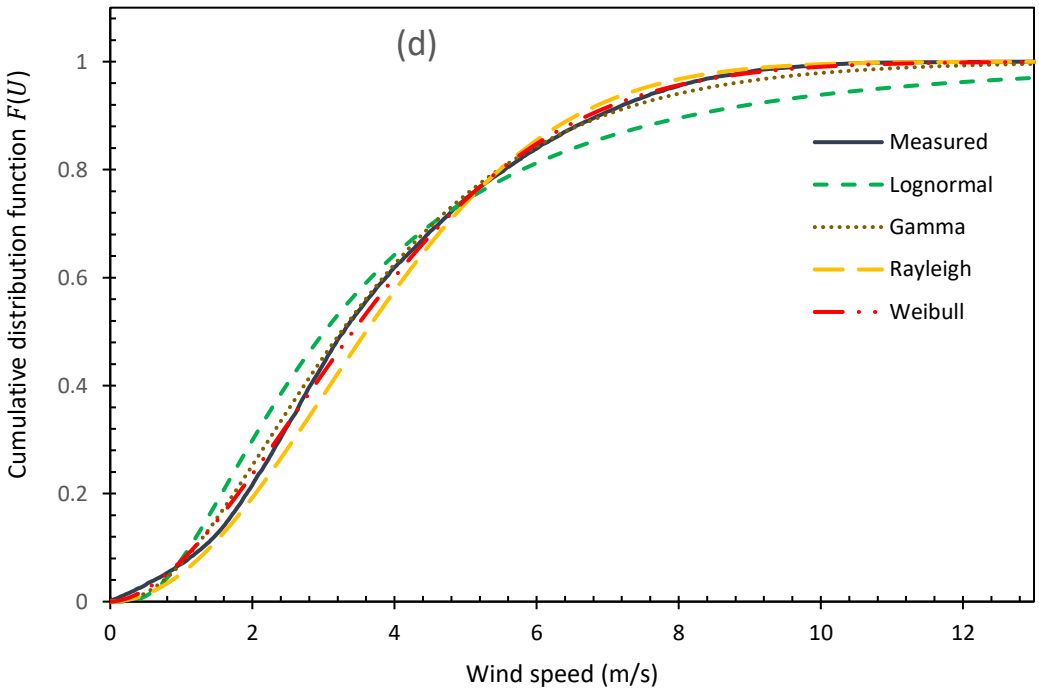

Continued on next page

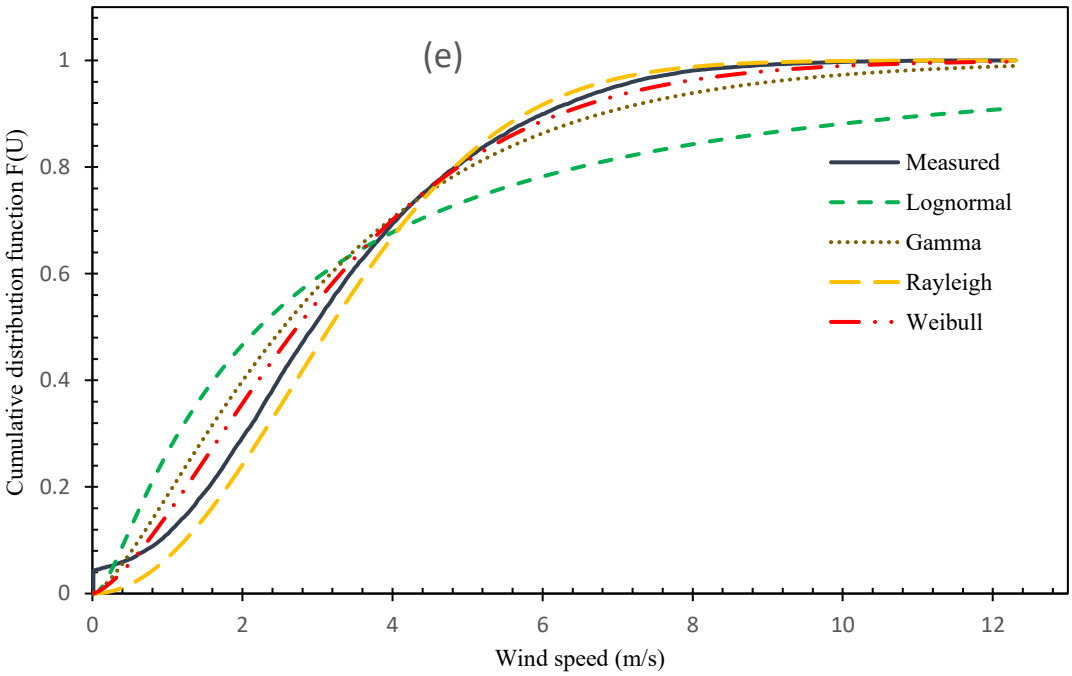

Figure 5.5. Cumulative distribution functions at Ballina **(a)**, Bega **(b)**, Deniliquin **(c)**, Merriwa **(d)**, and **(e)** Yanco.

5.3 Evaluation of wind probability density functions

The most popular statistical indicators are the coefficient of determination (R^2) and the root mean square error (RMSE), which test the goodness-of-fit. Larger R^2 values give better goodness-of-fit, while smaller RMSE values indicate a better fit. It can be seen from boxplots as shown in **Figure 5.6 (a,b)** that the R^2 values range from 0.905673 to 0.99899, except the value of 0.803537 for lognormal function concerning Yanco. The values of R^2 suggest the matching between probability distribution functions and the recorded data is very high. At the same time, the RMSE varies between 0.010771 and 0.094731 except the value of 0.117126 for lognormal function as far as Yanco is concerned. Weibull is the most accurate distribution according to R^2 and RMSE, thus RMSE variation is between 0.010771 and 0.027963. These are still lower values when compared with the performance of other distributions, while R^2 varies slightly between 0.992923 and 0.998999; those values are recorded from Merriwa and Yanco. The second distribution that had a good fit with less variation in the boxplot is the gamma distribution.

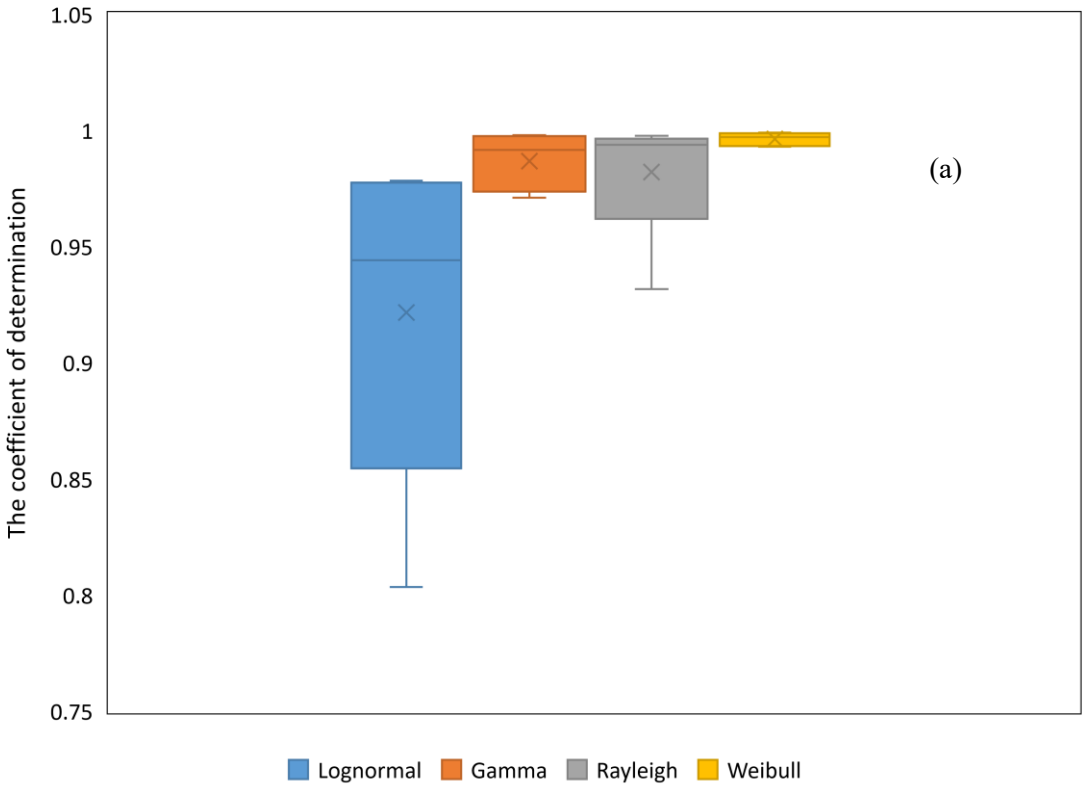

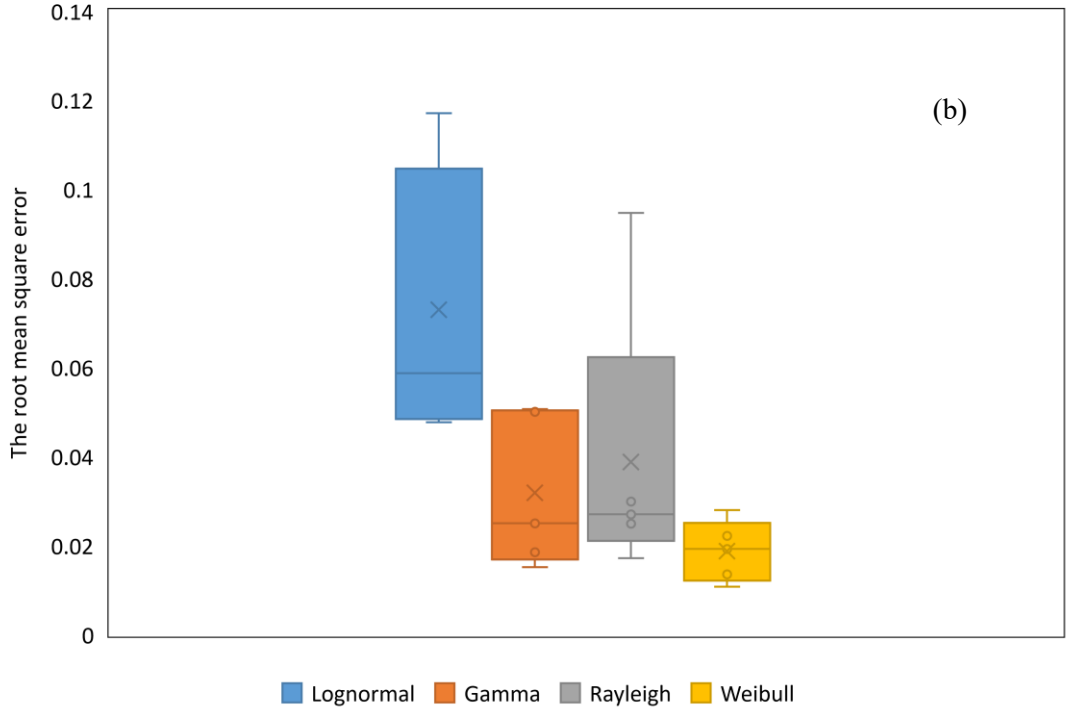

Figure 5.6. Boxplots of R^2 (a) and RMSE (b) of various distribution functions for selected sites.

Figure 5.7(a) illustrates the comparison between the calculated skewness values from the different employed distribution functions with the measured data for the five sites. Meanwhile, **Figure 5.7(b)** depicts the comparison of the kurtosis values. As shown in **Figure 5.7 (a)**, the Weibull distribution gives the nearby values of the skewness when compared with the skewness of recorded data at Ballina, Bega and Yanco. In Merriwa and Deniliquin, the gamma distribution offers the closest values of skewness when compared to the value of skewness from the measured data. It is also observed from **Figure 5.7(b)** that the kurtosis values from gamma distribution are the closest values for the measured kurtosis values at Ballina, Bega, Merriwa and Yanco.

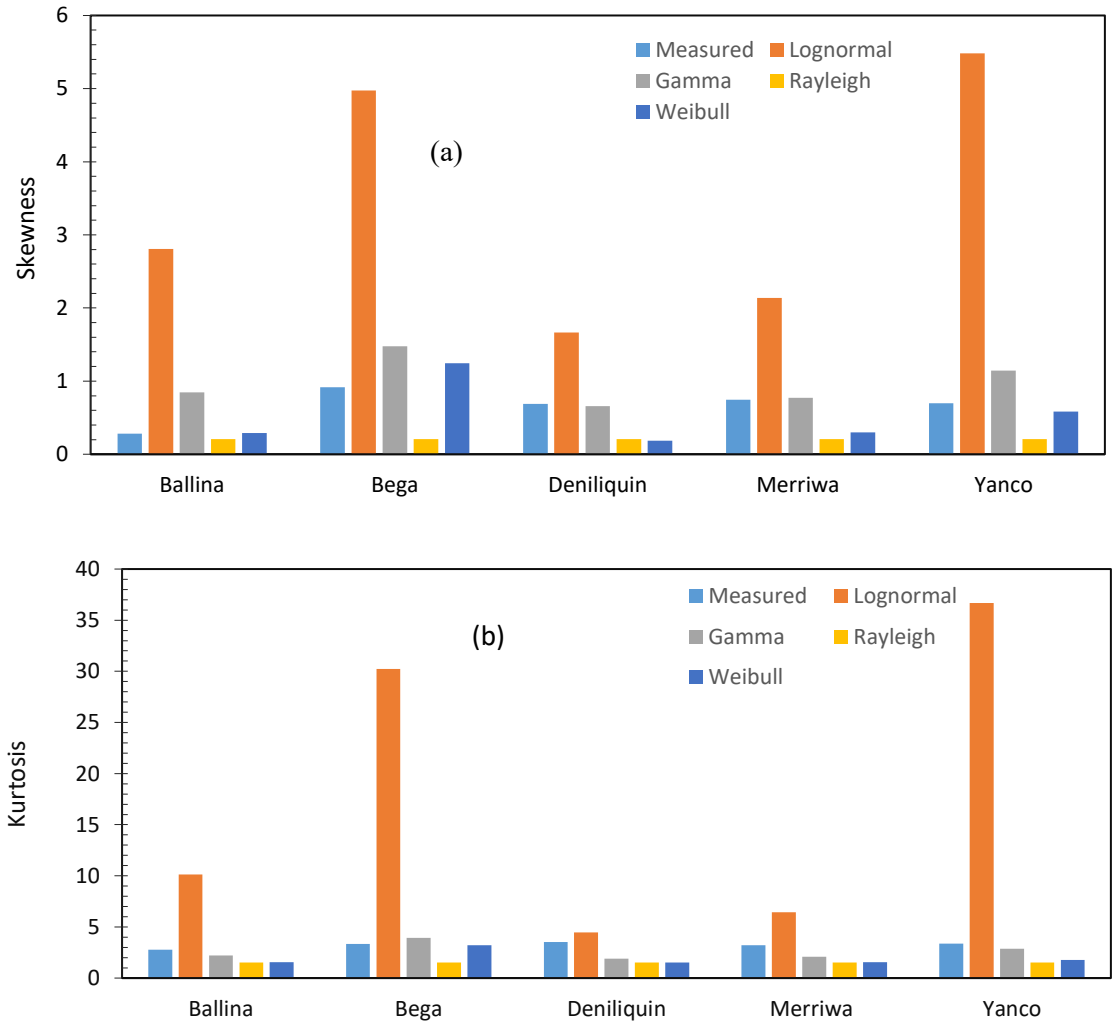

Figure 5.7. Comparison of skewness (a) and kurtosis (b) values of different distribution functions.

For more depth of the statistical indicators which compare the goodness-of-fit for different the probability density functions for selected sites, these are listed in **Table 5.2**. For Ballina, Deniliquin and Yanco, the Weibull distribution is the most accurate, followed by the Rayleigh distribution, which is also noted from probability density function and cumulative distribution function when compared to measured data. For Bega and Merriwa areas, the best fitting distribution for measured data is the Weibull distribution, followed by the gamma distribution. Therefore the lognormal distribution is the least accurate distribution used at the five sites. The outcome of this study agreed with Tar [129], who investigated lognormal, Weibull, and gamma distribution for seven Hungarian meteorological stations. The outcomes confirmed the good accuracy of Weibull distribution, and the shape and scale parameters of monthly average speeds at different altitudes of 20, 40, 60, 80, and 100 m were calculated.

For Ballina, the R^2 varies between 0.997073 and 0.905673; the highest value was for the Weibull distribution while the lowest value was for the lognormal distribution. The related value of RMSE for Weibull and lognormal are 0.019247 and 0.092157, respectively. For the Bega region, the highest value of R^2 is 0.993604 for Weibull distribution, followed by a gamma distribution having a value of 0.991548. For Deniliquin, the four probability density functions have a high R^2 which ranges between 0.998587 and 0.978405. The values represent the high accuracy of four models for fitting the measured data.

For Merriwa, Weibull distribution is the most accurate, which had R^2 of 0.998999, followed by the gamma function with a value of 0.997918 for R^2. Regarding Yanco, the coefficient of determination varied from 0.803537 to 0.992923. The highest value of R^2 is related to Weibull distribution as the most suitable probability function. Rayleigh emerges as the second-best method with a value of 0.992115, near the Weibull distribution function. The RMSE varies from 0.027963 concerning Weibull distribution to 0.117126 regarding lognormal distribution.

Table 5.2. Comparison of the goodness-of-fit between different distribution functions using statistical indicators.

		R^2	RMSE	AIC	BIC	Rank
Ballina						
	Lognormal	0.905673	0.092157	2.24974	10.207512	4
	Gamma	0.976339	0.050062	2.49842	10.456191	3
	Rayleigh	0.99377	0.027025	-1.517715	6.440057	2
	Weibull	0.997073	0.019247	-0.870346	7.087426	1
Bega						
	Lognormal	0.944095	0.058708	2.795589	10.783512	3
	Gamma	0.991548	0.025016	3.697678	11.685601	2
	Rayleigh	0.931653	0.094731	-0.44371	7.544213	4
	Weibull	0.993604	0.022187	-0.715431	7.272492	1
Deniliquin						
	Lognormal	0.978405	0.049123	2.071796	10.321163	4
	Gamma	0.997253	0.018551	1.599114	9.848481	3
	Rayleigh	0.997661	0.017197	-1.085798	7.163568	2
	Weibull	0.998587	0.013567	-1.797523	6.451844	1
Merriwa						
	Lognormal	0.976616	0.047698	2.262251	10.270025	4
	Gamma	0.997918	0.015198	2.202129	10.209903	2
	Rayleigh	0.995096	0.024927	-0.795949	7.211825	3
	Weibull	0.998999	0.010771	-1.430745	6.577029	1
Yanco						
	Lognormal	0.803537	0.117126	2.534005	10.430075	4
	Gamma	0.971053	0.050675	3.222925	11.118995	3
	Rayleigh	0.992115	0.029863	-0.540832	7.355238	2
	Weibull	0.992923	0.027963	-1.075328	6.820742	1

The Weibull function is the best function according to the wind analysis results for the five sites. According to R^2 and RMSE, the Weibull function – as previously discussed - matches well with the measured data. The results of this study agree with Togrul and

Ertekin [301], who used the Weibull function to determine the wind power potential at seven sites in Turkey. With this in mind, it is essential to investigate the Weibull parameters to discover the wind profiles of selected sites. These will be discussed in more detail in Chapter Six.

5.4 Summary

Only a few studies have investigated the wind speed characteristics and wind power potential in NSW, which could be used to predict wind applications. This chapter investigated the wind speed characteristics and the wind energy potential in five selected locations in NSW, Australia. The objective is to conduct an in-depth statistical assessment based on statistical indicators for different probability density functions. This study explicitly investigated the wind speed characteristics and wind power potential in NSW, which could be used to predict wind applications in those regions. Different descriptive statistics of the measured wind speed are investigated monthly and annually. There are two major results of this chapter, and they can be summarized here. Firstly, Bega and Deniliquin recorded the highest mean wind speed values in November 2018. For Ballina, Merriwa and Yanco areas, the highest mean wind speed value was achieved in February 2019. Secondly, the Weibull function is the best distribution based on indicators of R^2 and RMSE. The RMSE varied between 0.010771 and 0.027963, which is lower when compared with other distributions. Meanwhile R^2 varied in a narrow range between 0.992923 and 0.998999 at Yanco and Merriwa, respectively.

Chapter Six

6 Comparison of seven numerical methods for determining Weibull parameters for wind energy generation in NSW, Australia

As previously discussed in Chapter Five, the Weibull distribution is the most accurate method according to the statistical analysis of wind speed data. This chapter presents and discusses the statistical analysis of wind speed using two-parameter Weibull distribution in NSW, Australia. In the present study, this distribution is used, and several numerical ways to estimate the scale and shape parameters of the Weibull distribution function are reported. In this chapter, the comprehensive results of using the seven numerical methods for Weibull distribution are presented. Also presented and discussed here are the in-depth statistical evaluations of wind characteristics and energy potential using seven numerical methods for adjusting the Weibull distribution of wind speeds at five sites in NSW, Australia. Section 6.1 covers the probability density functions and cumulative distribution function of seven numerical methods. The performance of seven numerical methods for modelling the wind speed using statistical indicators is evaluated in section 6.2. Section 6.3 reports the power density and variation of monthly average wind speeds with different heights. The distribution of wind direction and frequency of wind speed in five sites are plotted in section 6.4. Finally, conclusions are drawn in section 6.5.

6.1 Probability density function and cumulative distribution function

To compare the seven numerical methods for adjusting the Weibull distribution of measured wind speeds, **Figures 6.1-6.5** illustrate wind speed frequency distribution at five sites in NSW, Australia. **Figure 6.1(a)** depicts the difference between observed data and fitting functions using graphical method, maximum likelihood method,

energy pattern factor method, modified maximum likelihood method, equivalent energy method, moment method, and empirical method. These all help to understand which probability functions offer the best fit of wind speed data in Ballina. Furthermore, **Figure 6.1(b)** presents the fitted cumulative distribution function plots with a measured wind speed curve for the Ballina station. As can be seen, the modified maximum likelihood method best fits the measured wind speed data in Ballina. The energy pattern factor and equivalent energy methods are less effective for the presented Weibull function fitting for measured data.

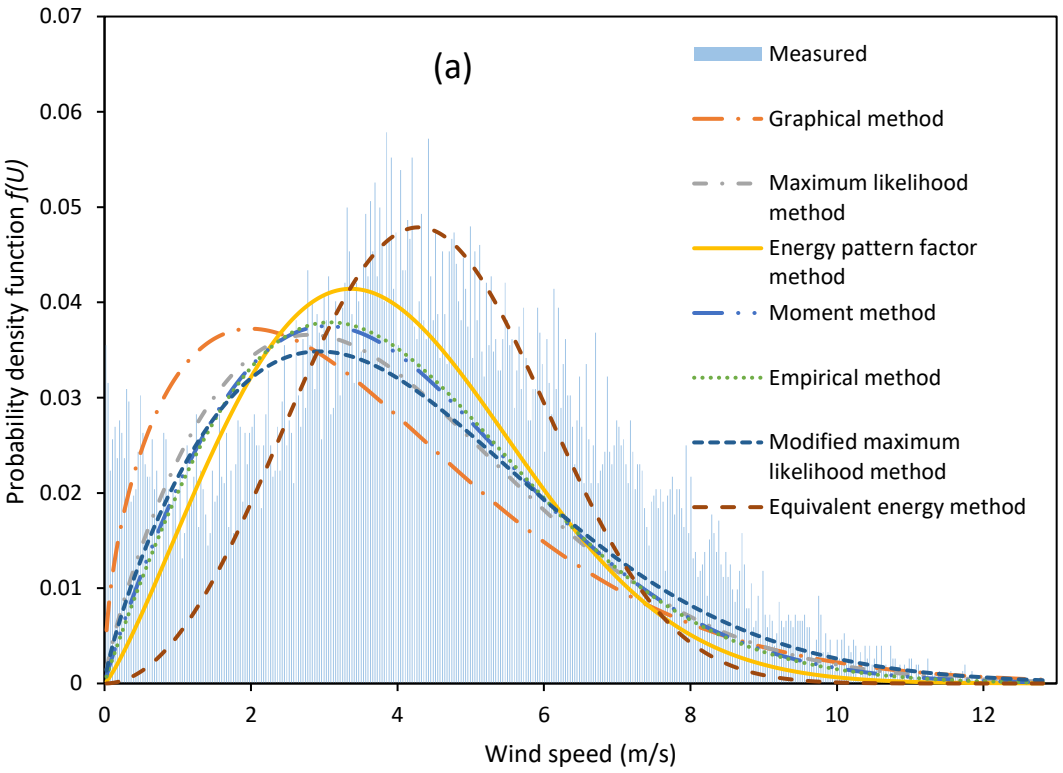

Continued on next page

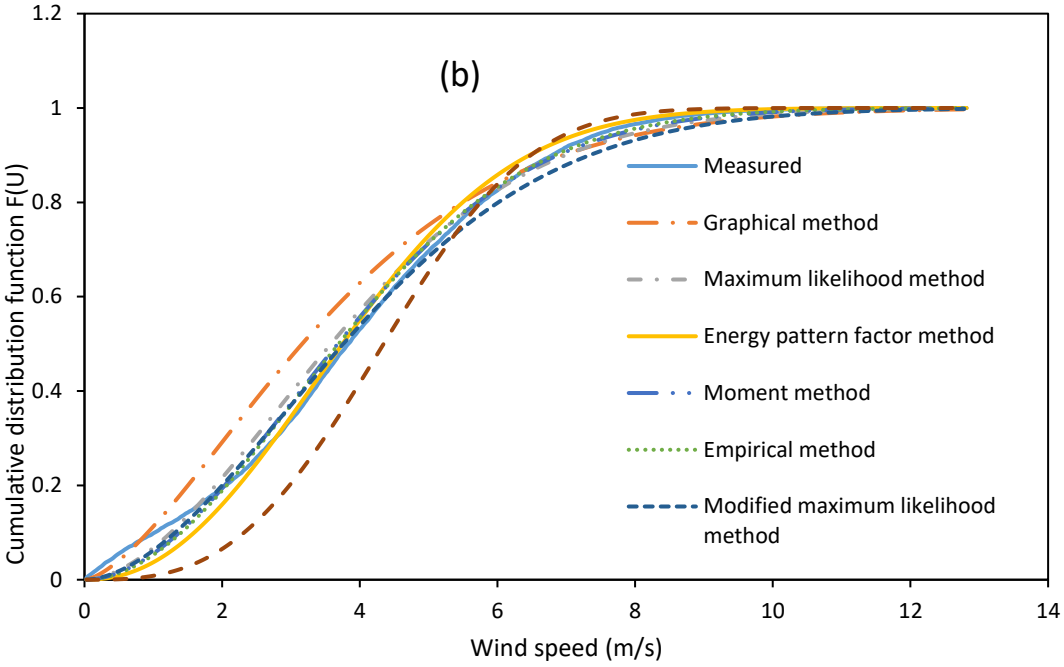

Figure 6.1. (a) Probability density function at Ballina and **(b)** Cumulative distribution function at Ballina.

As seen from **Figure 6.2**, the good fit between observed data in Bega and probability density functions is achieved with the equivalent energy method, the maximum likelihood method, and the modified maximum likelihood method. The least effective method is the graphical method.

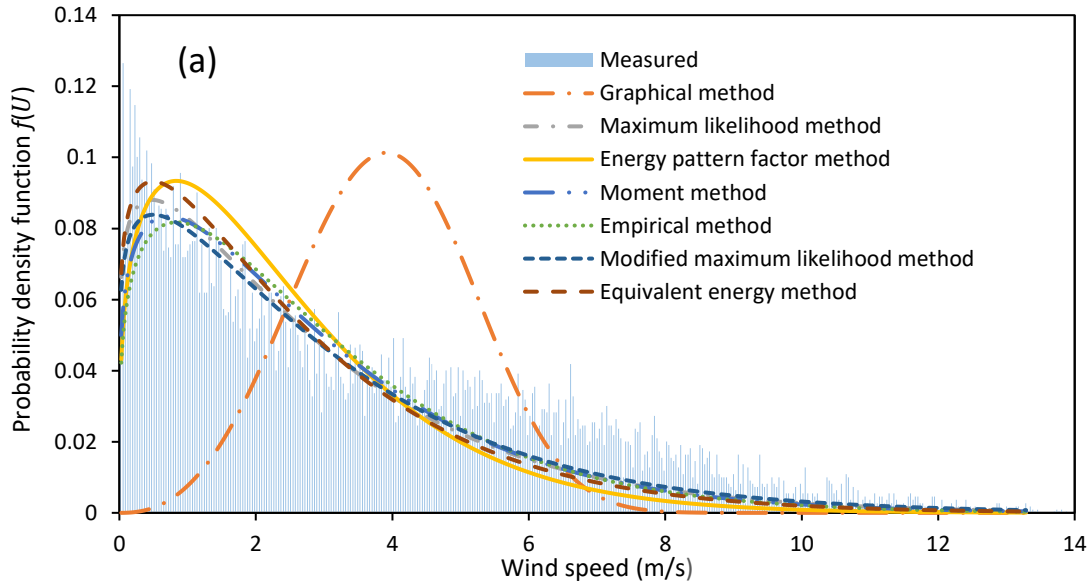

Continued on next page

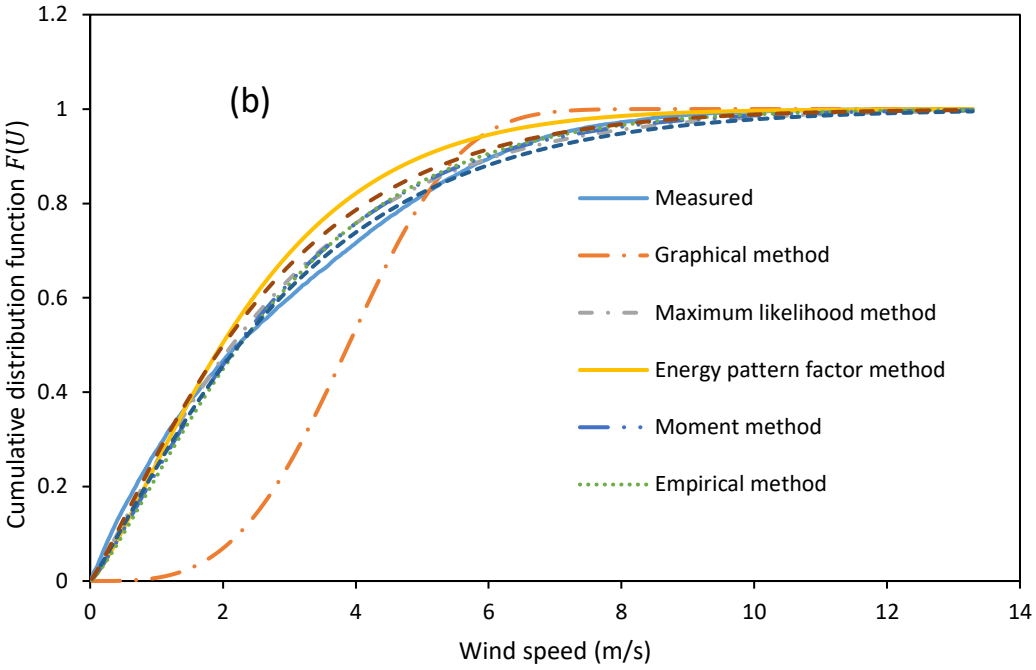

Figure 6.2. (a) Probability density function at the Bega area **(b)** Cumulative distribution function at the Bega area.

As seen from **Figure 6.3**, the modified maximum likelihood method has the best fit with measured data in Deniliquin; then, the moment method and maximum likelihood method have a near distribution compared with measured data. The energy pattern factor method is the least effective method.

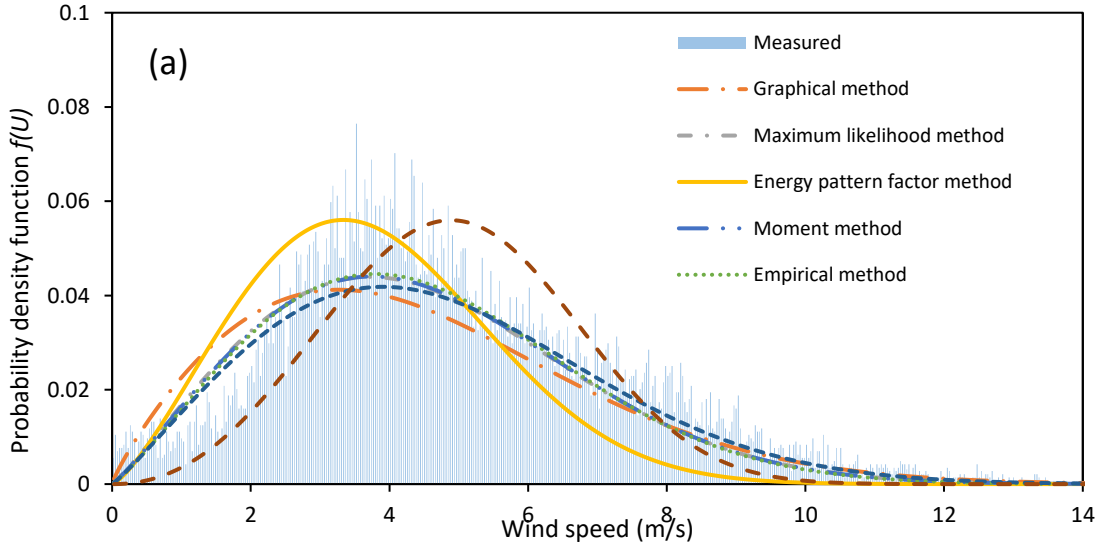

Continued on next page

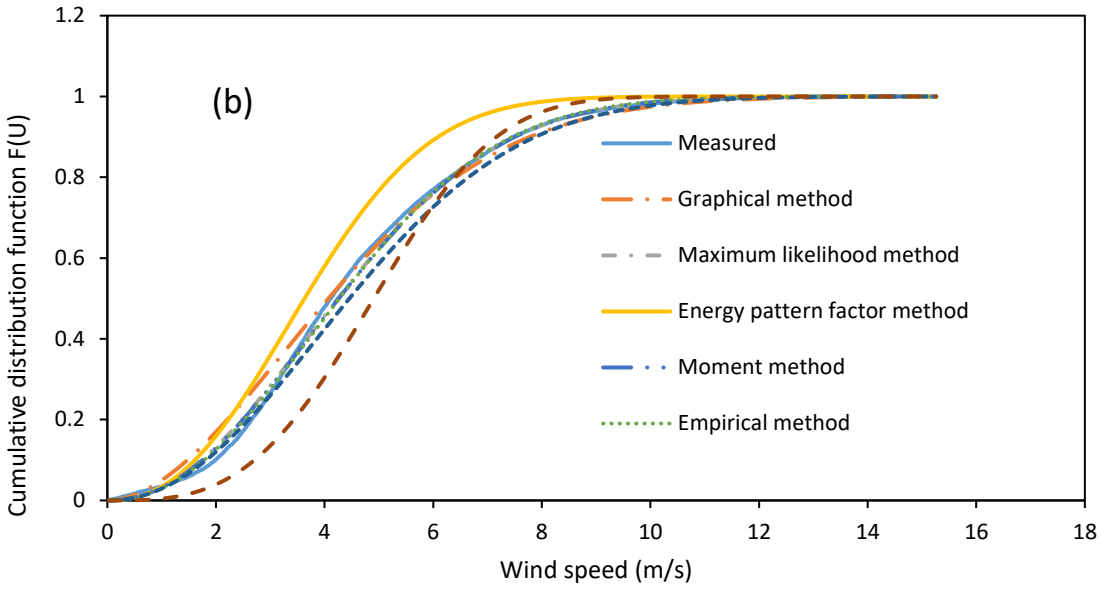

Figure 6.3. (a) Probability density function at Deniliquin and **(b)** Cumulative distribution function at Deniliquin.

The evaluation of the probability density function has shown a good fit for all seven models with measured data in Merriwa except the energy pattern factor, as shown in **Figure 6.4**. The equivalent energy method is a better efficient method that fits the measured data.

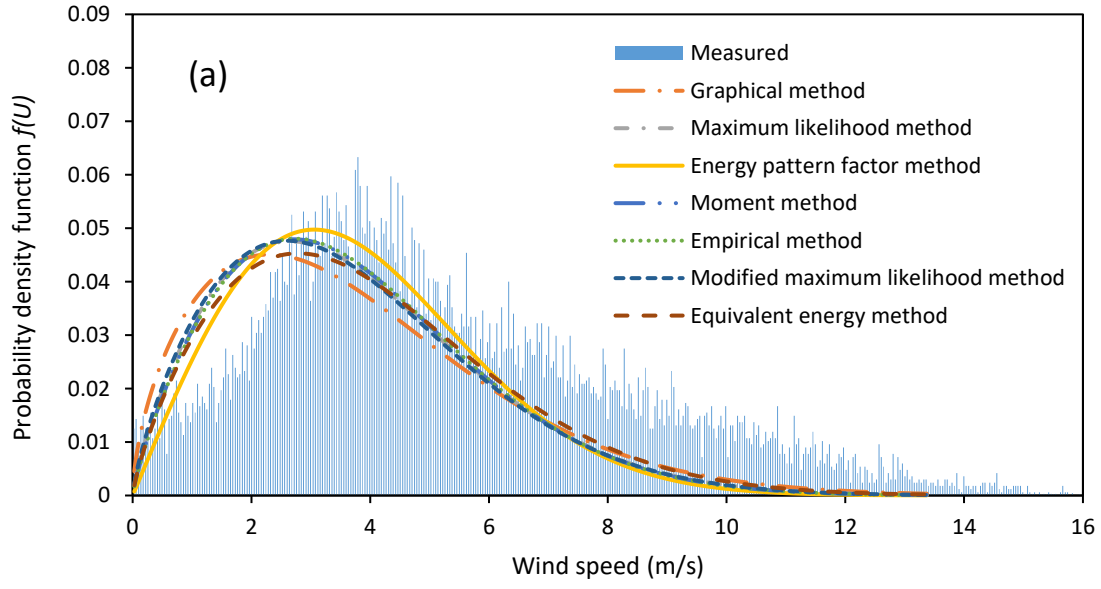

Continued on next page

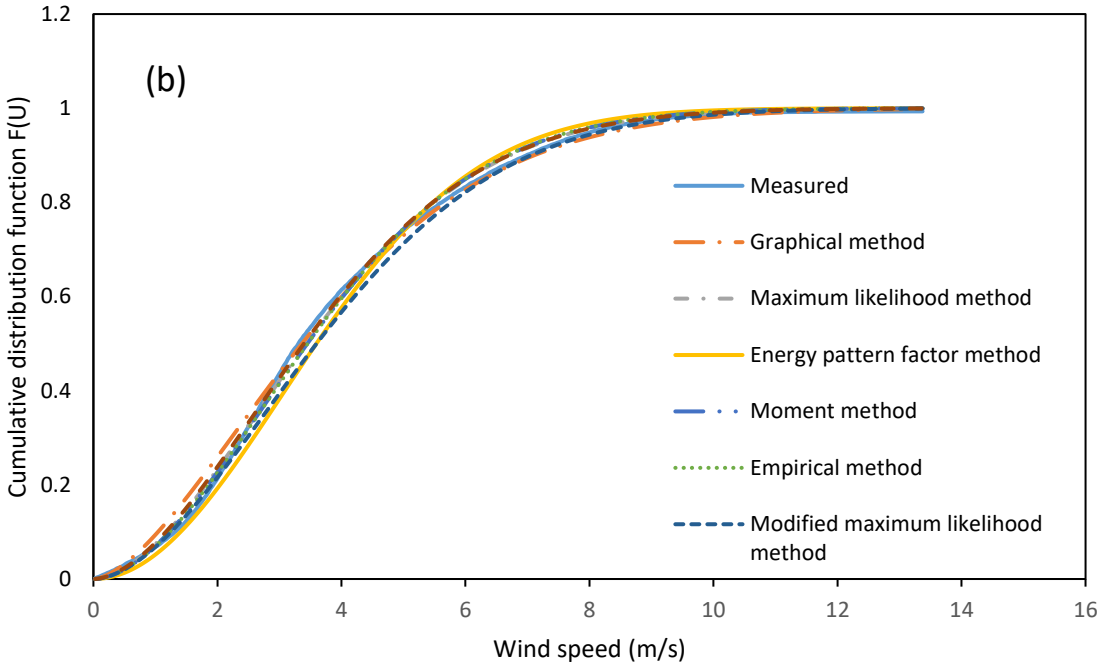

Figure 6.4. (a) Probability density function at Merriwa and **(b)** Cumulative distribution function at Merriwa.

The evaluation of the probability density function reveals a good fit for all seven models with measured data except the energy pattern factor method in Yanco, as shown in **Figure 6.5**. The equivalent energy method is a more efficient method that fits the measured data.

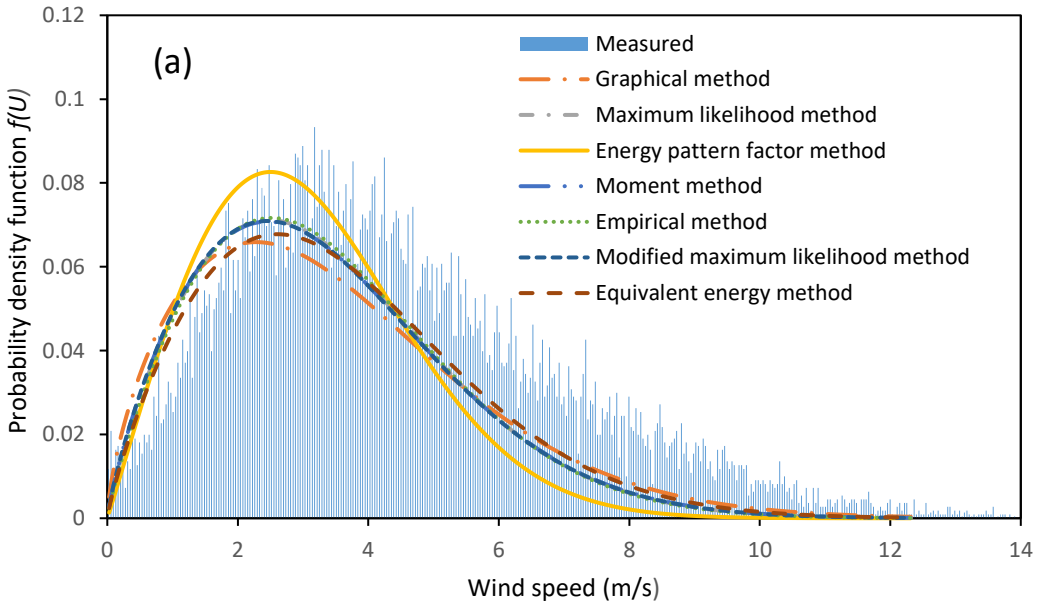

Continued on next page

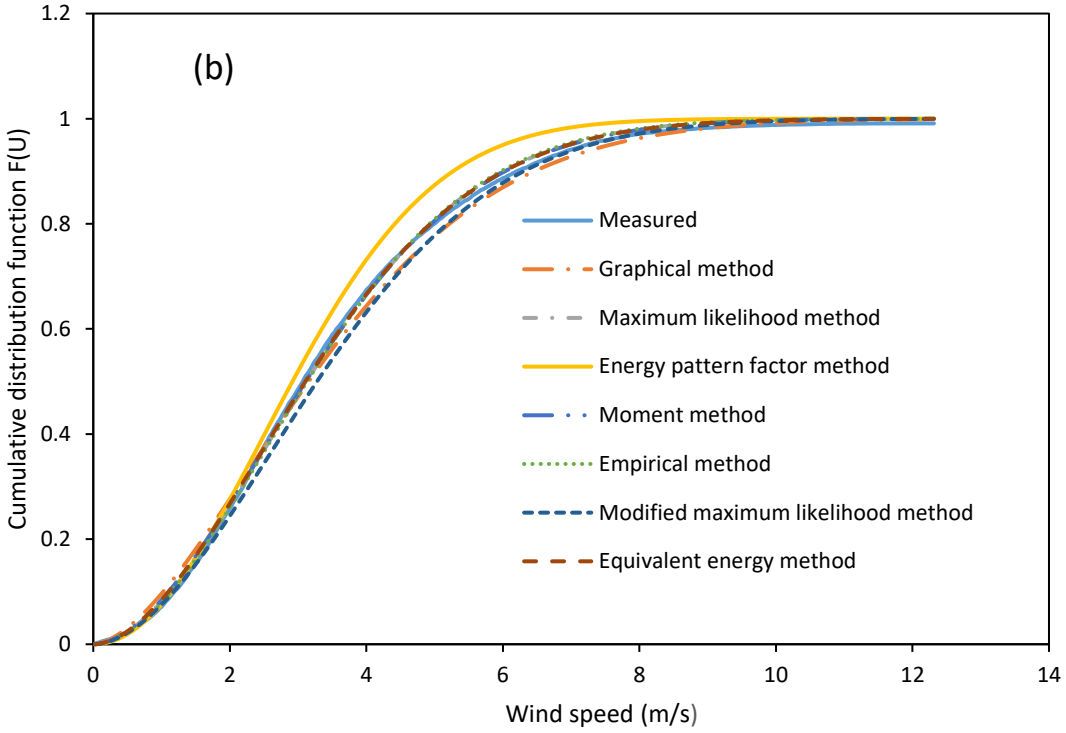

Figure 6.5. (a) Probability density function at Yanco and **(b)** Cumulative distribution function at Yanco.

6.2 Performance of seven numerical methods for modelling wind speed distribution using statistical indicators

Table 6.1 summarizes the performance of statistical analysis using the seven numerical methods. Different statistical indicators are used to describe the fit of each numerical method for wind data measurement in Ballina. The RMSE, X^2, and KS have very close values for all numerical methods used for data measurement. The values of R^2 will help determine the best numerical method to fit the measured data in Ballina. As observed, the highest value of 0.915621 refers to the modified maximum likelihood method, which is shown in probability density function in the prior section. In contrast, the least effective function is related to the energy pattern factor method, which had an R^2 value of 0.887629.

For this reason, it is essential to investigate the Weibull parameters to find the wind profiles of the chosen sites. **Table 6.2** tabulates the annual two Weibull parameters,

scale parameter *c* (m/s) and shape parameter K (dimensionless), for Ballina. It is seen from the table that the scale parameter varies between 4.022 m/s and 4.911 m/s; the shape parameter ranges from 1.524 to 3.000. Since the modified maximum likelihood method is the best one for measured data, the shape and scale parameters values are used to describe the Weibull distribution function, which is 1.796 and 4.613 m/s, respectively.

Table 6.1. Statistical indicators of different numerical methods for determining Weibull function in Ballina.

	RMSE	X^2	R^2	KS
Graphical method	0.043543	0.00006	0.910388	0.124205
Maximum likelihood method	0.033076	0.000035	0.90055	0.144828
Energy pattern factor method	0.0326	0.000034	0.887629	0.150992
Moment method	0.031322	0.000031	0.900791	0.148034
Empirical method	0.03117	0.000031	0.899726	0.148619
Modified maximum likelihood method	0.030944	0.00003	0.915621	0.145439
Equivalent energy method	0.045378	0.000065	0.896167	0.152091

Table 6.2. Annual Weibull parameters of Ballina

	K	*c*
Graphical method	1.524	4.022
Maximum likelihood method	1.787	4.384
Energy pattern factor method	2.203	4.427
Moment method	1.918	4.454
Empirical method	1.952	4.456
Modified maximum likelihood method	1.796	4.613
Equivalent energy method	3.000	4.911

As seen from **Table 6.3**, the performance of seven methods using RMSE, X^2, R^2, and

KS for wind data measurement at the Bega area perform well with the three numerical models. The highest value of R^2 is related to the equivalent energy method, while the second is the maximum likelihood method. The third method is a modified maximum likelihood method. It can be seen that the lowest R^2 is related to the graphical method, which explains that the graphical representation of this particular method fits less well to the measured data. The annual Weibull parameters of Bega for each numerical method are summarized in **Table 6.4**. The equivalent energy method has greater accuracy, related to Weibull parameters used to describe wind speed in the Bega region. Therefore the scale and shape parameters are, respectively, 2.753 m/s and 1.158.

Table 6.3. Statistical indicators of different numerical methods for determining Weibull function in Bega.

	RMSE	X^2	R^2	KS
Graphical method	0.122071	0.0005	0.724063	0.406714
Maximum likelihood method	0.028285	0.000027	0.815031	0.188513
Energy pattern factor method	0.041133	0.000057	0.784994	0.248913
Moment method	0.032972	0.000036	0.784317	0.234132
Empirical method	0.036001	0.000043	0.783008	0.256452
Modified maximum likelihood method	0.028245	0.000027	0.800982	0.20022
Equivalent energy method	0.030445	0.000031	0.824708	0.182285

Table 6.4. Annual Weibull parameters of Bega

	K	*c*
Graphical method	3.410	4.331
Maximum likelihood method	1.137	2.935
Energy pattern factor method	1.293	2.628
Moment method	1.211	3.000
Empirical method	1.252	3.024
Modified maximum likelihood method	1.142	3.093
Equivalent energy method	1.158	2.753

It is evident in **Table 6.5** that the performance of seven methods using RMSE, X^2, R^2, KS for wind data measurement of Deniliquin is good for all seven models. The modified maximum likelihood method had respective values for RMSE, X^2, and KS, and these are 0.025576, 0.000023, and 0.129922, respectively. The highest value of 0.903932 for R^2 is achieved by the modified maximum likelihood method. The annual values of Weibull parameters are shown in **Table 6.6**. The scale and shape parameters for wind speed in Deniliquin is used by the most accurate model, defined using statistical indicators of R^2. Thus, the value of shape and scale parameters for Deniliquin are 2.106 and 5.053 m/s, respectively.

Table 6.5. Statistical indicators of different numerical methods for determining Weibull function in Deniliquin.

	RMSE	X^2	R^2	KS
Graphical method	0.028804	0.000029	0.877028	0.125762
Maximum likelihood method	0.023708	0.000019	0.886600	0.119043
Energy pattern factor method	0.031447	0.000034	0.804366	0.102095
Moment method	0.023613	0.000019	0.886949	0.119158
Empirical method	0.023299	0.000019	0.885441	0.11804
Modified maximum likelihood method	0.025576	0.000023	0.903932	0.129922
Equivalent energy method	0.045752	0.000072	0.879776	0.142729

Table 6.6. Annual Weibull parameters of Deniliquin

	K	*c*
Graphical method	1.853	4.962
Maximum likelihood method	2.096	5.042
Energy pattern factor method	2.321	4.253
Moment method	2.120	5.065
Empirical method	2.157	5.066
Modified maximum likelihood method	2.106	5.053
Equivalent energy method	3.170	5.508

As seen in **Table 6.7**, the statistical indicators have close values for the seven numerical models and reveal virtually the near performance for fitting the Weibull distribution with measured values at Merriwa. **Table 6.8** shows the annual Weibull parameters values of the numerical models. The shape and scale parameter values for the equivalent energy method are 1.783 and 4.420 m/s, respectively, for Merriwa.

Table 6.7. Statistical indicators of different numerical methods for determining Weibull function in Merriwa.

	RMSE	X^2	R^2	KS
Graphical method	0.026864	0.000022	0.875387	0.102969
Maximum likelihood method	0.023564	0.000017	0.877362	0.091031
Energy pattern factor method	0.025819	0.000021	0.876762	0.085681
Moment method	0.023439	0.000017	0.876827	0.089621
Empirical method	0.023429	0.000017	0.876540	0.089216
Modified maximum likelihood method	0.02472	0.000019	0.875548	0.100315
Equivalent energy method	0.023681	0.000017	0.894127	0.090736

Table 6.8. Annual Weibull parameters of Merriwa

	K	c
Graphical method	1.606	4.228
Maximum likelihood method	1.771	4.197
Energy pattern factor method	2.004	4.317
Moment method	1.817	4.221
Empirical method	1.825	4.222
Modified maximum likelihood method	1.765	4.179
Equivalent energy method	1.783	4.420

It can be seen in **Table 6.9** that the highest value of R^2 is related to the equivalent energy method, which had a value of 0.879816, where the values of RMSE and KS are 0.019745 and 0.067195, respectively. The energy pattern factor method performs the least accurate numerical method with a smaller value R^2 compared with the other seven numerical methods. Depending on their evaluation, the equivalent method will

define the two parameters of the Weibull distribution at Yanco. The shape and scale parameters are 1.835 and 4.002 m/s, respectively.

Table 6.9. Statistical indicators of different numerical methods for determining Weibull function in Yanco

	RMSE	X^2	R^2	KS
Graphical method	0.023369	0.000016	0.856630	0.082678
Maximum likelihood method	0.019628	0.000012	0.861529	0.066573
Energy pattern factor method	0.023015	0.000016	0.814209	0.07496
Moment method	0.019776	0.000012	0.862406	0.067659
Empirical method	0.019535	0.000011	0.860548	0.065261
Modified maximum likelihood method	0.021649	0.000014	0.861571	0.077459
Equivalent energy method	0.019745	0.000012	0.879816	0.067195

Table 6.10. Annual Weibull parameters of Yanco

	K	*c*
Graphical method	1.675	3.927
Maximum likelihood method	1.835	3.811
Energy pattern factor method	2.030	3.495
Moment method	1.817	3.811
Empirical method	1.860	3.814
Modified maximum likelihood method	1.817	3.802
Equivalent energy method	1.835	4.002

6.3 Variation of mean wind speed and wind power density with height

6.3.1 Mean wind speed at the height of 40 m and 50 m

Figure 6.6 shows the monthly mean wind speed profile at different elevations at the selected five sites. The actual data was recorded at the height of 10 m, and the other remaining data at altitudes of 40 m and 50 m are calculated from the power-law

equation [302]. For Ballina, the highest mean wind speed was recorded in February 2019, as discussed in Chapter Five. Therefore, the fastest top mean wind speed at 50 m elevation is 6.306 m/s, while the lowest mean wind speed at the same height is recorded at 3.880 m/s in May 2019. The highest and lowest mean wind speeds for the Bega region were recorded in November 2018 and April 2019, respectively. Here the highest and lowest mean wind speeds at 50 m elevation are 4.445 m/s and 2.649 m/s, also respectively. For Deniliquin, the higher value of the mean wind speed of 6.699 m/s was recorded in November 2018 at the height of 50 m. For Merriwa, the higher value of mean wind speed at an elevation of 50 m is recorded in February 2019, with a value of 6.158 m/s. For Yanco, the lowest average monthly wind speed is measured in December 2018 as 2.758 m/s at 50 m height while the highest average monthly wind speed is in February 2019 at 4.918 m/s at 50 m.

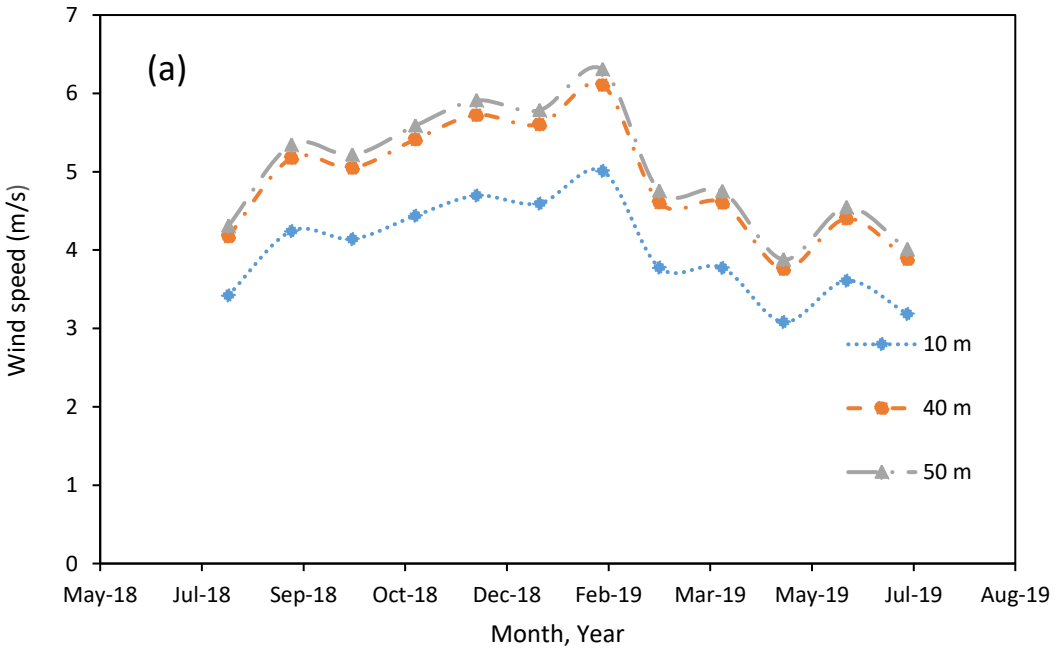

Continued on next page

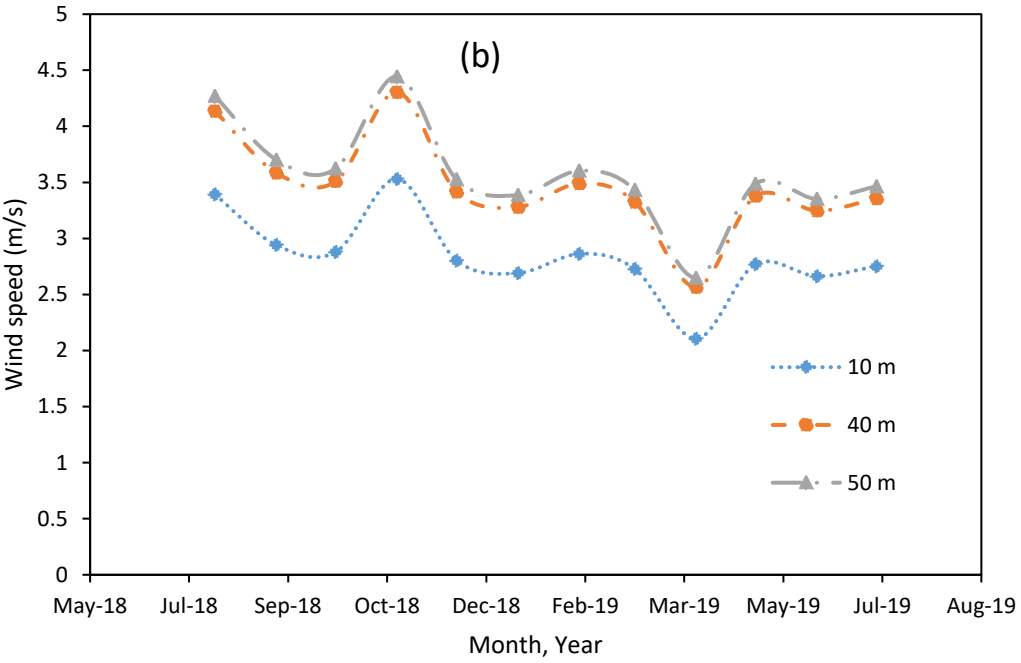

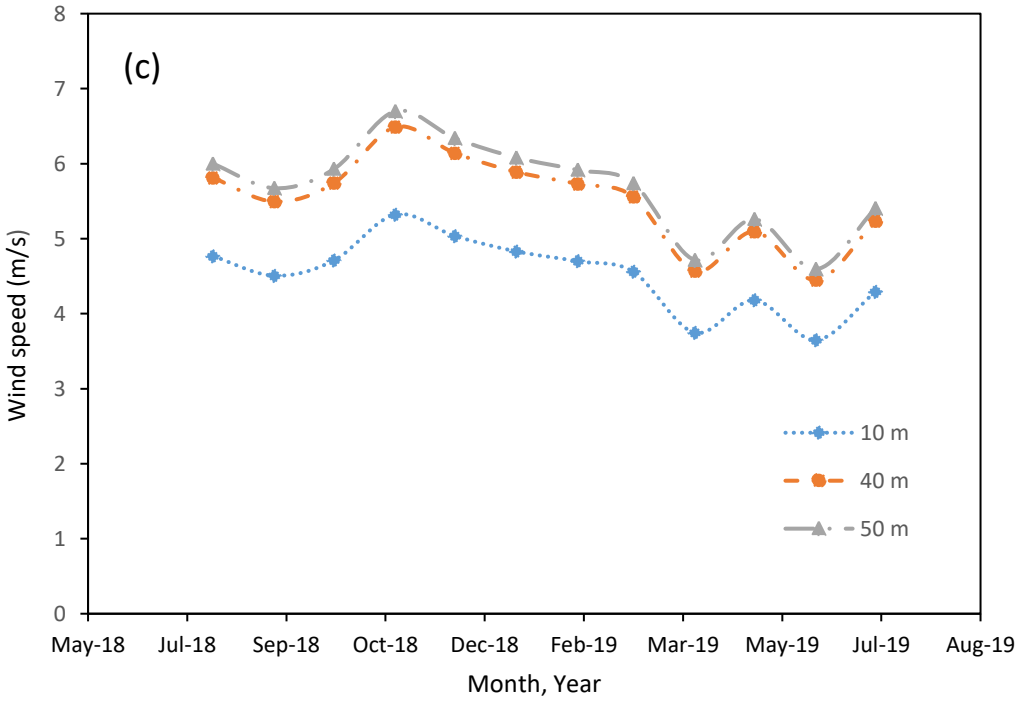

Continued on next page

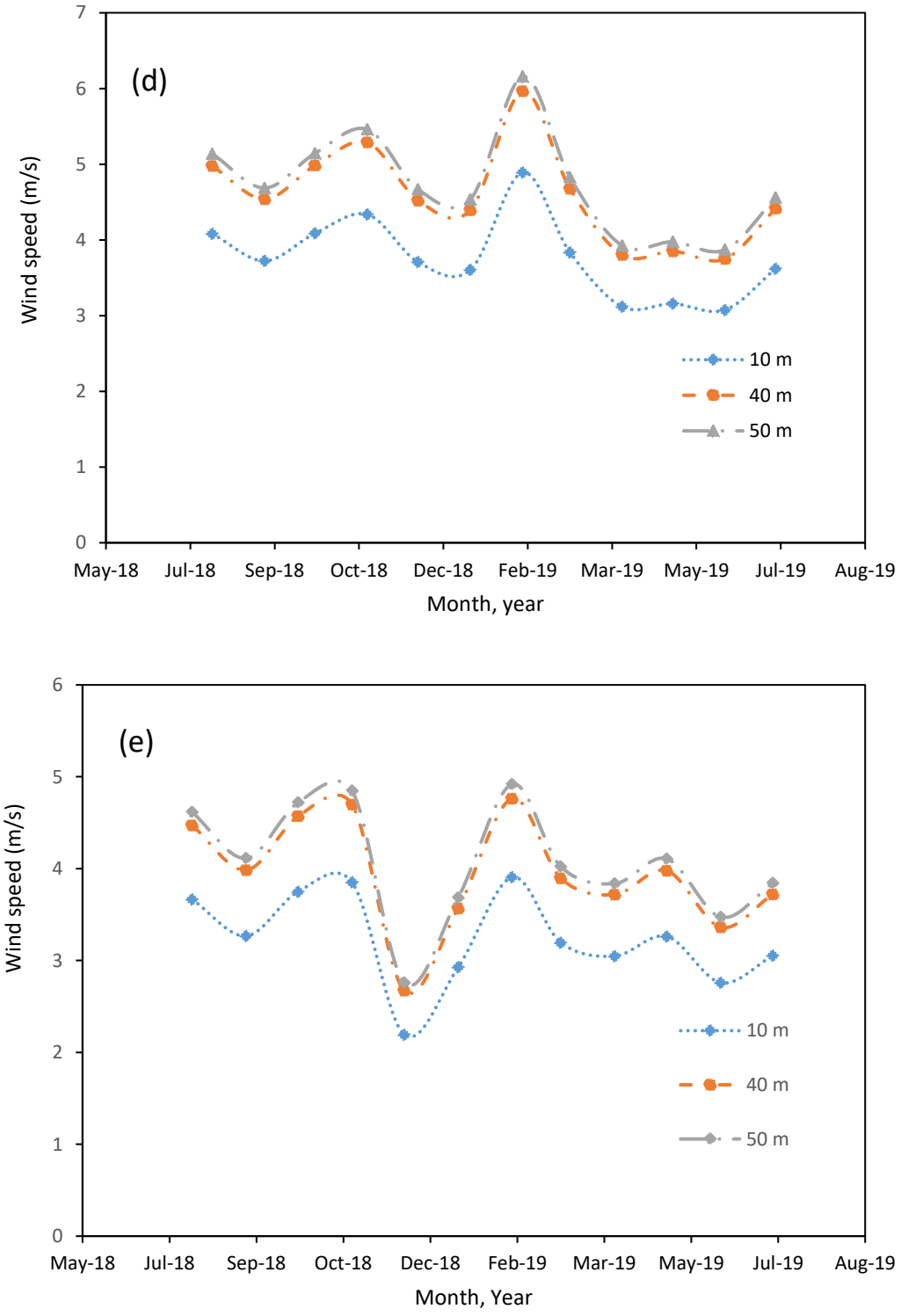

Figure 6.6. Monthly average wind speeds for different heights at the following locations: **(a)** Ballina, **(b)** Bega, **(c)** Deniliquin, **(d)** Merriwa, and **(e)** Yanco.

6.3.2 Wind power density

Wind power density gives a better indication than wind speed when evaluating wind resources in a specific region [303]. Therefore, the determination of wind power is

essential in wind project assessment. As discussed previously, Weibull distribution is the most accurate distribution function used in this analysis; this explained that the wind power density would be calculated depending on the shape and scale parameters of the Weibull method. As illustrated in **Table 6.11**, the annual mean power density at selected sites varies from 85.677 to 202.747 W/m^2 at 50 m elevation; this difference leads to a change of mean wind speed from one location to another. Consequently, the power density has a relationship that is proportional to the cube of the wind speed, which explains that the Bega area has a mean wind speed of 2.810 m/s and the lowest wind power density at 42.954 W/m^2 at 10 m elevation.

In comparison, Deniliquin has a mean wind speed of 4.530 m/s and the highest power density of 108.618 W/m^2 at the same altitude. Also, the increase in elevation plays a role in rising wind speed and power density. This is clear when comparing wind power density for Ballina and Merriwa, which had a mean wind speed at an elevation of 10 m 3.945 m/s and 3.745 m/s, respectively. The differences in mean wind speed at those sites are quite small, while the difference in wind power density is very slight at an elevation of 10 m. However, when increasing the elevation to 50 m, the differences between power densities are more prominent. For the Yanco site, the annual average wind power is 43.404 W/m^2 at an elevation of 10 m, while the annual average wind power data at 40 m and 50 m were 78.670 W/m^2 and 86.573 W/m^2, respectively.

Table 6.11. Power density with 10 m, 40 m, and 50 m elevation for selected sites.

	10 m	40 m	50 m
Site	Wind power density (W/m^2)	Wind power density (W/m^2)	Wind power density (W/m^2)
Ballina	65.618	118.933	130.882
Bega	42.954	77.855	85.677
Deniliquin	108.618	184.247	202.747
Merriwa	62.412	113.123	124.487
Yanco	43.404	78.670	86.573

According to **Table 6.12**, when classifying the sites according to wind power density, Ballina, Bega, Yanco and Merriwa are classified as class 1, so the wind speed at those places is not enough to generate a wind speed for large-scale wind generation applications [108]. However, it could be used for remote small electricity generation, agricultural activities, and water pumping. Deniliquin is classified as class 2, which means it is a marginal wind resource site [252].

Table 6.12. Classification of wind class according to wind speed and wind power density [253].

Wind class	10 m		50 m	
	Wind power density (W/m^2)	Wind speed (m/s)	Wind power density (W/m^2)	Wind speed (m/s)
1	<100	<4.4	<200	<5.6
2	<150	<5.1	<300	<6.4
3	<200	<5.6	<400	<7.0
4	<250	<6.0	<500	<7.5
5	<300	<6.4	<600	<8.0
6	<400	<7.0	<800	<8.8
7	<1000	<9.4	<2000	<11.9

6.4 Wind direction

The determination of wind direction is an essential step in the assessment of wind energy when using it properly. The wind rose diagram displays the wind speed frequency and corresponding wind directions. **Figures 6.7-6.11** indicate the wind rose diagrams for selected sites. Polar wind figures consist of 12 sectors, and each arc covers 30°. The direction percentages of different wind speeds are plotted in these diagrams. For Ballina, it is noted that the highest wind speed frequency (7%) occurs in the sector between 240° to 270°. The most wind originates in the sectors from 180°-240° and 30° - 60° for the Bega region, while the dominant wind speed frequency is

above (6%) at 180° - 210°. For Deniliquin, the wind direction is more evenly distributed when compared to other sites, with most wind movement occurring in the sector between 210° and 300°. The sector of 210° - 240° has the highest frequency value, around 5%. For Merriwa, the dominating wind is in the 90° - 120° and 270° - 300° ranges, while the maximum frequency above 10% is achieved between 90° - 120°. For Yanco, the highest frequency of 7% happened between 0° and 30° when the wind direction is more evenly distributed, but the most prevailing wind direction is between 180° and 240°. From the wind rose for four sites, it was evident that the dominant wind direction varied from one place to another. This outcome agreed with the finding of Allouhi et al. [252] for Laayoune, Tetouane, Hoceima, Assila, Essouira, and Dakhla in Morocco. They documented a diverse prevailing wind direction for the investigated sites.

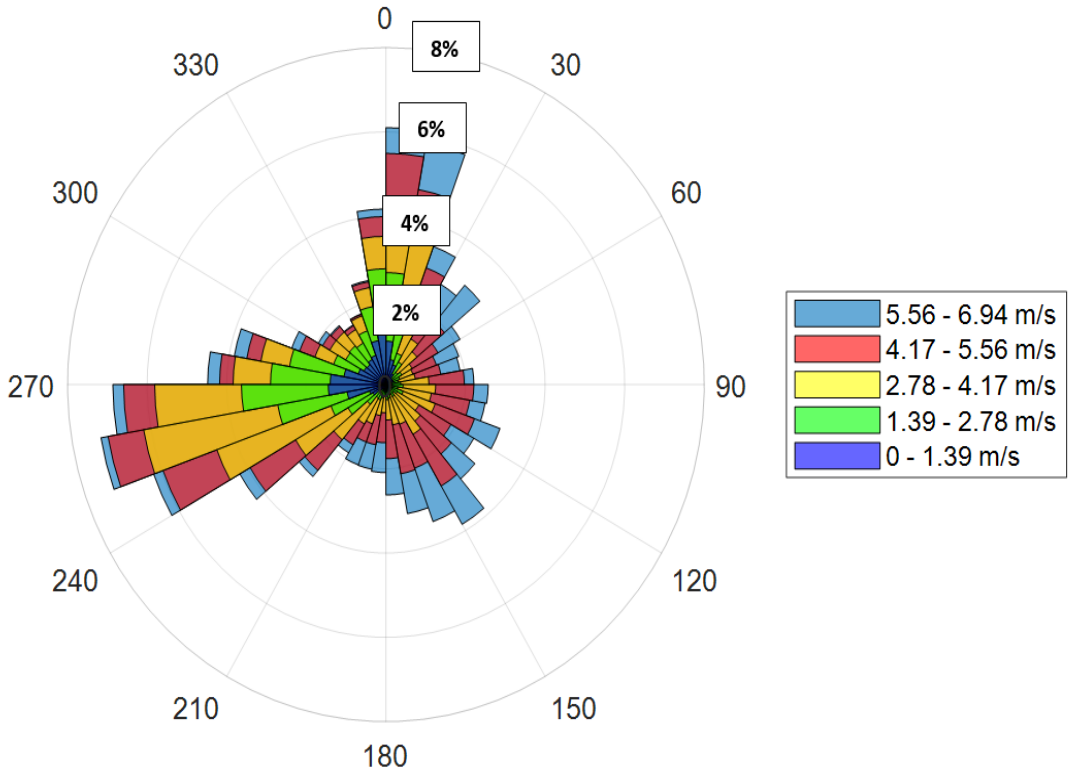

Figure 6.7. The wind rose of wind data collected from Ballina.

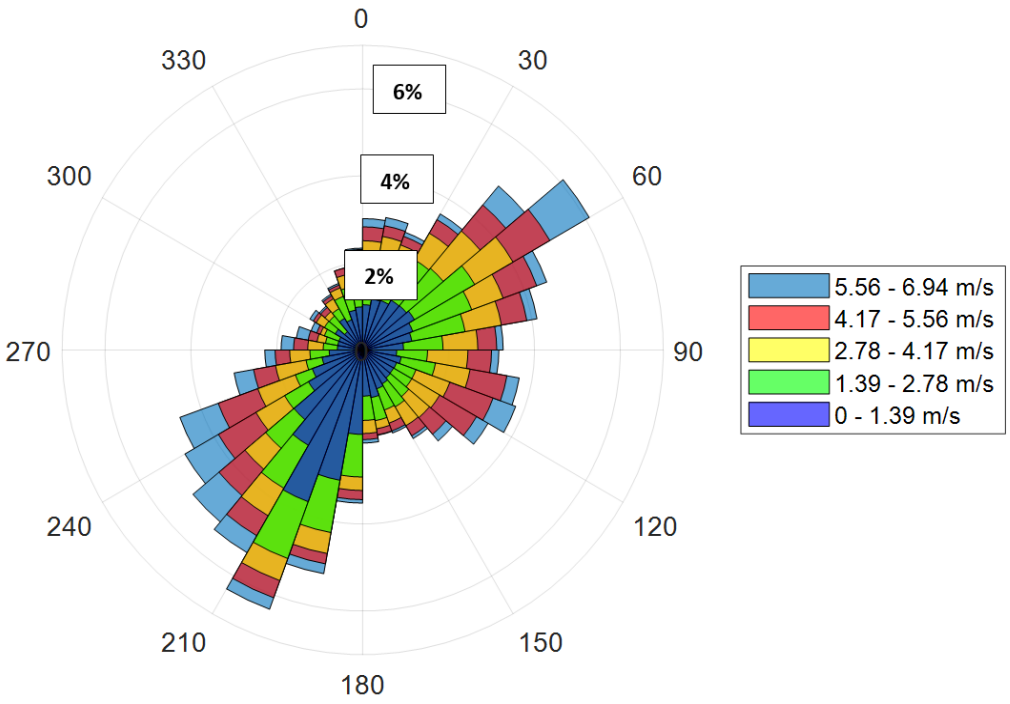

Figure 6.8. The wind rose of wind data collected from Bega.

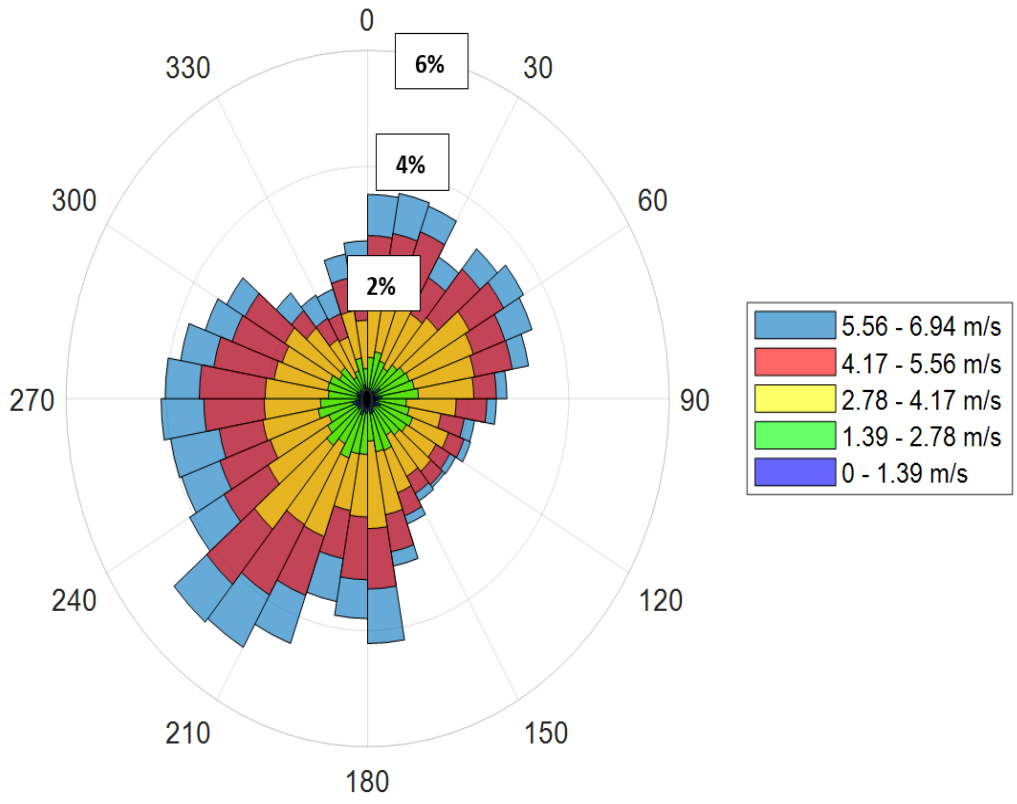

Figure 6.9. The wind rose of wind data collected from Deniliquin.

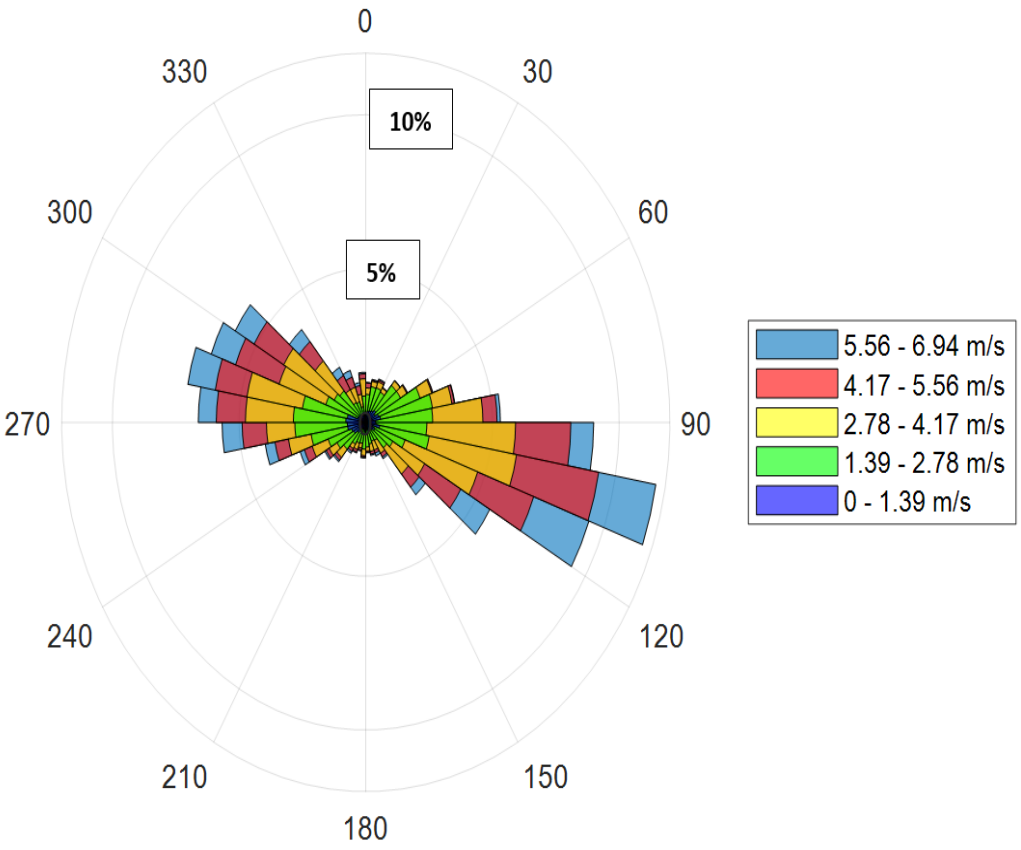

Figure 6.10. The wind rose of wind data collected from Merriwa.

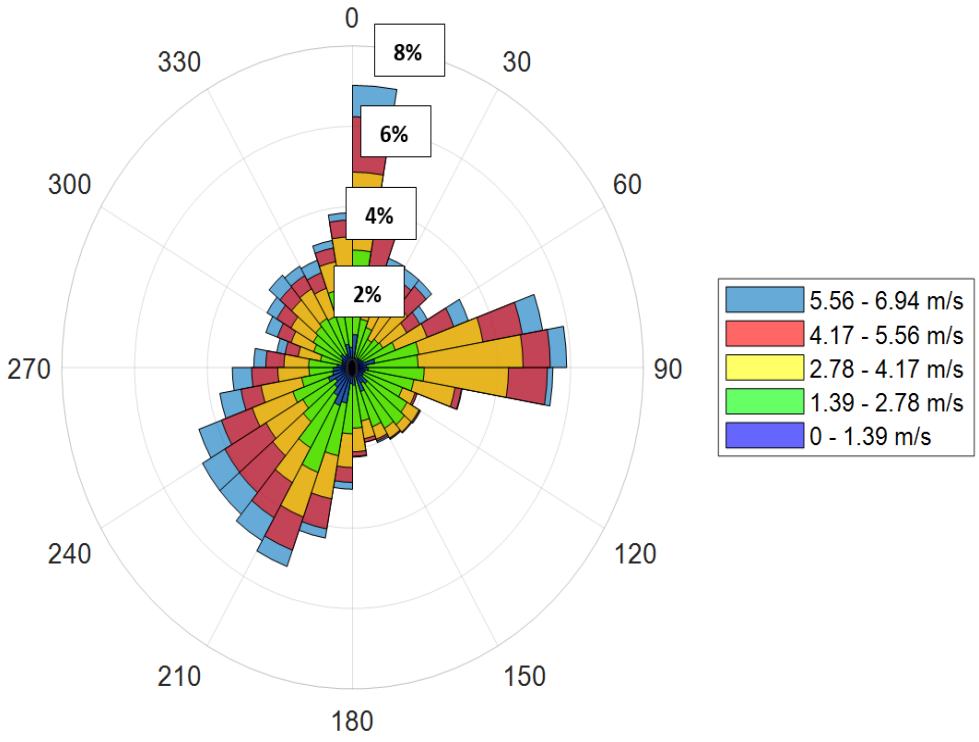

Figure 6.11. The wind rose of wind data collected from Yanco.

6.5 Summary

This chapter presented and discussed the analysis and comparison of seven numerical methods for assessing effectiveness in defining the parameters for the Weibull distribution, using wind speed data collected in five sites in NSW. The significant results of this chapter can be concluded as follows:

- The mean wind speed of the selected regions varied from 2.81 to 4.53 m/s at the height of 10 m. The wind power density varied between 42.95-108.62 W/m^2 at 10 m elevation and between 85.68-202.75 W/m^2 at a 50 m elevation. Thus the maximum wind power density was documented for Deniliquin with a wind class of 2, which showed it is a marginal wind speed resource. Meanwhile, Ballina, Bega and Merriwa had a wind class of 1 which means they were categorized as a poor wind resource.
- The numerical methods that use mathematical iterations to determine the shape and scale parameters present smaller errors in adjusting the Weibull distribution curves. Therefore, they are recommended when greater precision is required to provide more accurate results obtained with the Weibull distribution.
- The equivalent energy method efficiently determines the shape and scale parameters to fit Weibull distribution curves for wind speed data in the Yanco, Merriwa, and Bega regions. At the same time, the modified maximum likelihood method has the best fit to the measured wind speed data in Ballina and Deniliquin.

The statistical analysis results show that the highest wind potential was at Deniliquin, with Weibull shape and scale parameters of 2.106 and 5.053 m/s, respectively. These results encourage the utilization of small-scale wind energy project in this area. The next chapter discusses the aerodynamics optimization of the small wind turbine depending on the probability density function of wind data in the Deniliquin region. The objective is to increase the useful amount of annual energy production of the wind turbine.

Chapter Seven

7 Aerodynamics optimization for a wind turbine shape designed for the Deniliquin area

The preceding chapter's results concerning CFD modelling, which presents and investigate the 20 kW wind turbine performance under different wind speed ranges, are validated against the NREL test. The place where the wind turbine will be installed plays a key role in the performance of wind turbine output. Thus, understanding the environmental conditions using assessment based on the wind data recorded at five meteorological stations in NSW, Australia, has been undertaken. The four different probability density functions - Rayleigh, lognormal, gamma, and Weibull - are used to evaluate the wind resources at five investigated sites. The Weibull distribution reveals that the most accurate model determining the Weibull probability density function requires defining the shape and scale parameters using different estimation methods. Deniliquin has the best wind resource, so consequently, the optimization process will include shape and scale parameters as input parameters.

This chapter presents and discusses the aerodynamics optimization tool for the wind turbine using HARP_Opt software based on BEM theory and the genetic algorithm. This chapter is divided into three sections. Section 7.1 deals with the selection of the blade design's geometric parameters. In the second section, the effect of operating conditions on optimized wind turbine output is studied. For example, the power coefficient variation with wind speeds and change of rotor speed and pitch angle with wind speeds are covered here. The summary is reported in section 7.3, and it concerns the main results.

7.1 Selection of the geometric parameters of blade design

This study aims to maximize the annual energy production at the Deniliquin site; hence, for this study, Weibull parameters, of which the shape and scale parameters are 2.106 and 5.053 m/s, respectively, serve as inputs in HARP_Opt software. The probability density function is plotted by Harp_Opt, as seen in **Figure 7.1(a)**. Different variables should be considered when selecting other parameters such as the rotor diameter and cut-in speed because they affect the capacity factor. According to input parameters, the HARP _Opt generated a contour plot, as seen in **Figure 7.1(b)**, which illustrates the AEP and capacity factor related to selecting the rated power and diameter of the wind turbine.

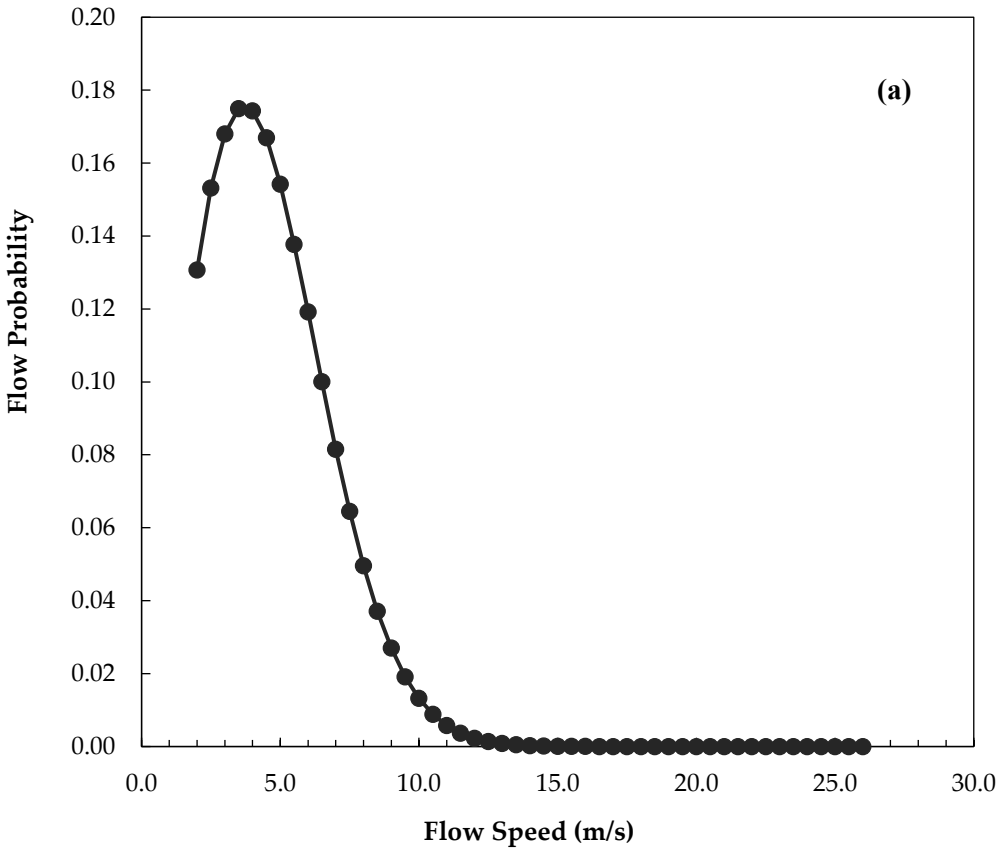

Continued on next page

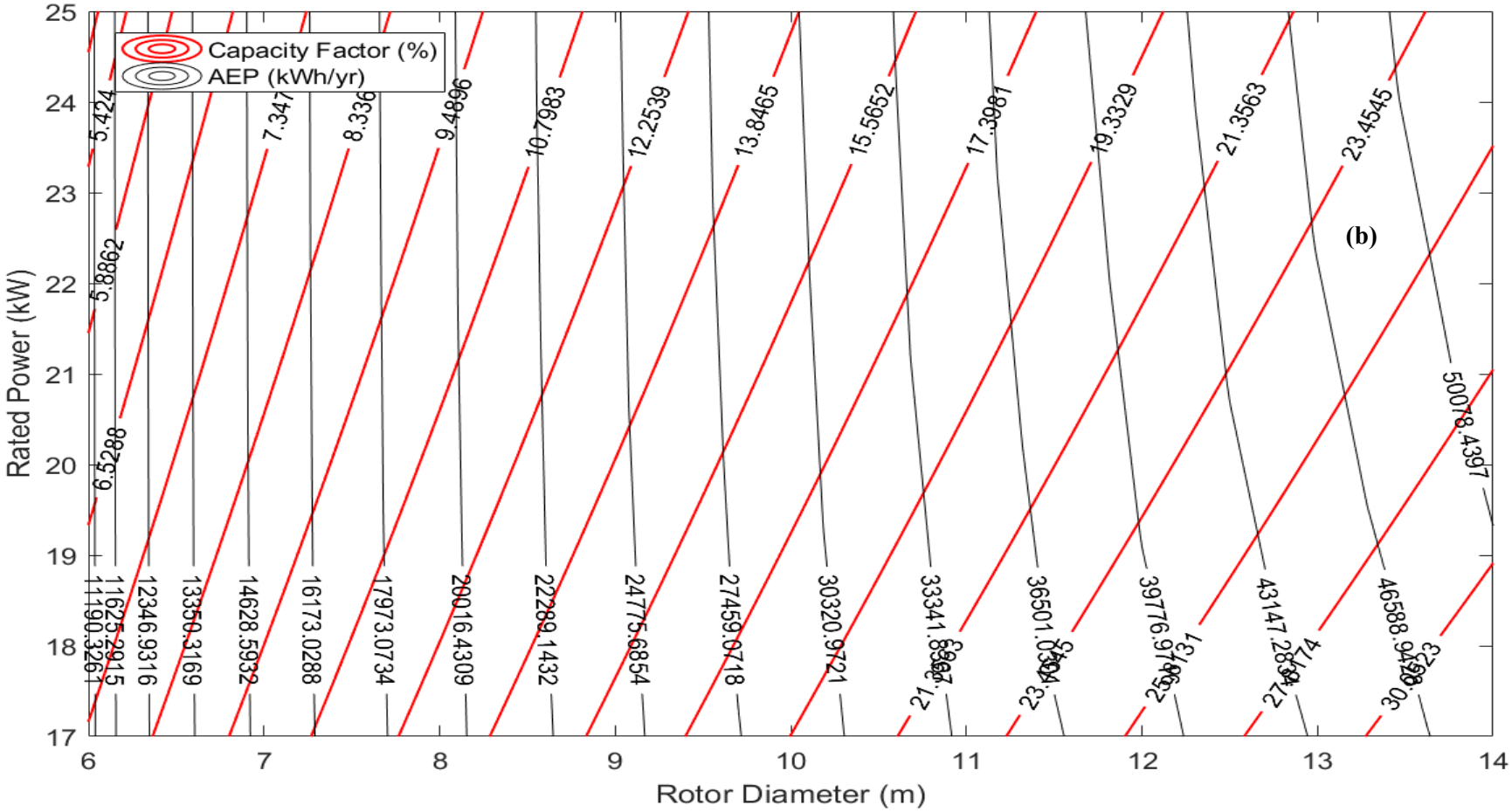

Figure 7.1. (**a**) Weibull probability density function at the Deniliquin site and (**b**) The AEP for different turbine diameters for Weibull function parameters: K= 2.106 and c = 5.053 m/s.

The shape of the wind turbine is defined by chord length and twist angle at each blade element. Chord length and twist angle distribution along the blade have a direct impact on AEP. Thus, it considers as design parameters those that are changing in the optimization process to maximize AEP. Bezier curves are used to achieve smooth spanwise distributions of chord length and twist angle. In this study, the optimization process modified the shape of the blade design using chord and twist distribution along the blade with the remaining airfoil shape (S809). The chord and twist distributions of the optimized wind turbine blade are shown in **Figure 7.2**. The wind turbine geometry had a maximum value of 0.713679 m for chord length at 1.21 m. at the same time, the maximum twist angle reached 19.9783° until the 0.22 span and later became zero at a 0.90 span and a negative value at a 1.00 span.

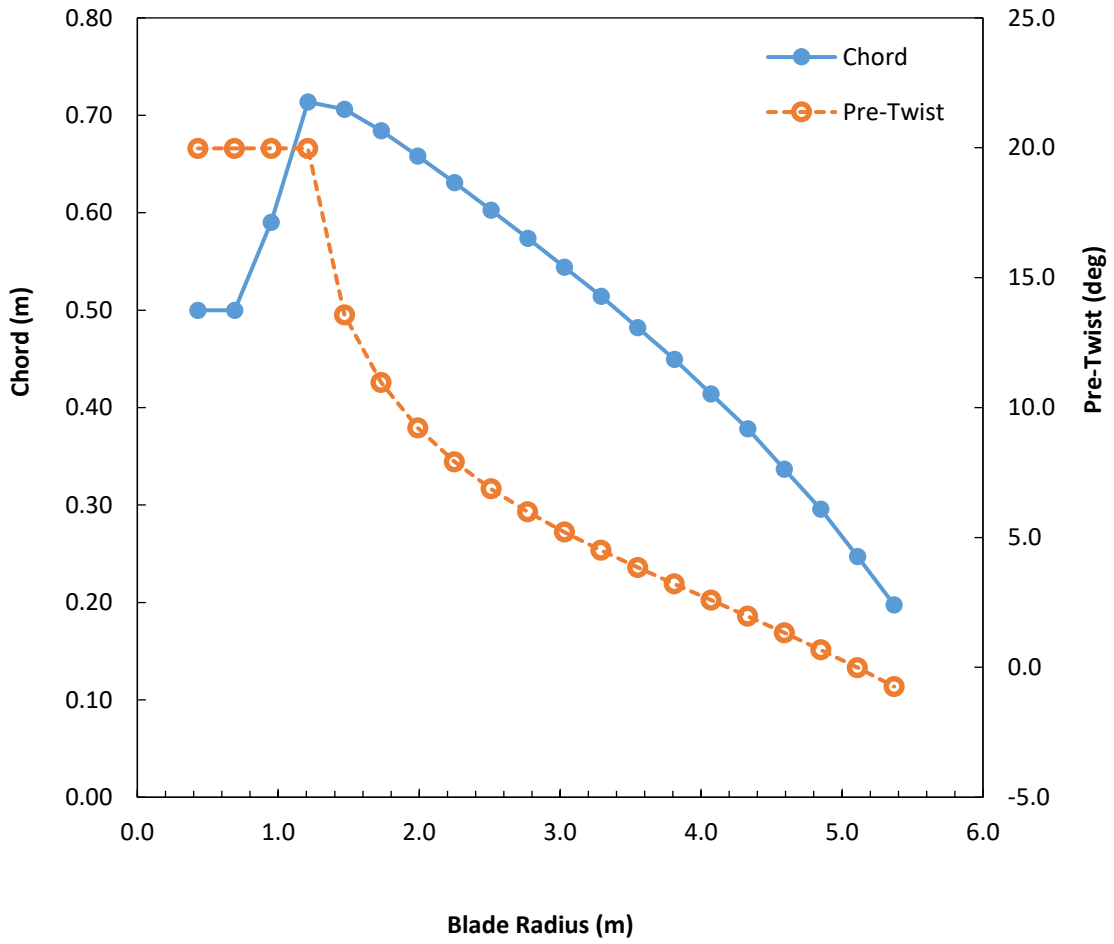

Figure 7.2 Twist angle and Chord length distribution along the blade.

7.2 Effect of operating conditions on optimized wind

turbine output

The power coefficient of the optimized rotor with wind speed is depicted in **Figure 7.3,** an output from HARP_Opt software. The power coefficient had the highest value of 0.433108 until the rated wind speed (9.5 m/s). Due to the Weibull probability density function being high in the low wind speed range, it is essential to have a high-power coefficient to increase the AEP.

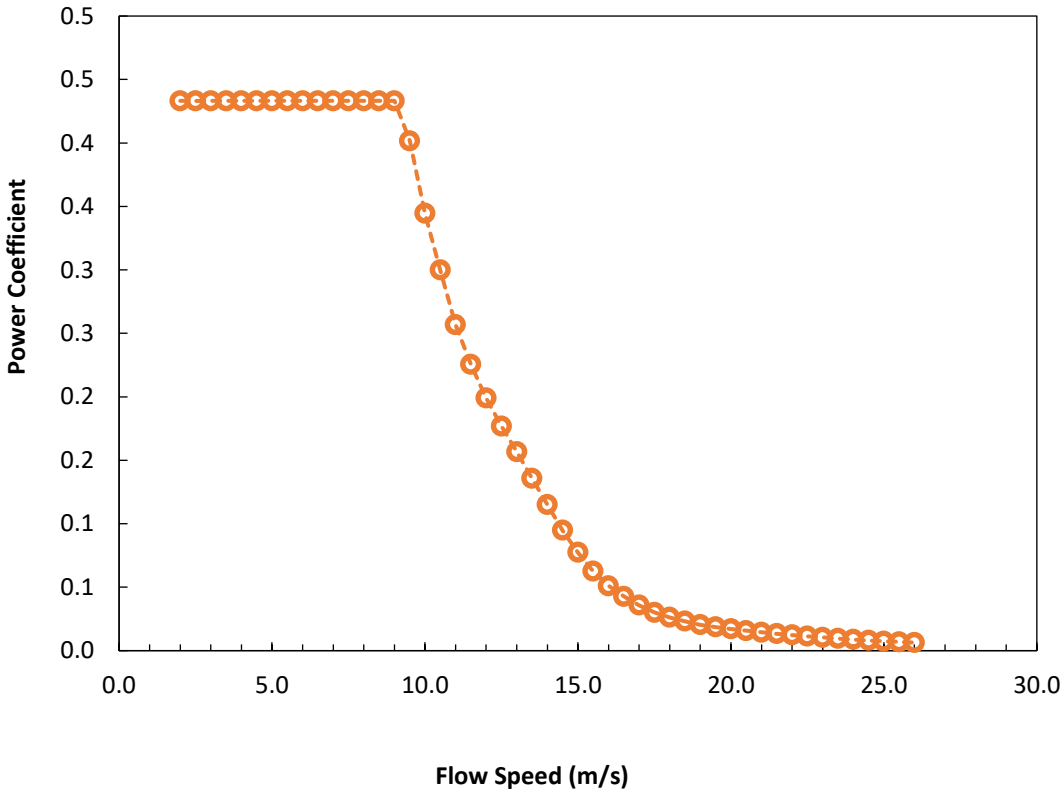

Figure 7.3. Variation of power coefficient with wind speeds.

The blade pitch control is the variable pitch to stall angle; the control system will safely brake the turbine at high winds. As shown in **Figure 7.4**, the variation of rotor speed and pitch angle with different wind speeds shows the change of rotor speed and pitch angle with varying speeds of wind. The rotor speed at the cut-in speed (2 m/s) was approximately 32.98848 rpm. The pitch remained at 0° while the rising wind speed improved the rotor speed to 148.4482 rpm at the rated speed of 9.5 m/s. The active pitch control began at this point and regulated the rotor speed to 150 rpm until 25 m/s was reached.

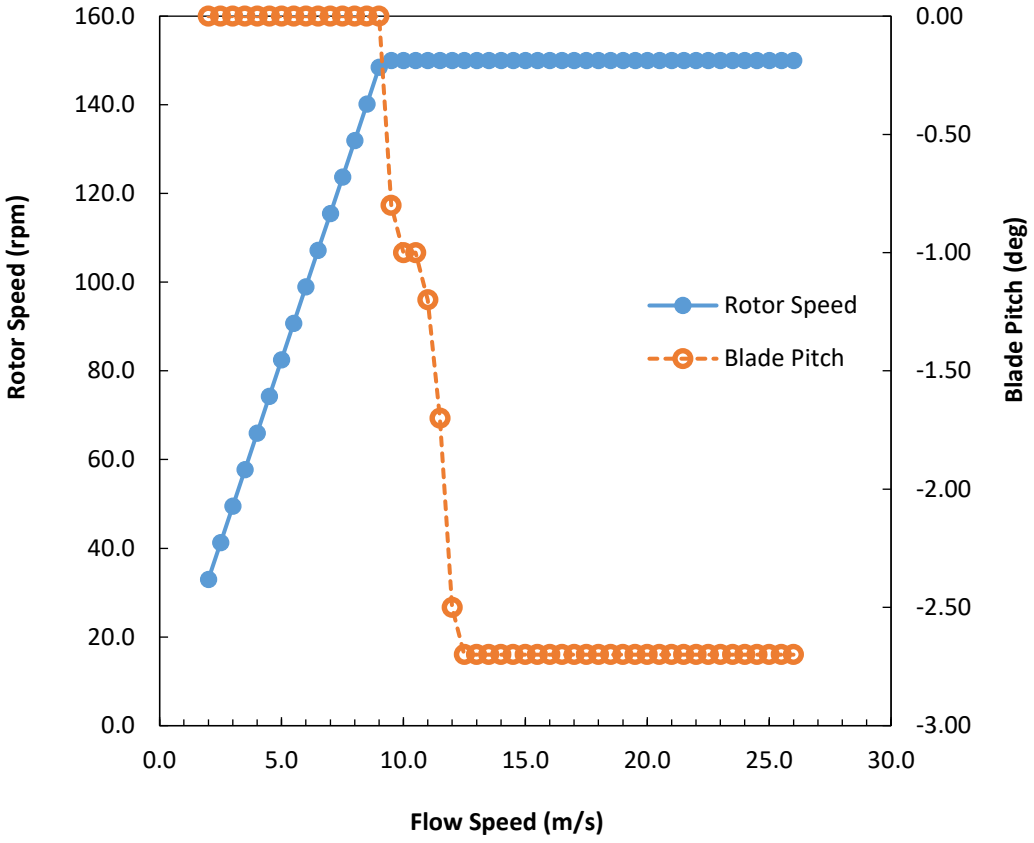

Figure 7.4. Change in rotor speed and pitch angle with wind speeds.

As seen below in **Figure 7.5**, the optimized rotor had a higher power output when compared to the reference rotor. According to the Weibull probability density function for the Deniliquin site, 2 m/s speed was a well-suited value for cut-in speed. For the optimized rotor, a cut-in speed produced only 0.201682 kW, which was approximately 1% of the rated power capacity. As the wind speed rose to 8 m/s, the turbine output was 18.37828 kW with a power coefficient of 0.433108. This output was approximately 76% of the turbine's rated capacity. At 9.5 m/s, the 20 kW rated power was attained. These differences between the power output of the tested and optimized rotor will be reflected in the AEP for the tested and optimized wind turbine. In this study, the AEP increased from 30,819.3 kW-hr/year in the original turbine to 33,614 kW-hr/year in the optimized wind turbine. Optimization improved the AEP by 9.068% when compared to the initial tested wind turbine design. The results obtained agree well with other published results [304, 305].

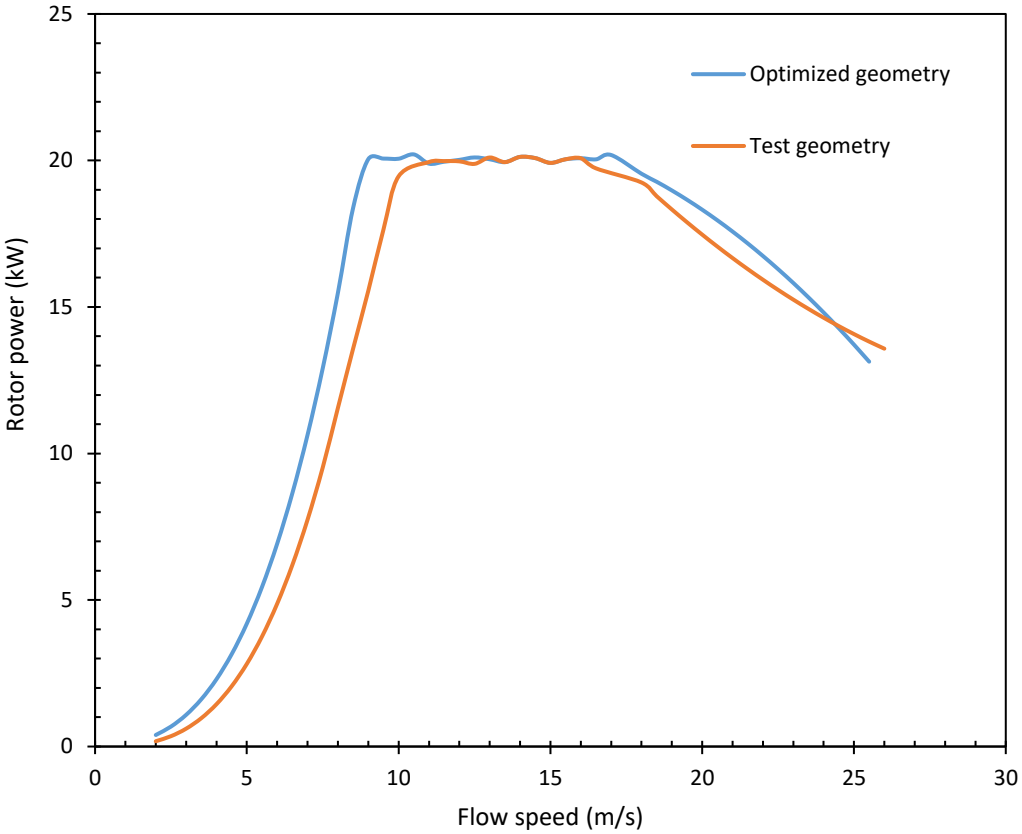

Figure 7.5. Power output of the reference tested rotor and optimized rotor.

7.3 Summary

In this chapter, a HARP_Opt code was used to optimize the wind turbine design using a genetic algorithm, aiming to maximize the AEP at the Deniliquin site. The major findings of this study are summarized as follows:

- The power coefficient had the highest value of 0.433108 until the rated wind speed (9.5 m/s) was achieved.
- The variation in rotor speed and pitch angle with different wind speeds shows the change of rotor speed and pitch angle with varying wind speeds. The pitch remained at 0° while the rising wind speed improved the rotor speed to 148.4482 rpm at the rated speed of 9.5 m/s.
- The shape of the rotor was modified by changing the chord and twist distribution along the blade, leading to a 9.1% improvement in AEP.

Chapter Eight

8 Conclusions and Future Work

8.1 Conclusions and Recommendations

Making good use of wind as a resource now plays an increasingly important role in the world's energy supply. The calculation of wind resources for a given location and the corresponding energy production is based on the wind potential assessment by anemometric measurement, followed by wind data processing to calculate the expected wind power yield for the proposed site. Wind speed distribution for a particular location determines the wind energy available and the performance of an energy conversion system. Once the probability distribution of wind speed is obtained, the wind energy potential can be determined accordingly. This research focuses on estimating wind energy potential using different probability density functions considering the prevailing environmental conditions in Australia. This study addresses the gap in our knowledge about combining wind turbine shape design and the available wind resources in Australia using updated and refined methodologies. This study aims to optimize a 20 kW wind turbine suitable for the natural environment in NSW, employing the horizontal axis rotor performance optimization (HARP_Opt) code to maximize AEP. This depends on the probability density function. This study presents and investigates an in-depth statistical analysis of wind energy's potential power source in NSW. Five sites have been selected to create practical insights into the wind potential in NSW. Specifically, Ballina, Bega, Deniliquin, Merriwa, and Yanco are the five locations evaluated here. The statistical analysis results show that the highest wind potential was at Deniliquin, with Weibull shape and scale parameters of 2.106 and 5.053 m/s, respectively.

Analysis of the aerodynamics performance of the wind turbine is used as a key improvement in the wind turbine's performance. This study concentrated on investigating the aerodynamics performance of the 20 kW wind turbine using CFD. Four turbulence models can improve our understanding of the aerodynamics flow around wind turbines when validating the aerodynamics performance of HAWT with experimental data. According to numerical results, it is possible to make the following conclusions:

1. A key important step for obtaining accurate aerodynamics of the wind turbine is choosing the most suitable computational domain and mesh. Although it is essential to compromise accuracy and computational time, it is crucial to achieving an independent mesh by monitoring the mechanical torque. For this reason, 3,559,082 mesh cells are deemed to constitute the most suitable mesh configuration in terms of computational time and efficiency.
2. The differences between four turbulence models under different wind speeds, which included stall conditions using blade pressure distribution along the blade, have been investigated. All RANS models excellently predict the flow around the wind turbine. Thus, RANS models agree well with the experimental data except for Realizable k-ε at the area where the flow is still attached. When increasing the wind speeds, the Transition SST model is capable of predicting the boundary layer for the flow region.
3. The angle of attack rose when increasing the wind speed and decreased with the radial position. The axial velocity varied along the blade, and it rose from the root to the tip. The tip section achieves the highest velocity is where the axial velocity increases at a uniform pattern along the blade.

The wind resource assessment is a critical stage in optimizing the wind turbine. Thus, in-depth statistical analysis of wind data is required to assess the wind profile from meteorological stations in Ballina, Merriwa, Deniliquin, Bega and Yanco. As such, there is a requirement to develop an efficient method to present the distribution of wind speeds. Probability density function describes the occurrence frequency of wind speed using common functions. The type of wind speed distribution function greatly influences the outcome of the available wind energy and wind turbine performance at a particular site. The major conclusions of the statistical analysis can be drawn as follows:

1. Some significant statistics values including yearly maximum, mean, median, standard deviation, skewness, and kurtosis, are studied. For the five sites the mean wind speed values vary from 2.81 to 4.53 m/s. The standard deviation has a value between 1.990 and 2.288.
2. The probability density function and cumulative distribution function's presentation compares the observed data and fitting functions using Rayleigh,

Weibull, gamma, and lognormal distribution that help explain which probability function provides the best fitting wind speed data. Weibull is the most accurate distribution according to R^2 and RMSE, thus RMSE variation is between 0.010771 and 0.027963.

This study used Weibull distribution to report on several numerical ways to estimate its function's scale and shape parameters. The comprehensive results of using the seven numerical methods for Weibull distribution are documented below in which the major conclusions can be made:

1. Graphical method, maximum likelihood method, energy pattern factor method, modified maximum likelihood method, equivalent energy method, moment method, and empirical method have been plotted using probability density function and cumulative distribution.

2. The equivalent energy method efficiently determines the shape and scale parameters to fit Weibull distribution curves for wind speed data in the Yanco, Merriwa, and Bega regions. At the same time, the modified maximum likelihood method fits the best to the measured wind speed data in Ballina and Deniliquin.

3. The most accurate model uses the scale and shape parameters for wind speed in Deniliquin. Thus, the value of shape and scale parameters for Deniliquin are 2.106 and 5.053 m/s, respectively, which is the best wind resource of all five sites.

4. The power density has a relationship that is proportional to the cube of the wind speed, which explains that the Bega area has a mean wind speed of 2.810 m/s and the lowest wind power density at 42.954 W/m^2 at 10 m elevation. In comparison, Deniliquin has a mean wind speed of 4.530 m/s and the highest power density of 108.618 W/m^2 at the same altitude.

The preceding results concerning CFD modelling, which presents and investigates the 20 kW wind turbine performance under different wind speed ranges, are validated against the NREL test. The place where the wind turbine would be installed plays a key role in the performance of wind turbine output. Thus, understanding the environmental conditions using assessment based on the wind data recorded at five meteorological stations in NSW, Australia, has been undertaken. The Weibull distribution reveals that the most accurate model determining the Weibull probability density function requires

defining the specific scale and shape parameters when using various estimation methods. Deniliquin has the best wind resource, so consequently, the optimization process will include scale and shape parameters as input parameters. The aerodynamics optimization tool for the wind turbine using HARP_Opt software was developed based on BEM theory and the genetic algorithm. The major outcomes of the optimization process are:

1. The optimization process modified the shape of the blade design using chord and twist distribution along the blade with the remaining airfoil shape (S809). The wind turbine geometry had a maximum value of 0.713679 m for chord length at 1.21 m. The maximum twist angle reached 19.9783° until the 0.22 span, then later reported as a spanwise of zero at 0.90 negative value applying a 1.00 span.

2. At 9.5 m/s, the 20 kW rated power was reached. The AEP increased from 30,819.3 kW-hr/year in the original turbine to 33,614 kW-hr/year in the optimized wind turbine. Optimization improved the AEP by 9.068% when compared to the initial tested wind turbine design.

This study recommended installing the small wind turbine's optimized design in the Deniliquin region. It has a mean wind speed of 4.530 m/s and the highest power density of 108.618 W/m^2 at the 10 m altitude. The wind direction is more evenly distributed than other sites, with most wind movement occurring in the sector between 210° and 300°. The power coefficient of the optimized rotor with wind speed is depicted in this study. The power coefficient had the highest value of 0.433108 until the rated wind speed (9.5 m/s). According to the Weibull probability density function for the Deniliquin site, 2 m/s speed was a well-suited value for cut-in speed. For the optimized rotor, a cut-in speed produced only 0.201682 kW, which was approximately 1% of the rated power capacity. As the wind speed rose to 8 m/s, the turbine output was 18.37828 kW with a power coefficient of 0.433108. This output was approximately 76% of the turbine's rated capacity. At 9.5 m/s, the 20 kW rated power was attained.

8.2 Suggestions for future work

Based on the current research and conclusions, a more detailed study may be needed in the following aspects. The CFD study was performed using one airfoil to validate the wind turbine model against experimental data. Thus, further airfoils could be used in the same wind turbine model to select optimum airfoil. This investigation may include different airfoils specifically designed for small turbines, for example, NREL S822 and

S823 blades. Due to the various airfoil geometries, the effect of roughness will vary between such airfoils. Thus, each airfoil may be tested with several roughness elements. Secondly, the wind data of the five locations' were used due to wind data availability in this research. Different areas should be investigated in further future analyses to cover more sites in NSW. Thirdly, a prototype study should be conducted in the Deniliquin area to provide experimental data under different environmental conditions, as these could affect the performance of a small wind turbine. Finally, this study focused on the aerodynamics optimization of wind turbines depending on wind data at Deniliquin. Future work will include structural, financial, and other parameters for the multi-optimization model based on this study.

References

[1] J. Conti, P. Holtberg, J. Diefenderfer, A. LaRose, J.T. Turnure, L. Westfall. International energy outlook 2016 with projections to 2040. USDOE Energy Information Administration (EIA), Washington, DC, United States (2016).

[2]. Energy Information Administration (EIA). International Energy Outlook 2013 (IEO2013) (2013).

[3] R.E. Sims, H.-H. Rogner, K. Gregory. Carbon emission and mitigation cost comparisons between fossil fuel, nuclear and renewable energy resources for electricity generation. Energy Policy. 31 (2003) 1315-26.

[4] World Wind Energy Association. Wind Power Capacity Worldwide Reaches 597 GW, 50,1 GW added in 2018. February 25, 2019.

[5] K. Kaygusuz. Energy for sustainable development: A case of developing countries. Renewable and Sustainable Energy Reviews. 16 (2012) 1116-26.

[6] Z.N. Ashrafi, M. Ghaderi, A. Sedaghat. Parametric study on off-design aerodynamic performance of a horizontal axis wind turbine blade and proposed pitch control. Energy Conversion and Management. 93 (2015) 349-56.

[7] World Wind Energy Association. World Wind Market has reached 486 GW from where 54 GW has been installed last year. (June 8, 2017).

[8] Global Wind Energy Council. GWEC forecasts 817 GW of wind power in 2021. Annual Market Update.

[9] World Wind Energy Association. Wind Power Capacity reaches 546 GW, 60 GW added in 2017. Press Releases, Statistics. (February 12, 2018).

[10] Department of the Environment and Energy (2018). Australian Energy Update 2018. (August 2018).

[11] T. Burton, N. Jenkins, D. Sharpe, E. Bossanyi. 1.1 Historical Development. Wind Energy Handbook (2nd Edition). John Wiley & Sons.

[12] M.M. Duquette, K.D. Visser. Numerical implications of solidity and blade number on rotor performance of horizontal-axis wind turbines. J Sol Energy Eng. 125 (2003) 425-32.

[13] International Renewable Energy Agency (IRENA). Renewable Power Generation Costs in 2019. (2019).

[14] International Renewable Energy Agency. The power to change: solar and wind cost reduction potential to 2025. (June 2016).

[15] Office of the National Wind Farm Commissioner. Office of the National Wind Farm Commissioner Annual Report to the Parliament of Australia. (2019).

[16] The NSW Department of Planning, and Environment NSW Electricity Strategy. “NSW

Electricity Strategy" (2019).
[17] The NSW Environment Protection Authority. "NSW State of the Environment 2018 –key findings". (April 2019).
[18] L. Goldstein. A proposal and a theoretical analysis of a novel concept of a tilted-axis wind turbine. Energy. 84 (2015) 247-54.
[19] A.C. Aranake, V.K. Lakshminarayan, K. Duraisamy. Computational analysis of shrouded wind turbine configurations using a 3-dimensional RANS solver. Renewable Energy. 75 (2015) 818-32.
[20] A. Tummala, R.K. Velamati, D.K. Sinha, V. Indraja, V.H. Krishna. A review on small scale wind turbines. Renewable and Sustainable Energy Reviews. 56 (2016) 1351-71.
[21] S. Rehman, M. Alam, L.M. Alhems, M.M. Rafique. Horizontal axis wind turbine blade design methodologies for efficiency enhancement—A review. Energies. 11 (2018) 506.
[22] R. Anant Kishore, S. Priya. Design and experimental verification of a high efficiency small wind energy portable turbine (SWEPT). Journal of Wind Engineering and Industrial Aerodynamics. 118 (2013) 12-9.
[23] C. Kress, N. Chokani, R.S. Abhari. Passive minimization of load fluctuations on downwind turbines. Renewable Energy. 89 (2016) 543-51.
[24] G. Bir, J. Jonkman. Aeroelastic Instabilities of Large Offshore and Onshore Wind Turbines. Journal of Physics: Conference Series. 75 (2007) 012069.
[25] W. Tong. Wind power generation and wind turbine design. WIT Press 2010.
[26] M.M.M. Saad, N. Asmuin. Comparison of horizontal axis wind turbines and vertical axis wind turbines. IOSR Journal of Engineering (IOSRJEN). 4 (2014) 27-30.
[27] R. McKenna, P. Ostman v.d. Leye, W. Fichtner. Key challenges and prospects for large wind turbines. Renewable and Sustainable Energy Reviews. 53 (2016) 1212-21.
[28] S. Heier. Grid integration of wind energy: onshore and offshore conversion systems. John Wiley & Sons 2014.
[29] I. Boldea, L.N. Tutelea. Electric Machines: Steady State, Transients, and Design with MATLAB®. CRC Press 2009.
[30] M. Orabi, F. El-Sousy, H. Godah, M. Youssef. High-performance induction generator-wind turbine connected to utility grid. INTELEC 2004 26th Annual International Telecommunications Energy Conference. IEEE2004. pp. 697-704.
[31] Wind energy engineering: a handbook for onshore and offshore wind turbines. Academic Press, London, 2017.
[32] J. Johansen, H.A. Madsen, M. Gaunaa, C. Bak, N.N. Sørensen. Design of a wind turbine rotor for maximum aerodynamic efficiency. Wind Energy: An International Journal for Progress and Applications in Wind Power Conversion Technology. 12 (2009) 261-73.
[33] R.N. Pinto, A. Afzal, L.V. D'Souza, Z. Ansari, A.M. Samee. Computational fluid dynamics

in turbomachinery: a review of state of the art. Archives of Computational Methods in Engineering. 24 (2017) 467-79.
[34] R. Mikkelsen, J.N. Sørensen, S. Øye, N. Troldborg. Analysis of power enhancement for a row of wind turbines using the actuator line technique. Journal of Physics: Conference Series. IOP Publishing 2007. p. 012044.
[35] M. Potsdam, D. Mavriplis. Unstructured mesh CFD aerodynamic analysis of the NREL Phase VI rotor. 47th AIAA Aerospace Sciences Meeting including The New Horizons Forum and Aerospace Exposition 2009. p. 1221.
[36] S. Wang, D.B. Ingham, L. Ma, M. Pourkashanian, Z. Tao. Turbulence modeling of deep dynamic stall at relatively low Reynolds number. Journal of Fluids and Structures. 33 (2012) 191-209.
[37] P. Zhou. CFD Simulation of the Wind Turbine Wake Under Different Atmospheric Boundary Conditions. Purdue University 2017.
[38] S. Schmidt, D. McIver, H.M. Blackburn, M. Rudman, G. Nathan. Spectral element based simulation of turbulent pipe flow. 14th Australasian Fluid Mechanics Conference 2001.
[39] H. Snel. Review of aerodynamics for wind turbines. Wind Energy: An International Journal for Progress and Applications in Wind Power Conversion Technology. 6 (2003) 203-11.
[40] A. Sargsyan. Simulation and modeling of flow field around a horizontal axis wind turbine (HAWT) using RANS method. Florida Atlantic University 2010.
[41] G. Alfonsi. Reynolds-Averaged Navier–Stokes Equations for Turbulence Modeling. Applied Mechanics Reviews. 62 (2009) 040802.
[42] B.E. Launder, B. Sharma. Application of the energy-dissipation model of turbulence to the calculation of flow near a spinning disc. Letters in Heat and Mass Transfer. 1 (1974) 131-7.
[43] E. Sagol, M. Reggio, A. Ilinca. Assessment of two-equation turbulence models and validation of the performance characteristics of an experimental wind turbine by CFD. ISRN Mechanical Engineering. 2012.
[44] T.-H. Shih, W.W. Liou, A. Shabbir, Z. Yang, J. Zhu. A new k-epsilon eddy viscosity model for high Reynolds number turbulent flows. Computer and Fluids. 24 (1994) 227-238.
[45] V. Yakhot, S. Orszag, S. Thangam, T. Gatski, C. Speziale. Development of turbulence models for shear flows by a double expansion technique. Physics of Fluids A: Fluid Dynamics. 4 (1992) 1510-20.
[46] V. Yakhot, S.A. Orszag. Renormalization group analysis of turbulence. I. Basic theory. Journal of Scientific Computing. 1 (1986) 3-51.
[47] M. Mohamed. Performance investigation of H-rotor Darrieus turbine with new airfoil shapes. Energy. 47 (2012) 522-30.
[48] A. Mielke, J. Naumann. On the existence of global-in-time weak solutions and scaling laws for Kolmogorov's two-equation model of turbulence. arXiv preprint arXiv:180102039. (2018).

[49] D.C. Wilcox. Formulation of the kw turbulence model revisited. AIAA Journal. 46 (2008) 2823-38.
[50] F.R. Menter. Review of the shear-stress transport turbulence model experience from an industrial perspective. International Journal of Computational Fluid Dynamics. 23 (2009) 305-16.
[51] P.E. Smirnov, F.R. Menter. Sensitization of the SST turbulence model to rotation and curvature by applying the Spalart–Shur correction term. Journal of Turbomachinery. 131 (2009) 041010.
[52] R.B. Langtry, F.R. Menter. Correlation-based transition modeling for unstructured parallelized computational fluid dynamics codes. AIAA Journal. 47 (2009) 2894-906.
[53] A. Bouhelal, A. Smaili, O. Guerri, C. Masson. Numerical investigation of turbulent flow around a recent horizontal axis wind Turbine using low and high Reynolds models. Journal of Applied Fluid Mechanics. 11 (2018) 151-64.
[54] E. Fares, W. Schröder. A general one-equation turbulence model for free shear and wall-bounded flows. Flow, Turbulence and Combustion. 73 (2005) 187-215.
[55] P. Spalart, S. Allmaras. A one-equation turbulence model for aerodynamic flows. 30th Aerospace Sciences Meeting and Exhibit 1992. p. 439.
[56] T.B. Gatski, C.L. Rumsey, R. Manceau. Current trends in modelling research for turbulent aerodynamic flows. Philosophical Transactions of the Royal Society A: Mathematical, Physical and Engineering Sciences. 365 (2007) 2389-418.
[57] P.R. Spalart, M. Shur. On the sensitization of turbulence models to rotation and curvature. Aerospace Science and Technology. 1 (1997) 297-302.
[58] M. Rahman, T. Siikonen, R. Agarwal. Improved low-Reynolds-number one-equation turbulence model. AIAA Journal. 49 (2011) 735-47.
[59] Large eddy simulation of complex engineering and geophysical flows. Cambridge University Press, Cambridge [England] 1993.
[60] A. Jimenez, A. Crespo, E. Migoya, J. García. Advances in large-eddy simulation of a wind turbine wake. Journal of Physics: Conference Series 2007. p. 012041.
[61] Y. Zhiyin. Large-eddy simulation: Past, present and the future. Chinese Journal of Aeronautics. 28 (2015) 11-24.
[62] J. Thé, H. Yu. A critical review on the simulations of wind turbine aerodynamics focusing on hybrid RANS-LES methods. Energy. 138 (2017) 257-89.
[63] P.R. Spalart. Detached-eddy simulation. Annual Review of Fluid Mechanics. 41 (2009) 181-202.
[64] P.R. Spalart, S. Deck, M.L. Shur, K.D. Squires, M.K. Strelets, A. Travin. A new version of detached-eddy simulation, resistant to ambiguous grid densities. Theoretical and Computational Fluid Dynamics. 20 (2006) 181.

[65] O. Verhoeven. Trailing Edge Noise Simulations: Using IDDES in OpenFOAM. Masters Thesis, Delft University of Technology (2011).
[66] A. Travin, M. Shur, M. Strelets, P. Spalart. Detached-eddy simulations past a circular cylinder. Flow, Turbulence and Combustion. 63 (2000) 293-313.
[67] Y. Li, K.-J. Paik, T. Xing, P.M. Carrica. Dynamic overset CFD simulations of wind turbine aerodynamics. Renewable Energy. 37 (2012) 285-98.
[68] A. El Kasmi, C. Masson. An extended k–ε model for turbulent flow through horizontal-axis wind turbines. Journal of Wind Engineering and Industrial Aerodynamics. 96 (2008) 103-22.
[69] A.M. AbdelSalam, V. Ramalingam. Wake prediction of horizontal-axis wind turbine using full-rotor modeling. Journal of Wind Engineering and Industrial Aerodynamics. 124 (2014) 7-19.
[70] S.A. Abdulqadir, H. Iacovides, A. Nasser. The physical modelling and aerodynamics of turbulent flows around horizontal axis wind turbines. Energy. 119 (2017) 767-99.
[71] A.M. Abdelsalam, K. Boopathi, S. Gomathinayagam, S.H.K. Kumar, V. Ramalingam. Experimental and numerical studies on the wake behavior of a horizontal axis wind turbine. Journal of Wind Engineering and Industrial Aerodynamics. 128 (2014) 54-65.
[72] R. Lanzafame, S. Mauro, M. Messina. Wind turbine CFD modeling using a correlation-based transitional model. Renewable Energy. 52 (2013) 31-9.
[73] D. Rajvanshi, R. Baig, R. Pandya, K. Nikam. Wind turbine blade aerodynamics and performance analysis using numerical simulations. Proceedings of the 11th Asian International Conference on Fluid Machinery, Chennai, India 2011. pp. 21-3.
[74] M. Moshfeghi, Y.J. Song, Y.H. Xie. Effects of near-wall grid spacing on SST-K-ω model using NREL Phase VI horizontal axis wind turbine. Journal of Wind Engineering and Industrial Aerodynamics. 107 (2012) 94-105.
[75] M.S. Siddiqui, A. Rasheed, M. Tabib, T. Kvamsdal. Numerical analysis of NREL 5MW wind turbine: A study towards a better understanding of wake characteristic and torque generation mechanism. Journal of Physics: Conference Series 2016. p. 032059.
[76] J.Y. You, D.O. Yu, O.J. Kwon. Effect of turbulence models on predicting HAWT rotor blade performances. Journal of Mechanical Science and Technology. 27 (2013) 3703-11.
[77] B. Plaza, R. Bardera, S. Visiedo. Comparison of BEM and CFD results for MEXICO rotor aerodynamics. Journal of Wind Engineering and Industrial Aerodynamics. 145 (2015) 115-22.
[78] N.N. Sørensen, J. Michelsen, S. Schreck. Navier–Stokes predictions of the NREL phase VI rotor in the NASA Ames 80 ft× 120 ft wind tunnel. Wind Energy: An International Journal for Progress and Applications in Wind Power Conversion Technology. 5 (2002) 151-69.
[79] J. Johansen, N.N. Sørensen, J. Michelsen, S. Schreck. Detached-eddy simulation of flow around the NREL Phase VI blade. Wind Energy: An International Journal for Progress and Applications in Wind Power Conversion Technology. 5 (2002) 185-97.

[80] E.P.N. Duque, M.D. Burklund, W. Johnson. Navier-Stokes and Comprehensive Analysis Performance Predictions of the NREL Phase VI Experiment. ASME 2003 Wind Energy Symposium 2003. pp. 43-61.
[81] J. Johansen, N.N. Sørensen. Aerofoil characteristics from 3D CFD rotor computations. Wind Energy: An International Journal for Progress and Applications in Wind Power Conversion Technology. 7 (2004) 283-94.
[82] N. Mandas, F. Cambuli, C.E. Carcangiu. Numerical prediction of horizontal axis wind turbine flow. University of Caglairi, EWEC. (2006).
[83] N. Sezer-Uzol, L. Long. 3-D time-accurate CFD simulations of wind turbine rotor flow fields. 44th AIAA Aerospace Sciences Meeting and Exhibit 2006. p. 394.
[84] D. Hu, O. Hua, Z. Du. A study on stall-delay for horizontal axis wind turbine. Renewable Energy. 31 (2006) 821-36.
[85] D. Simms, M. Robinson, M. Hand, L. Fingersh. Characterization and comparison of baseline aerodynamic performance of optimally twisted versus non-twisted HAWT blades. American Society of Mechanical Engineers, New York 1996.
[86] S. Wußow, L. Sitzki, T. Hahm. 3D-simulation of the turbulent wake behind a wind turbine. Journal of Physics: Conference Series. IOP Publishing 2007. p. 012033.
[87] C. Thumthae, T. Chitsomboon. Optimal angle of attack for untwisted blade wind turbine. Renewable Energy. 34 (2009) 1279-84.
[88] D.A. Simms, M. Hand, L. Fingersh, D. Jager. Unsteady aerodynamics experiment phases II-IV test configurations and available data campaigns. National Renewable Energy Lab., Golden, CO (US) 1999.
[89] T.M. Fletcher, R. Brown, D.H. Kim, O.J. Kwon. Predicting wind turbine blade loads using vorticity transport and RANS methodologies. European Wind Energy Conference and Exhibition, EWEC 20092009.
[90] N.N. Sørensen. CFD modelling of laminar-turbulent transition for airfoils and rotors using the γ− model. Wind Energy: An International Journal for Progress and Applications in Wind Power Conversion Technology. 12 (2009) 715-33.
[91] S. Gómez-Iradi, R. Steijl, G. Barakos. Development and validation of a CFD technique for the aerodynamic analysis of HAWT. Journal of Solar Energy Engineering. 131 (2009) 031009.
[92] N. Tachos, A. Filios, D. Margaris. A comparative numerical study of four turbulence models for the prediction of horizontal axis wind turbine flow. Proceedings of the Institution of Mechanical Engineers, Part C: Journal of Mechanical Engineering Science. 224 (2010) 1973-9.
[93] P. Fu, M. Farzaneh. A CFD approach for modeling the rime-ice accretion process on a horizontal-axis wind turbine. Journal of Wind Engineering and Industrial Aerodynamics. 98 (2010) 181-8.
[94] A. Bechmann, N.N. Sørensen, F. Zahle. CFD simulations of the MEXICO rotor. Wind

Energy. 14 (2011) 677-89.
[95] M.A. Elfarra, N. Sezer-Uzol, I.S. Akmandor. NREL VI rotor blade: numerical investigation and winglet design and optimization using CFD. Wind Energy. 17 (2014) 605-26.
[96] Y. Song, J.B. Perot. CFD simulation of the NREL Phase VI rotor. Wind Engineering. 39 (2015) 299-309.
[97] S. Derakhshan, A. Tavaziani. Study of wind turbine aerodynamic performance using numerical methods. Journal of Clean Energy Technologies. 3 (2015) 83-90.
[98] N.N. Sørensen, F. Zahle, K. Boorsma, G. Schepers. CFD computations of the second round of MEXICO rotor measurements. Journal of Physics: Conference Series. IOP Publishing 2016. p. 022054.
[99] L. Wang, R. Quant, A. Kolios. Fluid structure interaction modelling of horizontal-axis wind turbine blades based on CFD and FEA. Journal of Wind Engineering and Industrial Aerodynamics. 158 (2016) 11-25.
[100] L. Menegozzo, A. Dal Monte, E. Benini, A. Benato. Small wind turbines: A numerical study for aerodynamic performance assessment under gust conditions. Renewable Energy. 121 (2018) 123-32.
[101] D. Infield, L. Freris. Renewable energy in power systems. John Wiley & Sons 2020.
[102] G. Li, J. Shi. Application of Bayesian model averaging in modeling long-term wind speed distributions. Renewable Energy. 35 (2010) 1192-202.
[103] H. Bagiorgas, M. Assimakopoulos, D. Theoharopoulos, D. Matthopoulos, G. Mihalakakou. Electricity generation using wind energy conversion systems in the area of Western Greece. Energy Conversion and Management. 48 (2007) 1640-55.
[104] M. Gökçek, A. Bayülken, Ş. Bekdemir. Investigation of wind characteristics and wind energy potential in Kirklareli, Turkey. Renewable Energy. 32 (2007) 1739-52.
[105] A.A. Shata, R. Hanitsch. Evaluation of wind energy potential and electricity generation on the coast of Mediterranean Sea in Egypt. Renewable Energy. 31 (2006) 1183-202.
[106] M. Stevens, P. Smulders. The estimation of the parameters of the Weibull wind speed distribution for wind energy utilization purposes. Wind Engineering. (1979) 132-45.
[107] Z. Shu, Q. Li, P. Chan. Statistical analysis of wind characteristics and wind energy potential in Hong Kong. Energy Conversion and Management. 101 (2015) 644-57.
[108] M. Irwanto, N. Gomesh, M. Mamat, Y. Yusoff. Assessment of wind power generation potential in Perlis, Malaysia. Renewable and Sustainable Energy Reviews. 38 (2014) 296-308.
[109] Q. Hernandez-Escobedo, R. Saldaña-Flores, E. Rodríguez-García, F. Manzano-Agugliaro. Wind energy resource in Northern Mexico. Renewable and Sustainable Energy Reviews. 32 (2014) 890-914.
[110] A.S. Ahmed. Wind energy characteristics and wind park installation in Shark El-Ouinat, Egypt. Renewable and Sustainable Energy Reviews. 82 (2018) 734-42.

[111] I. Janajreh, L. Su, F. Alan. Wind energy assessment: Masdar City case study. Renewable Energy. 52 (2013) 8-15.
[112] A. Keyhani, M. Ghasemi-Varnamkhasti, M. Khanali, R. Abbaszadeh. An assessment of wind energy potential as a power generation source in the capital of Iran, Tehran. Energy. 35 (2010) 188-201.
[113] M. Islam, R. Saidur, N. Rahim. Assessment of wind energy potentiality at Kudat and Labuan, Malaysia using Weibull distribution function. Energy. 36 (2011) 985-92.
[114] A.N. Celik. A statistical analysis of wind power density based on the Weibull and Rayleigh models at the southern region of Turkey. Renewable Energy. 29 (2004) 593-604.
[115] D. Mentis, S. Hermann, M. Howells, M. Welsch, S.H. Siyal. Assessing the technical wind energy potential in Africa a GIS-based approach. Renewable Energy. 83 (2015) 110-25.
[116] C. Ozay, M.S. Celiktas. Statistical analysis of wind speed using two-parameter Weibull distribution in Alaçatı region. Energy Conversion and Management. 121 (2016) 49-54.
[117] Y. Oner, S. Ozcira, N. Bekiroglu, I. Senol. A comparative analysis of wind power density prediction methods for Çanakkale, Intepe region, Turkey. Renewable and Sustainable Energy Reviews. 23 (2013) 491-502.
[118] P.A.C. Rocha, R.C. de Sousa, C.F. de Andrade, M.E.V. da Silva. Comparison of seven numerical methods for determining Weibull parameters for wind energy generation in the northeast region of Brazil. Applied Energy. 89 (2012) 395-400.
[119] D. Solyali, M. Altunç, S. Tolun, Z. Aslan. Wind resource assessment of Northern Cyprus. Renewable and Sustainable Energy Reviews. 55 (2016) 180-7.
[120] A. Garcia, J. Torres, E. Prieto, A. De Francisco. Fitting wind speed distributions: a case study. Solar Energy. 62 (1998) 139-44.
[121] R. Kollu, S.R. Rayapudi, S. Narasimham, K.M. Pakkurthi. Mixture probability distribution functions to model wind speed distributions. International Journal of Energy and Environmental Engineering. 3 (2012) 27.
[122] J.A. Carta, P. Ramírez, S. Velázquez. A review of wind speed probability distributions used in wind energy analysis: Case studies in the Canary Islands. Renewable and Sustainable Energy Reviews. 13 (2009) 933-55.
[123] O. Alavi, A. Sedaghat, A. Mostafaeipour. Sensitivity analysis of different wind speed distribution models with actual and truncated wind data: a case study for Kerman, Iran. Energy Conversion and Management. 120 (2016) 51-61.
[124] N. Masseran, A. Razali, K. Ibrahim. An analysis of wind power density derived from several wind speed density functions: The regional assessment on wind power in Malaysia. Renewable and Sustainable Energy Reviews. 16 (2012) 6476-87.
[125] J. Zhou, E. Erdem, G. Li, J. Shi. Comprehensive evaluation of wind speed distribution models: A case study for North Dakota sites. Energy Conversion and Management. 51 (2010)

1449-58.
[126] Z.O. Olaofe, K.A. Folly. Wind energy analysis based on turbine and developed site power curves: A case-study of Darling City. Renewable Energy. 53 (2013) 306-18.
[127] B. Safari. Modeling wind speed and wind power distributions in Rwanda. Renewable and Sustainable Energy Reviews. 15 (2011) 925-35.
[128] V.L. Brano, A. Orioli, G. Ciulla, S. Culotta. Quality of wind speed fitting distributions for the urban area of Palermo, Italy. Renewable Energy. 36 (2011) 1026-39.
[129] K. Tar. Some statistical characteristics of monthly average wind speed at various heights. Renewable and Sustainable Energy Reviews. 12 (2008) 1712-24.
[130] V.T. Morgan. Statistical distributions of wind parameters at Sydney, Australia. Renewable Energy. 6 (1995) 39-47.
[131] Y.A. Katsigiannis, G.S. Stavrakakis. Estimation of wind energy production in various sites in Australia for different wind turbine classes: A comparative technical and economic assessment. Renewable Energy. 67 (2014) 230-6.
[132] D. Maunsell, T. Lyons, J. Whale. Wind resource assessment of a site in Western Australia. (2004).
[133] A.A. Prasad, R.A. Taylor, M. Kay. Assessment of solar and wind resource synergy in Australia. Applied Energy. 190 (2017) 354-67.
[134] L. Mishnaevsky Jr, O. Favorsky. Composite materials in wind energy technology. Thermal to Mechanical Energy Conversion: Engines and Requirements, EOLSS Publishers: Oxford, UK. (2011).
[135] T. Ashwill. Materials and innovations for large blade structures: research opportunities in wind energy technology. 50th AIAA/ASME/ASCE/AHS/ASC Structures, Structural Dynamics, and Materials Conference.
[136] P.-C. Ma, Y. Zhang. Perspectives of carbon nanotubes/polymer nanocomposites for wind blade materials. Renewable and Sustainable Energy Reviews. 30 (2014) 651-60.
[137] C.-H. Ong, S.W. Tsai. The use of carbon fibers in wind turbine blade design: a SERI-8 blade example. Sandia National Labs., Albuquerque, NM (US); Sandia National Labs 2000.
[138] L. Mishnaevsky, K. Branner, H.N. Petersen, J. Beauson, M. McGugan, B.F. Sørensen. Materials for wind turbine blades: an overview. Materials. 10 (2017) 1285.
[139] R.W. Thresher, D.M. Dodge. Trends in the evolution of wind turbine generator configurations and systems. Wind Energy: An International Journal for Progress and Applications in Wind Power Conversion Technology. 1 (1998) 70-86.
[140] G. Sieros, P. Chaviaropoulos, J.D. Sørensen, B.H. Bulder, P. Jamieson. Upscaling wind turbines: theoretical and practical aspects and their impact on the cost of energy. Wind Energy. 15 (2012) 3-17.
[141] H. Perez-Blanco. Optimization of Wind energy capture Using BET. Turbo Expo: Power

for Land, Sea, and Air 2011. pp. 879-87.
[142] V. Okulov, R. Mikkelsen, I. Litvinov, I. Naumov. Efficiency of operation of wind turbine rotors optimized by the Glauert and Betz methods. Technical Physics. 60 (2015) 1632-6.
[143] N.A. Satwika, Sarwono, R. Hantoro. Investigation Flow on Horizontal Axis Wind Turbine with Betz Chord Distribution, Twist, and Winglet. 2018 4th International Conference on Science and Technology (ICST) 2018. pp. 1-6.
[144] J.-J. Chattot. Optimization of wind turbines using helicoidal vortex model. Journal of Solar Energy Engineering 125 (2003) 418-24.
[145] R. Gasch, J. Twele. Wind Power Plants. Fundamentals, Design, Construction and Operation. Solarpraxis. Berlin, James & James Publ 2002.
[146] M. Jureczko, M. Pawlak, A. Mężyk. Optimisation of wind turbine blades. Journal of Materials Processing Technology. 167 (2005) 463-71.
[147] C. Kong, J. Bang, Y. Sugiyama. Structural investigation of composite wind turbine blade considering various load cases and fatigue life. Energy. 30 (2005) 2101-14.
[148] N. Karthikeyan, K.K. Murugavel, S.A. Kumar, S. Rajakumar. Review of aerodynamic developments on small horizontal axis wind turbine blade. Renewable and Sustainable Energy Reviews. 42 (2015) 801-22.
[149] K. Ameku, B.M. Nagai, J.N. Roy. Design of a 3 kW wind turbine generator with thin airfoil blades. Experimental Thermal and Fluid Science. 32 (2008) 1723-30.
[150] A. Vardar, I. Alibas. Research on wind turbine rotor models using NACA profiles. Renewable Energy. 33 (2008) 1721-32.
[151] D. Leung, Y. Deng, M. Leung. Design optimization of a cost-effective micro wind turbine. Proceedings of the World Congress on Engineering 2010. pp. 2078-0958.
[152] H. Hirahara, M.Z. Hossain, M. Kawahashi, Y. Nonomura. Testing basic performance of a very small wind turbine designed for multi-purposes. Renewable Energy. 30 (2005) 1279-97.
[153] M. Tahani, G. Kavari, M. Masdari, M. Mirhosseini. Aerodynamic design of horizontal axis wind turbine with innovative local linearization of chord and twist distributions. Energy. 131 (2017) 78-91.
[154] T.-P. Chang, F.-J. Liu, H.-H. Ko, S.-P. Cheng, L.-C. Sun, S.-C. Kuo. Comparative analysis on power curve models of wind turbine generator in estimating capacity factor. Energy. 73 (2014) 88-95.
[155] R.A. Kishore, S. Priya. Design and experimental verification of a high efficiency small wind energy portable turbine (SWEPT). Journal of Wind Engineering and Industrial Aerodynamics. 118 (2013) 12-9.
[156] R.K. Singh, M.R. Ahmed, M.A. Zullah, Y.-H. Lee. Design of a low Reynolds number airfoil for small horizontal axis wind turbines. Renewable Energy. 42 (2012) 66-76.
[157] J. Bukala, K. Damaziak, K. Kroszczynski, M. Krzeszowiec, J. Malachowski. Investigation

of parameters influencing the efficiency of small wind turbines. Journal of Wind Engineering and Industrial Aerodynamics. 146 (2015) 29-38.
[158] M. Ragheb, A.M. Ragheb. Wind turbines theory-the betz equation and optimal rotor tip speed ratio. Fundamental and Advanced Topics in Wind Power. 1 (2011) 19-38.
[159] R. Gasch, J. Twele. Wind power plants: fundamentals, design, construction and operation. Springer Science & Business Media 2011.
[160] S. Oerlemans, P. Sijtsma, B.M. López. Location and quantification of noise sources on a wind turbine. Journal of Sound and Vibration. 299 (2007) 869-83.
[161] T. Burton, N. Jenkins, D. Sharpe, E. Bossanyi. Wind Energy Handbook (2nd Edition). John Wiley & Sons.
[162] P.J. Schubel, R.J. Crossley. Wind turbine blade design. Energies. 5 (2012) 3425-49.
[163] P. Devinant, T. Laverne, J. Hureau. Experimental study of wind-turbine airfoil aerodynamics in high turbulence. Journal of Wind Engineering and Industrial Aerodynamics. 90 (2002) 689-707.
[164] A. Sedaghat, M. Mirhosseini. Aerodynamic design of a 300 kW horizontal axis wind turbine for province of Semnan. Energy Conversion and Management. 63 (2012) 87-94.
[165] T.M. Letcher. 9.1 Introduction. Wind Energy Engineering - A Handbook for Onshore and Offshore Wind Turbines. Elsevier.
[166] E. Hau. Wind turbines: fundamentals, technologies, application, economics. Springer Science & Business Media 2013.
[167] W. Timmer. An overview of NACA 6-digit airfoil series characteristics with reference to airfoils for large wind turbine blades. 47th AIAA Aerospace Sciences Meeting including the New Horizons Forum and Aerospace Exposition 2009. p. 268.
[168] F. Bertagnolio, N.N. Sørensen, J. Johansen, P. Fuglsang. Wind turbine airfoil catalogue. Denmark. Forskningscenter RISØ. RISØ -R, No. 1280 (EN). (2001).
[169] M.L. Nelson. A digital library for the National Advisory Committee for Aeronautics. NASA Technical Memorandum: 209127 (1999).
[170] M.J. Lawson, Y. Li, D.C. Sale. Development and verification of a computational fluid dynamics model of a horizontal-axis tidal current turbine. ASME 2011 30th International Conference on Ocean, Offshore and Arctic Engineering. American Society of Mechanical Engineers 2011. pp. 711-20.
[171] M. Yılmaz, H. Köten, E. Çetinkaya, Z. Coşar. A comparative CFD analysis of NACA0012 and NACA4412 airfoils. Journal of Energy Systems. 2 (2018) 145-59.
[172] K.S. Dahl, P. Fuglsang. Design of the wind turbine airfoil family RISØ-A-XX. U.S. Department of Energy Office of Scientific and Technical Information 1998.
[173] P. Fuglsang, C. Bak. Development of the Risø wind turbine airfoils. Wind Energy: An International Journal for Progress and Applications in Wind Power Conversion Technology. 7

(2004) 145-62.
[174] W. Timmer, R. Van Rooij. Summary of the Delft University wind turbine dedicated airfoils. Journal of Solar Energy Engineering. 125 (2003) 488-96.
[175] M.R. Ahmed. Blade sections for wind turbine and tidal current turbine applications–current status and future challenges. International Journal of Energy Research. 36 (2012) 829-44.
[176] J.L. Tangler, D.M. Somers. NREL airfoil families for HAWTs. National Renewable Energy Lab., Golden, CO (United States) 1995.
[177] D.M. Somers. S833, S834, and S835 Airfoils: November 2001--November 2002. National Renewable Energy Lab. (NREL), Golden, CO (United States) 2005.
[178] D.M. Somers, J.L. Tangler. Wind tunnel test of the S814 thick root airfoil. Journal of Solar Energy Engineering. 118 (1996) 217-221.
[179] K. Maalawi, M. Badr. A practical approach for selecting optimum wind rotors. Renewable Energy. 28 (2003) 803-22.
[180] R. Van Rooij, W. Timmer. Roughness sensitivity considerations for thick rotor blade airfoils. Journal of Solar Energy Engineering. 125 (2003) 468-78.
[181] P. Fuglsang, I. Antoniou, K.S. Dahl, H.A. Madsen. Wind tunnel tests of the FFA-W3-241, FFA-W3-301 and NACA 63-430 airfoils. RISO-REPORTS-RISO R. (1998).
[182] R. Lanzafame, M. Messina. Design and performance of a double-pitch wind turbine with non-twisted blades. Renewable Energy. 34 (2009) 1413-20.
[183] J. Laursen, P. Enevoldsen, S. Hjort. 3D CFD rotor computations of a multi-megawatt HAWT rotor. Proceedings of the European Wind Energy Conference, Milan, Italy 2007.
[184] J.-H. Jeong, S.-H. Kim. CFD investigation on the flatback airfoil effect of 10 MW wind turbine blade. Journal of Mechanical Science and Technology. 32 (2018) 2089-97.
[185] M.R. Ahmed, S. Narayan, M.A. Zullah, Y.-H. Lee. Experimental and numerical studies on a low Reynolds number airfoil for wind turbine blades. Journal of Fluid Science and Technology. 6 (2011) 357-71.
[186] M.A. Sayed, H.A. Kandil, A. Shaltot. Aerodynamic analysis of different wind-turbine-blade profiles using finite-volume method. Energy Conversion and Management. 64 (2012) 541-50.
[187] C. Sicot, P. Devinant, T. Laverne, S. Loyer, J. Hureau. Experimental study of the effect of turbulence on horizontal axis wind turbine aerodynamics. Wind Energy. 9 (2006) 361-70.
[188] J. Delnero, J. Marañon di Leo, F. Bacchi, J. Colman, U. Boldes. Experimental determination of the influence of turbulent scale on the lift and drag coefficients of low Reynolds number airfoils. Latin American Applied Research. 35 (2005) 183-8.
[189] K.E. Swalwell, J. Sheridan, W. Melbourne. The effect of turbulence intensity on stall of the NACA 0021 aerofoil. 14th Australasian Fluid Mechanics Conference 2001. pp. 10-4.
[190] J.W. Larsen, S.R. Nielsen, S. Krenk. Dynamic stall model for wind turbine airfoils. Journal

of Fluids and Structures. 23 (2007) 959-82.
[191] J.A. Hoffmann. Effects of freestream turbulence on the performance characteristics of an airfoil. AIAA Journal. 29 (1991) 1353-4.
[192] Y. Kamada, T. Maeda, J. Murata, T. Toki, A. Tobuchi. Effects of turbulence intensity on dynamic characteristics of wind turbine airfoil. Journal of Fluid Science and Technology. 6 (2011) 333-41.
[193] J.F. Manwell, J.G. McGowan, A.L. Rogers. Wind energy explained: theory, design and application. John Wiley & Sons 2010.
[194] K. Gharali, D.A. Johnson. Numerical modeling of an S809 airfoil under dynamic stall, erosion and high reduced frequencies. Applied Energy. 93 (2012) 45-52.
[195] M.O. Hansen. Aerodynamics of wind turbines. Routledge 2015.
[196] C.-J. Bai, W.-C. Wang. Review of computational and experimental approaches to analysis of aerodynamic performance in horizontal-axis wind turbines (HAWTs). Renewable and Sustainable Energy Reviews. 63 (2016) 506-19.
[197] S. Schreck, M. Robinson, M. Hand, D. Simms. HAWT dynamic stall response asymmetries under yawed flow conditions. Wind Energy: An International Journal for Progress and Applications in Wind Power Conversion Technology. 3 (2000) 215-32.
[198] M.-H. Chiang. A novel pitch control system for a wind turbine driven by a variable-speed pump-controlled hydraulic servo system. Mechatronics. 21 (2011) 753-61.
[199] A.P. Deshmukh, J.T. Allison. Multidisciplinary dynamic optimization of horizontal axis wind turbine design. Structural and Multidisciplinary Optimization. 53 (2016) 15-27.
[200] I. Munteanu. Optimal Control of Wind Energy Systems Towards a Global Approach. 1st ed. 2008. Springer London, 2008.
[201] N. Wang, K.E. Johnson, A.D. Wright. Comparison of strategies for enhancing energy capture and reducing loads using LIDAR and feedforward control. IEEE Transactions on Control Systems Technology. 21 (2013) 1129-42.
[202] T.K. Barlas, G.A. van Kuik. Review of state of the art in smart rotor control research for wind turbines. Progress in Aerospace Sciences. 46 (2010) 1-27.
[203] E. Bossanyi, B. Savini, M. Iribas, M. Hau, B. Fischer, D. Schlipf, et al. Advanced controller research for multi-MW wind turbines in the UPWIND project. Wind Energy. 15 (2012) 119-45.
[204] M. Soltani, R. Wisniewski, P. Brath, S. Boyd. Load reduction of wind turbines using receding horizon control. 2011 IEEE International Conference on Control Applications (CCA). IEEE 2011. pp. 852-7.
[205] E. Alpman. Effect of selection of design parameters on the optimization of a horizontal axis wind turbine via genetic algorithm. Journal of Physics: Conference Series. IOP Publishing 2014. p. 012044.
[206] A.S. Darwish, S. Shaaban, E. Marsillac, N.M. Mahmood. A methodology for improving

wind energy production in low wind speed regions, with a case study application in Iraq. Computers & Industrial Engineering. 127 (2019) 89-102.
[207] X. Liu, L. Wang, X. Tang. Optimized linearization of chord and twist angle profiles for fixed-pitch fixed-speed wind turbine blades. Renewable Energy. 57 (2013) 111-9.
[208] A. Al-Abadi, O. Ertunç, F. Beyer, A. Delgado. Torque-matched aerodynamic shape optimization of HAWT rotor. Optimization. 3 (2014) 5-6.
[209] S. Derakhshan, A. Tavaziani, N. Kasaeian. Numerical shape optimization of a wind turbine blades using artificial bee colony algorithm. Journal of Energy Resources Technology. 137 (2015) 051210.
[210] M. Hand, D. Simms, L. Fingersh, D. Jager, J. Cotrell, S. Schreck, et al. Unsteady aerodynamics experiment phase VI: wind tunnel test configurations and available data campaigns. National Renewable Energy Lab., Golden, CO (US) 2001.
[211] P. Giguere, M. Selig. Design of a tapered and twisted blade for the NREL combined experiment rotor. National Renewable Energy Lab., Golden, CO (US) 1999.
[212] D.C. Planchard, M.P. Planchard. SolidWorks 2013 Tutorial. SDC Publications2013.
[213] D.M. Somers. Design and experimental results for the S809 airfoil. National Renewable Energy Lab., Golden, CO (United States) 1997.
[214] P.I. Muiruri, O.S. Motsamai. Three Dimensional CFD Simulations of A Wind Turbine Blade Section; Validation. Journal of Engineering Science & Technology Review. 11 (2018) 138-45.
[215] K.L. Lawrence. ANSYS tutorial release 13. SDC Publications 2011.
[216] ANSYS. ANSYS Fluent Tutorial Guide, Release 18.0. 2017.
[217] C. Argyropoulos, N. Markatos. Recent advances on the numerical modelling of turbulent flows. Applied Mathematical Modelling. 39 (2015) 693-732.
[218] S. Benjanirat, L.N. Sankar, G. Xu. Evaluation of turbulence models for the prediction of wind turbine aerodynamics. Wind Energy Symposium 2003. pp. 73-83.
[219] P.A.C. Rocha, H.H.B. Rocha, F.O.M. Carneiro, M.E. Vieira da Silva, A.V. Bueno. k–ω SST (shear stress transport) turbulence model calibration: A case study on a small scale horizontal axis wind turbine. Energy. 65 (2014) 412-8.
[220] M. Asli, B. Mashhadi Gholamali, A. Mesgarpour Tousi. Numerical analysis of wind turbine airfoil aerodynamic performance with leading edge bump. Mathematical Problems in Engineering. (2015) 493293.
[221] F. Calomino, G. Alfonsi, R. Gaudio, A. D'Ippolito, A. Lauria, A. Tafarojnoruz, et al. Experimental and numerical study of free-surface flows in a corrugated pipe. Water. 10 (2018) 638.
[222] D.C. Wilcox. Turbulence modeling for CFD. DCW industries La Canada, CA 1998.
[223] C.L. Rumsey, P.R. Spalart. Turbulence model behavior in low Reynolds number regions

of aerodynamic flowfields. AIAA Journal. 47 (2009) 982-93.
[224] S.R. Allmaras, F.T. Johnson. Modifications and clarifications for the implementation of the Spalart-Allmaras turbulence model. Seventh international conference on computational fluid dynamics (ICCFD7) 2012. pp. 1-11.
[225] B. Aupoix, P. Spalart. Extensions of the Spalart–Allmaras turbulence model to account for wall roughness. International Journal of Heat and Fluid Flow. 24 (2003) 454-62.
[226] K. Mansour, M. Yahyazade. Effects of turbulence model in computational fluid dynamics of horizontal axis wind turbine aerodynamic. WSEAS Trans Appl Theor Mech. 3 (2011).
[227] F. Menter, R. Langtry, S. Völker. Transition modelling for general purpose CFD codes. Flow, Turbulence and Combustion. 77 (2006) 277-303.
[228] P. Bourdin, J.D. Wilson. Windbreak aerodynamics: is computational fluid dynamics reliable? Boundary-layer Meteorology. 126 (2008) 181-208.
[229] G. Sahu, R. Rathore. Determination of Torque Produced by Horizontal Axis Wind Turbine Blade Using FSI Analysis for Low Wind Speed Regime. IJISET-International Journal of Innovative Science, Engineering & Technology. 2 (2015) 1069-73.
[230] A. Sudhamshu, M.C. Pandey, N. Sunil, N. Satish, V. Mugundhan, R.K. Velamati. Numerical study of effect of pitch angle on performance characteristics of a HAWT. Engineering Science and Technology, an International Journal. 19 (2016) 632-41.
[231] W. Hallgren, U.B. Gunturu, A. Schlosser. The potential wind power resource in Australia: a new perspective. PloS One. 9 (2014) e99608.
[232] SEDA. 03–04 Annaul Report Sustainable Energy Developmentg Authority of NSW. (2004).
[233] G.A. "Australian government (Department of Industry, Bureau of Resources and Energy Economics)". Australian Energy Resource Assessment. Canberra, Australia.
[234] P.E. Bett, H.E. Thornton, R.T. Clark. Using the Twentieth Century Reanalysis to assess climate variability for the European wind industry. Theoretical and Applied Climatology. 127 (2017) 61-80.
[235] H. MacGillivray, K. Balanda. The relationships between skewness and kurtosis. Australian Journal of Statistics. 30 (1988) 319-37.
[236] K.V. Mardia. Measures of multivariate skewness and kurtosis with applications. Biometrika. 57 (1970) 519-30.
[237] J. Bai, S. Ng. Tests for Skewness, Kurtosis, and Normality for Time Series Data. Journal of Business & Economic Statistics. 23 (2005) 49-60.
[238] D. Joanes, C. Gill. Comparing measures of sample skewness and kurtosis. Journal of the Royal Statistical Society: Series D (The Statistician). 47 (1998) 183-9.
[239] B. Sürücü. Goodness-of-fit tests for multivariate distributions. Communications in Statistics-Theory and Methods. 35 (2006) 1319-31.

[240] M.S. Srivastava. A measure of skewness and kurtosis and a graphical method for assessing multivariate normality. Statistics & Probability Letters. 2 (1984) 263-7.
[241] J. Wang, J. Hu, K. Ma. Wind speed probability distribution estimation and wind energy assessment. Renewable and sustainable energy Reviews. 60 (2016) 881-99.
[242] K.P. Balanda, H. MacGillivray. Kurtosis: a critical review. The American Statistician. 42 (1988) 111-9.
[243] G. Brys, M. Hubert, A. Struyf. Robust measures of tail weight. Computational Statistics & Data Analysis. 50 (2006) 733-59.
[244] J. Wu, J. Wang, D. Chi. Wind energy potential assessment for the site of Inner Mongolia in China. Renewable and Sustainable Energy Reviews. 21 (2013) 215-28.
[245] A.N. Celik. Energy output estimation for small-scale wind power generators using Weibull-representative wind data. Journal of Wind Engineering and Industrial Aerodynamics. 91 (2003) 693-707.
[246] A. Dahmouni, M.B. Salah, F. Askri, C. Kerkeni, S.B. Nasrallah. Wind energy in the Gulf of Tunis, Tunisia. Renewable and Sustainable Energy Reviews. 14 (2010) 1303-11.
[247] A. Ucar, F. Balo. Assessment of wind power potential for turbine installation in coastal areas of Turkey. Renewable and Sustainable Energy Reviews. 14 (2010) 1901-12.
[248] E.K. Akpinar, S. Akpinar. A statistical analysis of wind speed data used in installation of wind energy conversion systems. Energy Conversion and Management. 46 (2005) 515-32.
[249] E.C. Morgan, M. Lackner, R.M. Vogel, L.G. Baise. Probability distributions for offshore wind speeds. Energy Conversion and Management. 52 (2011) 15-26.
[250] I. Mert, C. Karakuş. A statistical analysis of wind speed data using Burr, generalized gamma, and Weibull distributions in Antakya, Turkey. Turkish Journal of Electrical Engineering & Computer Sciences. 23 (2015) 1571-86.
[251] K. Bury. Statistical distributions in engineering. Cambridge University Press 1999.
[252] A. Allouhi, O. Zamzoum, M. Islam, R. Saidur, T. Kousksou, A. Jamil, et al. Evaluation of wind energy potential in Morocco's coastal regions. Renewable and Sustainable Energy Reviews. 72 (2017) 311-24.
[253] J. Kamau, R. Kinyua, J. Gathua. 6 years of wind data for Marsabit, Kenya average over 14 m/s at 100 m hub height; An analysis of the wind energy potential. Renewable Energy. 35 (2010) 1298-302.
[254] F. Fazelpour, N. Soltani, S. Soltani, M.A. Rosen. Assessment of wind energy potential and economics in the north-western Iranian cities of Tabriz and Ardabil. Renewable and Sustainable Energy Reviews. 45 (2015) 87-99.
[255] F. Fazelpour, N. Soltani, M.A. Rosen. Wind resource assessment and wind power potential for the city of Ardabil, Iran. International Journal of Energy and Environmental Engineering. 6 (2015) 431-8.

[256] J. Seguro, T. Lambert. Modern estimation of the parameters of the Weibull wind speed distribution for wind energy analysis. Journal of Wind Engineering and Industrial Aerodynamics. 85 (2000) 75-84.
[257] S.F. Khahro, K. Tabbassum, A.M. Soomro, L. Dong, X. Liao. Evaluation of wind power production prospective and Weibull parameter estimation methods for Babaurband, Sindh Pakistan. Energy conversion and Management. 78 (2014) 956-67.
[258] N. Masseran, A.M. Razali, K. Ibrahim. An analysis of wind power density derived from several wind speed density functions: The regional assessment on wind power in Malaysia. Renewable and Sustainable Energy Reviews. 16 (2012) 6476-87.
[259] N. Masseran. Evaluating wind power density models and their statistical properties. Energy. 84 (2015) 533-41.
[260] C. Forbes, M. Evans, N. Hastings, B. Peacock. Statistical distributions. John Wiley & Sons 2011.
[261] B.M. Bolstad. Comparing some iterative methods of parameter estimation for censored gamma data. University of Waikato, Master of Science thesis. Hamilton, New Zealand. (1998).
[262] T. Chai, R.R. Draxler. Root mean square error (RMSE) or mean absolute error (MAE)? Geoscientific Model Development Discussions. 7 (2014) 1525-34.
[263] T. Tjur. Coefficients of determination in logistic regression models—A new proposal: The coefficient of discrimination. The American Statistician. 63 (2009) 366-72.
[264] D.J. Spiegelhalter, N.G. Best, B.P. Carlin, A. Van der Linde. The deviance information criterion: 12 years on. Journal of the Royal Statistical Society: Series B: Statistical Methodology. (2014) 485-93.
[265] D.K. Pauler. The Schwarz criterion and related methods for normal linear models. Biometrika. 85 (1998) 13-27.
[266] O. Alavi, K. Mohammadi, A. Mostafaeipour. Evaluating the suitability of wind speed probability distribution models: A case of study of east and southeast parts of Iran. Energy Conversion and Management. 119 (2016) 101-8.
[267] T.P. Chang. Performance comparison of six numerical methods in estimating Weibull parameters for wind energy application. Applied Energy. 88 (2011) 272-82.
[268] E. Erdem, J. Shi. ARMA based approaches for forecasting the tuple of wind speed and direction. Applied Energy. 88 (2011) 1405-14.
[269] N.M. Al-Abbadi. Wind energy resource assessment for five locations in Saudi Arabia. Renewable Energy. 30 (2005) 1489-99.
[270] G. Gualtieri, S. Secci. Extrapolating wind speed time series vs. Weibull distribution to assess wind resource to the turbine hub height: A case study on coastal location in Southern Italy. Renewable Energy. 62 (2014) 164-76.
[271] M.E. Okorie, F. Inambao, Z. Chiguvare. Evaluation of wind shear coefficients, surface

roughness and energy yields over inland locations in Namibia. Procedia Manufacturing. 7 (2017) 630-8.
[272] A. Bagavathsingh, C. Srinivas, R. Baskaran, B. Venkatraman, P. Sardar Maran. Wind direction dependent vertical wind shear and surface roughness parameter in two different coastal environments. Proceedings of the International Conference on Radiological Safety in Workplace, Nuclear Facilities and Environment: Book of Abstracts 2016.
[273] O.N. Laban, C.M. Maghanga, K. Joash. Determination of the Surface Roughness Parameter and Wind Shear Exponent of Kisii Region from the On-Site Measurement of Wind Profiles. Journal of Energy. 2019 (2019).
[274] M. Hussain. Dependence of power law index on surface wind speed. Energy Conversion and Management. 43 (2002) 467-72.
[275] W. Zhou, H. Yang, Z. Fang. Wind power potential and characteristic analysis of the Pearl River Delta region, China. Renewable Energy. 31 (2006) 739-53.
[276] G. Van Kuik, J.N. Sørensen, V. Okulov. Rotor theories by Professor Joukowsky: momentum theories. Progress in Aerospace Sciences. 73 (2015) 1-18.
[277] V. Okulov, J.N. Sørensen. Maximum efficiency of wind turbine rotors using Joukowsky and Betz approaches. Journal of Fluid Mechanics. 649 (2010) 497.
[278] S. Drzewiecki. Théorie Générale de l'Hélice Propulsive. Paris. French "General Theory of the Propulsive Helix". (1920).
[279] Z. Sun, J. Chen, W.Z. Shen, W.J. Zhu. Improved blade element momentum theory for wind turbine aerodynamic computations. Renewable Energy. 96 (2016) 824-31.
[280] R. Lanzafame, M. Messina. Fluid dynamics wind turbine design: Critical analysis, optimization and application of BEM theory. Renewable Energy. 32 (2007) 2291-305.
[281] D.C. Sale. HARP_Opt User's Guide. NWTC Design Codes, Available: http://wind nrel gov/designcodes/simulators/HARP_Opt/Last modified. (2010).
[282] T.-t. Zhang, Z.-g. Wang, W. Huang, L. Yan. Parameterization and optimization of hypersonic-gliding vehicle configurations during conceptual design. Aerospace Science and Technology. 58 (2016) 225-34.
[283] M.S. Selig, V.L. Coverstone-Carroll. Application of a genetic algorithm to wind turbine design. Journal of Energy Resources Technology 118 (1996) 22-28.
[284] A. Platt, M. Buhl. Wt perf user guide for version 3.05. Golden, CO: National Renewable Energy Laboratory. (2012).
[285] G. Kröger, U. Siller, J. Dabrowski. Aerodynamic Design and Optimization of a Small Scale Wind Turbine. Turbo Expo: Power for Land, Sea, and Air. American Society of Mechanical Engineers 2014. p. V02BT45A021.
[286] Ö. Ceyhan. Aerodynamic design and optimization of horizontal axis wind turbines by using BEM theory and genetic algorithm. Thesis, Graduate School of Natural and Applied Sciences of

Middle East Technical University, 2008.
[287] L. Wang, X. Tang, X. Liu. Optimized chord and twist angle distributions of wind turbine blade considering Reynolds number effects. Wind Energy: Materials, Engineering and Policies (WEMEP). (2012).
[288] D. Vučina, I. Marinić-Kragić, Z. Milas. Numerical models for robust shape optimization of wind turbine blades. Renewable Energy. 87 (2016) 849-62.
[289] X. Shen, H. Yang, J. Chen, X. Zhu, Z. Du. Aerodynamic shape optimization of non-straight small wind turbine blades. Energy Conversion and Management. 119 (2016) 266-78.
[290] A. Hassanzadeh, A.H. Hassanabad, A. Dadvand. Aerodynamic shape optimization and analysis of small wind turbine blades employing the Viterna approach for post-stall region. Alexandria Engineering Journal. 55 (2016) 2035-43.
[291] J. Seo, J.-H. Yi, J.-S. Park, K.-S. Lee. Review of tidal characteristics of Uldolmok Strait and optimal design of blade shape for horizontal axis tidal current turbines. Renewable and Sustainable Energy Reviews. 113 (2019) 109273.
[292] W. Xudong, W.Z. Shen, W.J. Zhu, J.N. Sørensen, C. Jin. Shape optimization of wind turbine blades. Wind Energy: An International Journal for Progress and Applications in Wind Power Conversion Technology. 12 (2009) 781-803.
[293] Y. Li, J.-H. Yi, D. Sale. Recent improvement of optimization methods in a tidal current turbine optimal design tool. 2012 Oceans. IEEE 2012. pp. 1-8.
[294] K. Hamada, T. Smith, N. Durrani, N. Qin, R. Howell. Unsteady flow simulation and dynamic stall around vertical axis wind turbine blades. 46th AIAA Aerospace Sciences Meeting and Exhibit 2008. p. 1319.
[295] M. Ge, D. Tian, Y. Deng. Reynolds number effect on the optimization of a wind turbine blade for maximum aerodynamic efficiency. Journal of Energy Engineering. 142 (2014) 04014056.
[296] Z. Du, M. Selig. The effect of rotation on the boundary layer of a wind turbine blade. Renewable Energy. 20 (2000) 167-81.
[297] G. Bangga, T. Lutz, E. Krämer. Numerical investigation of unsteady aerodynamic effects on thick flatback airfoils. arXiv preprint arXiv:170504211. (2017).
[298] D.P. Doane, L.E. Seward. Measuring skewness: a forgotten statistic? Journal of Statistics Education. 19 (2011) 1-18.
[299] G. Brys, M. Hubert, A. Struyf. A robust measure of skewness. Journal of Computational and Graphical Statistics. 13 (2004) 996-1017.
[300] N. Aries, S.M. Boudia, H. Ounis. Deep assessment of wind speed distribution models: A case study of four sites in Algeria. Energy Conversion and Management. 155 (2018) 78-90.
[301] I.T. Togrul, C. Ertekin. A statistical investigation on the wind energy potential of Turkey's geographical regions. Energy Sources, Part A: Recovery, Utilization, and Environmental Effects.

33 (2011) 1399-421.
[302] C.W. Kent, C.S.B. Grimmond, D. Gatey, J.F. Barlow. Assessing methods to extrapolate the vertical wind-speed profile from surface observations in a city centre during strong winds. Journal of Wind Engineering and Industrial Aerodynamics. 173 (2018) 100-11.
[303] B.H. Bailey, S.L. McDonald, D.W. Bernadett, M.J. Markus, K.V. Elsholz. Wind resource assessment handbook: Fundamentals for conducting a successful monitoring program. National Renewable Energy Lab., Golden, CO (US); AWS Scientific, Inc. 1997.
[304] G. Eke, J. Onyewudiala. Optimization of wind turbine blades using genetic algorithm. Global Journal of Research In Engineering. 10 (2010) 22-26.
[305] M.G. Trudeau. Structural and hydrodynamic design optimization enhancements with application to marine hydrokinetic turbine blades. Penn State Electronic Theses and Dissertations for Graduate School 2011.